

2

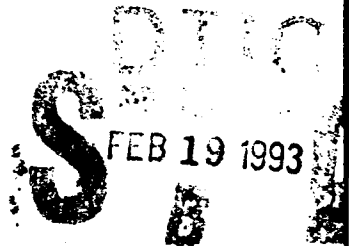
AD-A260 879



**Damage-Survivable
and
Damage-Tolerant
Laminated Composites
with
Optimally placed
Piezoelectric Layers**

Final Report No. 1

**S. P. Joshi
W.S. Chan**

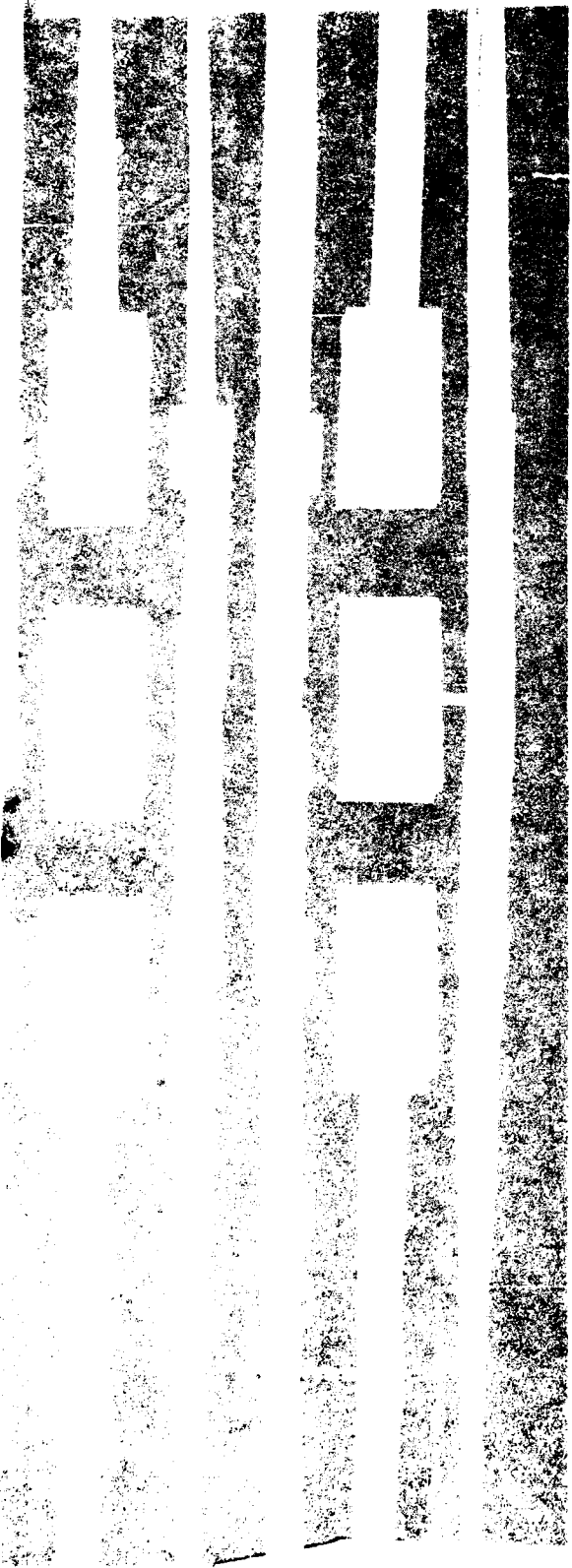


**November 1992
U.S. Army Research Office
Grant No. DAAL03-89-G-0090**

**University of Texas at Arlington
Arlington, TX 76019**

**Approved For Public Release
Distribution Unlimited.**

93-03530



UNCLASSIFIED

SECURITY CLASSIFICATION OF THIS PAGE

REPORT DOCUMENTATION PAGE

1a. REPORT SECURITY CLASSIFICATION Unclassified		1b. RESTRICTIVE MARKINGS	
2a. SECURITY CLASSIFICATION AUTHORITY		3. DISTRIBUTION/AVAILABILITY OF REPORT Approved for public release; distribution unlimited.	
2b. DECLASSIFICATION/DOWNGRADING SCHEDULE			
4. PERFORMING ORGANIZATION REPORT NUMBER(S) Final Report No. 1		5. MONITORING ORGANIZATION REPORT NUMBER(S) ARO 27167.3-EG-SM	
6a. NAME OF PERFORMING ORGANIZATION Univ. of Texas at Arlington	6b. OFFICE SYMBOL (If applicable)	7a. NAME OF MONITORING ORGANIZATION U. S. Army Research Office	
6c. ADDRESS (City, State, and ZIP Code) Mechanical and Aerospace Engineering Dept. The University of Texas at Arlington Arlington, TX 76019		7b. ADDRESS (City, State, and ZIP Code) P. O. Box 12211 Research Triangle Park, NC 27709-2211	
8a. NAME OF FUNDING/SPONSORING ORGANIZATION U. S. Army Research Office	8b. OFFICE SYMBOL (If applicable)	9. PROCUREMENT INSTRUMENT IDENTIFICATION NUMBER DAAL 03-89-G-0090	
8c. ADDRESS (City, State, and ZIP Code) P. O. Box 12211 Research Triangle Park, NC 27709-2211		10. SOURCE OF FUNDING NUMBERS	
		PROGRAM ELEMENT NO.	PROJECT NO.
		TASK NO.	WORK UNIT ACCESSION NO.
11. TITLE (Include Security Classification) Damage Survivable and Damage-Tolerant Laminated Composites With Optimally Placed Piezoelectric Layers			
12. PERSONAL AUTHOR(S) S.P. Joshi, W.S. Chan			
13a. TYPE OF REPORT Final Report	13b. TIME COVERED FROM Aug. 89 TO Dec. 92	14. DATE OF REPORT (Year, Month, Day) 1992, November 13	15. PAGE COUNT -
16. SUPPLEMENTARY NOTATION The view, opinions and/or findings contained in this report are those of the author(s) and should not be construed as an official Department of the Army position, policy, or decision, unless so designated by other documentation.			
17. COSATI CODES		18. SUBJECT TERMS (Continue on reverse if necessary and identify by block number)	
FIELD	GROUP	SUB-GROUP	
		Smart Structures	
19. ABSTRACT (Continue on reverse if necessary and identify by block number) The main objective of the research is to assure that the embedded sensors/actuators in a smart laminated composite structure are damage-survivable and damage-tolerant. The research requires development of analytical and computational techniques and tools together with the experimental evaluation of smart composite structural elements. An understanding of electroelastic constitutive behavior is critical to predicting the response of a structure with embedded piezoelectric material. Our research efforts in this area has produced a concise formulation of linear constitutive relations that has been extended to the nonlinear case. The CDA (Composite Delamination Analysis) and SDACL (Static and Dynamic Analysis for Composite Laminated Plates) packages have been modified to incorporate piezoelectric coupling in a quasi-3D and plane stress analysis. These codes are capable of analyzing laminated composites with arbitrarily placed piezoceramic patches. Both actuation and sensing can be simulated by using these codes. Edge stresses in the vicinity of an embedded piezoceramic patch and stress distribution in the vicinity of electrodes due to an actuation electric			
20. DISTRIBUTION/AVAILABILITY OF ABSTRACT <input type="checkbox"/> UNCLASSIFIED/UNLIMITED <input type="checkbox"/> SAME AS RPT. <input type="checkbox"/> DTIC USERS		21. ABSTRACT SECURITY CLASSIFICATION Unclassified	
22a. NAME OF RESPONSIBLE INDIVIDUAL		22b. TELEPHONE (Include Area Code)	22c. OFFICE SYMBOL

field are obtained by using these codes. A detailed stress field in the vicinity of piezoceramic sensors in a laminated plate under impact loading is also obtained by using one of the modified codes.

Three analytical approaches are identified and incorporated into numerical simulations to estimate the impact location and the magnitude of the impact pulse at the origin. The first method uses a moving time window technique to calculate the origin of the signal. The second method uses the phase difference of signals recorded at two locations to estimate the origin. The third method makes the first guess of distance of the origin by estimating the time interval between the maximum and minimum frequency components arriving at the recording location and the signal is reconstructed by transformation. The iteration procedure used in this method is based on the fact that the impact pulse at the origin is all positive. The phase difference method is being evaluated experimentally.

Typically, piezoceramics have an allowable strain-to-failure that is one tenth that of most graphite/epoxy composites. Residual thermal stresses and strains gain importance in designing such composite laminates. Accurate analysis of these stresses is critical. If the thermally induced strains are too large, it is possible to modify the laminate's coefficient of thermal expansion by adding plies of a dissimilar material such as fiberglass/epoxy. These modifications can relieve much of the thermal stress of the piezoceramic.

The fabrication and curing processes for smart composite laminates involve additional parameters arising from the placement of sensors and actuators. We have successfully fabricated and cured laminated panels with a large number of embedded piezoceramics. Various aspects of the fabrication and curing processes for laminates with multiple embedded piezoceramic sensors and actuators have been identified.

Tensile material tests are performed on coupons with and without piezoceramics embedded in them. These coupons are cut from a single panel to reduce the influence of fabrication and curing procedures. These test results show that the passive presence of piezoceramics have a negligible effect on the tensile properties of the laminate. Damage initiation in the vicinity of a piezoceramic may become critical under complex loading and may also cause a deterioration in the performance of piezoceramics as sensors and actuators. It is well known that a transverse impact by a foreign object creates extensive damage in the form of matrix cracking and delamination. A set of impact tests are performed to evaluate the effect of the presence of piezoceramic wafers on impact induced damage. Initial results indicate that the presence of the piezoceramic does not adversely effect the incipient damage due to a transverse impact. Optical microscopic pictures, X-ray radiographs and ultrasonic C-scans are employed to characterize the impact damage. Piezoceramic wafers are subjected to the curing cycle's pressure and temperature without embedding them in a laminate. These wafers are then tested to evaluate the effect of the curing cycle on the piezoelectric properties.

The research presented in this report merely addresses some of the initial concerns with the use of structures with embedded sensors and actuators, but it is an important beginning.

Acknowledgments

Authors acknowledge and greatly appreciate the continuous support and encouragement from Dr. Gary Anderson during the course of the research presented in this report. The experimental evaluation of smart laminates could not have been possible without the personal involvement of Prof. Roger Goolsby at various stages of the program. He was instrumental in making the experimental program proceed in a timely manner.

This report contains research work by the following graduate students:

Dipen Shah
John Mannas
Curtis Chapin
Chi-ming Lu
Suresh Subramanian

DTIC QUALITY INSPECTED 3

Accession For	
NTIS GRA&I	<input checked="" type="checkbox"/>
DTIC TAB	<input type="checkbox"/>
Unannounced	<input type="checkbox"/>
Justification	
By _____	
Distribution/	
Availability Codes	
Dist	Avail and/or Special
A-1	

The following undergraduate students participated in the project:

Clint Bauer
Danis Creede
Victor Jacklin
Randy Lawrence
Jason Stephens
G. Botha
A. Howard

I am thankful to Mr. Dipen Shah for the help during the manuscript preparation.

Shiv P. Joshi
Associate Professor

TABLE OF CONTENTS

Chapter 1	SMART MATERIALS AND STRUCTURES	1
	1.1 Smart Materials	2
	1.2 Smart Structures	3
	1.3 Smart Structures Research at UTA	5
	1.3.1 Analytical Research	5
	1.3.2 Experimental Research	7
Chapter 2	NONLINEAR CONSTITUTIVE RELATIONS FOR PIEZOCERAMICS	10
	2.1 Piezoelectric Field Equations	10
	2.2 Linear Constitutive Equations	11
	2.3 Nonlinear Constitutive Equations	13
Chapter 3	FINITE ELEMENT ANALYSIS OF SMART PLATES	17
	3.1 The General Laminate Theory	18
	3.2 Inplane Plate Finite Element Analysis	19
	3.2.1 Formulation Including Piezoelectric Constitutive Relation	19
	3.2.2 Stress Smoothing and Evaluation of Nodal Stresses	22
	3.3 Quasi-3D Finite Element Analysis	24
	3.3.1 Formulation of Finite Element Equations	25
	3.4 Some Numerical Simulations	27
	3.4.1 Inplane Analysis	27
	3.4.2 Combination of Quasi-3D and Plate Finite Element Analysis	44
	3.4.3 Quasi-3D Analysis of Laminates with Embedded Piezoelectric Layers	50
	3.4.4 Response of Piezoelectric Layer Due to Surface Electrodes	57
	Appendix 3A :Nodal Loads Due to Piezoelectric Stress Traction	64
Chapter 4	IMPACT SENSING BY PIEZOCERAMIC PATCHES	67
	4.1 Linear Constitutive Relations	67
	4.2 Finite Element Code Modification	68
	4.3 Model Properties	71
	4.4 Model Verification	73
	4.5 Results And Discussion	74
	4.5.1 Effect of Piezoelectric Patch Location on Load and Global Strain	74
	4.5.2 Electric Field Variation Due to Piezoelectric Patch Location	77
	4.5.3 Electric Field Variation Due to Piezoelectric Patch Size and Shape	80
	4.5.4 Electric Field Across Piezoelectric Patches	81
	4.6 Conclusions And Recommendations	85
Chapter 5	IMPACT LOCATION ESTIMATION	87
	5.1 Dispersive Signal Analysis	87
	5.2 Moving Window Approach	88
	5.3 Phase Difference Approach	94
	5.4 Reconstruction Approach	95
	5.5 Computer Simulations	97
	5.5.1 Moving Window Simulation	97
	5.5.2 Phase Difference Simulation	100

5.5.3 Reconstruction Simulation	101
5.6 Conclusions	102
Chapter 6 RESIDUAL THERMAL STRESSES IN SMART LAMINATES	109
6.1 Analysis	109
6.2 Discussion Of Results	111
6.2.1 Edge Effects	112
6.3 Smart Laminate Design Implications	116
Chapter 7 FABRICATION AND CURING PROCESSES	117
7.1 Piezoceramics	117
7.2 Fabrication	117
7.3 Curing Procedure	122
7.4 Effect of Curing on a Piezoceramic.	123
Chapter 8 EXPERIMENTAL CHARACTERIZATION OF SMART LAMINATES	131
8.1 Mechanical Properties Characterization	133
8.2 Impact Induced Fracture	135

LIST OF FIGURES

FIGURE 1 . 1	Smart structures	1
FIGURE 1 . 2	Smart materials	2
FIGURE 1 . 3	Four categories of existing smart structures grouped according to their main capability	4
FIGURE 3 . 1	Nine-noded isoparametric element.	19
FIGURE 3 . 2	Stresses distributions obtained using a) gaussian point averaging and b) quadratic least squares extrapolation scheme.	22
FIGURE 3 . 3	Representative section of laminate for quasi-3D finite element analysis.	25
FIGURE 3 . 4	A square plate with different shapes of piezoelectric patches.	28
FIGURE 3 . 5	Finite element meshes for different configurations of the piezoelectric patches	29
FIGURE 3 . 6	Distribution of normalized stress σ_x in the plate with square piezoelectric patch.	30
FIGURE 3 . 7	Stress distribution of σ_y in the plate with square piezoelectric patch.. . . .	31
FIGURE 3 . 8	Stress distribution of σ_{xy} in the plate with square piezoelectric patch.	31
FIGURE 3 . 9	Stress Distribution of σ_x in plate with circular piezoelectric patch	32
FIGURE 3 . 10	Distribution of shear stress σ_{xy} in plate with circular piezoelectric patch	32
FIGURE 3 . 11	Distribution of stresses σ_r , σ_θ , and $\sigma_{r\theta}$ along the circumference of the circular piezoelectric patch on the aluminum side.	33
FIGURE 3 . 12	Distribution of stresses σ_r , σ_θ , and $\sigma_{r\theta}$ along the circumference of the circular piezoelectric patch on the piezoelectric side.	33
FIGURE 3 . 13	Distribution of stresses σ_r and σ_θ along the radial direction at $\theta = 45^\circ$ in the plate with the circular patch.	34
FIGURE 3 . 14	Distribution of normalized stress σ_x in the plate with elliptical piezoelectric patch.	34
FIGURE 3 . 15	Stress distribution of σ_{xy} in the plate with elliptical piezoelectric patch.	35
FIGURE 3 . 16	Distribution of stresses σ_n , σ_t , and σ_{nt} along the circumference of the elliptical piezoelectric patch on the aluminum side.	36
FIGURE 3 . 17	Distribution of stresses σ_n , σ_t , and σ_{nt} along the circumference of the elliptical piezoelectric patch on the piezoelectric side.	36
FIGURE 3 . 18	Comparison of the distributions of σ_x along the x-axis in the plate for all the patches.	37
FIGURE 3 . 19	Comparison of the distributions of σ_x along the y-axis in the plate for all the patches.	37
FIGURE 3 . 20	Distribution of σ_y along the y-axis in the plate.	38
FIGURE 3 . 21	Distribution of σ_y along the x-axis of the plate.	38
FIGURE 3 . 22	Distribution of σ_x along the x-axis in the aluminum layer (layer 1) for the layered plate with square patch and with rectangular patch.	40
FIGURE 3 . 23	Distribution of σ_x along the x-axis in the combined layer (layer 2) for the layered plate with square patch and with rectangular patch.	40
FIGURE 3 . 24	Distribution of σ_y along the x-axis in the aluminum layer (layer 1) for the layered plate with square patch and with rectangular patch.	41
FIGURE 3 . 25	Distribution of σ_y along the x-axis in the combined layer (layer 2) for the layered plate with square patch and with rectangular patch.	41
FIGURE 3 . 26	Distribution of σ_x along the y-axis in the aluminum layer (layer 1) for the layered plate with square patch and with rectangular patch.	42

FIGURE 3 . 27	Distribution of σ_x along the y-axis in the combined layer (layer 2) for the layered plate with square patch and with rectangular patch.42
FIGURE 3 . 28	Distribution of σ_y along the y-axis in the aluminum layer (layer 1) for the layered plate with square patch and with rectangular patch.43
FIGURE 3 . 29	Distribution of σ_y along the y-axis in the combined layer (layer 2) for the layered plate with square patch and with rectangular patch.43
FIGURE 3 . 30	Quasi-3-D finite element modeling of the plate around the material interface.44
FIGURE 3 . 31	Strain distribution along the x-axis of the plate from plate FEM.44
FIGURE 3 . 32	Distribution of σ_x along x-axis at midplane.46
FIGURE 3 . 33	Distribution of σ_y along x-axis at midplane.46
FIGURE 3 . 34	Distribution of σ_z along x-axis at midplane.46
FIGURE 3 . 35	Distribution of σ_x along the x-axis in the middle layer near the surface of the patch.47
FIGURE 3 . 36	Distribution of σ_y along the x-axis in the middle layer near the surface of the patch.47
FIGURE 3 . 37	Distribution of σ_z along the x-axis in the middle layer near the surface of the patch.47
FIGURE 3 . 38	Distribution of σ_x along the x-axis in the aluminum layer near the surface of the patch.48
FIGURE 3 . 39	Distribution of σ_y along the x-axis in the aluminum layer near the surface of the patch.48
FIGURE 3 . 40	Distribution of σ_z along the x-axis in the aluminum layer near the surface of the patch.48
FIGURE 3 . 41	Distribution of strain ϵ_x through the thickness in plate and Q3D models.49
FIGURE 3 . 42	Distribution of strain ϵ_z through the thickness.49
FIGURE 3 . 43	Laminate configuration.50
FIGURE 3 . 44	Free edge interlaminar stress distributions through the thickness in baseline laminates with piezoelectric layer. (case 1).52
FIGURE 3 . 45	Free edge interlaminar stress distributions through the thickness in baseline laminates with piezoelectric layer. (case 2).52
FIGURE 3 . 46	Free edge interlaminar stress distributions through the thickness in baseline laminates with piezoelectric layer. (case 3).53
FIGURE 3 . 47	Free edge interlaminar stress distributions through the thickness in baseline laminates with piezoelectric layer. (case 4).53
FIGURE 3 . 48	Free edge interlaminar stress distributions through the thickness in laminates with piezoelectric layer and adjacent glass plies. (case 1)54
FIGURE 3 . 49	Free edge interlaminar stress distributions through the thickness in laminates with piezoelectric layer and adjacent glass plies. (case 2)54
FIGURE 3 . 50	Free edge interlaminar stress distributions through the thickness in laminates with piezoelectric layer and adjacent glass plies. (case 3)55
FIGURE 3 . 51	Free edge interlaminar stress distributions through the thickness in laminates with piezoelectric layer and adjacent glass plies. (case 4)55
FIGURE 3 . 52	Comparison of interlaminar stress at the glass/piezoelectric interface for all four cases.56
FIGURE 3 . 53	Comparison of interlaminar stress at the glass/piezoelectric interface for all four cases.56
FIGURE 3 . 54	Piezoelectric strip with an array of electrodes58

FIGURE 3 . 55	A repeating unit of the strip for finite element analysis59
FIGURE 3 . 56	Distribution of normalized stress σ_{xx} versus y/a59
FIGURE 3 . 57	Distribution of normalized stress σ_{yy} versus y/a60
FIGURE 3 . 58	Distribution of normalized stress σ_{zz} versus y/a60
FIGURE 3 . 59	Distribution of normalized stress σ_{yz} versus y/a61
FIGURE 3 . 60	σ_{xx} comparison in open and closed circuit region without surface electrode charge.61
FIGURE 3 . 61	Normalized stress σ_{xx} for various sizes of surface electrodes.62
FIGURE 3 . 62	Plate element showing tractions on the plate.64
FIGURE 4 . 1	Model 1 Layout, Piezo-patch Locations and Numbering71
FIGURE 4 . 2	Model 2 Element Layout with 2x2 Piezoelectric Patch72
FIGURE 4 . 3	Model 2 Element Layout with 7x5 and 5x7 Piezoelectric Patches.72
FIGURE 4 . 4	Model 2 Element Layout with Triangular Piezoelectric Patches72
FIGURE 4 . 5	Model 2 Element Layout with Nine 4x4 Piezoelectric Patches.73
FIGURE 4 . 6	Lamina Offset Using a Fake Layer74
FIGURE 4 . 7	Load History for Model 1a.74
FIGURE 4 . 8	Load History for Model 1b.75
FIGURE 4 . 9	Curvatures Near Piezoelectric Elements in Model 1a75
FIGURE 4 . 10	Curvatures Four Elements Away From Piezoelectric Elements in Model 1a76
FIGURE 4 . 11	Curvatures Four Elements Away From Piezoelectric Elements in Model 1b76
FIGURE 4 . 12	Electric Field in Model 1a due to One Piezoelectric Ply.77
FIGURE 4 . 13	Electric Field in Model 1b due to One Piezoelectric Ply.77
FIGURE 4 . 14	Electric Field in Model 2 due to Two Piezoelectric Plies78
FIGURE 4 . 15	Average Electric Field Generated by Piezoelectric Patches 'a' and 'b'78
FIGURE 4 . 16	Average Electric Field Generated by Piezoelectric Patches 'c' Through 'e'79
FIGURE 4 . 17	Time Between Impact and Generation of 0.002 V/cm Average Electric Field79
FIGURE 4 . 18	Average Electric Field for Piezoelectric Patches f, g, c, h, and i80
FIGURE 4 . 19	Average Electric Field for Square Piezoelectric Patches.80
FIGURE 4 . 20	Average Electric Field for Different Shaped Piezoelectric Patches81
FIGURE 4 . 21	Electric Field Plots for 4x4 Element Piezoelectric Patch82
FIGURE 4 . 22	Electric Field Plots for 7x5 Element Piezoelectric Patch83
FIGURE 4 . 23	Electric Field Plots for 4x4 Element Piezoelectric Patch on $[0_s/90_s/0_s]_T$ Layup84
FIGURE 5 . 1	Artificial Dispersive signal.89
FIGURE 5 . 2	The first overlapping window (0-200 point of the artificial dispersive signal).90
FIGURE 5 . 3	The second overlapping window (25-225 point of the artificial dispersive signal).91
FIGURE 5 . 4	The third overlapping window (50-250 point of the artificial dispersive signal).92
FIGURE 5 . 5	The fourth overlapping window (75-275 point of the artificial dispersive signal).93
FIGURE 5 . 6	The fifth overlapping window (100-300 point of the artificial dispersive signal).94

FIGURE 5 . 7	The first window of the moving window approach (0-400 points)	98
FIGURE 5 . 8	The second window of the moving window approach (50-450 points)	99
FIGURE 5 . 9	The third window of the moving window approach (100-500 points)	100
FIGURE 5 . 10	Estimates of the impact point after the second iteration of the phase difference method	101
FIGURE 5 . 11	Underestimate at $x=0.143$ m (exact $x=0.2$ m)	103
FIGURE 5 . 12	Overestimate at $x=0.29$ m (exact $x=0.2$ m)	104
FIGURE 5 . 13	Underestimate at $x=0.1989$ (exact $x=0.2$ m)	105
FIGURE 5 . 14	Overestimate at $x=0.208$ m (exact $x=0.2$ m)	106
FIGURE 5 . 15	Final iteration of the reconstruction approach estimating exact impact location $x=0.2$ m	107
FIGURE 6 . 1	Typical three-dimensional model used for finite element analysis	110
FIGURE 6 . 2	In-plane normal strain distribution through the thickness of laminates shown sufficiently far away from the free edges.	111
FIGURE 6 . 3	X-direction strain at the midplane of the laminates with 0° outer-ply.	112
FIGURE 6 . 4	Z-direction stress at the first $0^\circ/90^\circ$ interface away from the laminate midplane	112
FIGURE 6 . 5	X-Z shear stress at the first $0^\circ/90^\circ$ interface away from the laminate midplane	113
FIGURE 6 . 6	X-direction strain at the free edge shown through the thickness of the laminates with 0° outer plies	113
FIGURE 6 . 7	X-direction strain at the free edge shown through the thickness of the laminates with 90° outer-ply.	114
FIGURE 6 . 8	X-direction strain at the midplane of the laminates with 90° outer-ply.	114
FIGURE 6 . 9	Z-direction stress at the first $90^\circ/0^\circ$ interface away from the laminate midplane	115
FIGURE 6 . 10	X-Z shear stress at the first $90^\circ/0^\circ$ interface away from the laminate midplane	115
FIGURE 7 . 1	Schematic of a laminated plate lay-up with multiple piezoceramic wafers	118
FIGURE 7 . 2	Brass ribbon electrode patterns, piezoceramic patches and bonding surfaces	118
FIGURE 7 . 3	X-Ray radiographs showing the electrode configurations in laminated panels with embedded piezoceramic patches.	119
FIGURE 7 . 4	Nine piezoceramic wafers with brass terminal strips encapsulated in glass/epoxy insulating plies.	120
FIGURE 7 . 5	X-ray radiograph showing undamaged and damaged embedded piezoceramic wafers in the insulating glass/epoxy plies. The cracks initiated at the edges of thick patches of cold-solder epoxy	120
FIGURE 7 . 6	A laminated plate with embedded piezoceramic patches being prepared for autoclave curing.	122
FIGURE 7 . 7	Curing cycles for graphite/epoxy and glass/epoxy prepregs.	123
FIGURE 7 . 8	Variation of the in-plane normal strain due to application of electric field in the thickness direction	124
FIGURE 7 . 9	In-plane normal strain induced by the transverse electric field in the uncured piezoceramic NC1.	125
FIGURE 7 . 10	In-plane normal strain induced by the transverse electric field in the uncured piezoceramic NC3.	125

FIGURE 7 . 11	In-plane normal strain induced by the transverse electric field in the uncured piezoceramic NC4, data-set 1	125
FIGURE 7 . 12	In-plane normal strain induced by the transverse electric field in the uncured piezoceramic NC4, data-set 3 and 4	126
FIGURE 7 . 13	In-plane normal strain induced by the transverse electric field in the uncured piezoceramic NC5.	126
FIGURE 7 . 14	In-plane normal strain induced by the transverse electric field in the uncured piezoceramic NC6, data-set 1,2 and 3	126
FIGURE 7 . 15	In-plane normal strain induced by the transverse electric field in the uncured piezoceramic NC9, data-set 1,2 and 3	127
FIGURE 7 . 16	In-plane normal strain induced by the transverse electric field in the cured piezoceramic C1, data-set 1, 3 and 6.	127
FIGURE 7 . 17	In-plane normal strain induced by the transverse electric field in the cured piezoceramic C1, data-set 2, 4 and 5.	127
FIGURE 7 . 18	In-plane normal strain induced by the transverse electric field in the cured piezoceramic C2	128
FIGURE 7 . 19	In-plane normal strain induced by the transverse electric field in the cured piezoceramic C4, data-set 1, 2, 3 and 4	128
FIGURE 7 . 20	In-plane normal strain induced by the transverse electric field in the cured piezoceramic C4, data-set 5	128
FIGURE 7 . 21	Domain reorientation in piezoceramic (NC2_200) when subjected to corrosive electric field	129
FIGURE 8 . 1	Microscopic cross section view of an embedded piezoceramic patch. . .	131
FIGURE 8 . 2	High magnification microscopic view showing conductive epoxy and brass electrodes	132
FIGURE 8 . 3	Scanning electron microscope photograph of uncured piezoceramic . . .	132
FIGURE 8 . 4	Scanning electron microscope photograph of cured piezoceramic . . .	133
FIGURE 8 . 5	Schematic of the 9 inch X 9 inch panel showing placement of piezoceramic patches, brass terminals and test coupon outlines	133
FIGURE 8 . 6	Stress-strain plots of coupons with and without symmetrically placed piezoceramic patches subjected to longitudinal tensile load	134
FIGURE 8 . 7	Photographs showing mode of failure of unidirectional laminated composite with embedded piezoceramic patches	135
FIGURE 8 . 8	Schematic showing placement of piezoceramic patches and terminals at each 0/90 interface of the base laminate.	136
FIGURE 8 . 9	Transverse cross section through the impact center of a base laminate showing matrix cracks and delamination.	137
FIGURE 8 . 10	Part of the transverse cross sectional view of an impacted specimen containing embedded piezoceramic patches.	138
FIGURE 8 . 11	The continuing part of the cross sectional view of an impacted specimen shown in Figure 8.10.	139
FIGURE 8 . 12	The longitudinal cross section of an impacted specimen showing matrix cracks and delamination.	140

TABLE 1 . 1	Publications acknowledging URI-ARO Grant	7
TABLE 3 . 2	Dimensions of the aluminum plate and the piezoelectric patches	28
TABLE 3 . 3	Material properties for aluminum plate and piezoelectric G1195.	29
TABLE 3 . 4	Material properties used in analysis.	51
TABLE 3 . 5	Stacking sequences used for the different cases.	51
TABLE 3 . 6	Material properties for the piezoceramic G1195.	58
TABLE 4 . 1	Macro MATE	69
TABLE 4 . 2	ELEM Macro	70
TABLE 4 . 3	PIEZ Macro.	70
TABLE 4 . 4	Lamina and Piezoceramic Properties	70
TABLE 6 . 1	Mechanical properties of the graphite/epoxy used in the analysis	109

Chapter 1.

SMART MATERIALS AND STRUCTURES

In the early days, structural integrity was ensured by over-designing. As safety margins have decreased, requirements for preventive inspection and maintenance have increased. Structures in the near future will be able to prevent damage to a certain extent, able to sense the damage, and survive the damage by incorporating adaptive control. They will also be able to alert us to proper maintenance. These structures are termed as "smart structures". Remarkable inventions in sensor technology, discoveries of new materials and increase in computing capabilities have made it possible for the first time to build smart structures. These structures have to be highly redundant, self testing, damage survivable and fault tolerant.

A conventional structure has an unadaptable geometry and load carrying characteristics. In recent years, attempts have been made to introduce structures capable of monitoring and adapting to their environment, providing a "smart" response to external conditions. Although a precise universal definition of a smart structure is not possible, certain attributes are necessary for a structure to qualify as a smart structure. In a broad sense, the structure should be capable of sensing a set of external conditions and responding in a way that is beneficial to its survival. Furthermore, the sensing and responding elements should be integral to the structure (see Figure 1.1). The materials used in the sensing and responding elements of the structure are commonly called smart materials. Any synthetic or natural material whose constitutive behavior can be utilized for sensing and/or responding purposes can be considered to be a smart material.

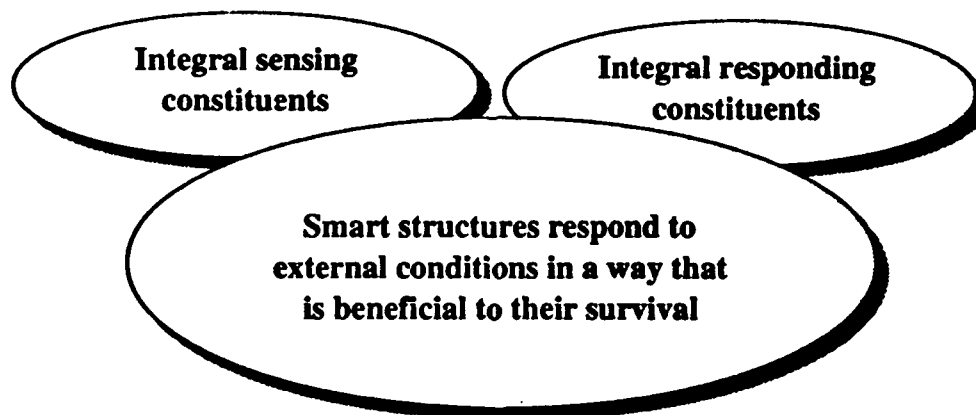


FIGURE 1.1 Smart structures

The idea of a smart structure is relatively new. One component of a smart structure is the "active-structural-element" which has become a focus of research due to its potential applications in the proposed space station. The main thrust of this research has been, until recently, in vibration control and geometric shape manipulation. The references mentioned below are among the technical articles that have given impetus to smart materials and structures research. Dean and James [1] suggested the use of a large number of piezoelectric elements to correct errors in a precision mirror surface. Swigert and Forward [2,3] used piezoelectric elements directly attached to the structure to actively damp vibration. Chen [4] used a piezoelectric material to adjust the stiffness of the wires

to control the response of a structure. Chen, Fanson, Caughey, Hanagud and Baily initiated experimental and theoretical research on smart beam type structures with piezoceramics as integral sensors and actuators [5-9]. Crawley showed that piezoceramic patches can be embedded in composite laminates to control a precision structure [10, 11].

1.1 Smart Materials

Smart materials are the functional constituents of a smart structure. In general, they possess constitutive behavior relating mechanical field variables to electrical, magnetic and optical field variables. Smart materials can be grouped under two broad categories: passive and active. A passive smart material has a desirable but actively unalterable constitutive behavior. On the other hand, an active smart material has an alterable constitutive behavior (see Figure 1.2). The alteration in the constitutive behavior is achieved by a small change in a triggering field variable.

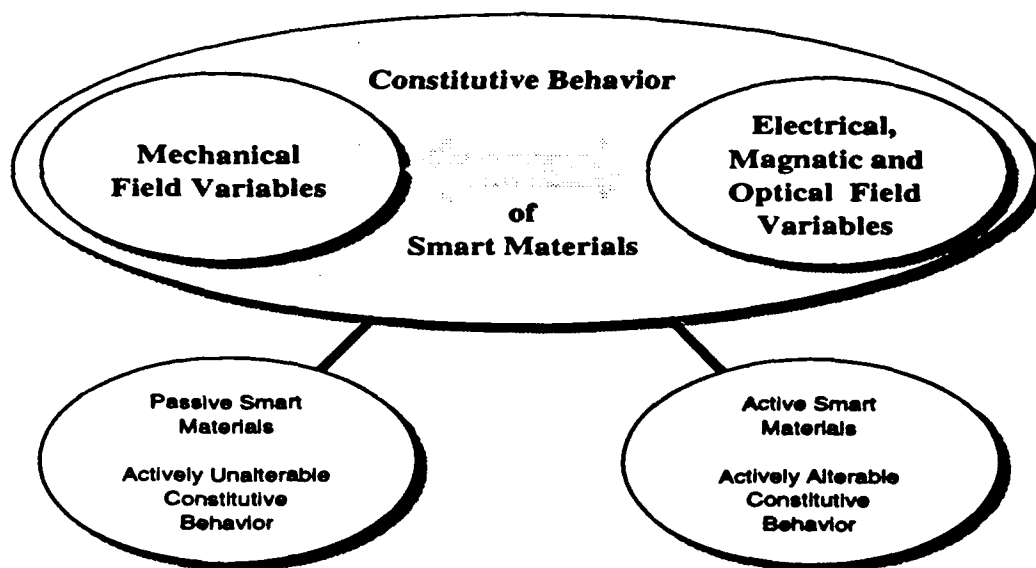


FIGURE 1.2 Smart materials

A piezoelectric material produces electric charges when it is mechanically deformed and conversely, an electric potential causes mechanical deformation of the material. This property makes it suitable for sensor and transducer applications in the structural area. Ceramics such as PZT (Lead-Zirconate-Titanate) and polarized homopolymer of vinylidene fluoride (PVDF) are the two most commonly used piezoelectric materials. Ceramics are especially useful as actuators because of their high piezoelectric strain coefficients. On the other hand, the polymer is suitable for sensor applications because of its high piezoelectric voltage coefficients.

Electrostrictive materials show behavior similar to piezoelectric materials but the relationship between mechanical deformation and electric field is quadratic. The phenomenon of depoling does not exist as it does in piezoceramics. Lead-magnesium-niobate exhibits the electrostrictive effect. The nonlinear behavior and the strong effect of temperature on electrostriction are the two problems with the use of Lead-magnesium-niobate as an actuation constituent. Some ceramics exhibit a large electrostriction without any hysteresis and aging effect during an electric field cycle. They should find some applications as actuation constituents.

Magnetostrictor materials show a relationship between magnetic and mechanical field variables. A relatively new actuator material exhibiting extremely high strains is the magnetostrictor

Terfenol. Its main constituents are terbium and iron. A more recent alloy, Terfenol-D, contains an additional rare-earth element, dysprosium, which leads to "giant" magnetostriction effects. In certain ferroelectrics, a photostrictive behavior is observed: a constant electromotive force is generated when the material is exposed to light. This behavior is a result of the coupling between the photovoltaic and inverse piezoelectric effects.

Smart molecules are designed to receive a stimulus, transmit or process it, and respond by producing a desirable effect. Modular molecules consisting of oligomers with particular receptor or functional properties, are synthesized separately and then combined in appropriate ways.

Shape memory materials (SMM) are an active class of thermomechanical smart materials. A plastically deformed material that recovers its original shape when heated is known as a shape memory material. This phenomenon results from a crystalline phase change known as the thermoelastic martensitic transformation. At temperatures below the transformation temperature, the material is martensitic. In this phase the material is very soft and can be deformed easily. Heating above the transformation temperature recovers the original shape by a transformation to the austenitic phase. The transformation from austenite to martensite and vice versa does not take place at the same temperature.

A semiconductive piezoelectric material provides a non-uniform distribution of an electric field which can be utilized in producing beneficial deformation fields. Magnetostrictive materials such as Lead Zirconate Titanate-based ceramics reach up to 0.4% strain which is much larger than that expected in electrostrictor or piezoelectric materials. These strains are associated with phase transitions from the antiferroelectric to the ferroelectric phase. The magnetostrictive behavior of rare earth iron alloys and high permeability amorphous magnetic materials make them attractive for mechanical transduction and ultrasensitive strain detection. A proper balance of magnetic anisotropy and magnetostriction, and a proper choice of crystal axes in these materials can transfer a large amount of energy between the magnetic and mechanical states with the application of a small triggering magnetic field.

Electrorheological (ER) fluids consist of highly-polarizable fine particles dispersed in an insulating fluid medium. The rheological properties of ER fluids are altered by the application of an electric field. In addition to ER fluids, certain classes of ionizable polymeric solutions containing polyacids and polybases are capable of undergoing substantial expansions and contractions if subjected to electrolytic ionization that changes the pH of the solutions.

Optical fibers are also considered to be a smart constituent of a structure. The main advantage of Fiber Optic Sensors (FOS) is their relative immunity to electromagnetic induction. Some promising FOS concepts are RF- Modulated Phase-Locked Loop sensors, Sagnac-type Interferometer strain sensors, Mach-Zehnder strain sensors held at null by a PZT stretcher, Mach-Zehnder strain sensors with different fiber cores, Double Mach-Zehnder strain sensors with fiber cores, and elliptic -core two-mode fiber interferometers.

1.2 Smart Structures

Research related to smart structures has increased dramatically in the last few years. Most of the research has been concentrated on geometric shape modification and vibration and acoustic control. The details of recent smart structures research have been reported at recent conferences in the US, Japan, and Europe, and an excellent review of recent developments in smart structures is presented by Wada [12].

We classify smart structures according to four major categories. The first of these covers control configured or variable geometry structures. Active geometric adaptation is the main feature

of this class of structures. Structures which have active damping, vibration suppression, and acoustic control capabilities fall into the second category. The third category of smart structures are self diagnosing and damage monitoring structures. All other special purpose smart structures may be grouped under the fourth special purpose category as shown in Figure 1.3.

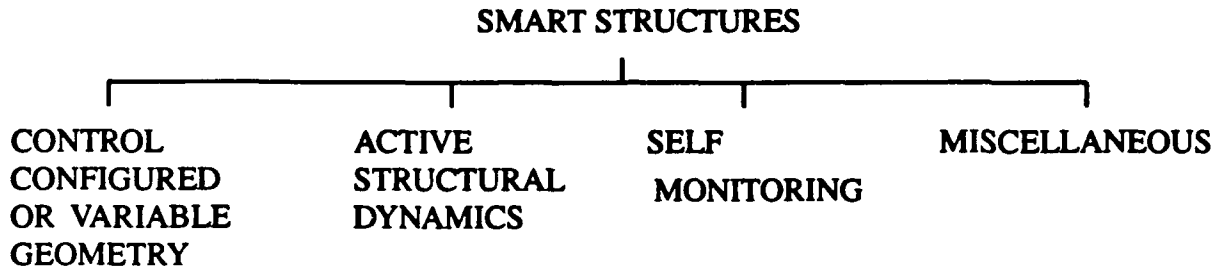


FIGURE 1.3 Four categories of existing smart structures grouped according to their main capability

Martin Marietta is utilizing shape memory alloy wires as embedded actuator elements in compliant wing sections to develop adaptive control surfaces for aircraft applications. Significant possible applications include mission adaptive aircraft wings for extended range and expanded flight envelope, and compliant control fins for submarines and torpedoes to reduce noise, turbulence and system weight. The Jet Propulsion Laboratory has developed a ground based testbed to validate technologies for future large space structures and lunar missions. The goal of the program is to reject disturbances in flexible structures and maintain an ultra precise alignment with extremely small jitter, with a performance several orders of magnitude better than conventional technologies. Ultrastable structures, based upon controlled structures concepts, have been developed at the Los Alamos National Laboratory. These structures combine inherent passive stability with the network of motion and acceleration sensors, coupled in a feedback architecture, with force transducers for actively controlling mechanical stability. The prototype demonstrated a precision of less than one micro-radian over its 2.5 meter length. Many future space missions will require major advances in the areas of controlling, aligning, and pointing optical instruments mounted on large flexible structures. JPL has demonstrated that maintaining the optical path length to better than five nanometers peak to peak is possible with emerging smart structures technologies. A testbed has been developed (the JPL CSI Phase B testbed) consisting of active and passive flexible truss structures.

Smart tuned mass dampers (TMD) have been developed at CSA Engineering, Inc. by implementing an active control system. The dynamics of the TMD and base structure are sensed and the temperature of the viscoelastic material in the TMD is controlled for optimum tuning. Damping characteristics of a structure have been controlled with the help of smart damping materials such as electro-rheological fluids. A smart helicopter rotor blade with actively suppressed vibrations is being developed at the University of Maryland. A neural network for state estimation purposes in a system for active control of structural vibrations and other smart structures applications is being studied at present. A distributed control system architecture for large space applications based on artificial neural networks (ANN) will be a realistic possibility in the near future. A control system of this type does not require accurate knowledge of the structure to be controlled because the structure "learns" to formulate control strategies from operational experience. An active vibration isolation system for microgravity applications on the space station using piezoelectric actuators is being developed.

The thrust toward quieter submarines has resulted in new innovative approaches to active sound suppression. 0-3 piezoelectric copolymers are used in underwater active sound control systems. The materials are used to provide both sensing and actuator functions. Vibration and acoustic control of cylinders for underwater applications has been demonstrated using piezoelectric sensors and actuators. A current program at NASA Langley Research Center involves the evaluation of alternative sound sources and their application to the noise control problem. Optical fibers and piezoelectric actuators are proposed for structural acoustic control. Active acoustic echo reduction is accomplished by using a piezoelectric coating. The possibility to simultaneously reduce transmitted and reflected sound by properly exciting bilaminate actuators used as an integral part of the structure is also being investigated.

Sensitive interferometric fiber optic strain sensors embedded in a laminated composite structure are being used to detect acoustic energy associated with the formation of internal damage. They are also being used to monitor the state of cure of thermoset composites during their fabrication. Optical fiber sensors coated with linear work hardening elastic-plastic materials provide a "memory" to the fiber by forcing it to undergo permanent deformations in response to predefined excursions in the strain field. The possible use of these fibers in structural health monitoring is being considered at present. Work is currently in progress to develop an advanced Health Monitoring System (HMS) for application to large airframes. HMS determines structural abnormalities using a network of distributed sensor modules and signal processors. Using an active sensing technique and pattern recognition software, the system is taught to interpret the sensor signals and identify structural damage in real time.

A proximity sensing skin is proposed for collision avoidance in space telerobotic operations. Smart electromagnetic structures are being studied at present. Based on their sensing capabilities they may be able to detect and modify the EM fields around them as well as their far field image. A traveling wave with specified and controllable phase velocity, amplitude, wavelength and shape is being considered to generate and trap vortices in the troughs of a flexible wall. Analytical studies have shown that an appropriate tailoring of traveling waves to flow parameters results in an ordered vortical flow and associated reduction in drag to a level substantially below flat plate values. An autonomous swimming robotic structure is being studied at the University of New Mexico. The robotic structure is like a submarine structure which is partially encapsulated in an elastic or flexible membrane filled with a counterionic electrolyte. Specifically arranged polyacrylamide or PVA-PAA polymeric cylindrical fibers or bundles are placed in the electrolyte. The polyacrylamide fibers are capable of generating propagating transverse waves to propel the partially encapsulated membrane structure in any direction and in any desired manner. Polymeric muscles that can be directly and actively controlled by computer to provide expansion and contraction capabilities to the flexible structure are also a subject of recent research.

1.3 Smart Structures Research at UTA

Research at the University of Texas at Arlington is being conducted under grant no. DAAL03-89-G-0090 from the Army Research Office. This research is focused on damage-survivable and damage-tolerant laminated composites with optimally placed piezoelectric layers. This report describes accomplishments of the research conducted under the ARO grant.

1.3.1 Analytical Research

An understanding of electroelastic constitutive behavior is critical to predicting the response of a structure with embedded piezoelectric material. Our research efforts in this area has produced a concise formulation of linear constitutive relations [I] that has been extended to the nonlinear case[II]. Chapter 2 describes the constitutive behavior of piezoceramic materials.

The CDA (Composite Delamination Analysis) and SDACLP (Static and Dynamic Analysis for Composite Laminated Plates) packages have been modified to incorporate piezoelectric coupling in a quasi-3D and plane stress analysis. Edge stresses in the vicinity of an embedded piezoceramic patch [III] and stress distribution in the vicinity of electrodes due to an actuation electric field [IV] are obtained by using these codes. A detailed stress field in the vicinity of piezoceramic sensors in a laminated plate under impact loading is also obtained by using one of the modified codes [V]. The finite element formulations and their applications are discussed in Chapter 3. The numerical simulation of impact sensing by piezoceramic patches is discussed separately in Chapter 4.

Three analytical approaches are identified and incorporated into numerical simulations to estimate the impact location and the magnitude of the impact pulse at the origin [VIII]. The dispersive signal from the measurement site and the dispersive relations for the medium are the only two known conditions. The first method uses a moving time window technique to calculate the origin of the signal. The second method uses the phase difference of signals recorded at two locations to estimate the origin. The third method makes the first guess of distance of the origin by estimating the time interval between the maximum and minimum frequency components arriving at the recording location and the signal is reconstructed by transformation. The iteration procedure used in this method is based on the fact that the impact pulse at the origin is all positive. The phase difference method is being evaluated experimentally. The research on impact location and magnitude estimation is described in Chapter 5.

Typically, piezoceramics have an allowable strain-to-failure that is one tenth that of most graphite/epoxy composites. Residual thermal stresses and strains gain importance in designing such composite laminates. Accurate analysis of these stresses is critical [IX]. If the thermally induced strains are too large, it is possible to modify the laminate's coefficient of thermal expansion by adding plies of a dissimilar material such as fiberglass/epoxy. These modifications can relieve much of the thermal stress of the piezoceramic. Chapter 6 contains discussion of residual thermal stresses in laminated composites.

Advanced composite materials suffer from initiation and growth of microcracks even at low loads. Such growth affects substantially the overall behavior of composite materials under subsequent complex loadings. It is important to understand the behavior of materials containing an acceptable level of damage in order to predict the remaining life. Two continuum damage models are being developed to understand damage evolution in laminated composites [VI, VII]. The results of these studies will be used in damage detection and prevention in smart laminated composites.

The first continuum damage model is based on the possibility of the coexistence and interaction of two hypothetical material phases: the damaged phase, characterizing the nucleation and evolution of microstructures in the form of microcracks; and an undamaged phase accommodating such microstructures. The theory of mixtures or interacting continua is used to describe macroscopic behavior. A rudimentary mechanics-based microscopic constitutive model is presented for the damaged phase of the material. In addition, a simple damage phase evolution model is introduced. The model provides an effective tool for describing the influence of microscopic damage evolution on the macroscopic behavior of a material.

The second model utilizes random material characteristics to predict damage evolution in laminated composites. It is based on a division of a laminated composite into a statistically large number of mesovolumes. Damage formation in a ply and in a laminate as a whole for a given plane stress-strain state are calculated from the probabilities of mesovolume failure. These probabilities are directly utilized in reducing ply material constants.

The damage related research is described in a separate report.

1.3.2 Experimental Research

The fabrication and curing processes for smart composite laminates involve additional parameters arising from the placement of sensors and actuators. We have successfully fabricated and cured laminated panels with a large number of embedded piezoceramics. Various aspects of the fabrication and curing processes for laminates with multiple embedded piezoceramic sensors and actuators have been identified [X]. Fabrication and curing issues are discussed in Chapter 7. Piezoceramic wafers are subjected to the curing cycle's pressure and temperature without embedding them in a laminate. These wafers are then tested to evaluate the effect of the curing cycle on the piezoelectric properties. The piezoelectric strain coefficient (d_{31}) is compared with virgin wafers. These results are also included in Chapter 7.

Tensile material tests are performed on coupons with and without piezoceramics embedded in them. These coupons are cut from a single panel to reduce the influence of fabrication and curing procedures. The test results show that the passive presence of piezoceramics have a negligible effect on the tensile properties of the laminate. Experiments are underway to characterize damage initiation in the vicinity of a piezoceramic at various loading levels up to the ultimate failure load. Such damage may become critical under complex loading and may also cause a deterioration in the performance of piezoceramics as sensors and actuators. It is well known that a transverse impact by a foreign object creates extensive damage in the form of matrix cracking and delamination. A set of impact tests are performed to evaluate the effect of the presence of piezoceramic wafers on impact induced damage. Initial results indicate that the presence of the piezoceramic does not adversely effect the incipient damage due to a transverse impact. The damage to piezoceramics in the vicinity of an impact is also minimal. Optical microscopic pictures, X-ray radiographs and ultrasonic C-scans are employed to characterize the impact damage. Material and structural testing results are presented in Chapter 8.

TABLE 1.1 Publications acknowledging URI-ARO Grant

- I. Joshi, S.P., "Constitutive models for Piezoceramic Materials", *Constitutive Laws for Engineering Materials, Recent Advances and Industrial and Infrastructure Applications, Proceedings of the Third International Conference on Constitutive Laws for Engineering Materials: Theory and Applications*, Tucson, Arizona, January 7-12, 1991, pp 605-608.
- II. Joshi, S.P., "Nonlinear Constitutive Relations for Piezoceramic Materials", *Journal of Smart Materials and Structures, Vol. 1, No. 1, 1992, pp. 80-83. Also presented at the Conference on Active Materials and Adaptive Structures*, Alexandria, Virginia, November 5-7, 1991.
- III. Shah, D.K., Chan, W.S., Joshi, S.P., and Subramanian, S., "Analysis of Laminates with Embedded Piezoceramic Layers", *Recent Developments in Composite Materials Structures* (Ed: David hui and C.T.Sun), AD-Vol. 19, AMD-Vol. 113, presented at the Winter Annual Meeting of the American Society of Mechanical Engineers, Dallas, Texas, November 25-30, 1990, pp 19-24.
- IV. Shah, D., Chan, W., and Joshi, S.P., "Response of piezoelectric Layered Laminates Due to Electro-Mechanical Loads", *33rd AIAA/ASME/AHS/ASC Structural Dynamics and Materials Conference*, April 13-15, 1992.
- V. Mannas, J. and Joshi, S.P., "Numerical Simulation of a Smart Laminated Plate under Impact", *American Society for Composites 7th Technical Conference on Composite Materials*, October 13-15, 1992, Penn State, University Park, Pa.
- VI. Joshi, S.P., "Two Phase Continuum Damage Mechanics: Application to Brittle Matrix Composites", *The Third International Symposium on Brittle Matrix Composites*, 17-19 September 1991, Warsaw, Poland.
- VII. Dzenis, Y.A., Joshi, S.P., and Bogdanovich, A.E., "Damage Evolution Modeling in Orthotropic Laminated Composites", *33rd AIAA/ASME/AHS/ASC Structural Dynamics and Materials Conference*, April 13-15, 1992.

- VIII. Lu, C. M. and Joshi, S.P., "Impact Location Estimation by Dispersive Signal Analysis", *The Conference on Active Materials and Adaptive Structures*, Alexandria, Virginia, November 5-7, 1991.
- IX. Chapin, C.M. and Joshi, S.P., "Variation of Residual Thermal Stresses in Graphite/Epoxy Laminates", *Composite Engineering, an International Journal*, Vol.2, No. 1, 1992, pp. 47-53. Also presented at the *8th International Conference on Composite Materials*, Honolulu, Hawaii, July 15-19, 1991.
- X. Joshi, S.P. and Chan, W.S., "Fabrication and Curing of Laminates with Multiple Embedded Piezoceramic Sensors and Actuators", *The Conference on Active Materials and Adaptive Structures*, Alexandria, Virginia, November 5-7, 1991.
- XI. Joshi, S.P., Goode, R.J., "Laminated Plate Finite Element with Damage Evolution Constitutive Laws", *Proceedings of the American Society for Composites, Fifth Technical Conference*, Technomic Publishing Co., Inc., 1990, pp 296-308.
- XII. Goolsby, R.D., Chan, W.S., Joshi, S.P., and Reynolds, J.R., "Composite materials Education Programs at The University of Texas at Arlington", *35th International SAMPE Symposium*, Anaheim, CA, April 2-5, 1990.
- XIII. Joshi, S.P., "Smart Materials and Structures: A Weight Saving Proposition", *51st Annual Conference of Allied Weight Engineers, Inc.*, Hartford, Connecticut, 18-20 May 1992.
- XIV. Joshi, S.P., "Smart Constituents and the Host Structure Interaction: A Mechanics Perspective", *Accelerated Research Initiative in Adaptive Structures with Active Materials*, ONR Workshop, May 18-19, 1992.
- XV. Joshi, S.P., "Damage Evolution in a Gradient Stress Field in Laminated Composites", *The Second International Symposium on Composite Materials and Structures*, August 3-7, 1992, Beijing, China.
- XVI. Dzenis, Y.A., Joshi, S.P., and Bogdanovich, A.E., "Damage Evolution Analysis of Laminates Subjected to Random Quasistatic Loading", *American Society for Composites 7th Technical Conference on Composite Materials*, October 13-15, 1992, Penn State, University Park, Pa.

REFERENCES

17. Dean, D.R. and James, L.T., "Adaptive Laser Optics Techniques (ALOT)," *1st DOD Conference on High Energy Laser Technology*, Navel Training Center, San Diego, California, October 1974.
18. Swigert, C.J. and Forward, R.L., "Electronic Damping of Orthogonal Bending Modes in a Cylindrical Mast-Theory," *Journal of Spacecraft and Rockets*, Vol. 18, No. 1, 1981, pp. 5-10.
19. Forward, R.L., "Electronic Damping of Orthogonal Bending Modes in a Cylindrical Mast-Experimental," *Journal of Spacecraft and Rockets*, Vol. 18, No. 1, 1981, pp. 11-17.
20. Chen, J.C., "Response of Large Space Structures with stiffness control," *Journal of Spacecraft and Rockets*, Vol. 21, No. 5, 1984, pp. 463-467.
21. Caughey, T. K., Fanson, J. L., and Chen J.C., "Stiffness Control of Large Space Structures," *Proceedings of the Workshop on Identification and Control of Flexible Space Structures*, 1985.
22. Fanson, J.L., "An Experimental Investigation of Vibration Suppression in Large Space Structures Using Positive Position Feedback", *Ph.D. Thesis*, California Institute of Technology, Pasadena, California, 1987.
23. Fanson, J.L. and Caughey, T.K., "Positive Position Feedback Control for Large Space Structures," *AIAA 87-0902, AIAA/ASME/ASCE/AHS 28th Structures, Structural Dynamics and Materials Conference*, Monterey, April 1987, Part 2B, 588-598.

24. Hanagud, S., Obal, M.W. and Meyyappa, "Electronic Damping Techniques and Active vibration Control", *26th Structures, Structural Dynamics, and Materials Conference*, 1985.
25. Baily, T. and Hubbard, J.E., "Distributed Piezoelectric-Polymer Active Vibration Control of a Cantilever Beam", *Journal of Guidance, Control, and Dynamics*, Vol. 7, No. 4, 1984, 437-442.
26. Crawley, E.F. and de Luis, J., "Use of Piezoelectric Actuators as element of intelligent Structures", *AIAA Journal*, Vol. 25, No. 10, 1987.
27. Crawley, E.F., Lazarus, K.B., and Anderson, E.H., "Induced Strain Actuation of Isotropic and Anisotropic Plates", *Proceedings of the 30th SDM Conference*, Mobile, AL, April, 1989.

Chapter 2.

NONLINEAR CONSTITUTIVE RELATIONS FOR PIEZOCERAMICS

The Curies first showed the presence of piezoelectricity in crystals in 1880. The first practical use of the piezoelectric effect was during World War I when Langevin's sonar emitter was effectively used to detect German submarines. Prior to World War II, researchers at MIT discovered that certain ceramics such as PZT (Lead-Zirconate-Titanate) could be polarized to yield a high piezo response [1]. Piezoceramics consists of a large number of small crystallites sintered together and polarized by an external electric field. Kawai [2] discovered that the polarized homopolymer of vinylidene fluoride (PVDF) developed far greater piezo activity than any other synthetic or natural polymer. Poled PVDF still dominates all other materials in terms of its intensity of piezo activity [1].

Although the behavior of piezoelectric materials in non-structural applications has been investigated extensively, the treatment is often simplistic. The recent interest in "Smart Structures" has put especial emphasis on the rigorous understanding of electroelastic behavior of piezoceramics as an integral part of a structure.

The nonlinear theory of dielectrics has been studied by Toupin [3], Nelson [4] and Tiersten [5]. The relation between the equations of linear piezoelectricity and the more general electroelastic equations is discussed by Tiersten [5]. Nelson presented a completely deductive derivation of the dynamical equations and constitutive relations for elastic, electric, and electroelastic phenomena based on the fully electrodynamic Lagrangian theory of elastic dielectrics. Penfield and Hans [6] developed a linear piezoelectric theory which does not account for gradient of polarization and electrostatic interference. Mindlin [7] derived a system of two dimensional equations for high frequency motions of crystal plates accounting for coupling of mechanical, electrical and thermal fields. Readers interested in this area may refer to books by Nye [8], Berlincourt et.al. [9], and Landau and Lifshitz [10]. A phenomenological description of the dynamic response of piezoceramics to an external electric field, including domain reorientation processes and the dynamics of dipole moment in each domain, has been developed by Chen et.al. [11, 12, 13, 14].

A concise formulation of linear constitutive equations for piezoelectric materials is presented by Joshi [15]. It has been extended to include some important nonlinear effects encountered by piezoceramics in "smart structures" applications [16].

2.1 Piezoelectric Field Equations

The physics involved in the piezoelectric theory may be regarded as a coupling between Maxwell's equations of electromagnetism and elastic stress equations of motion. The coupling takes place through the piezoelectric constitutive equations.

Maxwell's equations in vector form are written as,

$$\nabla \cdot \hat{D} = \rho_f \quad \nabla \cdot B = 0 \quad (1)$$

$$\nabla \times E = -\mu_o \frac{\partial H}{\partial t} \quad \nabla \times H = \frac{\partial \hat{D}}{\partial t} \quad (2)$$

where B is magnetic induction, E is electric field intensity, H is magnetic field vector and \hat{D} is electric flux density also known as electric displacement vector. The free-space permeability,

μ_0 , is used because piezoelectric materials are nonmagnetic. In the quasi-electrostatic approximation [16], which is usually adequate for the study of piezoelectric phenomena, time-derivative terms in the electromagnetic equations may be dropped. Then the electric field may be expressed as,

$$\mathbf{E} = -\nabla\phi \quad (3)$$

and the only electromagnetic equation which need to be considered is

$$\nabla \cdot \hat{\mathbf{D}} = 0 \quad (4)$$

The elastic stress equation of motion is,

$$\nabla \cdot \boldsymbol{\sigma} = \rho \ddot{\mathbf{u}} \quad (5)$$

where $\boldsymbol{\sigma}$ is stress tensor, ρ is mass density and $\ddot{\mathbf{u}}$ is acceleration vector. Coupling among eqn. 3-5 is introduced by piezoelectric constitutive equations.

2.2 Linear Constitutive Equations

We will adopt index notations in the remainder of this Chapter for convenience. We will employ the thermodynamic Gibbs potential to derive constitutive equations and will consider the σ_{ij} (stress components), E_k (electric field components), and T (absolute temperature) as independent variables.

$$G = U - \sigma_{ij}\epsilon_{ij} - E_k \hat{D}_k - TS \quad (6)$$

where G is the Gibbs potential, S is the entropy, and U is the internal energy. For adiabatically insulated reversible system, the total differential of internal energy is

$$dU = \sigma_{ij}d\epsilon_{ij} + E_k d\hat{D}_k + TdS \quad (7)$$

and therefore the total differential of Gibbs potential is

$$dG = -\epsilon_{ij}d\sigma_{ij} - \hat{D}_k dE_k - SdT \quad (8)$$

Expressing the Gibbs potential in Taylor series and neglecting higher order terms, we obtain,

$$dG = \left(\frac{\partial G}{\partial \sigma_{ij}}\right)_{E,T} d\sigma_{ij} + \left(\frac{\partial G}{\partial E_k}\right)_{\sigma,T} dE_k + \left(\frac{\partial G}{\partial T}\right)_{\sigma,E} dT \quad (9)$$

From eqs.8 and 9

$$\epsilon_{ij} = -\left(\frac{\partial G}{\partial \sigma_{ij}}\right)_{E,T} \quad \hat{D}_k = -\left(\frac{\partial G}{\partial E_k}\right)_{\sigma,T} \quad S = -\left(\frac{\partial G}{\partial T}\right)_{\sigma,E} \quad (10)$$

The total differentials of dependent variables ϵ_{ij} , \hat{D}_k , and S is given as a function of independent variables as

$$\begin{aligned} d\epsilon_{ij} &= \left(\frac{\partial \epsilon_{ij}}{\partial \sigma_{lm}}\right)_{E,T} d\sigma_{lm} + \left(\frac{\partial \epsilon_{ij}}{\partial E_n}\right)_{\sigma,T} dE_n + \left(\frac{\partial \epsilon_{ij}}{\partial T}\right)_{\sigma,E} dT \\ d\hat{D}_k &= \left(\frac{\partial \hat{D}_k}{\partial \sigma_{lm}}\right)_{E,T} d\sigma_{lm} + \left(\frac{\partial \hat{D}_k}{\partial E_n}\right)_{\sigma,T} dE_n + \left(\frac{\partial \hat{D}_k}{\partial T}\right)_{\sigma,E} dT \\ dS &= \left(\frac{\partial S}{\partial \sigma_{lm}}\right)_{E,T} d\sigma_{lm} + \left(\frac{\partial S}{\partial E_n}\right)_{\sigma,T} dE_n + \left(\frac{\partial S}{\partial T}\right)_{\sigma,E} dT \end{aligned} \quad (11)$$

where

$$s_{ijlm}^{E,T} = \left(\frac{\partial \epsilon_{ij}}{\partial \sigma_{lm}} \right)_{E,T}, \quad d_{ijn}^T = \left(\frac{\partial \epsilon_{ij}}{\partial E_n} \right)_{\sigma,T} = \left(\frac{\partial \hat{D}_n}{\partial \sigma_{ij}} \right)_{E,T}, \quad \alpha_{ij}^E = \left(\frac{\partial \epsilon_{ij}}{\partial T} \right)_{\sigma,E} = \left(\frac{\partial S}{\partial \sigma_{ij}} \right)_{E,T},$$

$$\epsilon_{kn}^{\sigma,T} = \left(\frac{\partial \hat{D}_k}{\partial E_n} \right)_{\sigma,T}, \quad p_k^\sigma = \left(\frac{\partial \hat{D}_k}{\partial T} \right)_{\sigma,E} = \left(\frac{\partial S}{\partial E_k} \right)_{\sigma,T}, \quad \frac{\rho c^{\sigma,E}}{T_0} = \left(\frac{\partial S}{\partial T} \right)_{\sigma,E}$$

are elastic compliance coefficients, piezoelectric strain constants, coefficients of thermal expansion, dielectric permittivities, pyroelectric coefficients, respectively; and $c^{\sigma,E}$ is the specific heat and ρ is the mass density. Integrating eq. 11, we obtain,

$$\begin{aligned} \epsilon_{ij} &= s_{ijlm}^{E,T} \sigma_{lm} + d_{ijn}^T E_n + \alpha_{ij}^E \Delta T \\ \hat{D}_k &= d_{klm}^T \sigma_{lm} + \epsilon_{kn}^{\sigma,T} E_n + p_k^\sigma \Delta T \\ \Delta S &= \alpha_{lm}^E \sigma_{lm} + p_n^\sigma E_n + \frac{c^{\sigma,E}}{T_0} \Delta T \end{aligned} \quad (12)$$

Piezoceramics are widely used, therefore we will specialize eq.12 for them. The constitutive equations of the transversely polarized piezoceramics are equivalent to the equations for a piezocrystal of the hexagonal 6mm symmetry class. In abbreviated subscript notation these equations may be written as

$$\begin{aligned} \epsilon_{11} &= s_{11}^{E,T} \sigma_{11} + s_{12}^{E,T} \sigma_{22} + s_{13}^{E,T} \sigma_{33} + d_{31}^T E_3 + \alpha_1^E \Delta T \\ \epsilon_{22} &= s_{12}^{E,T} \sigma_{11} + s_{11}^{E,T} \sigma_{22} + s_{13}^{E,T} \sigma_{33} + d_{31}^T E_3 + \alpha_1^E \Delta T \\ \epsilon_{33} &= s_{13}^{E,T} \sigma_{11} + s_{13}^{E,T} \sigma_{22} + s_{33}^{E,T} \sigma_{33} + d_{33}^T E_3 + \alpha_3^E \Delta T \\ \epsilon_{23} &= s_{44}^{E,T} \sigma_{23} + d_{15}^T E_2, \quad \epsilon_{13} = s_{44}^{E,T} \sigma_{13} + d_{15}^T E_1, \quad \epsilon_{12} = \left(\frac{s_{11}^{E,T} - s_{12}^{E,T}}{2} \right) \sigma_{12} \\ \hat{D}_1 &= d_{15}^T \sigma_{13} + \epsilon_{11}^{\sigma,T} E_1 + p_1^\sigma \Delta T, \quad \hat{D}_2 = d_{15}^T \sigma_{23} + \epsilon_{11}^{\sigma,T} E_2 + p_1^\sigma \Delta T \\ \hat{D}_3 &= d_{31}^T (\sigma_{11} + \sigma_{22}) + d_{33}^T \sigma_{33} + \epsilon_{33}^{\sigma,T} E_3 + p_3^\sigma \Delta T \\ \Delta S &= \alpha_1^E (\sigma_{11} + \sigma_{22}) + \alpha_3^E \sigma_{33} + p_1^\sigma (E_1 + E_2) + p_3^\sigma E_3 + \frac{c^{\sigma,T}}{T_0} \Delta T \end{aligned} \quad (13)$$

In cases where temperature variation is negligible, neglecting temperature terms and writing eq. 13 in compact matrix notation, we obtain

$$\begin{aligned} \{\epsilon\} &= [S^E] \{\sigma\} + [d] \{E\} \\ \{\hat{D}\} &= [d]^T \{\sigma\} + [\epsilon^\sigma] \{E\} \end{aligned} \quad (14)$$

Where,

$$[S^E] = \begin{bmatrix} S_{11} & S_{12} & S_{13} & 0 & 0 & 0 \\ S_{12} & S_{11} & S_{13} & 0 & 0 & 0 \\ S_{13} & S_{13} & S_{33} & 0 & 0 & 0 \\ 0 & 0 & 0 & S_{44} & 0 & 0 \\ 0 & 0 & 0 & 0 & S_{44} & 0 \\ 0 & 0 & 0 & 0 & 0 & \frac{S_{11} - S_{12}}{2} \end{bmatrix}, \quad [d] = \begin{bmatrix} 0 & 0 & d_{31} \\ 0 & 0 & d_{31} \\ 0 & 0 & d_{33} \\ 0 & d_{15} & 0 \\ d_{15} & 0 & 0 \\ 0 & 0 & 0 \end{bmatrix}, \quad [\epsilon^\sigma] = \begin{bmatrix} \epsilon_{11} & 0 & 0 \\ 0 & \epsilon_{11} & 0 \\ 0 & 0 & \epsilon_{33} \end{bmatrix} \quad (15)$$

The alternative constitutive formulations may be obtained by considering other potentials. The final linear constitutive relations in compact matrix notation are presented below. The temperature change is assumed negligible and therefore not included in the relations.

$$\begin{aligned} \{\sigma\} &= [C^E] \{\epsilon\} - [g] \{E\} \\ \{\hat{D}\} &= [g]^T \{\epsilon\} + [\epsilon^e] \{E\} \\ &\text{or} \\ \{\sigma\} &= [C^D] \{\epsilon\} - [h] \{\hat{D}\} \\ \{E\} &= -[h]^T \{\epsilon\} + [\beta^e] \{\hat{D}\} \end{aligned} \quad (16)$$

Where,

$$\begin{aligned} [C^E] &= [S^E]^{-1} & [g] &= [C^E] [d] & [\epsilon^e] &= [\epsilon^s] - [g]^T [d] \\ [C^D] &= [C^E] + [g] [\beta^e] [g]^T & [h] &= [g] [\beta^e] & [\beta^e] &= [\epsilon^e]^{-1} \end{aligned} \quad (17)$$

Eqs. 16 gives alternative forms of linear constitutive relations. The coefficients are related to each other as given by eq. 17.

2.3 Nonlinear Constitutive Equations

The strain, electric displacement and entropy are assumed to depend linearly on the stress, electric field and temperature (eq. 11) in deriving eq. 12. Some higher order effects can be brought about by including second order terms in eq. 11, as follows;

$$\begin{aligned} d\epsilon_{ij} &= \left(\frac{\partial \epsilon_{ij}}{\partial \sigma_{lm}} \right)_E d\sigma_{lm} + \left(\frac{\partial \epsilon_{ij}}{\partial E_n} \right)_\sigma dE_n + \frac{1}{2} \left[\left(\frac{\partial^2 \epsilon_{ij}}{\partial \sigma_{lm} \partial \sigma_{pq}} \right)_E d\sigma_{lm} d\sigma_{pq} + \left(\frac{\partial^2 \epsilon_{ij}}{\partial E_n \partial E_r} \right)_\sigma dE_n dE_r + 2 \left(\frac{\partial^2 \epsilon_{ij}}{\partial \sigma_{lm} \partial E_n} \right) d\sigma_{lm} dE_n \right] \\ d\hat{D}_k &= \left(\frac{\partial \hat{D}_k}{\partial \sigma_{lm}} \right)_E d\sigma_{lm} + \left(\frac{\partial \hat{D}_k}{\partial E_n} \right)_\sigma dE_n + \frac{1}{2} \left[\left(\frac{\partial^2 \hat{D}_k}{\partial \sigma_{lm} \partial \sigma_{pq}} \right)_E d\sigma_{lm} d\sigma_{pq} + \left(\frac{\partial^2 \hat{D}_k}{\partial E_n \partial E_r} \right)_\sigma dE_n dE_r + 2 \left(\frac{\partial^2 \hat{D}_k}{\partial \sigma_{lm} \partial E_n} \right) d\sigma_{lm} dE_n \right] \end{aligned} \quad (18)$$

where,

$$\begin{aligned} S_{ijlmpq}^E &= \left(\frac{\partial^2 \epsilon_{ij}}{\partial \sigma_{lm} \partial \sigma_{pq}} \right)_E & d_{ijnr} &= \left(\frac{\partial^2 \epsilon_{ij}}{\partial E_n \partial E_r} \right)_\sigma = \left(\frac{\partial^2 \hat{D}_k}{\partial \sigma_{lm} \partial E_n} \right) \\ \kappa_{ijlmn} &= \left(\frac{\partial^2 \epsilon_{ij}}{\partial \sigma_{lm} \partial E_n} \right) & \epsilon_{knr} &= \left(\frac{\partial^2 \hat{D}_k}{\partial E_n \partial E_r} \right)_\sigma \end{aligned} \quad (19)$$

are nonlinear elastic compliance coefficients, electrostriction coefficients, elastostriction coefficients and nonlinear dielectric permittivity coefficients, respectively. Integrating equation 13, we obtain,

$$\begin{aligned} \epsilon_{ij} &= S_{ijlm}^E \sigma_{lm} + d_{ijn} E_n + \frac{1}{2} S_{ijlmpq}^E \sigma_{lm} \sigma_{pq} + \frac{1}{2} d_{ijnr} E_n E_r + \kappa_{ijlmn} \sigma_{lm} E_n \\ \hat{D}_k &= d_{klm} \sigma_{lm} + \epsilon_{kn}^s E_n + \frac{1}{2} \kappa_{klmpq} \sigma_{lm} \sigma_{pq} + \frac{1}{2} \epsilon_{knr}^s E_n E_r + d_{klmn} \sigma_{lm} E_n \end{aligned} \quad (20)$$

Piezoceramics are brittle materials and elastically behave linearly up to the failure. Electrostriction coefficients are important at high electric field strengths. In cases, where mechanical stresses are applied in addition to electric field (piezoceramic is constrained from freely deforming), the elastostriction coefficients should be included in constitutive relations. We will neglect nonlinear elastic compliance coefficients and nonlinear dielectric permittivity coefficients, and

write eqs. (15) in an abbreviated subscript notation.

$$\begin{aligned}\epsilon_{\alpha} &= S_{\alpha\beta}^E \sigma_{\beta} + d_{\alpha n} E_n + \frac{1}{2} d_{\alpha nr} E_n E_r + \kappa_{\alpha\beta n} \sigma_{\beta} E_n \\ \hat{D}_k &= d_{k\beta} \sigma_{\beta} + \epsilon_{kn}^S E_n + \frac{1}{2} \kappa_{k\beta\gamma} \sigma_{\beta} \sigma_{\gamma} + d_{k\beta n} \sigma_{\beta} E_n\end{aligned}\quad (21)$$

Where greek subscripts take values one to six and others one to three. The electrostriction coefficients and elastostriction coefficients are reduced for a piezoceramic poled in the 3-direction which is also an axis of symmetry. The coefficients associated with the nonlinear terms in the expression for σ_{α} are written in abbreviated matrix form in the following equations.

$$[d_{\alpha nr}] = \begin{bmatrix} d_{111} & d_{122} & d_{133} & 0 & 0 & 0 \\ d_{122} & d_{111} & d_{133} & 0 & 0 & 0 \\ d_{133} & d_{133} & d_{333} & 0 & 0 & 0 \\ 0 & 0 & 0 & d_{423} & 0 & 0 \\ 0 & 0 & 0 & 0 & d_{423} & 0 \\ 0 & 0 & 0 & 0 & 0 & \frac{1}{2}(d_{111} - d_{122}) \end{bmatrix}\quad (22)$$

$$[\kappa_{\alpha\beta n}] = \begin{bmatrix} \kappa_{111} & \kappa_{121} & \kappa_{131} & 0 & 0 & 0 & \kappa_{121} & \kappa_{121} & \kappa_{132} & 0 & 0 & 0 & \kappa_{131} & \kappa_{132} & \kappa_{133} & 0 & 0 & 0 \\ \kappa_{121} & \kappa_{121} & \kappa_{132} & 0 & 0 & 0 & \kappa_{121} & \kappa_{111} & \kappa_{131} & 0 & 0 & 0 & \kappa_{132} & \kappa_{131} & \kappa_{133} & 0 & 0 & 0 \\ \kappa_{131} & \kappa_{132} & \kappa_{133} & 0 & 0 & 0 & \kappa_{132} & \kappa_{131} & \kappa_{133} & 0 & 0 & 0 & \kappa_{133} & \kappa_{133} & \kappa_{333} & 0 & 0 & 0 \\ 0 & 0 & 0 & \kappa_{441} & 0 & 0 & 0 & 0 & 0 & 0 & 0 & 0 & 0 & 0 & 0 & \kappa_{443} & 0 & 0 \\ 0 & 0 & 0 & 0 & 0 & 0 & 0 & 0 & 0 & 0 & \kappa_{441} & 0 & 0 & 0 & 0 & 0 & \kappa_{443} & 0 \\ 0 & 0 & 0 & 0 & 0 & 0 & 0 & 0 & 0 & 0 & 0 & 0 & 0 & 0 & 0 & 0 & 0 & \kappa_{663} \end{bmatrix}\quad (23)$$

The corresponding vectors $E_n E_r$ and $\sigma_{\beta} E_n$ are

$$\begin{aligned}& [E_1^2, E_2^2, E_3^2, E_2 E_3, E_1 E_3, E_1 E_2]^T \\ & [\sigma_1 E_1, \sigma_2 E_1, \sigma_3 E_1, \sigma_4 E_1, \sigma_5 E_1, \sigma_6 E_1, \sigma_1 E_2, \sigma_2 E_2, \sigma_3 E_2, \sigma_4 E_2, \sigma_5 E_2, \sigma_6 E_2, \sigma_1 E_3, \sigma_2 E_3, \sigma_3 E_3, \sigma_4 E_3, \sigma_5 E_3, \sigma_6 E_3]^T\end{aligned}\quad (24)$$

The tensors appearing in the nonlinear terms of the expression for \hat{D}_k are written in a convenient abbreviated matrix notation as eq. 25 and eq. 26.

$$\begin{bmatrix} d_{111} & 0 & 0 & d_{122} & 0 & 0 & d_{423} & d_{66} & 0 & 0 & 0 & d_{66} & 0 & 0 & d_{133} & 0 & d_{122} & 0 \\ 0 & d_{122} & 0 & 0 & d_{111} & 0 & d_{66} & d_{423} & 0 & 0 & 0 & d_{423} & 0 & 0 & d_{66} & d_{122} & 0 & 0 \\ 0 & 0 & d_{133} & 0 & 0 & d_{423} & 0 & 0 & d_{333} & d_{66} & d_{423} & 0 & d_{133} & d_{66} & 0 & 0 & 0 & d_{66} \end{bmatrix}\quad (25)$$

$$\begin{bmatrix} \kappa_{111} & \kappa_{121} & \kappa_{133} & \kappa_{441} & 0 & 0 & \kappa_{132} & \kappa_{131} & \kappa_{121} \\ \kappa_{121} & \kappa_{222} & \kappa_{133} & 0 & \kappa_{441} & 0 & \kappa_{131} & \kappa_{132} & \kappa_{121} \\ \kappa_{131} & \kappa_{131} & \kappa_{333} & \kappa_{443} & \kappa_{443} & \kappa_{663} & \kappa_{133} & \kappa_{133} & \kappa_{132} \end{bmatrix}\quad (26)$$

where $d_{66} = (d_{111} - d_{122})/2$ and the corresponding vectors $\sigma_{\beta} E_n$ and $\sigma_{\beta} \sigma_{\gamma}$ are

$$\begin{aligned}& [\sigma_1 E_1, \sigma_1 E_2, \sigma_1 E_3, \sigma_2 E_1, \sigma_2 E_2, \sigma_2 E_3, \sigma_3 E_1, \sigma_3 E_2, \sigma_3 E_3, \sigma_4 E_1, \sigma_4 E_2, \sigma_4 E_3, \sigma_5 E_1, \sigma_5 E_2, \sigma_5 E_3, \sigma_6 E_1, \sigma_6 E_2, \sigma_6 E_3]^T \\ & [\sigma_1 \sigma_1, \sigma_2 \sigma_2, \sigma_3 \sigma_3, \sigma_4 \sigma_4, \sigma_5 \sigma_5, \sigma_6 \sigma_6, \sigma_2 \sigma_3, \sigma_1 \sigma_3, \sigma_1 \sigma_2]^T\end{aligned}\quad (27)$$

Similar expressions can be obtained by considering strain and electric field or strain and

electric displacement as independent variables. These alternative forms of nonlinear constitutive relations are presented as eqs. 28 and 29.

$$\sigma_{ij} = C_{ijlm}^E \epsilon_{lm} - g_{ijn} E_n + \frac{1}{2} C_{ijlm pq}^E \epsilon_{lm} \epsilon_{pq} - \frac{1}{2} g_{ijnr} E_n E_r - \gamma_{ijlmn} \epsilon_{lm} E_n \quad (28)$$

$$\hat{D}_k = g_{klm} \epsilon_{lm} + \epsilon_{kn}^e E_n + \frac{1}{2} \gamma_{klmpq} \epsilon_{lm} \epsilon_{pq} + \frac{1}{2} \epsilon_{ijnr}^e E_n E_r + g_{klmn} \epsilon_{lm} E_n$$

$$\sigma_{ij} = C_{ijlm}^D \epsilon_{lm} - h_{ijn} \hat{D}_n + \frac{1}{2} C_{ijlm pq}^D \epsilon_{lm} \epsilon_{pq} - \frac{1}{2} h_{ijnr} \hat{D}_n \hat{D}_r - \tau_{ijlmn} \epsilon_{lm} \hat{D}_n \quad (29)$$

$$E_k = -h_{klm} \epsilon_{lm} + \beta_{kn}^e \hat{D}_n - \frac{1}{2} \tau_{klmpq} \epsilon_{lm} \epsilon_{pq} + \frac{1}{2} \beta_{knr}^e \hat{D}_n \hat{D}_r - h_{klmn} \epsilon_{lm} \hat{D}_n$$

We will neglect nonlinear stiffness coefficients, nonlinear permittivity and nonlinear dielectric coefficients, and rewrite eqs 28 and 29 in abbreviated subscript notation.

$$\sigma_\alpha = C_{\alpha\beta}^E \epsilon_\beta + g_{\alpha n} E_n - \frac{1}{2} g_{\alpha nr} E_n E_r - \gamma_{\alpha\beta n} \epsilon_\beta E_n$$

$$\hat{D}_k = g_{k\beta} \epsilon_\beta + \epsilon_{kn}^e E_n + \frac{1}{2} \gamma_{k\beta\eta} \epsilon_\beta \epsilon_\eta + g_{k\beta n} \epsilon_\beta E_n$$

$$\sigma_\alpha = C_{\alpha\beta}^E \epsilon_\beta - h_{\alpha n} E_n - \frac{1}{2} h_{\alpha nr} \hat{D}_n \hat{D}_r - \tau_{\alpha\beta n} \epsilon_\beta \hat{D}_n$$

$$E_k = -h_{k\beta} \epsilon_\beta + \epsilon_{kn}^e \hat{D}_n - \frac{1}{2} \tau_{k\beta\eta} \epsilon_\beta \epsilon_\eta - h_{\alpha\beta n} \epsilon_\beta \hat{D}_n \quad (30)$$

$g_{\alpha nr}$ and $h_{\alpha nr}$ have non-zero coefficients corresponding to the non-zero coefficients of $d_{\alpha nr}$. $\gamma_{\alpha\beta n}$ and $\tau_{\alpha\beta n}$ have non-zero coefficients corresponding to the non-zero coefficients of $\kappa_{\alpha\beta n}$. Relationships between coefficients given by eq. 18 are not applicable to nonlinear constitutive equations.

REFERENCES

28. Manual, "Kynar Piezo Film", *Pennwalt Corporation*.
29. Kawai, H., "The Piezoelectricity of Polyrinydene Fluoride", *Japan Journal of applied physics*, No. 8, 1979, pp. 975-976.
30. Toupin, R.A., "A Dynamical Theory of Elastic Dielectrics", *Int. J. Eng. Sci.*, Vol. 1, 1983, pp 101-126.
31. Nelson, D.F., "Theory of Nonlinear Electroacoustics of Dielectric, Piezoelectric Crystals", *J. Acoust. Soc. Am.*, Vol. 63, June 1978, pp. 1738-1748.
32. Tiersten, H.F., "Electroelastic Interactions and the Piezoelectric Equations", *J. Acoust. Soc. Am.*, Vol. 70, December 1981, pp. 1567-1576.
33. Penfield, P. Jr and Hans, H.A., "Electrodynamics of moving media", *Research Monograph, No. 40*, Massachusetts Institute of Technology Press, Cambridge, Massachusetts, 1967.
34. Mindlin, R.D., "Equations of High Frequency Vibration of Thermopiezoelectric Crystal Plates", *Int. J. Solids Struct.*, Vol. 10, No. 6, 1974, pp. 625-637.
35. Nye, J.F., "Physical Properties of Crystals", Oxford, *Clarendon Press*, 1964.
36. Berlincourt, D.A., Curren, D.R., Jaffe, H., "Piezoelectric and Piezomagnetic Materials and Their Function as Transducers", *In: Physical Acoustics*, Mason W.P. (Ed.), Vol. 1-Part A, Academic Press, New York, 1964.

37. Landau, L.D., Lifshitz, E.M., "Electrodynamics of Continuous Media", *Pergamon Press, Oxford-London-New York-Paris*, 1960.
38. Chen, P.J., "Characterization of the Three-Dimensional Properties of Poled PZT-65/35 in the Absence of Losses", *Acts Mech.*, Vol. 47, 1983, pp. 95-106.
39. Chen, P.J., "Three-Dimensional Dynamic Electromechanical Constitutive Relations of Ferroelectric Materials", *Int. J. Solids Struct.*, Vol. 16, No. 12, 1980, pp 1059-1067.
40. Chen, P.J., Peercy, P.S., "One-Dimensional Dynamic Electromechanical Constitutive Relations for Ferroelectric Materials, *Acta Mech.*, Vol. 31, No. 3, 1979, pp. 231-241.
41. Chen, P.J., Tucker, T.J., "Determination of the Polar Equilibrium Properties of the Ferroelectric Ceramic PZT-65/35", *Acta Mech.*, Vol. 38, No. 3-4, 1981, pp. 209-218.
42. Auld, B.A., "Wave Propagation and Resonance in piezoelectric materials", *J. Acoust. Soc. Am.*, Vol. 70, No. 6, December 1981, pp. 1577-1585.
43. Joshi, S.P., "Constitutive Models for Piezoelectric Materials", *Constitutive Laws for Engineering Materials: Recent Advances and Industrial and Infrastructure Applications* (Ed: C.S. Desai, E. Krempl, G. Frantziskonis, H. Saadatmanesh), ASME Press, 1991, pp.605-608.

Chapter 3.

FINITE ELEMENT ANALYSIS OF SMART PLATES

The idea of 'smart structures' is relatively new (Wada, et.al. [1]). One component of these smart structures is the 'active-structural-element' which has become the focus of research in recent years. The primary function of the active structural element is to induce actuation or sense the required response. Of the many available sensors and actuators is the piezoelectric sensor. Various actuation techniques and geometries have been analyzed and tested. Among the most common have been the application of segmented piezoceramics to the surface of a beam (Forward and Swigert[2]). Various analytical models of this have been developed (Crawley and Anderson[3]) and used in output feedback (Bailey and Hubbard[4]), (Hanagud, et al,[5]) and (Lee et al.,[6]) and positive position feedback (Fanson and Caughey[7]) for active damping and in the modification of wave propagation. Shape control of plates with surface mounted piezoelectric has also been demonstrated (Crawley and Lazarus[8]).

An alternative to surface bonding of the strain actuation material is to embed the material inside a composite structure (Crawley and De Luis[9]). The advantage of such embedding is that the load transfer from the actuation material to the host structure is enhanced and the surface of the structure is relatively free of fragile components and connections. In addition, embedding affords the designer to more options for finding the optimal geometry. However, complications of electric insulation and manufacturing must be faced.

An understanding of the electroelastic constitutive behavior is critical in predicting the response of a structure with piezoelectric layers. Due to complexities in satisfying equations of equilibrium, and boundary conditions, exact solutions to problems of laminated plates with piezoelectric layers are not available. The complex state of stress in plates and laminated composites is often determined with the help of the finite element analysis technique. Research in recent years in this area is now focused on the development of finite element techniques incorporating piezoelectric constitutive relations to obtain an electro-mechanical response of these structures.

The objective of this chapter is to incorporate constitutive equations of piezoelectrics into the finite element analysis to determine the structural response of plates with embedded piezoceramic layers. Finite Element formulations will be discussed for inplane and through-the-thickness analysis. The Classical Lamination Theory can be modified to study the inplane response of a laminated plate with embedded piezoelectric layer / layers. Detailed inplane analysis can be achieved by finite element techniques incorporating piezoelectric constitutive relations. Since these laminated plates may consist of distinct layers the interlaminar response and delamination characteristics of the laminated plates are also important. Discontinuous and singular stress distributions in the vicinity of electrodes and piezoceramic layers in plates are common causes for delamination and damage in plates and laminates. Two finite element techniques SDACL (Static and Dynamic Analysis for Composite Laminated plates) for inplane analysis and CDA (Composite Delamination Analysis) for through-the-thickness analysis have been developed. These codes are used to investigate stress distributions in plates and laminated composites with piezoelectric layers. Stress distributions in the vicinity of electrodes due to an actuation electric field in piezoceramic layers are obtained using these FEA codes. The following paragraphs and sections will discuss the basis for finite element formulations for both, inplane and through-the-thickness analysis. Applications of these codes to solve different problems are also demonstrated.

3.1 The General Laminate Theory

A laminated plate consists of a number of plies perfectly bonded together. Each ply can have principal material axes oriented at an angle different from the plate reference axes. The stress-strain relations in the k^{th} ply in the plate reference axes are given as

$$\begin{bmatrix} \sigma_{xx} \\ \sigma_{yy} \\ \sigma_{xy} \\ \sigma_{yz} \\ \sigma_{xz} \end{bmatrix}_k = \begin{bmatrix} \bar{Q}_{11} & \bar{Q}_{12} & \bar{Q}_{16} & 0 & 0 \\ \bar{Q}_{21} & \bar{Q}_{22} & \bar{Q}_{26} & 0 & 0 \\ \bar{Q}_{16} & \bar{Q}_{26} & \bar{Q}_{66} & 0 & 0 \\ 0 & 0 & 0 & \bar{Q}_{44} & \bar{Q}_{45} \\ 0 & 0 & 0 & \bar{Q}_{54} & \bar{Q}_{55} \end{bmatrix}_k \begin{bmatrix} \epsilon_{xx} \\ \epsilon_{yy} \\ \gamma_{xy} \\ \gamma_{yz} \\ \gamma_{xz} \end{bmatrix}_k \quad (31)$$

where $\bar{Q}_{ij,k}$ are the reduced stiffness coefficients of the k^{th} ply.

The displacement functions for a laminated plate are assumed to be of the form

$$\begin{aligned} u(x, y, z) &= u^o(x, y) + z\theta_x(x, y) \\ v(x, y, z) &= v^o(x, y) + z\theta_y(x, y) \\ w(x, y, z) &= w^o(x, y) \end{aligned} \quad (32)$$

where u^o , v^o , and w^o are the midplane displacement components in the x-, y-, and z- directions, respectively. The θ_x and θ_y are the rotations of the cross section perpendicular to the x- and y- axes. It is assumed that the u and v displacement components vary linearly in the thickness directions. Thus the in-plane strains, the out-of-plane strains and the curvatures in the k -th ply are given as

$$\begin{bmatrix} \epsilon \\ \kappa \\ \gamma \end{bmatrix}_k = \begin{bmatrix} \epsilon^o \\ \kappa \\ \gamma \end{bmatrix} + z \begin{bmatrix} \kappa \\ 0 \\ 0 \end{bmatrix} \quad (33)$$

where ϵ^o and κ are the mid-plane strains and curvatures and γ is defined as

$$[\gamma] = \begin{bmatrix} \gamma_{yz} \\ \gamma_{xz} \end{bmatrix} \quad (34)$$

The stress resultants acting on the laminate are obtained by integration of the stress in each ply through the thickness. Hence the laminate plate constitutive equations including the transverse shear terms become

$$\begin{bmatrix} N \\ M \\ Q \end{bmatrix} = \begin{bmatrix} A & B & 0 \\ B & D & 0 \\ 0 & 0 & A^* \end{bmatrix} \begin{bmatrix} \epsilon^o \\ \kappa \\ \gamma \end{bmatrix} \quad (35)$$

where

$$N_i = \int_{-h/2}^{h/2} \sigma_i dz \quad M_i = \int_{-h/2}^{h/2} \sigma_i z dz \quad Q_x = \int_{-h/2}^{h/2} \sigma_{xz} z dz \quad Q_y = \int_{-h/2}^{h/2} \sigma_{yz} z dz \quad (36)$$

$$(A_{ij}, B_{ij}, D_{ij}) = \int_{-h/2}^{h/2} \bar{Q}_{ij} \left(1, \frac{z}{2}, \frac{z^2}{3}\right) dz \quad i, j = 1, 2, 6 \quad (37)$$

and

$$A^*_{ij} = \int_{-h/2}^{h/2} \bar{Q}_{ij} dz \quad i, j = 4, 5 \quad (38)$$

and h is the total laminate thickness of the laminate.

3.2 Inplane Plate Finite Element Analysis

In this section a finite element formulation is developed for static response of structures using plate bending elements. Piezoelectric constitutive equations are incorporated into a finite element analysis to study the static structural response of structures with embedded piezoelectric sensors.

3.2.1 Formulation Including Piezoelectric Constitutive Relation.

The constitutive relations of a piezoelectric media can be written as

$$\begin{aligned} \epsilon_{ij} &= s_{ijlm}^E \sigma_{lm} + d_{ijn}^T E_n + \alpha_{ij}^E \Delta T \\ D_k &= d_{klm}^T \sigma_{lm} + \epsilon_{kn}^{\sigma, T} E_n + p_k^{\sigma} \Delta T \end{aligned} \quad (39)$$

where symbols are defined in Chapter 2.

The total potential energy of the system is a sum of the internal strain energy and the work done due the external forces and in matrix notation is given by

$$\Pi_p = U - PE = \left(\frac{1}{2} \int_V [\sigma]^T [\epsilon] dV - \int_V [\sigma]^T [d]^T [E] dV - \int_V [\epsilon]^T [C] [\epsilon_{th}] dV \right) - \int_S [\bar{u}]^T [\bar{T}] dS \quad (40)$$

where the thermal strains ϵ_{th} are given by $\alpha \Delta T$ where α is the coefficient of thermal expansion and ΔT is the temperature difference from the reference state. The superscript T of a matrix denotes the transpose of the matrix and that to a symbol denotes the state of constant temperature.

The above equation clearly shows the distinct components of the internal strain energy. The first term in eqn. 10 is the mechanical strain energy the second term is the electromechanical and the third is the thermomechanical energy.

Nine-node isoparametric quadrilateral elements as shown in Figure 3.1 are used to model the laminated plate. Each node has five degrees of freedom, three translations in the coordinate axes and two rotations about the x- and y- axes for the cross section perpendicular to the axes.

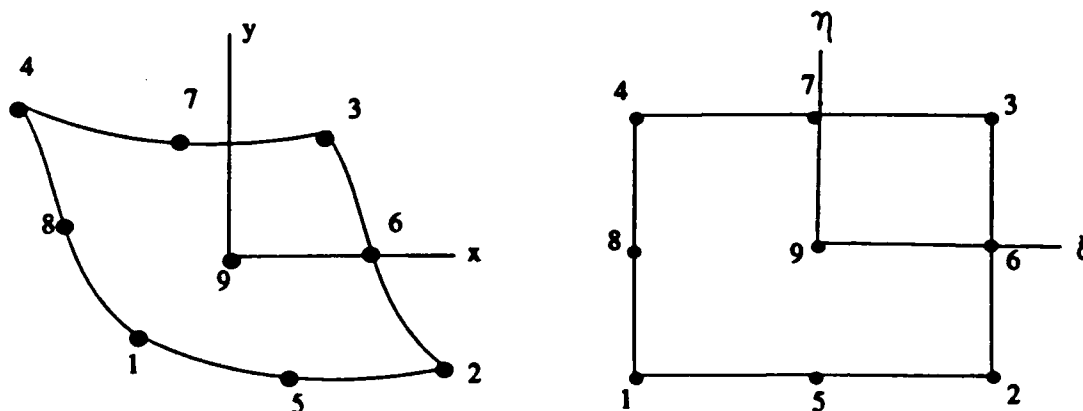


FIGURE 3.1 Nine-noded isoparametric element.

The plate finite element degrees of freedom are

$$[\bar{u}] = \begin{bmatrix} u \\ v \\ w \\ \Phi_x \\ \Phi_y \end{bmatrix} = \sum_1^9 [\bar{N}_i] \begin{bmatrix} u_i \\ v_i \\ w_i \\ \Phi_{xi} \\ \Phi_{yi} \end{bmatrix} = \sum_1^9 [\bar{N}_i] [u_i] \quad (41)$$

The isoparametric plate finite elements use the following shape functions:

For nodes at $\xi = \pm 1$ and $\eta = \pm 1$ (corner nodes)

$$\bar{N}_i = \left(\frac{1}{4}\right) (1 + \xi_o) (1 + \eta_o) (\xi_o + \eta_o - 1) \quad (42)$$

For nodes at $\xi = 0$ and $\eta = \pm 1$

$$\bar{N}_i = \left(\frac{1}{2}\right) (1 - \xi^2) (\eta_o + \eta^2) \quad (43)$$

For nodes at $\xi = \pm 1$ and $\eta = 0$

$$\bar{N}_i = \left(\frac{1}{2}\right) (\xi_o + \xi^2) (1 - \eta^2) \quad (44)$$

For the center node at $\xi = 0$ and $\eta = 0$

$$\bar{N}_i = (1 - \xi^2) (1 - \eta^2) \quad (45)$$

In the above shape functions ξ and η are the normalized local coordinates and $\xi_o = \xi \xi_i$ and $\eta_o = \eta \eta_i$ where ξ_i and η_i are the natural coordinates of node i as shown in Figure 1.

The first term representing the mechanical strain energy as given in eqn.1 can be written as

$$\frac{1}{2} \int_V [\sigma]^T [\epsilon] dV = \frac{1}{2} \int_A \begin{bmatrix} \epsilon^o \\ \kappa \\ \gamma \end{bmatrix}^T \begin{bmatrix} A & B & 0 \\ B & D & 0 \\ 0 & 0 & A^* \end{bmatrix} \begin{bmatrix} \epsilon^o \\ \kappa \\ \gamma \end{bmatrix} dA \quad (46)$$

The strain-curvature vector can be expressed in terms of the derivatives of the shape functions and the nodal displacement vector as

$$\begin{bmatrix} \epsilon^o \\ \kappa \\ \gamma \end{bmatrix} = [\bar{B}] [\bar{u}] \quad \text{where} \quad [\bar{B}]^T = \begin{bmatrix} \frac{\partial \bar{N}_i}{\partial x} & 0 & \frac{\partial \bar{N}_i}{\partial y} & 0 & 0 & 0 & 0 & 0 \\ 0 & \frac{\partial \bar{N}_i}{\partial y} & \frac{\partial \bar{N}_i}{\partial x} & 0 & 0 & 0 & 0 & 0 \\ 0 & 0 & 0 & 0 & 0 & 0 & \frac{\partial \bar{N}_i}{\partial y} & \frac{\partial \bar{N}_i}{\partial x} \\ 0 & 0 & 0 & \frac{\partial \bar{N}_i}{\partial x} & 0 & \frac{\partial \bar{N}_i}{\partial y} & 0 & \bar{N}_i \\ 0 & 0 & 0 & 0 & \frac{\partial \bar{N}_i}{\partial y} & \frac{\partial \bar{N}_i}{\partial x} & \bar{N}_i & 0 \end{bmatrix} \quad (47)$$

Thus

$$\frac{1}{2} \int_V [\sigma]^T [E] dV = \frac{1}{2} \int_A [\bar{u}]^T [\bar{B}]^T [C] [\bar{B}] [\bar{u}] dA \quad (48)$$

The [ABDA*] in the above equations has been renamed as [c] and represents the modified stiffness matrix of the plate.

The second term in eqn. 10 represents the electromechanical strain energy. Expressing the product $[d]^T [E]$ as the piezoelectric strain vector $\{\epsilon^p\}$ we get

$$\int_V [\sigma]^T [d]^T [E] dV = \int_V [\sigma]^T [\epsilon^p] dV \quad (49)$$

Also stress vector $\{\sigma\}^T$ can be expressed as $\{\epsilon\}^T [\bar{Q}]$

$$\int_V [\sigma]^T [d]^T [E] dV = \int_V [\epsilon]^T [\bar{Q}] [\epsilon^p] dV \quad (50)$$

The piezoelectric strain $\{\epsilon^p\}$ with $[\bar{Q}]$ is the piezoelectric stress $\{\sigma^p\}$

$$\int_V [\sigma]^T [d]^T [E] dV = \int_V [\epsilon]^T [\sigma^p] dV \quad (51)$$

The strain in the plate can be obtained by differentiating the displacements. Expressing the strain in terms of the midplane strains and curvatures we get and integrating the piezoelectric stresses through the thickness we get

$$\int_V [\sigma]^T [d]^T [E] dV = \int_A \begin{bmatrix} \epsilon^o \\ \kappa \\ \gamma \end{bmatrix}^T \begin{bmatrix} N^p \\ M^p \\ Q^p \end{bmatrix} dA \quad (52)$$

Expressing the strain- curvature vector in terms of the nodal displacements and derivatives of the shape functions we have

$$\int_V [\sigma]^T [d]^T [E] dV = \int_A [\bar{u}]^T [\bar{B}]^T \begin{bmatrix} N^p \\ M^p \\ Q^p \end{bmatrix} dA \quad (53)$$

The third term in eqn. 10 represents the thermo-elastic strain energy and can be written as

$$\int_V [\sigma]^T [\epsilon^{th}] dV = \int_V [\epsilon]^T [\bar{Q}] [\epsilon^{th}] dV \quad (54)$$

Expressing the strains in terms of the midplane strains and curvatures and integrating the thermal stresses we get the thermal stress resultants $[N^{th}, M^{th}, Q^{th}]$. Thus

$$\int_V [\sigma]^T [\epsilon^{th}] dV = \int_A \begin{bmatrix} \epsilon^o \\ \kappa \\ \gamma \end{bmatrix}^T \begin{bmatrix} N^{th} \\ M^{th} \\ Q^{th} \end{bmatrix} dA \quad (55)$$

Expressing the strain-curvature vector in terms of the nodal displacements and derivatives of the shape functions we have

$$\int_V [\sigma]^T ([\epsilon^{ih}] dV) = \int_A [\underline{u}]^T [\underline{B}]^T \begin{bmatrix} N^{ih} \\ M^{ih} \\ Q^{ih} \end{bmatrix} dA \quad (56)$$

Thus the sum of the three terms is

$$U = \frac{1}{2} \int_A [\underline{\bar{u}}]^T [\underline{B}]^T [C] [\underline{B}] [\underline{\bar{u}}] dA - \int_A [\underline{u}]^T [\underline{B}]^T \begin{bmatrix} N^p \\ M^p \\ Q^p \end{bmatrix} dA - \int_A [\underline{u}]^T [\underline{B}]^T \begin{bmatrix} N^{ih} \\ M^{ih} \\ Q^{ih} \end{bmatrix} dA \quad (57)$$

The potential energy due to the external work is given by

$$\dot{P} \dot{E} = - \int [\underline{\bar{u}}]^T [\underline{T}] dS \quad (58)$$

Differentiating the total potential energy with respect to the nodal load vector, load displacement equations are

$$\left[\int_A [\underline{B}]^T [C] [\underline{B}] dA \right] [\underline{\bar{u}}] = \int [\underline{\bar{N}}_i]^T [\underline{T}] dS + \int_A [\underline{B}]^T \begin{bmatrix} N^p \\ M^p \\ Q^p \end{bmatrix} dA + \int_A [\underline{B}]^T \begin{bmatrix} N^{ih} \\ M^{ih} \\ Q^{ih} \end{bmatrix} dA \quad (59)$$

Alternative formulation of piezoelectric induced loads is shown in Appendix 3A.

3.2.2 Stress Smoothing and Evaluation of Nodal Stresses

In finite element analysis, stresses are usually evaluated at the gaussian points in the element. However in problems involving stress discontinuity, they are best desired at the element boundary, i.e. at nodes on the element. The simplest way of achieving this is by gaussian point averaging, in which stress values at gaussian points nearest to the desired node are averaged and assigned to the node. In case of material discontinuity, gaussian point stresses cannot be averaged for elements with different materials. In such cases gaussian stresses are assigned to the nodes, which introduces small discontinuity in the display of stress distributions. An example of this is shown in

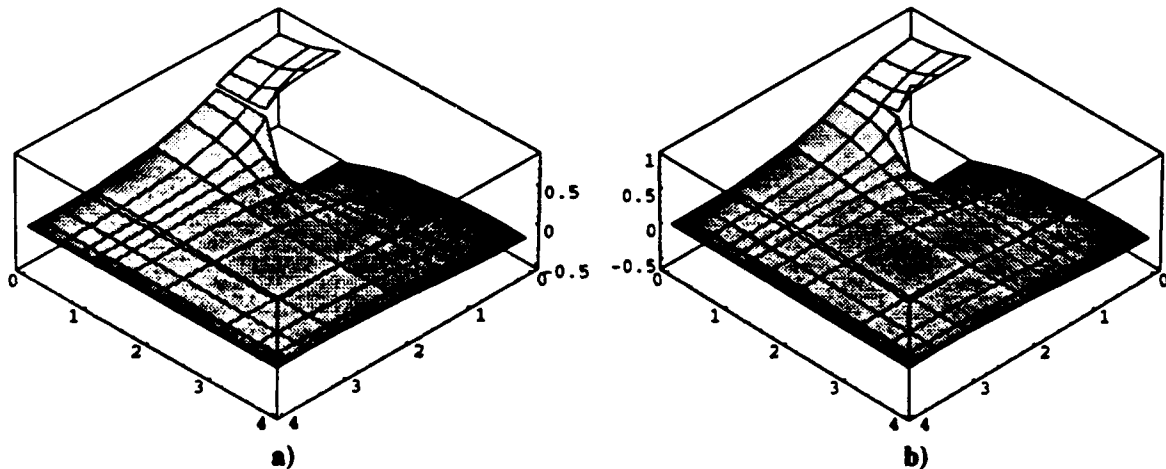


FIGURE 3.2 Stresses distributions obtained using a) gaussian point averaging and b) quadratic least squares extrapolation scheme.

Figure 3.2a, which uses gaussian point averaging. This is a distribution of σ_x in a plate with material discontinuity. Even though σ_x is a continuous function along the x-direction, we see that gaussian point averaging shows a small discontinuity.

An alternative to the above mentioned scheme is to extrapolate gaussian stresses to nodal values. The extrapolated stress state must be as representative to the element as the gaussian stresses are. In order to achieve this, a least-squares formulation for the error between the true stress state and gaussian stress state at any point in the element is required. This technique is a form of local stress smoothing in the finite element domain. Stress distribution plots using this technique can be seen in Figure 3.2b and are more representative of the state of stress in the structure. Also the process gives nodal stresses values for each element. This technique is based on the formulation by Hinton and Campbell [10]. In their formulation they devised a method to obtain linear stress extrapolation based on only the four corner nodes and gaussian points in an element. Mid-side nodal stresses were then obtained using bisection. In this analysis a quadratic least squares extrapolation scheme is used in which all the 9 gaussian points and all the 9 nodes are used. The formulation can be modified to unequal number of nodes and gaussian points as pointed out in the article[10]. The scheme is most suited to the inplane analysis in this chapter, and examples of its use will be seen in the sections to follow. Following paragraphs discuss the formulation as computed using symbolic mathematical tools as 'Mathematica'.

The error between the smoothed and unsmoothed stress at any point in the element is given by

$$e(\xi, \eta) = \sigma(\xi, \eta) - g(\xi, \eta) \quad (60)$$

Using a least-squares formulation and expressing the stress at any point in the element as a combination of the shape functions and nodal stresses, the problem becomes of finding a set of smoothed nodal stresses which minimizes the functional,

$$\chi = \sum_j^{nsp} [\sigma_j(\xi_r, \eta_j) - \bar{N}_i(\xi_r, \eta_j) \bar{\sigma}_i]^2 \quad i = 1 \text{ to } 9 \quad (61)$$

where nsp are the no. of sampling points.

Differentiating the functional with respect to the unknown nodal stresses $\bar{\sigma}_i$ and setting it equal to zero we get

$$\frac{\partial \chi}{\partial \bar{\sigma}_i} = \sum_{j=1}^{nsp} 2 [\sigma_j(\xi_r, \eta_j) - \bar{N}_k(\xi_r, \eta_j) \bar{\sigma}_k] [-\bar{N}_i(\xi_r, \eta_j)] = 0 \quad i, k = 1 \text{ to } 9 \quad (62)$$

or

$$\left\{ \sum_{j=1}^{nsp} [\bar{N}_i(\xi_r, \eta_j) \bar{N}_k(\xi_r, \eta_j) \bar{\sigma}_k] \right\} = \left\{ \sum_{j=1}^{nsp} \bar{N}_i(\xi_r, \eta_j) \sigma_j(\xi_r, \eta_j) \right\} \quad i, k = 1 \text{ to } 9 \quad (63)$$

The above equation in matrix form is then written as

$$\begin{bmatrix} \sum_{j=1}^{nsp} \bar{N}_1(\xi_r, \eta_j) \bar{N}_1(\xi_r, \eta_j) & \dots & \sum_{j=1}^{nsp} \bar{N}_1(\xi_r, \eta_j) \bar{N}_9(\xi_r, \eta_j) \\ \vdots & \ddots & \vdots \\ \sum_{j=1}^{nsp} \bar{N}_9(\xi_r, \eta_j) \bar{N}_1(\xi_r, \eta_j) & \dots & \sum_{j=1}^{nsp} \bar{N}_9(\xi_r, \eta_j) \bar{N}_9(\xi_r, \eta_j) \end{bmatrix} \begin{bmatrix} \bar{\sigma}_1 \\ \vdots \\ \bar{\sigma}_9 \end{bmatrix} = \begin{bmatrix} \bar{N}_1(\xi_r, \eta_j) & \dots & \bar{N}_9(\xi_r, \eta_j) \\ \vdots & \ddots & \vdots \\ \bar{N}_9(\xi_r, \eta_j) & \dots & \bar{N}_9(\xi_r, \eta_j) \end{bmatrix} \begin{bmatrix} \sigma_1 \\ \vdots \\ \sigma_9 \end{bmatrix} \quad (64)$$

or

$$[kk] [\tilde{\sigma}_i] = [ff] [\sigma_j] \quad i(\text{nodes}) = 1\text{to}9 \quad j(\text{nsp}) = 1\text{to}9 \quad (65)$$

Inverting [kk] and carrying out the product with [ff] we get the transformation from Gaussian stresses to extrapolated nodal stresses. The process is repeated over all the elements and nodal stresses are obtained. The stress distribution are thus said to be utilizing local stress smoothing. The transformation matrix for a bi-quadratic nine node quadrilateral element and 3 x 3 Gaussian integration is given by [T] as in eqn. 36. This matrix [T] is the same for all the elements.

$$T = \begin{bmatrix} 2.18694 & 0.27778 & 0.03528 & 0.27778 & -0.98588 & -0.12522 & -0.12522 & -0.98588 & 0.44444 \\ 0.27778 & 2.18694 & 0.27778 & 0.03528 & -0.98588 & -0.98588 & -0.12522 & -0.12522 & 0.44444 \\ 0.03528 & 0.27778 & 2.18694 & 0.27778 & -0.12522 & -0.98588 & -0.98588 & -0.12522 & 0.44444 \\ 0.27778 & 0.03528 & 0.27778 & 2.18694 & -0.12522 & -0.12522 & -0.98588 & -0.98588 & 0.44444 \\ 0 & 0 & 0 & 0 & 1.47883 & 0 & 0.18784 & 0 & -0.66666 \\ 0 & 0 & 0 & 0 & 0 & 1.47883 & 0 & 0.18784 & -0.66666 \\ 0 & 0 & 0 & 0 & 0.18784 & 0 & 1.47883 & 0 & -0.66666 \\ 0 & 0 & 0 & 0 & 0 & 0.18784 & 0 & 1.47883 & -0.66666 \\ 0 & 0 & 0 & 0 & 0 & 0 & 0 & 0 & 1.00000 \end{bmatrix} \quad (66)$$

and nodal stresses are given by

$$\begin{bmatrix} \tilde{\sigma}_1 \\ \tilde{\sigma}_9 \end{bmatrix} = [T] \begin{bmatrix} \sigma_1 \\ \sigma_9 \end{bmatrix} \quad (67)$$

3.3 Quasi-3D Finite Element Analysis

A commonly observed failure mode in laminated composites is delamination between its layers or plies. One of the major causes of delamination is the interlaminar stresses that develop in the region where structural or material discontinuities exist such as cutouts, free edges or presence of foreign material in the laminates. The interlaminar stresses exist only in a small region near the discontinuities and vanish rapidly away from the region. A number of factors influence the magnitude of these interlaminar stresses namely stacking sequence, poisson's ratio and coefficient of mutual influence mismatch between the adjacent plies, ply thicknesses etc. Due to complexities in satisfying equations of equilibrium and boundary conditions, exact solutions are not available. Hence, finite element methods are used in the analysis.

The complex state of stress in a laminate is often determined with the help of finite element analysis technique. Interlaminar stresses are the stresses in the thickness direction which, in general, can be analyzed by the 3-D modelling of the laminate. An accurate 3-D analysis introduces a large number of degrees of freedom resulting into enormous memory and computational time requirements. A quasi-3D modelling technique is incorporated in this study for an efficient and accurate numerical analysis.

This section is focussed on the quasi-3D finite element analysis to study the interlaminar stresses in laminated composites and to obtain the detailed state of stress in the vicinity of high stress gradient regions in piezoelectric layers. The mechanical excitation of a piezoelectric element is usually performed by means of thin electrodes deposited on the surface of the element and subjected to a given potential difference. It is therefore necessary that these structures be treated by piezoelectric theory combined with methods for solving boundary value problems with discontinu-

uous boundary conditions. The interaction of surface electrodes with a piezoelectric material, and the interaction of these piezoelectric layers in laminated composite structures is of particular importance in analysis of smart laminated composites.

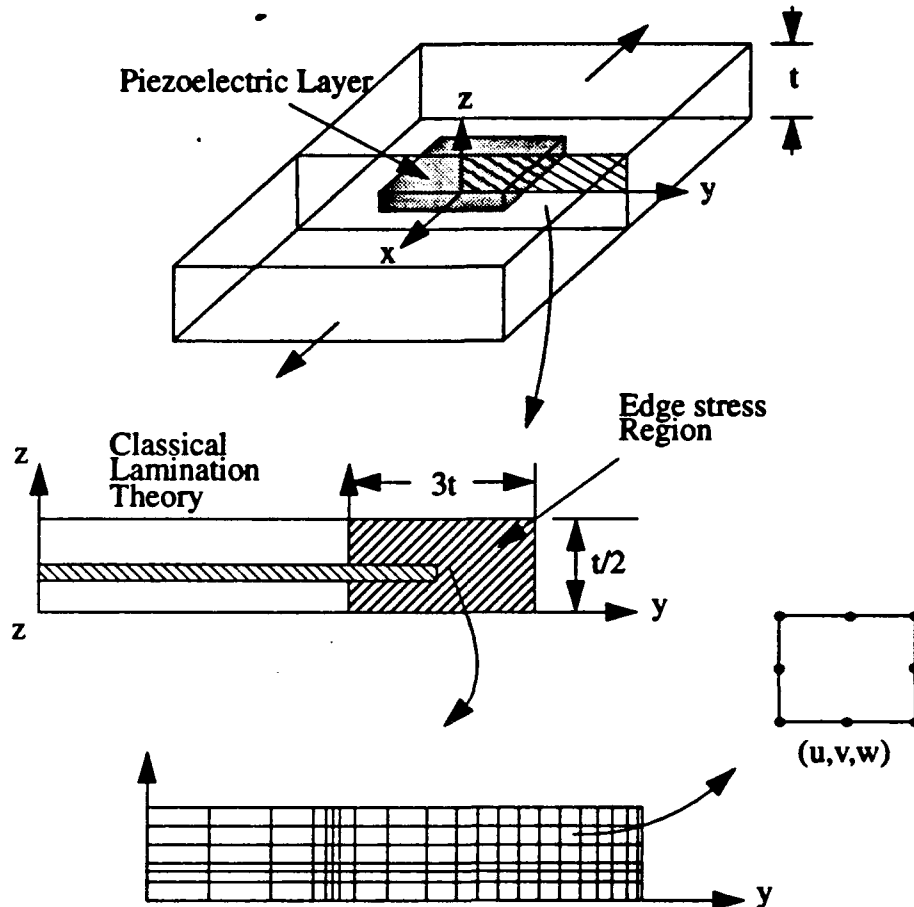


FIGURE 3.3 Representative section of laminate for quasi-3D finite element analysis.

The objective of this section is to develop the quasi-3D analytical method that is capable for determining the state of stress in plates and laminated composites with piezoelectric layers, and around material and stress discontinuities.

3.3.1 Formulation of Finite Element Equations

The complex state of stress in a laminate can be analyzed by the 3-D modelling of the medium as shown in Figure 3.3. A complete 3-D analysis introduces a large number of degrees of freedom resulting into enormous memory and computational time requirements. A quasi-3D modelling technique which only models the structure in the two dimensions but allowing a degree of freedom in the 3rd direction, has been developed to analyze the interlaminar stresses of laminates under a uniform bending, uniform twisting and uniform extensional loads (Chan and Ochoa [11]). The displacement functions used are as shown below:

$$\begin{aligned}
 U(x, y, z) &= \epsilon_0 x + kz + u(y, z) \\
 V(x, y, z) &= Cz + v(y, z) \\
 W(x, y, z) &= -\frac{1}{2}kx^2 - Cxy + w(y, z)
 \end{aligned}
 \tag{68}$$

where ϵ_o is the uniform extension in the x-direction and k and $2C$ are the longitudinal and twisting curvatures, as obtained from

$$\begin{aligned}\kappa_x &= \frac{\partial^2 w}{\partial x^2} = k \\ \kappa_{xy} &= -2 \frac{\partial^2 w}{\partial x^2} = 2C\end{aligned}\quad (69)$$

thus a constant curvature through the structure is enforced. The finite elements used in the model were eight-noded isoparametric elements with each node having three displacement degrees of freedom $u(y, z)$, $v(y, z)$ and $w(y, z)$.

The strains are given by $\{\epsilon\} = \{\epsilon\}_o + \{\epsilon\}_L$ where

$$\{\epsilon\}_o = \left[\left(\frac{\partial u}{\partial x} \right) \left(\frac{\partial v}{\partial y} \right) \left(\frac{\partial w}{\partial z} \right) \left(\frac{\partial v}{\partial z} + \frac{\partial w}{\partial y} \right) \left(\frac{\partial u}{\partial z} + \frac{\partial w}{\partial x} \right) \left(\frac{\partial u}{\partial y} + \frac{\partial v}{\partial x} \right) \right]^T \quad (70)$$

and

$$\{\epsilon\}_L = \left[(\epsilon_o) \quad (0) \quad (0) \quad (0) \quad (-Cy) \quad (Cz) \right]^T \quad (71)$$

The constitutive equations of material subjected to mechanical (ϵ), Thermal (T) as well as electrical (E) loads are given in section 1.4.1 by eqn. 9.

The internal potential energy can be written as

$$\Omega = \int_{vol} \left\{ \frac{1}{2} \{\epsilon\}^T [C^{E,T}] \{\epsilon\} - \frac{1}{2} \{E\}^T [\eta^{E,T}] \{E\} - \{\epsilon\}^T [C^{E,T}] [d]^T \{E\} - \{p\}^T \{E\} \Theta - \{\epsilon\}^T \{\lambda\} \Theta - \frac{1}{2} \frac{C^{E,E}}{T} \Theta^2 \right\} dvol \quad (72)$$

It should be noted that the superscript T outside the brackets is referred to the transpose of the matrix in the bracket. Assuming the thermal terms appear only as initial temperature strains ϵ_{th} , and keeping only the terms that include the strain ϵ_{ij} , and also since $\{\lambda\} \Theta = [C^{E,T}] \{\epsilon_{th}\}$ and $\{\epsilon\} = \{\epsilon\}_o + \{\epsilon\}_L$ we have

$$\begin{aligned}d\Omega &= \frac{1}{2} (\{\epsilon\}_o + \{\epsilon\}_L)^T [C^{E,T}] (\{\epsilon\}_o + \{\epsilon\}_L) - (\{\epsilon\}_o + \{\epsilon\}_L)^T [C^{E,T}] \{\epsilon\}_{th} \\ &\quad - (\{\epsilon\}_o + \{\epsilon\}_L)^T [C^{E,T}] [d]^T \{E\} + \text{other 'terms' not including } \epsilon\end{aligned}\quad (73)$$

Let $\{\bar{u}\}$ be the nodal displacement matrix and $[\bar{B}]$ be the matrix relationship between the element strain and nodal displacements. Setting $\{\epsilon\}_o = [\bar{B}] \{\bar{u}\}$ we have

$$\begin{aligned}d\Omega &= \frac{1}{2} \{\bar{u}\}^T [\bar{B}]^T [C^{E,T}] [\bar{B}] \{\bar{u}\} + \frac{1}{2} \{\bar{u}\}^T [\bar{B}]^T [C^{E,T}] \{\epsilon\}_L + \frac{1}{2} \{\epsilon\}_L^T [C^{E,T}] [\bar{B}] \{\bar{u}\} \\ &\quad + \frac{1}{2} \{\epsilon\}_L [C^{E,T}] \{\epsilon\}_L - \frac{1}{2} \{\bar{u}\}^T [\bar{B}]^T [C^{E,T}] \{\epsilon_{th}\} - \frac{1}{2} \{\epsilon\}_L^T [C^{E,T}] \{\epsilon_{th}\} \\ &\quad - \frac{1}{2} \{\bar{u}\}^T [\bar{B}]^T [C^{E,T}] [d]^T \{E\} - \frac{1}{2} \{\epsilon\}_L^T [C^{E,T}] [d]^T \{E\} + \text{other 'terms' not including } \epsilon\end{aligned}\quad (74)$$

Also potential energy due to external loads is given by

$$\Psi = - \int_{vol} \{\bar{u}\}^T \{f\} dvol \quad (75)$$

Differentiating the sum of internal and external potential energy with respect to $\{u\}$ we have from principle of minimum potential

$$\frac{\partial \Omega}{\partial \{u\}} + \frac{\partial \Psi}{\partial \{u\}} = 0 \quad (76)$$

which gives

$$\begin{aligned} \left(\int_{vol} [\tilde{B}]^T [C^{E,T}] [\tilde{B}] dvol \right) \{\bar{u}\} = f - \left(\int_{vol} [\tilde{B}]^T [C^{E,T}] \{\epsilon\}_L dvol \right) \\ + \left(\int_{vol} [\tilde{B}]^T [C^{E,T}] \{\epsilon_{th}\} dvol \right) + \left(\int_{vol} [\tilde{B}]^T [C^{E,T}] [d]^T \{E\} dvol \right) \end{aligned} \quad (77)$$

Expressing the thermal strain in terms of α the above equation becomes

$$\begin{aligned} \left(\int_{vol} [\tilde{B}]^T [C^{E,T}] [\tilde{B}] dvol \right) \{u\} = f - \left(\int_{vol} [\tilde{B}]^T [C^{E,T}] \{\epsilon\}_L dvol \right) \\ + \left(\int_{vol} [\tilde{B}]^T [C^{E,T}] \{\alpha\} \Delta T dvol \right) + \left(\int_{vol} [\tilde{B}]^T [C^{E,T}] [d]^T \{E\} dvol \right) \end{aligned} \quad (78)$$

The load displacement relation thus becomes

$$[K] \{\bar{u}\} = \{F\}^* \quad (79)$$

where $[K]$ is the element stiffness and $\{F\}^*$ is the generalized load vector. They are expressed as

$$[K] = \int_{vol} [\tilde{B}]^T [C^{E,T}] [\tilde{B}] dvol \quad (80)$$

and

$$\begin{aligned} \{F\}^* = f - \left(\int_{vol} [\tilde{B}]^T [C^{E,T}] \{\epsilon\}_L dvol \right) + \left(\int_{vol} [\tilde{B}]^T [C^{E,T}] \{\epsilon_{th}\} dvol \right) \\ + \left(\int_{vol} [\tilde{B}]^T [C^{E,T}] [d]^T \{E\} dvol \right) \end{aligned} \quad (81)$$

3.4 Some Numerical Simulations

The results discussed in this section shows application of plate finite element, quasi-3D finite element and an efficient combination of the two formulations in analysis of plates and laminates with piezoelectric patches.

3.4.1 Inplane Analysis

In order to implement the finite element formulation derived in the previous sections, a square plate with different shapes of piezoelectric patches was used. Two cases are considered. The first case has the piezoelectric patch through the entire thickness of the plate and is as shown in Figure 3.4a. The second case has a piezoelectric patch embedded between two layers of aluminum plates as shown in Figure 3.4b In both the cases of embedding, four different shapes of patches are used. Figure 3.4 along with Table 3.1 shows the dimensions of the plate and the orientation of the piezoelectric patches.

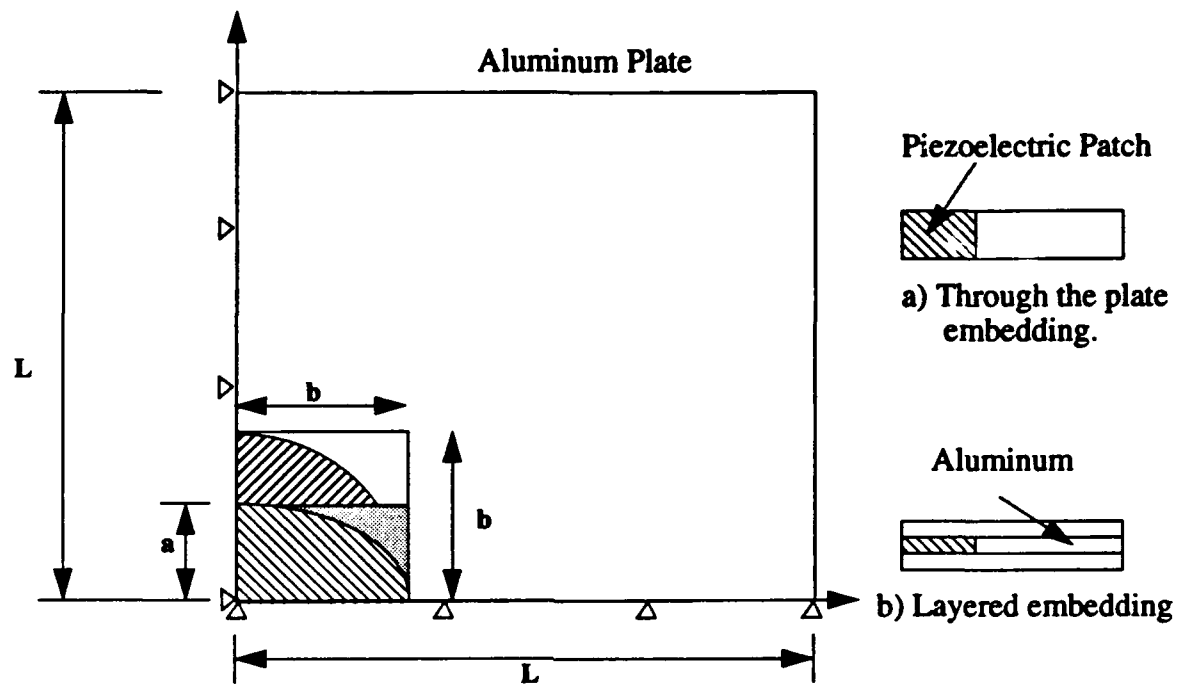


FIGURE 3.4 A square plate with different shapes of piezoelectric patches.

TABLE 3.2 Dimensions of the aluminum plate and the piezoelectric patches

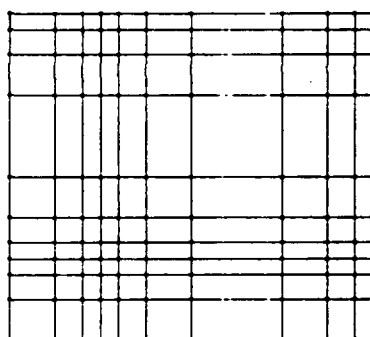
Plate	$L = 4''$, $W = 4''$
Square	side = $b = 1''$
Rectangle	Height = $b = 1''$, Length = $c = 2''$
Circle	radius = $b = 1''$
Ellipse	major axis = $b = 1''$, minor axis = $a = 0.5''$

Due to symmetry in the problem, only a quarter of the plate is modelled. Displacement boundary conditions along the x-axis and y-axis are also shown in the Figure 3.4. Table 3.2 shows the material properties of aluminum plate and the piezoelectric patches. A constant potential difference in the thickness direction is applied to the piezoelectric patches in order to induce an electric field.

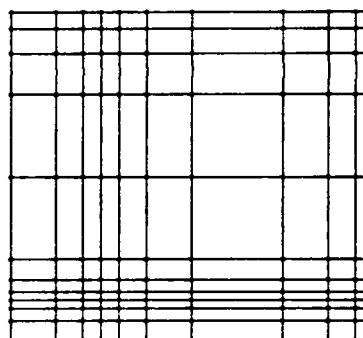
TABLE 3.3 Material properties for aluminum plate and piezoelectric G1195.

Property	Aluminum	PZT - G1195
$E_1 = E_2$ (Msi)	69.0×10^9	63.0×10^9
G_{12} (Msi)	26.0×10^9	22.0×10^9
ν_{12}	0.3100	0.3100
$d_{31}=d_{32}$ m/V	—	-166.0×10^{-12}
d_{33} m/V	—	360.0×10^{-12}
$d_{24}=d_{15}$ m/V	—	540×10^{-12}

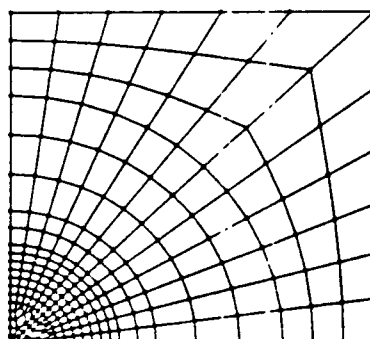
Finite element meshes used for the analysis for each cases are as shown in Figure 3.5 below.



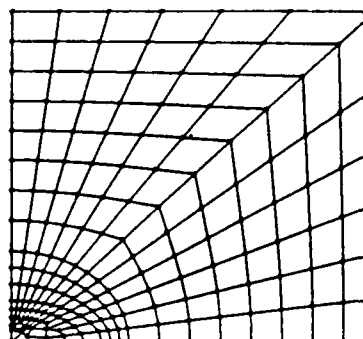
Square Piezoelectric Patch



Rectangular Piezoelectric Patch



Circular Piezoelectric Patch



Elliptical Piezoelectric Patch

FIGURE 3.5 Finite element meshes for different configurations of the piezoelectric patches

All the stresses are normalized by the stress, σ_0 which is due to a Voltage of 1 V (electric field of 3937 V/m) on a piezoelectric under plane stress conditions. The value of σ_0 thus obtained is 59.68 kPa and is computed as

$$\sigma_o = E_3 g_{31} \left[1 - \frac{C_{13}^E g_{33}}{C_{33}^E g_{31}} \right] = \sigma_{x_o} = \sigma_{y_o} \quad (82)$$

where symbols are as defined in Chapter 2.

Stress distributions are obtained due to electric field applied to the piezoelectric patches. The magnitude of the stress is shown along the z-axis and the element coordinates are shown along x- and y-axes. The grey-scale shade represents the stress magnitude in the elements. The highest stresses are shown in white and the lowest in black. Only a few representative stress distributions using grey-scale plots are shown in this section. Some of the figures to follow will show in the upper corners of the figures, the embedding case and the layer / layers for which the stresses are shown.

Figures 3.6 and 3.7 show the distributions of σ_x and σ_y in the plate with a square patch. Since σ_x is a normal traction on the x-faces the distribution of σ_x along the x-direction is continuous. The distribution of σ_x along the y-axis is discontinuous. As we move away from the patch, stresses reduce to zero at the far field of the plate since there are no far field stresses applied to the edges. However, due to the finite dimensions of the plate, a boundary effect can be seen along the y-axis for σ_x and along the x-axis for σ_y , i.e. there is a non-zero stress in the region away from the patch along the two axes. The distribution of the in-plane stress σ_y in the plate as shown in Figure 3.7, looks similar to that of the in-plane stress σ_x . The σ_y distribution is a rotated image of the σ_x distribution which is due to the axial symmetry in the problem. Figure 3.8 shows the shear stress σ_{xy} distribution in the plate. The shear stress is zero almost everywhere except in the vicinity of the corner of the square piezoelectric patch. This is due to the discontinuity of σ_x and σ_y in the y and x directions respectively, around the corner of the patch.

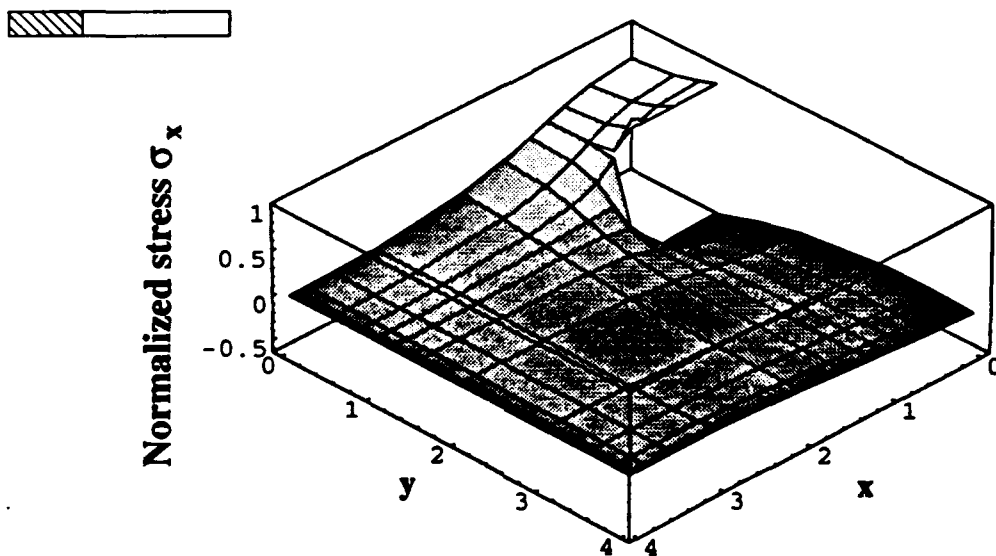


FIGURE 3.6 Distribution of normalized stress σ_x in the plate with square piezoelectric patch

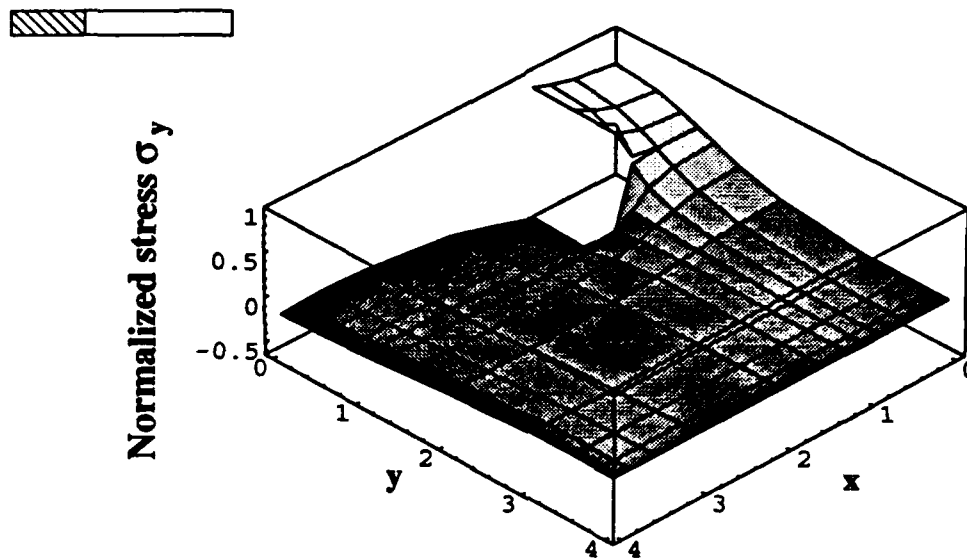


FIGURE 3.7 Stress distribution of σ_y in the plate with square piezoelectric patch.

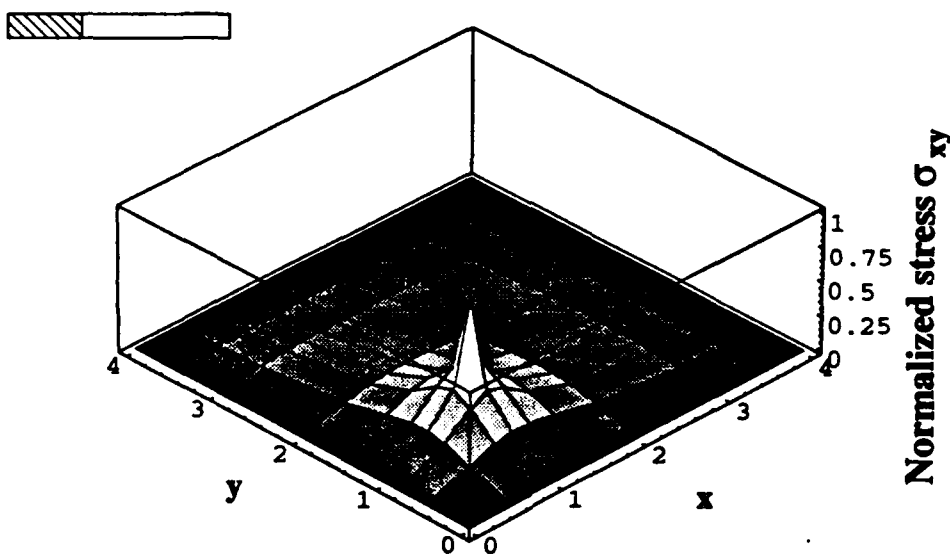


FIGURE 3.8 Stress distribution of σ_{xy} in the plate with square piezoelectric patch.

Figure 3.9 shows the distribution of σ_x in the plate with a circular piezoelectric patch. The stress changes gradually from a continuous to a discontinuous one as we go from the x-axis to the y-axis. The normal stress component σ_x is constant in the piezoelectric due to the cylindrical symmetry.

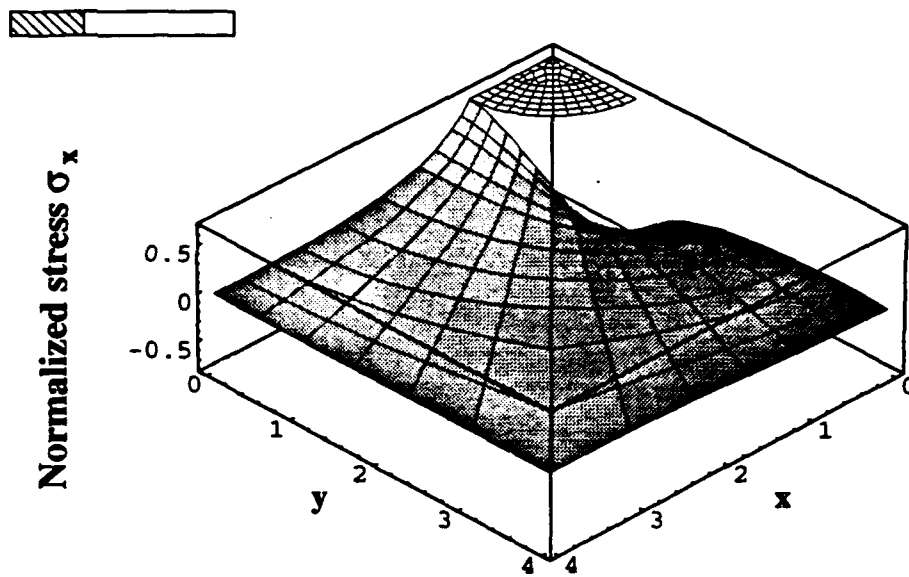


FIGURE 3.9 Stress Distribution of σ_x in plate with circular piezoelectric patch

Figure 3.10. shows a plot of the shear stress σ_{xy} in the plate with circular patch. The shear stress σ_{xy} is highest at the material interface of piezoelectric patch and aluminum plate at 45° to the x-axis and almost zero elsewhere on the plate.

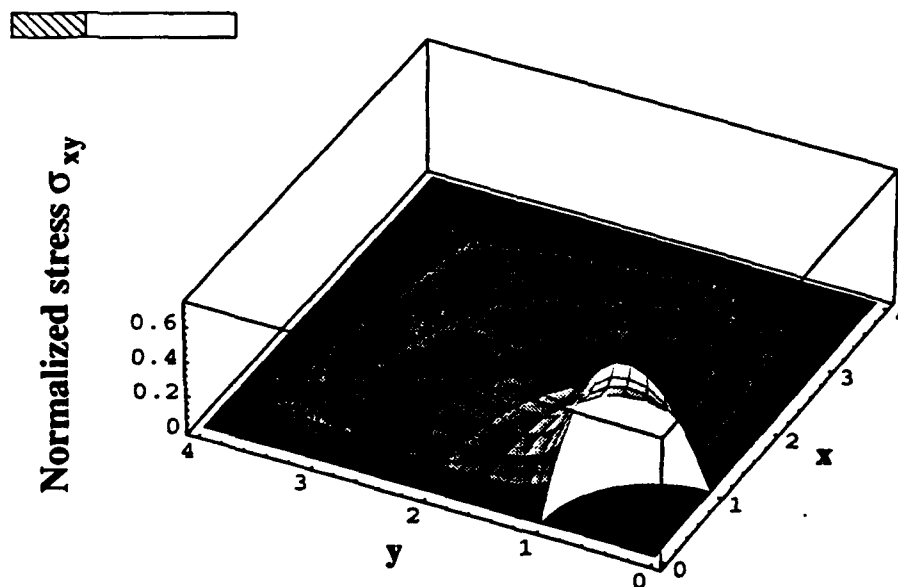


FIGURE 3.10 Distribution of shear stress σ_{xy} in plate with circular piezoelectric patch

Figure 3.11 shows the distributions of stresses in the r - θ coordinate systems. The radial stress σ_r , and the tangential stress σ_θ on the aluminum side of the plate along the circumference are both constant. In Figure 3.12 the stress σ_θ changes sign as we go to the piezoelectric side of the plate.

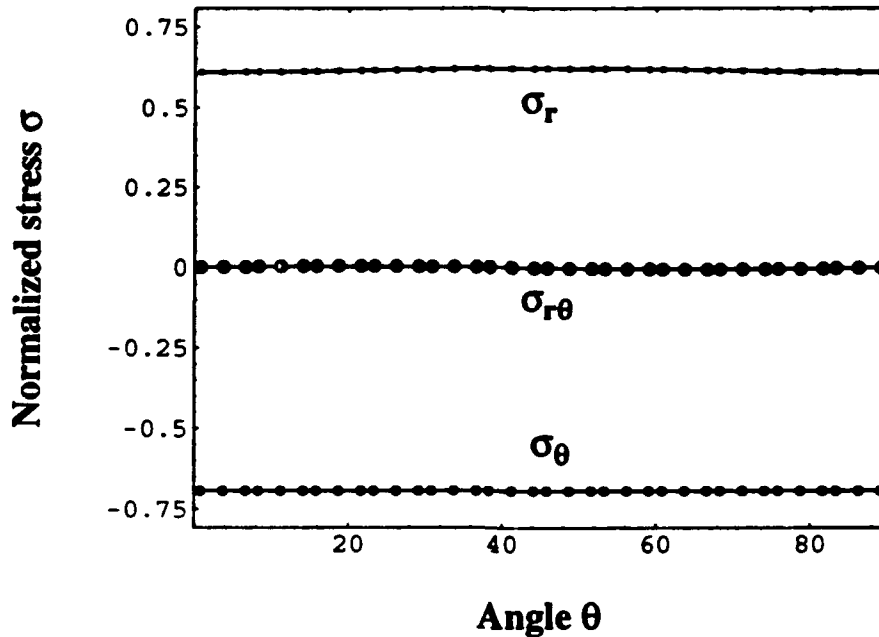


FIGURE 3.11 Distribution of stresses σ_r , σ_θ , and $\sigma_{r\theta}$ along the circumference of the circular piezoelectric patch on the aluminum side.

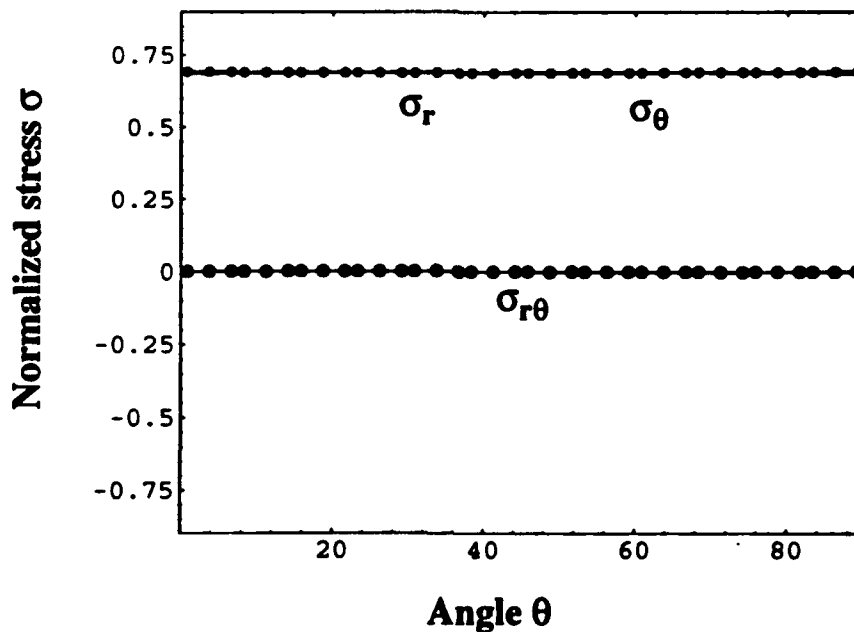


FIGURE 3.12 Distribution of stresses σ_r , σ_θ , and $\sigma_{r\theta}$ along the circumference of the circular piezoelectric patch on the piezoelectric side.

Also shear stress $\sigma_{r\theta}$ along circumference or edge of the piezoelectric is zero. Figure 3.13 shows the distribution of the radial and tangential stresses radially along a line 45° to the x-axis. The change in sign of the stress σ_θ from positive to the negative as we move radially from the piezoelectric to the aluminum side of the plate is much clearly seen. There is a continuous gradual

drop in the radial stress along the radial direction. Again far-field stresses are zero as we move away from the piezoelectric patch. Shear stress $\sigma_{r\theta}$ is zero all along the radial direction.

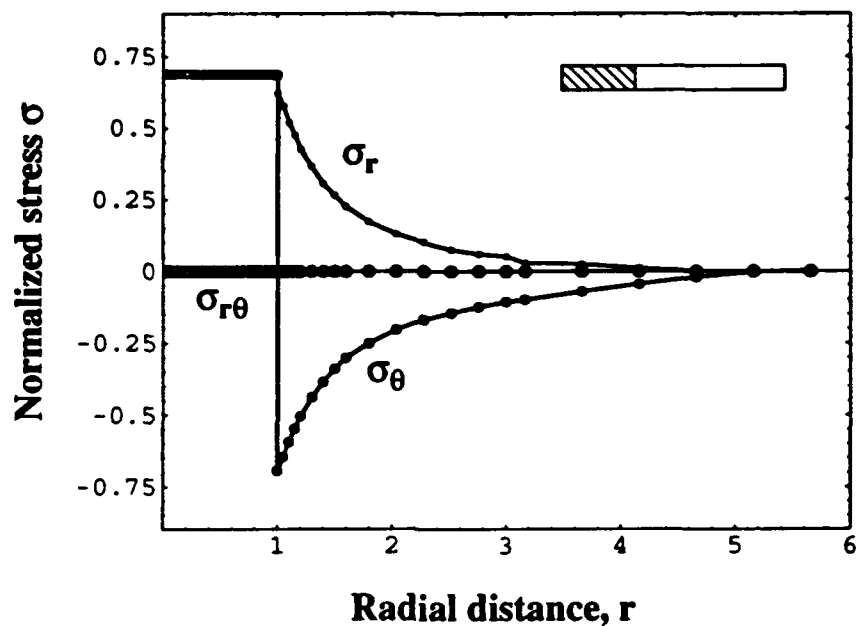


FIGURE 3.13 Distribution of stresses σ_r and σ_θ along the radial direction at $\theta = 45^\circ$ in the plate with the circular patch.

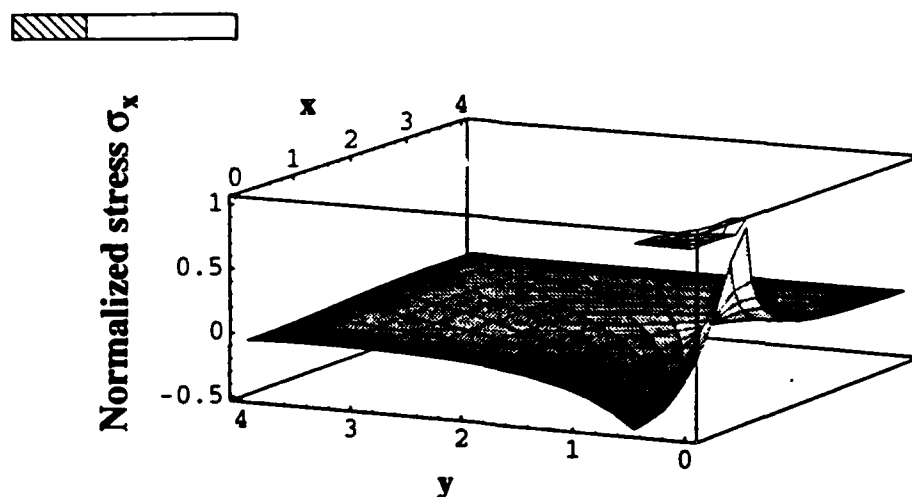


FIGURE 3.14 Distribution of normalized stress σ_x in the plate with elliptical piezoelectric patch

Stress distribution (σ_x) in the plate with an elliptical patch is shown in Figure 3.14. The stress distribution is similar to the one in plate with a circular piezoelectric. The stress is continuous

along the x-axis and discontinuous along the y-axis. However, due to the aspect ratio of the elliptical patch, the stress is higher in magnitude than that in plate with circular patch. This change in magnitude was also seen between the cases of plate with square and rectangular patches. Far field stresses can be seen to approach zero as we move away from the patch.

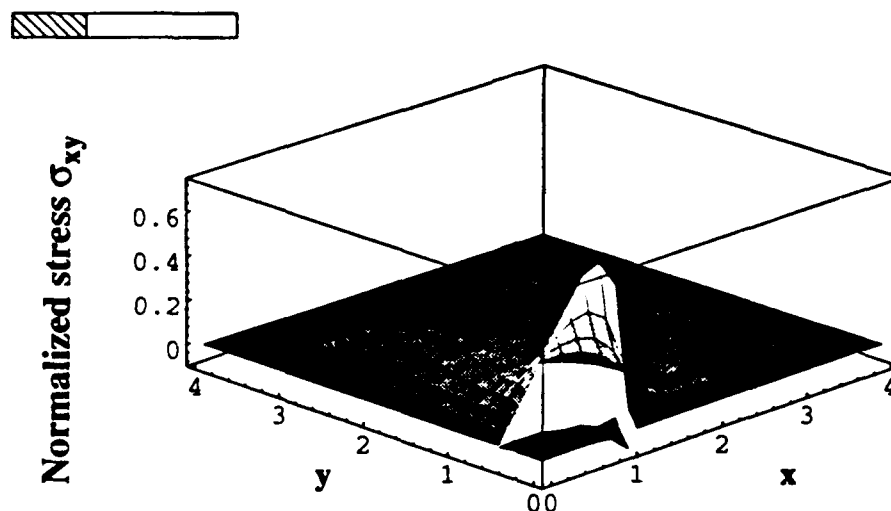


FIGURE 3.15 Stress distribution of σ_{xy} in the plate with elliptical piezoelectric patch.

Figure 3.15 shows the distribution of shear stress σ_{xy} in the plate with an elliptical piezoelectric patch. This distribution is also similar to that in plate with circular patch. However, this case shows that maximum value of the shear stress does not occur at 45° to the x-axis. In fact the location of the maximum has changed to about 20° to the x-axis. Again this is due to the aspect ratio not being equal to 1.0.

Figure 3.16 shows distributions of the normal and tangential stresses along the circumference of the elliptical patch and on the aluminum side of the plate. The normal and tangential directions at any point on the circumference where computed from the derivative of the equation of the curve.

Unlike the case with circular patch, the stresses do not remain constant with the angle from the x-axis. As we approach the y-axis, the normal stress σ_n reduces in magnitude and the tangential stress σ_t increases in magnitude. Also shear stress σ_{nt} is not zero along the circumference of the patch. The magnitude of the shear stress is however, much smaller as compared to that of the other two components σ_n and σ_t .

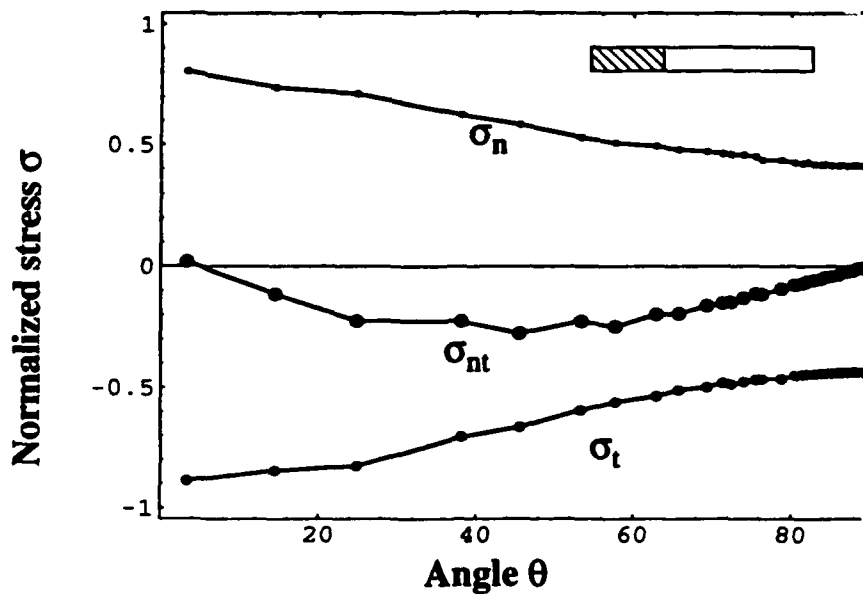


FIGURE 3.16 Distribution of stresses σ_n , σ_t , and σ_{nt} along the circumference of the elliptical piezoelectric patch on the aluminum side.

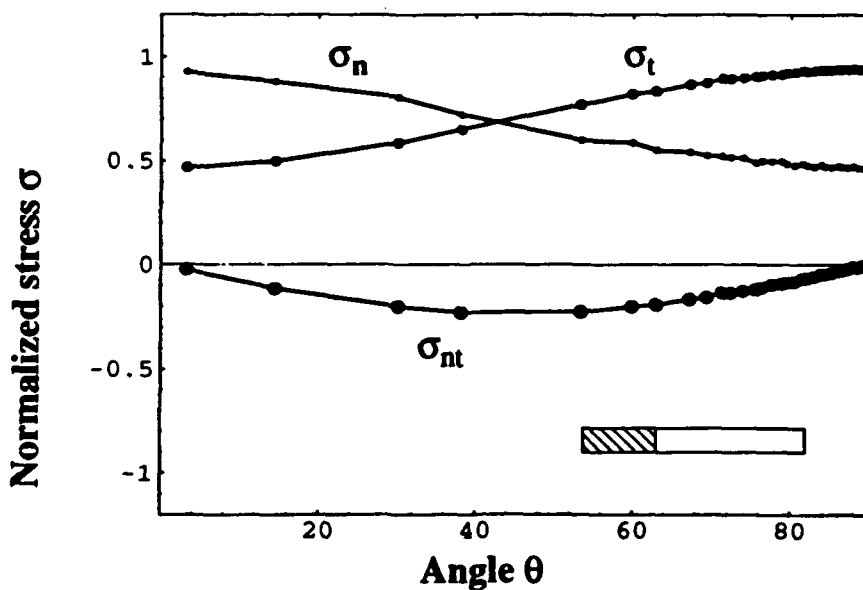


FIGURE 3.17 Distribution of stresses σ_n , σ_t , and σ_{nt} along the circumference of the elliptical piezoelectric patch on the piezoelectric side.

A similar distribution for the normal and tangential stresses along the circumference of the

patch on the piezoelectric side of the plate can be seen in Figure 3.17. The tangential stress σ_y is positive on this side. The trend for σ_y is the same as before i.e. increasing with the angle θ .

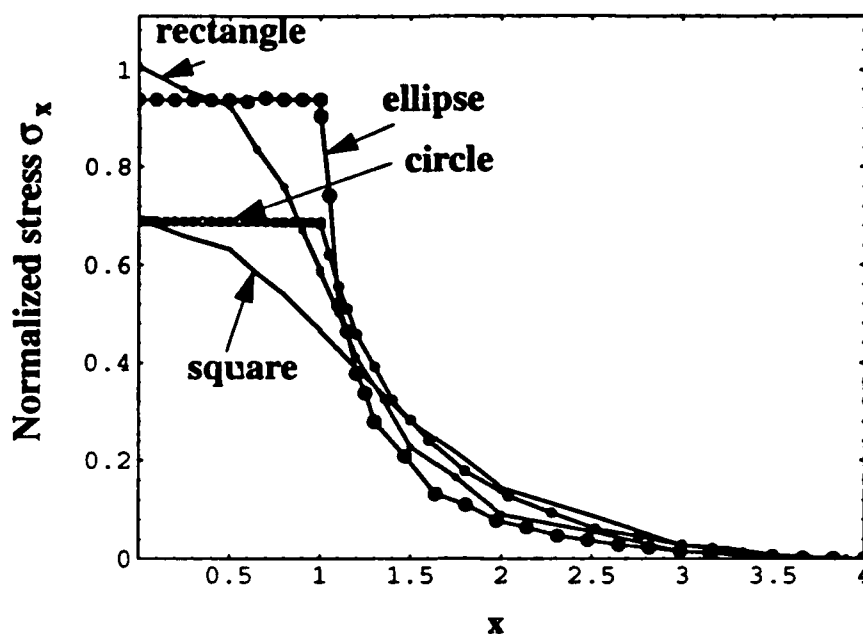


FIGURE 3.18 Comparison of the distributions of σ_x along the x-axis in the plate for all the patches.

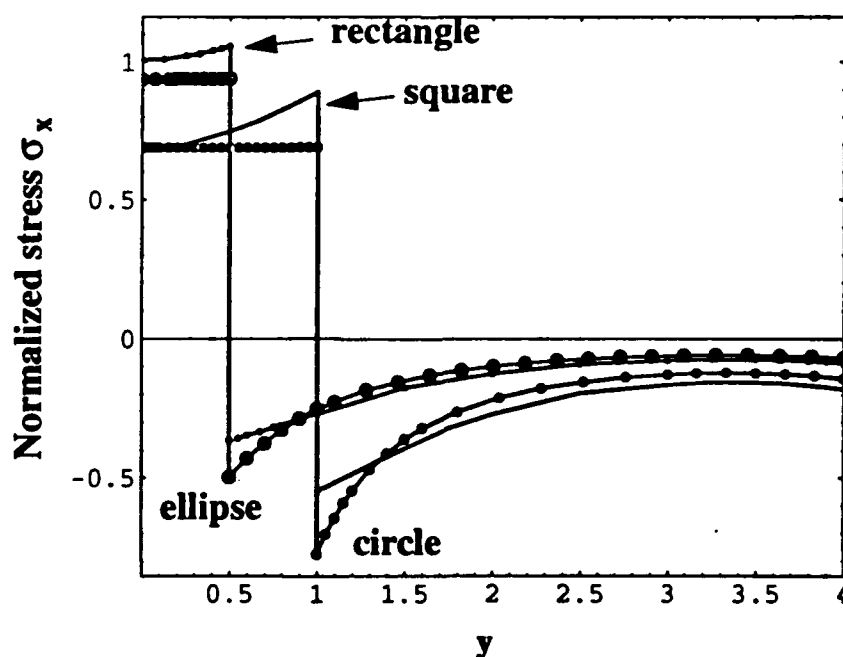


FIGURE 3.19 Comparison of the distributions of σ_x along the y-axis in the plate for all the patches.

Figure 3.18. shows the comparison of the stress distributions (σ_x) along the x-axis in the plate with all four types of patches. As observed in the grey scaled plots in this section, they are all continuous traction distributions. The stresses in the plate with rectangular patch are higher than the stresses in the plate with square patch due to the width of the rectangular patch being half the

width of square patch. Similarly, stresses in plate with an elliptical patch are higher than the stresses in plate with the circular patch.

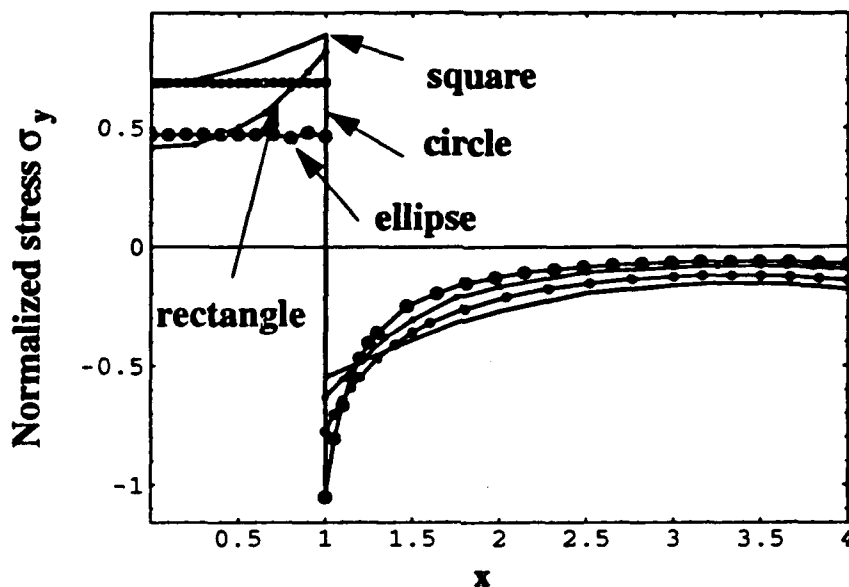


FIGURE 3.20 Distribution of σ_y along the y -axis in the plate.

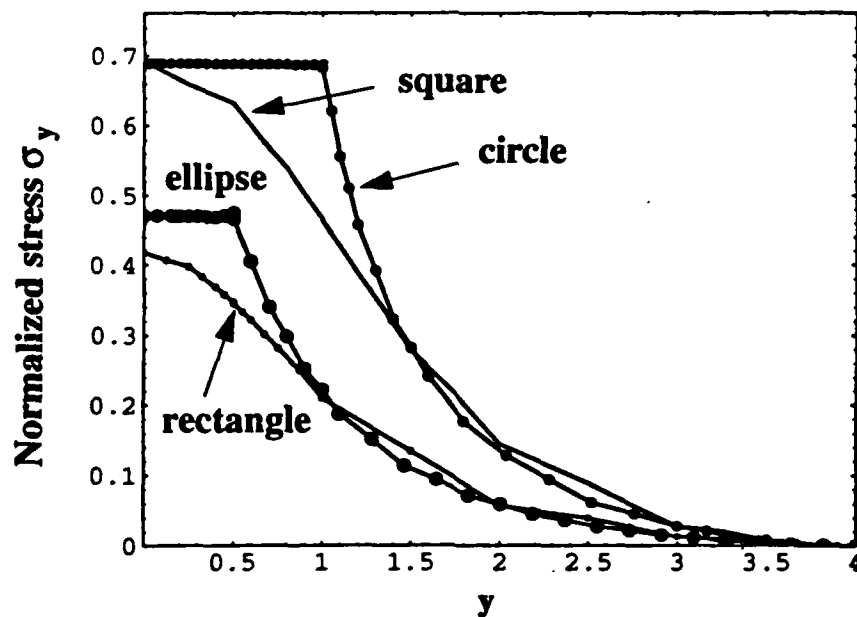


FIGURE 3.21 Distribution of σ_y along the x -axis of the plate.

Figure 3.19. shows a distribution of σ_x along the y -axis for all four cases. The discontinuous behavior as observed in the grey-scaled plots can be clearly seen. The stresses are higher for the rectangular and elliptical cases than for the square and circular cases. In the case of square and rectangular patches, stress increases as we approach the edge of the piezoelectric patch. There is a 30% rise in the stress σ_x along y -axis for the square case and about a 10% rise for the rectangular

case. Since the square patch is wider than the rectangular patch, we see a higher rise in the peak stress for the square patch. Similar discontinuous stress distributions with rise towards the edge of the patch, have been observed in piezoelectric layers near the edge of the electrode (see section 3.6.4).

Figure 3.20 shows the distribution of σ_y along the x-axis for the square and rectangular patches. Again this is not a traction on the interface and therefore shows discontinuous behavior. In this case the peak stress shows an approximately 30% rise for the square case and about 50% rise for the rectangular case. Notice that the rise in the case of σ_y along the x-axis is higher than the rise of σ_x along the y-axis for the rectangular patched plate. This is due to the fact that the rectangular patch is wider along the x-axis and shorter along the y-axis.

Figure 3.21 shows the distribution of σ_y along the y-axis. This is a continuous distribution which monotonically goes to zero since there is no far field stress applied to the plate. The stress σ_y in the cases with rectangular patch and elliptical patch is less than that of the square and circular patch cases. In the case of plate with circular and elliptical patches, the stress is constant in the piezoelectric and gradually decreases to zero in the surrounding material. In the case of plate with square and rectangular patches, the stress starts decreasing in the piezoelectric and continue to decrease in the surrounding material.

For the discontinuous stress distributions of σ_x along y-axis (Figure 3.19) and for σ_y along the x-axis (Figure 3.21) the drop in stresses at the material interface is the same for all cases. However, the rectangle patch case shows the highest magnitude of σ_x along the y-axis and the square case shows the highest stress magnitude of σ_y along the x-axis. For the distribution of σ_y along the x-axis the rectangular patch case shows the highest stress gradient in the piezoelectric patch and the plate with ellipse shows the highest stress gradient in the aluminum side of the plate. Also the stresses in the circular and elliptical patches does not show a rise in the stresses as we approach the edge of the patch, but remain constant throughout the patch. Also, from previous stress plots it can be seen that the sharp corners in the cases of square and rectangle patches, show a high shear stress. These factors show that it would be better to use patches that do not have sharp corners, which is in favor of the circular and elliptical patches. Based on the aspect ratio of the patch, as in rectangular and elliptical patches, it seems that stresses and stress gradients within the patch are high and will probably get higher as the aspect ratio increases. The shape of the patches have a direct effect on the stress field within the patch and in the surrounding material. The choice of the shape of the patches depends on the desired stress field, however, in general sharp corners should be avoided.

The stress distributions for the plates with piezoelectric patches that are inserted through the entire thickness of the plate are discussed in the previous paragraphs. The following paragraphs will discuss stress distributions for the cases in which the piezoelectric layer is embedded in a layered plate. Stress distributions in different layers in the plate with an embedded piezoelectric layer are obtained. Figure 3.22 and 3.23 show the distribution of stress σ_x along the x-axis in layer 1 and layer 2, respectively. The positive electric field in the thickness direction of the piezoelectric patch causes it to shrink in the x-y plane and expand in the z-direction. This induces a compressive in-plane normal stress in the aluminum layer above and below it. However, since the plate restricts the piezoelectric patch from free shrinking, the piezoelectric layer itself is subjected to tension in the x-y plane. The inplane compression in the aluminum and the inplane tension in the piezoelectric layers can be clearly seen in the Figures. The stress σ_x in the x-direction as seen in the figures appears to be a discontinuous distribution. In the plate finite element analysis, only integrated tractions need to be continuous in the x-direction. Therefore traction in the individual plies are discontinuous at the material interface but the integrated tractions through the thickness are continuous. The stresses in the plate are correct at almost everywhere except in the region very close to

the material interface. The reason behind this being that the plate finite element code assumes that strains through the thickness vary linearly. However, at the material interface the strains do not vary linearly and a detailed 3-D analysis is required to get accurate through-the-thickness stresses and strains in this region. The interaction between 2-D and 3-D stress analysis to obtain stresses around the material interface will be discussed in the next section. The present discussion is valid for the study of the stress state in the layers away from the material interface.

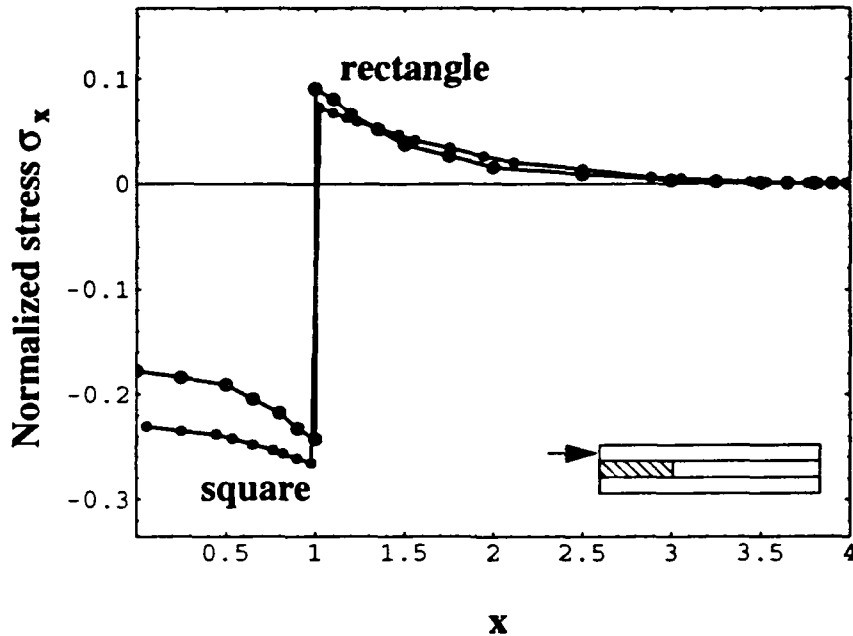


FIGURE 3.22 Distribution of σ_x along the x-axis in the aluminum layer (layer 1) for the layered plate with square patch and with rectangular patch.

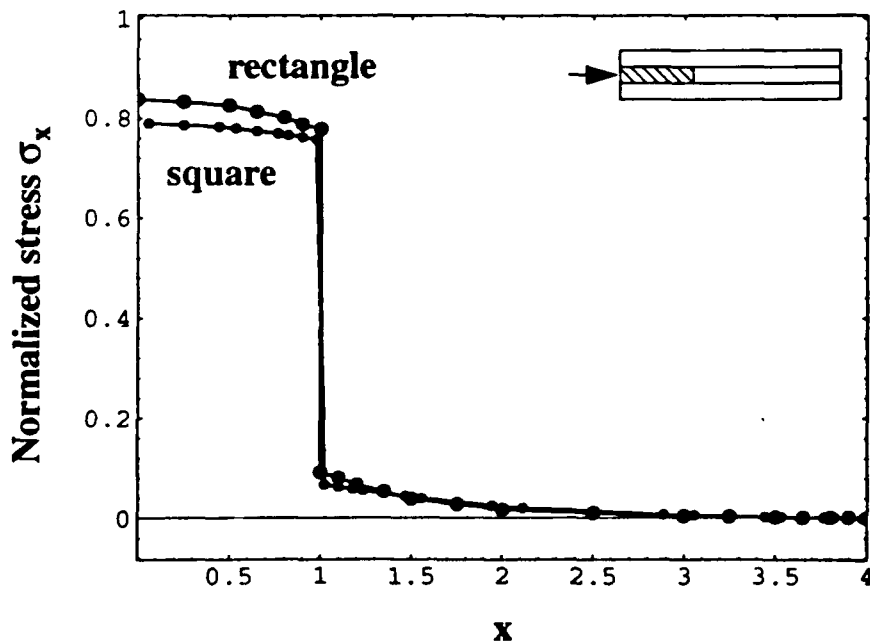


FIGURE 3.23 Distribution of σ_x along the x-axis in the combined layer (layer 2) for the layered plate with square patch and with rectangular patch.

Figures 3.24 and 3.25 show the distribution of σ_y along the x-axis. This is a disor

distribution at the interface. It should be noted that this stress distribution is not required to be continuous. The piezoelectric patch is in tension in the x-y plane and the aluminum above and below it is in compression. Unlike the case in which the piezoelectric patch was inserted through the entire thickness, these distributions do not show a sharp stress gradient near the edge of the piezoelectric (see Figure 3.20).

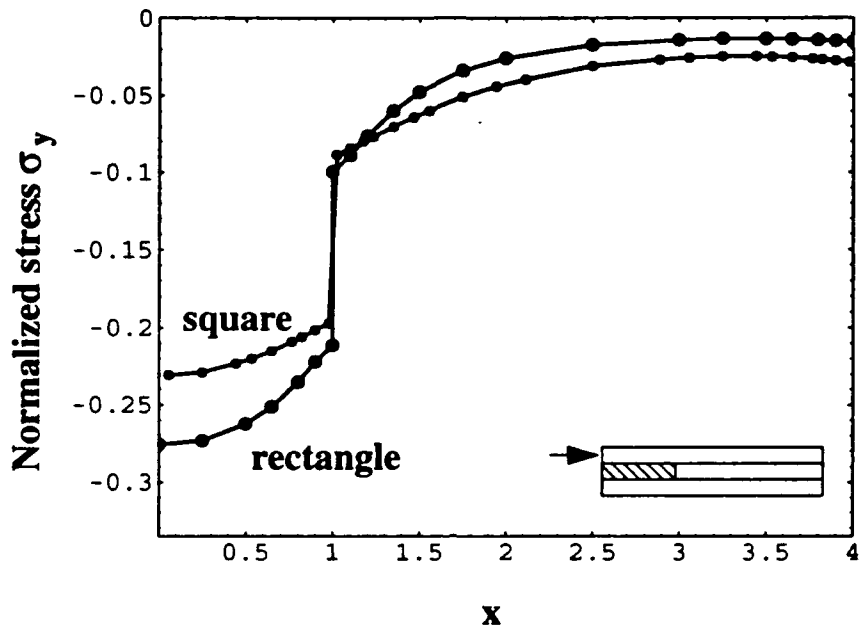


FIGURE 3.24 Distribution of σ_y along the x-axis in the aluminum layer (layer 1) for the layered plate with square patch and with rectangular patch.

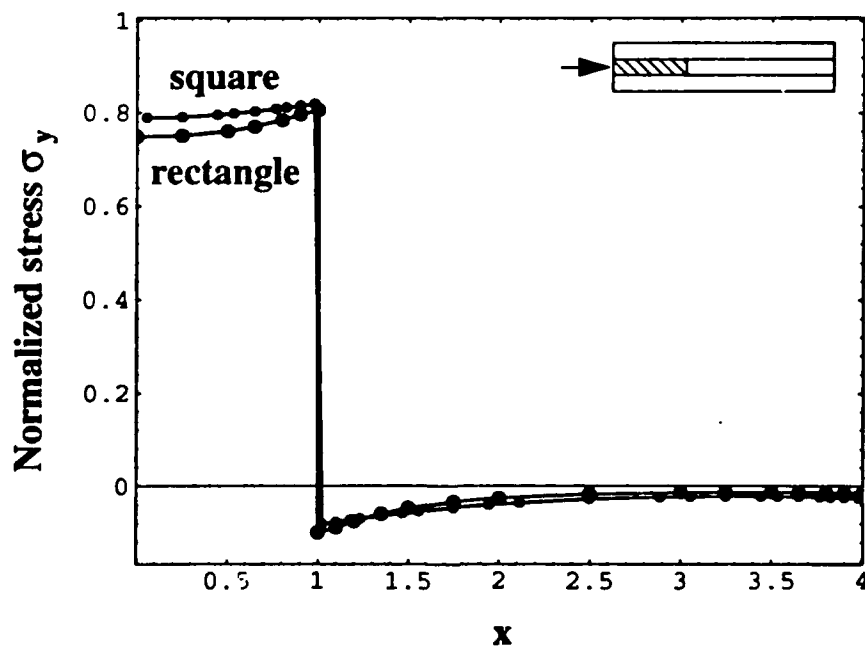


FIGURE 3.25 Distribution of σ_y along the x-axis in the combined layer (layer 2) for the layered plate with square patch and with rectangular patch

Figures 3.26 through 3.29 show similar stress distributions of σ_x and σ_y along the y -axis of the plate for the two cases. The distributions distinctly show inplane tensile in the piezoelectric and inplane compressive stresses in the aluminum layers. Magnitude of the stresses in the aluminum layer not directly above the piezoelectric is small for the two cases. The stresses gradually reduce to zero away from the patches.

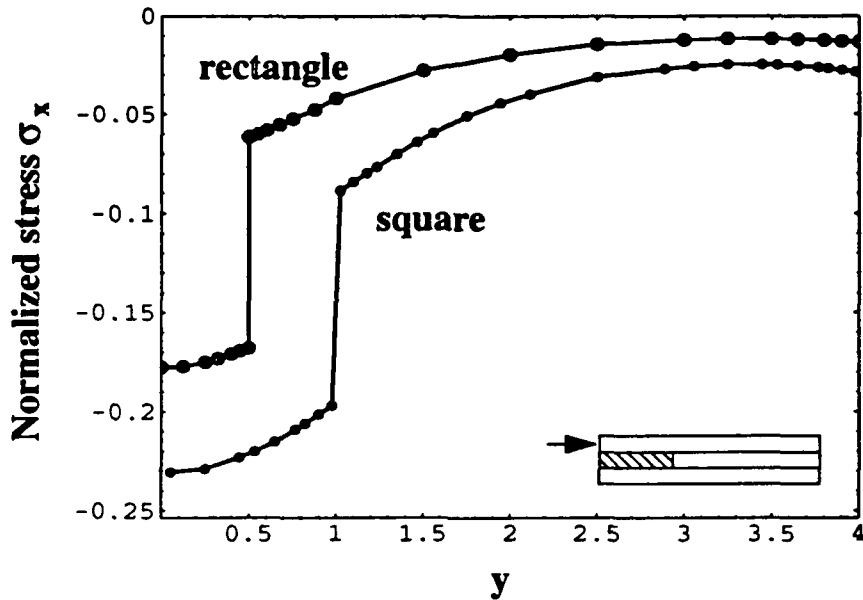


FIGURE 3.26 Distribution of σ_x along the y -axis in the aluminum layer (layer 1) for the layered plate with square patch and with rectangular patch

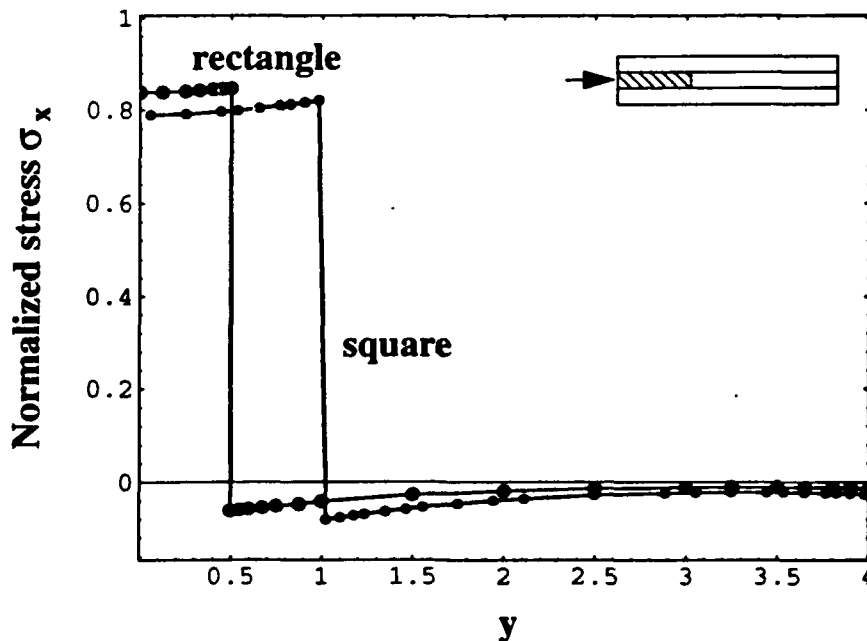


FIGURE 3.27 Distribution of σ_x along the y -axis in the combined layer (layer 2) for the layered plate with square patch and with rectangular patch

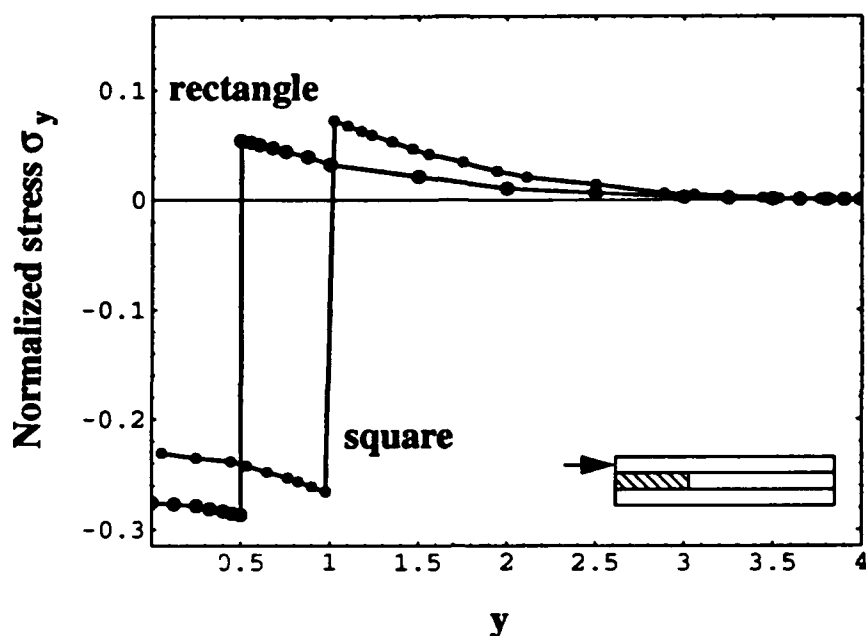


FIGURE 3.28 Distribution of σ_y along the y-axis in the aluminum layer (layer 1) for the layered plate with square patch and with rectangular patch

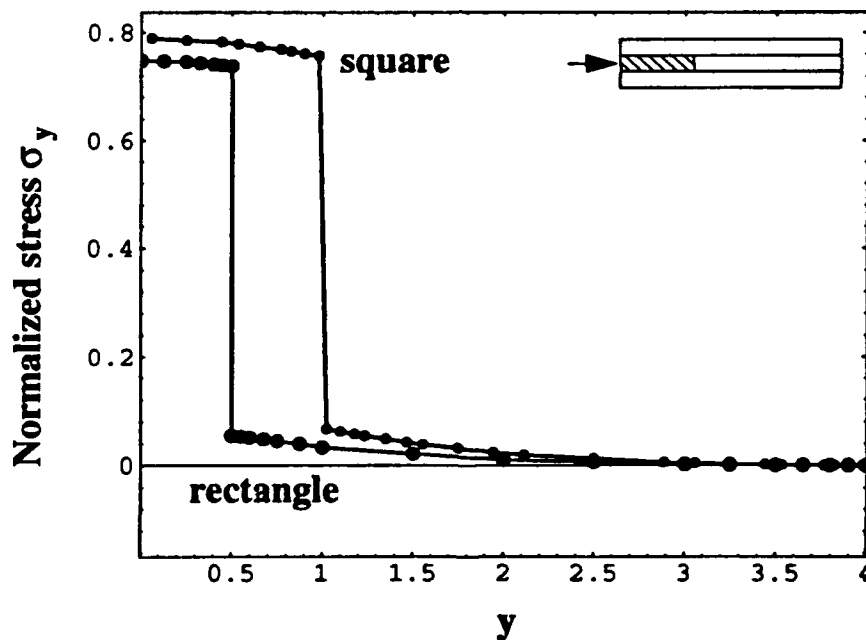


FIGURE 3.29 Distribution of σ_y along the y-axis in the combined layer (layer 2) for the layered plate with square patch and with rectangular patch

The stress obtained for the different cases of the plate with piezoelectric patches that are embedded in the plate are valid everywhere in the plate except at the material interfaces. The cross-section planes at material interfaces do not have linear strains through the thickness as assumed by the plate finite element analysis. If detailed stresses and interlaminar stresses are required a 3D analysis must be performed. However such a 3D analysis is expensive and a sufficiently efficient Quasi-3D analysis may prove to be useful. The use of Quasi-3D analysis to determine detailed state of stress near the material interfaces in the plate will be demonstrated in the following section.

3.4.2 Combination of Quasi-3D and Plate Finite Element Analysis.

In the previous section we discussed the validity of stresses in the regions around the material interface. Plate finite element analysis assumes that the strains in the thickness direction are linear. It is true everywhere in the plate except around the material discontinuities where the strains are non-linear. Thus stresses evaluated using plate FEA are not valid in a small region (about two to three plate thicknesses) around the material interface.

In order to see a detailed stress distribution around the material interface a quasi-3D analysis is performed. A small region of the plate around the material interface is modeled in the thickness direction. A typical finite element mesh for this section is as shown in Figure 3.30. Notice that only a quarter of the plate cross-section needs to be modeled because of the symmetry.

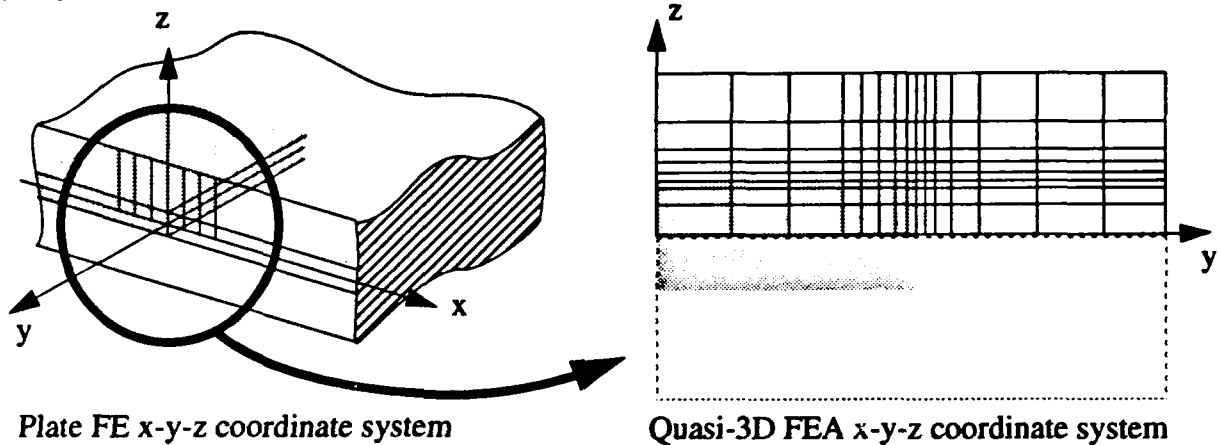


FIGURE 3.30 Quasi-3-D finite element modeling of the plate around the material interface.

The mid-plane strain (ϵ_y) distribution along the x-axis of the plate is as shown in Figure 3.31. The strain distribution in the vicinity of the material interface, as circled in Figure 3.31a and as seen enlarged in Figure 3.31b, can be used as the uniform strain of $3000 \mu\epsilon$ on the cross section of the plate modelled using Q3D in the thickness direction with out affecting the stress distributions at the material interface[12].

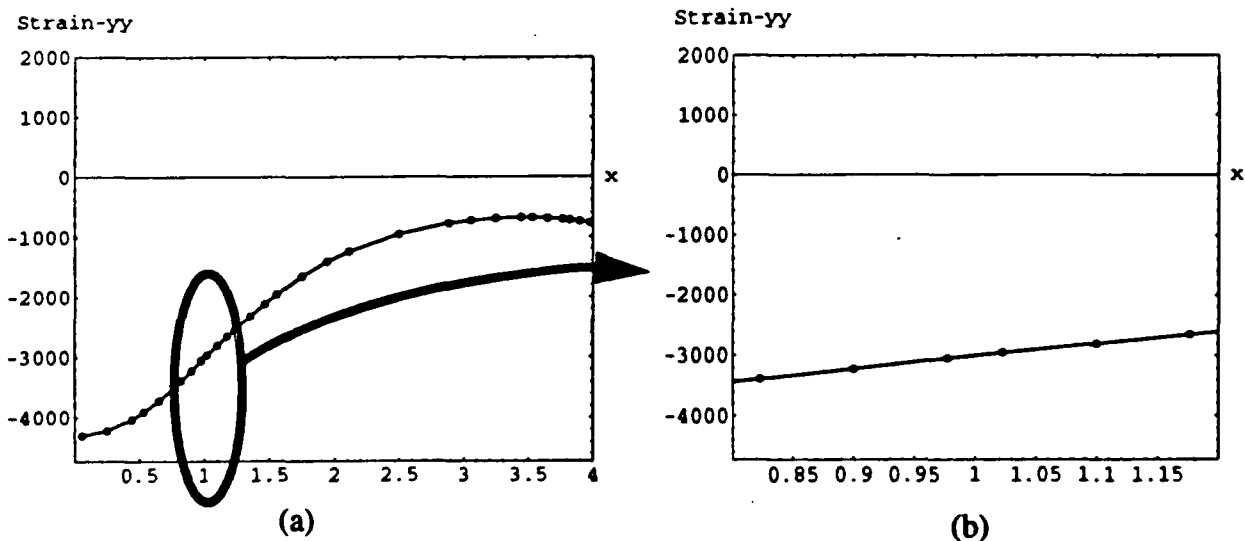


FIGURE 3.31 Strain distribution along the x-axis of the plate from plate FEM.

The displacements along the x-axis, from the plate model are used as boundary conditions for the Q3D model. Figures 3.32 through 3.34 show the stresses obtained by Q3D analysis along the x-axis at the midplane of the plate in a small region near the material interface. The distribution of the stress σ_x along the x-axis of the plate in the piezoelectric in the vicinity of the material interface is shown in Figure 3.32. The stress is continuous at the material interface along the x-axis, unlike the distribution obtained using plate analysis (see Figure 3.23). Figure 3.33 shows the distribution of σ_y along the x-axis. This stress is discontinuous along the x-axis. Comparing the stress distributions from Q3d and plate analysis (Figures 3.23/3.25 and Figures 3.32/3.33), the stresses away from the material interface do not agree. This is due to the approximate constant strain distribution (ϵ_y) applied in the Q3d analysis. Figure 3.34. shows the distribution of σ_z . There is a sharp gradient of the stress σ_z at the material interface. The piezoelectric patch is under compression and the aluminum is under tension in the vicinity of the interface, because the piezoelectric patch is constrained to expand in the z-direction. The stress reduces to zero in about two times the plate thickness.

Figures 3.35 through 3.37 show distributions of σ_x , σ_y and σ_z along x-axis and just below the surface of the piezoelectric patch. Figure 3.35 shows the distribution of σ_x in the piezoelectric. There is a sharp stress gradient as z approaches the surfaces of the piezoelectric patch. Figure 3.36 shows the distribution of σ_y near the surface of the patch. Figure 3.37 shows the distribution of σ_z at the surface of the piezoelectric layer. The distribution of this stress is similar to that observed at the midplane, however the magnitude is less than that at the midplane. The aspect ratio of elements are high even in the vicinity of the corner which is due to computational memory limitations. The exact nature of stress distribution around the corner of the piezoelectric patch needs further investigation.

Figures 3.38 through 3.40 show the stress distributions for σ_x , σ_y and σ_z in the aluminum layer near the surface of the piezoelectric patch. The stresses show a sharp gradients near the corner. The stress σ_x shown in Figure 3.38 shows that the stress first becomes more compressive as it approaches the corner of the patch and then starts to decrease at very near to the interface. Similar behavior for stress σ_y is shown in Figure 3.39.

The above stress distributions show that plate finite element analysis cannot be used to determine detailed stress distributions around material discontinuities. The strains through the thickness in plate finite element were assumed to be linear which causes invalid prediction of stress distributions in a small region around material interfaces. Figure 3.41 shows the strain distribution through the thickness of the plate. Notice that due to electrical loads the piezoelectric shrinks and thereby is under compressive strains at the material interface. The plate is also under compressive strains but much less than the piezoelectric. The strain obtained by plate FEA as shown in the Figure 3.41 is linear. However a through thickness analysis shows that the strains are non-linear in the thickness direction. Distribution of strain ϵ_z through the thickness is shown in Figure 3.42.

The stresses obtained by this analysis are valid only in a region about two times the plate thickness from the edge of the piezoelectric. Recall that the strain distribution along the x-axis obtained from the inplane model was approximated by a uniform strain of $3000 \mu\epsilon$ at and near $x=1.0$. This leads to slight inaccuracy in stress values as you go away from the edge at $x=1.0$. An absolutely true stress distribution valid all over the plate can only be obtained if the strain distribution obtained from inplane analysis is fed to the Q3D model. For this analysis it is not necessary to create a larger model and stress are sufficiently valid around two times the plate thickness from the edge of the piezoelectric patch.

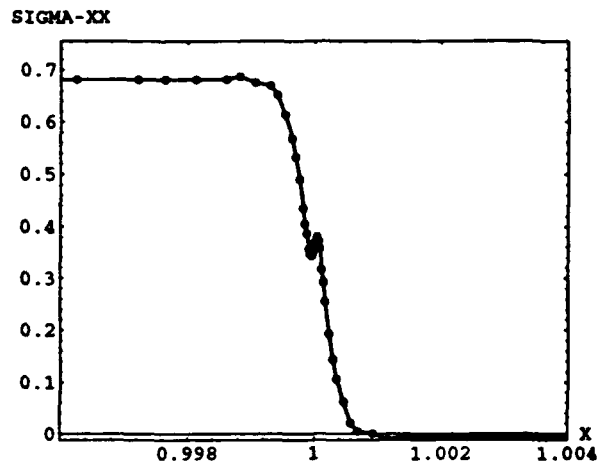


FIGURE 3.32 Distribution of σ_x along x-axis at midplane.

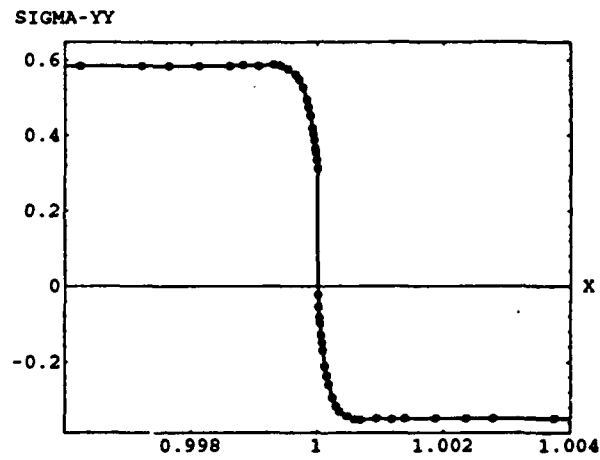


FIGURE 3.33 Distribution of σ_y along x-axis at midplane.

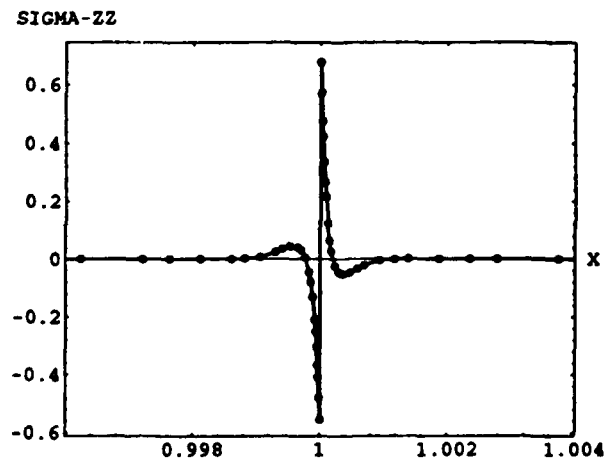


FIGURE 3.34 Distribution of σ_z along x-axis at midplane.

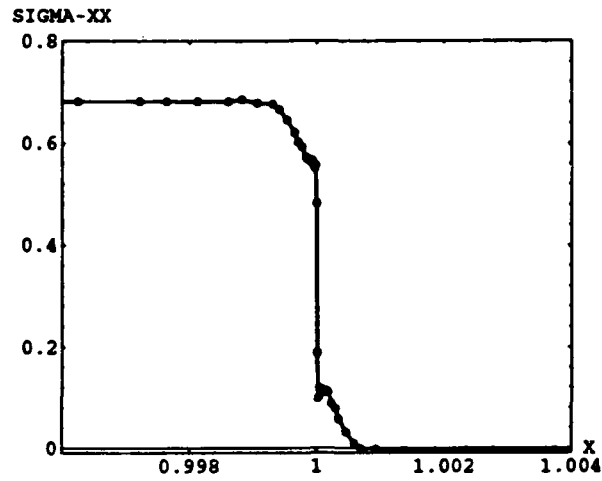


FIGURE 3.35 Distribution of σ_x along the x-axis in the middle layer near the surface of the patch.

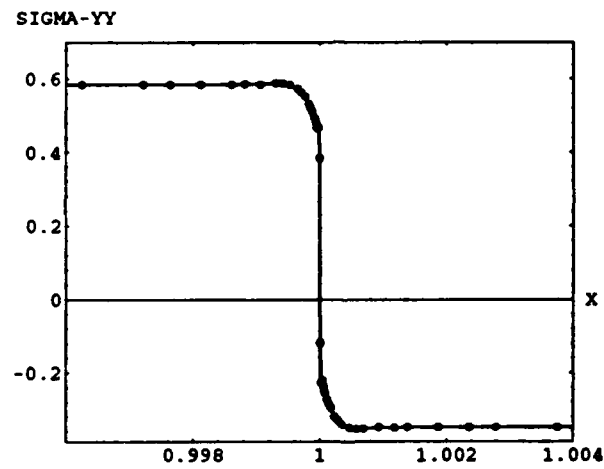


FIGURE 3.36 Distribution of σ_y along the x-axis in the middle layer near the surface of the patch.

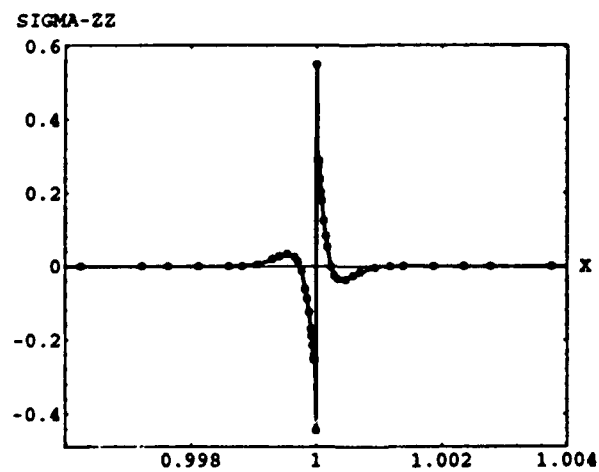


FIGURE 3.37 Distribution of σ_z along the x-axis in the middle layer near the surface of the patch.

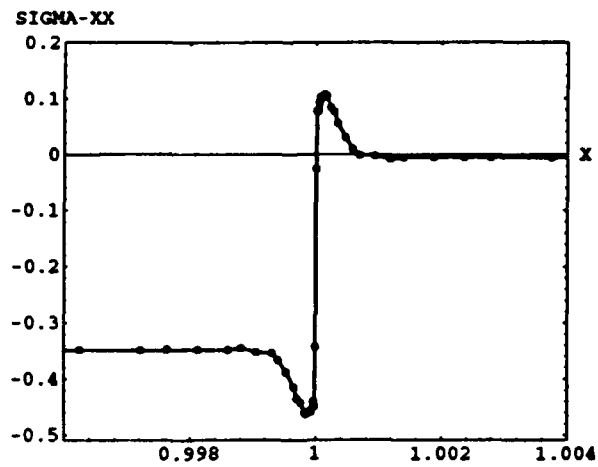


FIGURE 3.38 Distribution of σ_x along the x-axis in the aluminum layer near the surface of the patch.

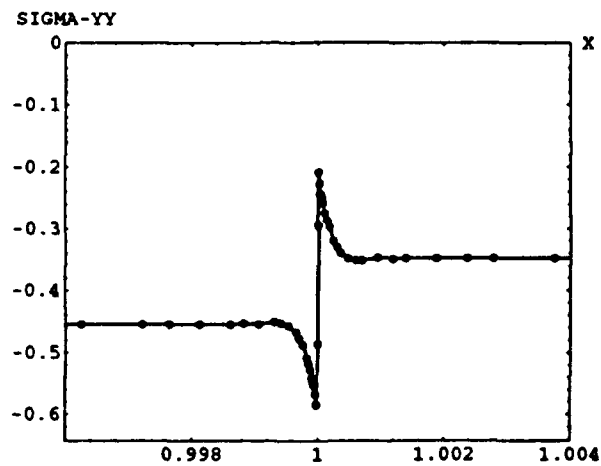


FIGURE 3.39 Distribution of σ_y along the x-axis in the aluminum layer near the surface of the patch.

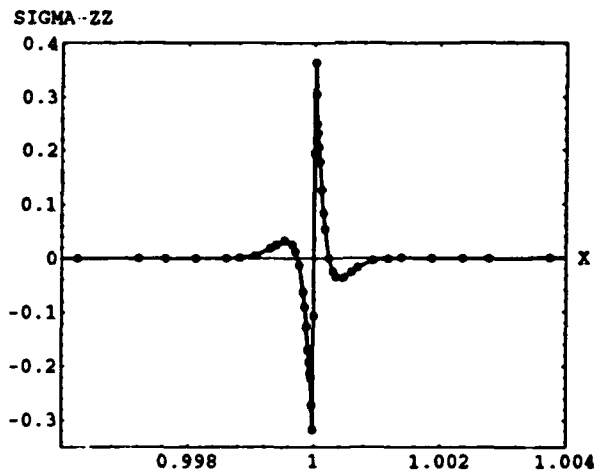


FIGURE 3.40 Distribution of σ_z along the x-axis in the aluminum layer near the surface of the patch.

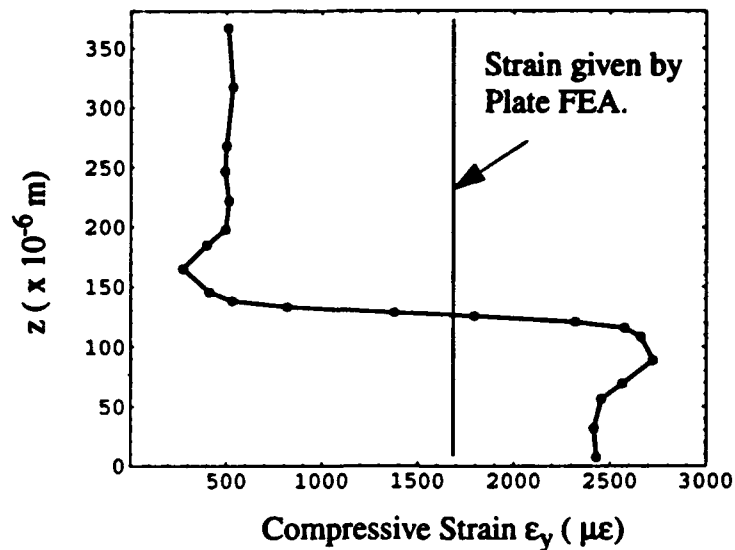


FIGURE 3.41 Distribution of strain ϵ_x through the thickness in plate and Q3D models.

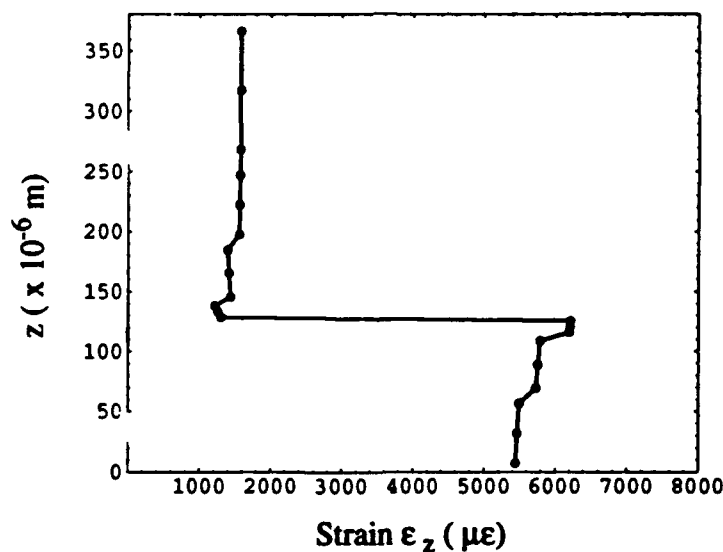


FIGURE 3.42 Distribution of strain ϵ_z through the thickness.

Thus we see that detailed stress analysis in problems involving material discontinuities can be obtained by using a combination of Plate and Q3D finite element analysis. A complete 3D FEA is not necessary for this type of analysis and is much more expensive and time consuming. A proper combination of Plate and Q3D Finite element analysis using planer finite elements provides an efficient method for problems involving material interfaces and delamination in composite laminates. The present section discussed the use of these methods for analysis of isotropic plates with piezoelectric layers. The following sections will discuss the use of the technique to analyze composite laminates and interlaminar stresses in laminated composites. The technique has also been used to determine discontinuous stress distributions in surface electroded piezoelectric layers with an array of electrodes and will be presented in the following sections.

3.4.3 Quasi-3D Analysis of Laminates with Embedded Piezoelectric Layers

This study is focussed on the analysis of smart laminated composite structure with embedded piezoelectric sensor. The presence of the piezoelectric layer alters the mechanical response of the laminates. A quasi-three-dimensional finite element model is utilized to obtain the detailed state of stress in the vicinity of embedded piezoelectric layer in a laminated composite. Interlaminar stress distributions for a typical quasi-isotropic $[+45,-45,0,90]_s$ graphite/epoxy laminate are obtained with the piezoelectric layer placed at different interfaces. The objective of this work is to determine interlaminar stress distributions in laminates with embedded piezoelectric layers. The piezoelectric layer is placed at various interfaces and the interlaminar stress distributions were analyzed to determine its optimal placement in the laminate. Since the graphite/epoxy material is electrically conductive it is necessary to electrically isolate it from the piezoelectric material. Glass/epoxy plies around the piezoelectric layer is used to achieve this objective. In this analysis, the effect of the introduction of glass layers in the laminate is investigated in addition to the placement of piezoelectric layer at various interfaces.

A typical quasi-isotropic layup of $(45,0,90)_s$ graphite/epoxy laminate as shown in Figure 3.43 is selected for this analysis. Two types of laminates are studied. The first type of laminate

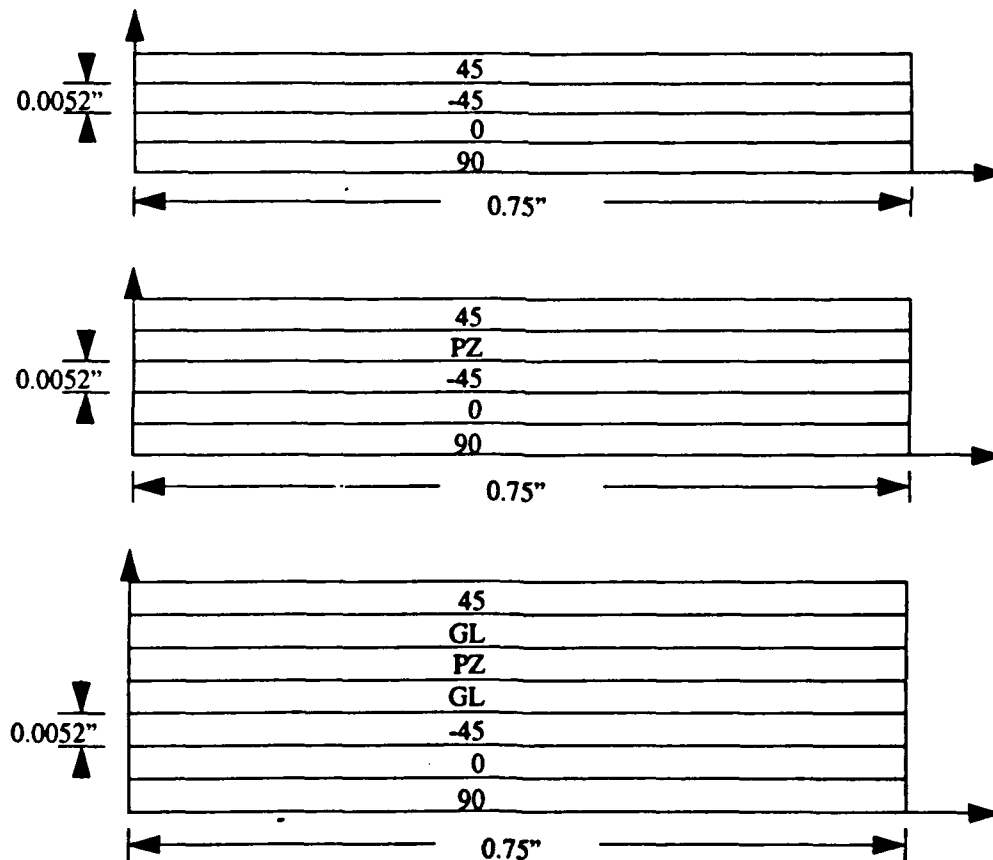


FIGURE 3.43 Laminate configuration.

consisted of the graphite/epoxy quasi-isotropic laminate with a piezoelectric layer embedded in it. This laminate is referred to as the baseline laminate in this analysis. The other laminate consisted of the graphite/epoxy laminate with embedded piezoelectric layer surrounded by glass layers above and below it. The piezoelectric layer is placed at various interfaces in the two different

types of laminates described above. The material properties are shown in Table 3.3.

TABLE 3.4 Material properties used in analysis.

Property	Graphite/Epoxy	Glass/Epoxy	Piezoelectric
E_1 (Msi)	19.30	6.00	9.14
E_2 (Msi)	1.80	1.60	9.14
G_{12} (Msi)	0.85	0.80	3.49
ν_{12}	0.30	0.30	0.31
t_{ply} (inch)	0.0052	0.0088	0.01

Due to the symmetry in loading and geometry only a quarter of the laminate is analyzed. The model consisted of 100 elements and 1350 degrees of freedom. Since the interlaminar stresses are dominant near the edge, the region close to the free edge is modelled with a refined mesh. The region away from the free edge is modelled with a coarse mesh.

The location of the piezoelectric layer in the laminate for the various cases are listed in Table 3.4.

TABLE 3.5 Stacking sequences used for the different cases.

Case	Stacking Sequence of Basic Laminate.	Stacking Sequence of Laminate with Glass Ply
1	$(+45,0,90,PZ)_s$	$(+45,0,90,GL,PZ)_s$
2	$(+45,0,PZ,90)_s$	$(+45,0,GL,PZ,GL,90)_s$
3	$(+45,PZ,0,90)_s$	$(+45,GL,PZ,GL,0,90)_s$
4	$(+45,PZ,-45,0,90)_s$	$(+45,GL,PZ,GL,-45,0,90)_s$

PZ = Piezoelectric Layer

GL = 0° Glass/Epoxy Layer

In case 1 the piezoelectric layer is located at the midplane of the laminate. In case 2, the piezoelectric layer is located at the $[-/0/90/-]$ interface. In case 3 the piezoelectric layer is located at the $[-/0/-45/-]$ interface and in case 4 at the $[-/-45/45/-]$ interface. For all cases a uniform unit strain is applied in the x-direction.

Figures 3.44 through 3.47 show the interlaminar stress distributions across the thickness

near the free edge for the piezoelectric layer placed at the various interfaces in the baseline laminates. The stresses are normalized by the applied load. The results indicate that the peak of the interlaminar normal stress occurs within the 90° plies regardless of the location of the piezoelectric layer. All the peaks of the interlaminar shear stresses, and are at least less than one half of the magnitude of the interlaminar normal stress. Case 2, the $(45,0,pz,90)_s$ laminate, has the highest peak of the interlaminar normal stress. It should be noted that the interlaminar normal stress within the

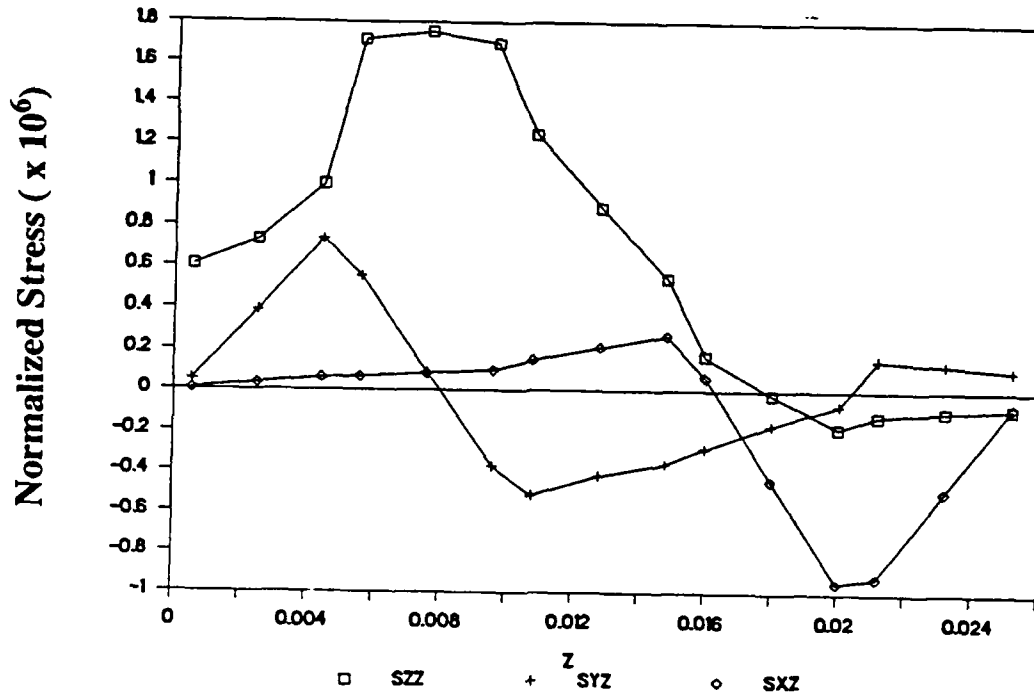


FIGURE 3.44 Free edge interlaminar stress distributions through the thickness in baseline laminates with piezoelectric layer. (case 1)

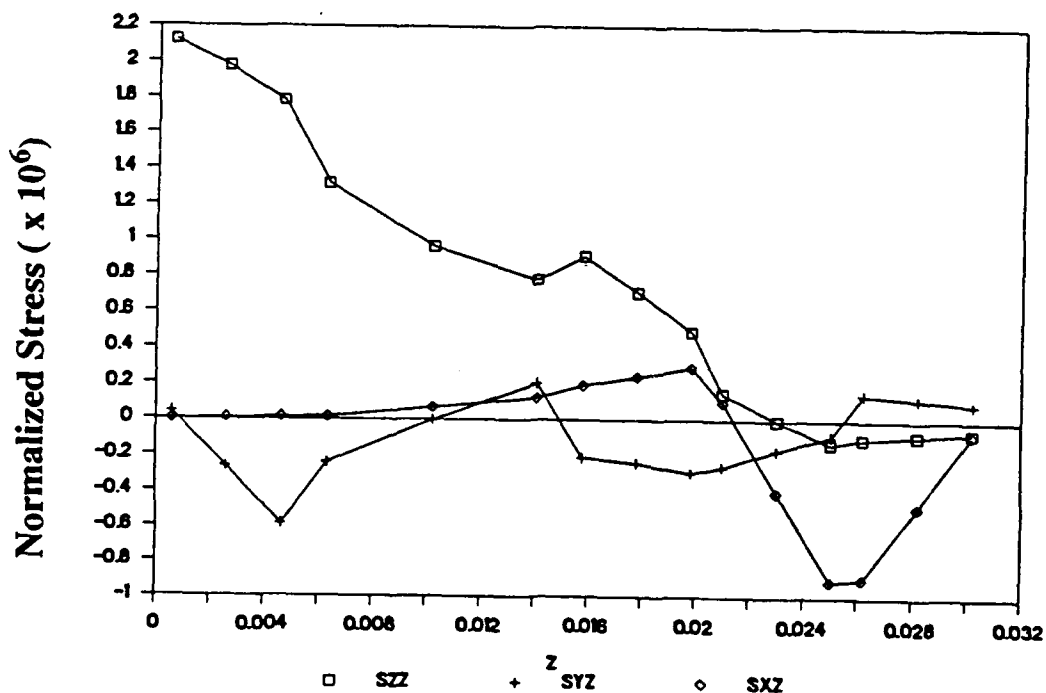


FIGURE 3.45 Free edge interlaminar stress distributions through the thickness in baseline laminates with piezoelectric layer. (case 2)

piezoelectric layer is in tension for all the baseline laminates except for Case 4. Moreover, the peak of the interlaminar shear stress between the $[-45/-45/-]$ plies reduces because of the presence of the piezoelectric layer. Figures 3.48 through 3.51 show the distributions of the interlaminar stresses across the thickness near the free edge for the laminates with a glass ply adjacent to the piezoelectric layer. A similar stress distribution is observed as shown in Figure 3.44 through 3.47. It is also noted that the compressive interlaminar normal stress exists in the region of the $[-/\text{glass}/\text{piezoelectric}/\text{glass}/-]$ layers.

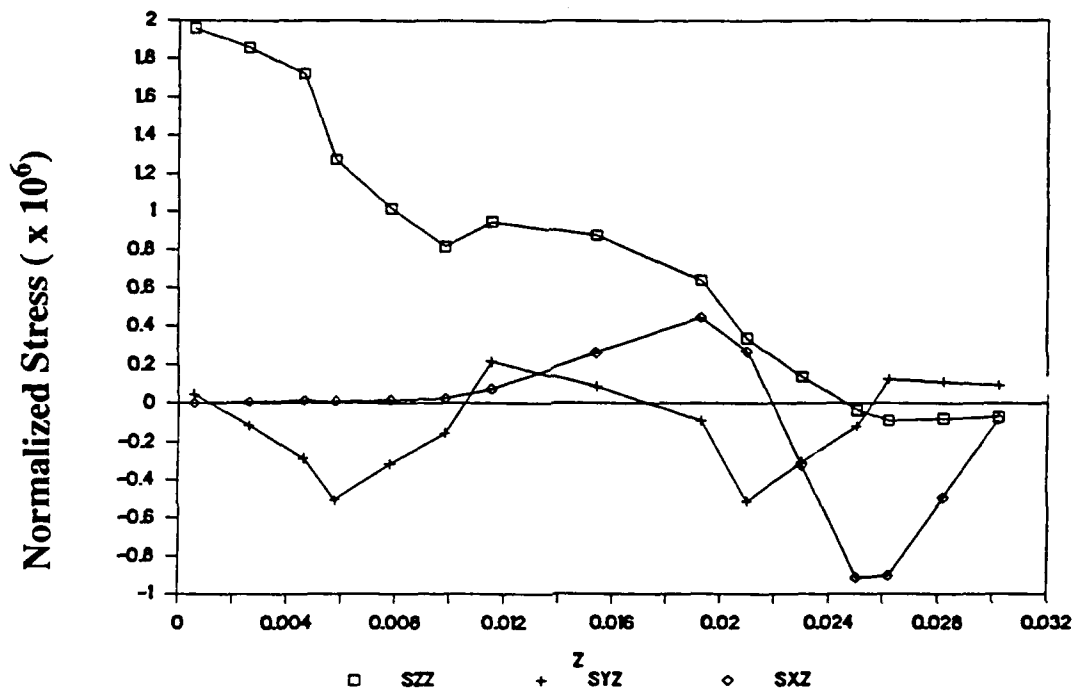


FIGURE 3.46 Free edge interlaminar stress distributions through the thickness in baseline laminates with piezoelectric layer. (case 3)

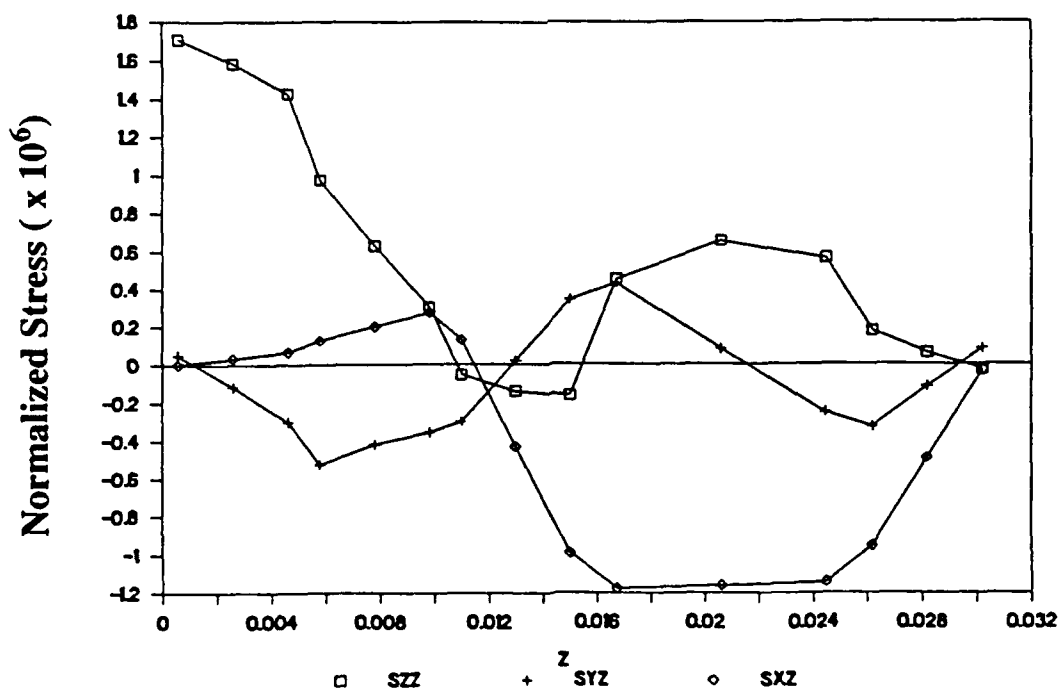


FIGURE 3.47 Free edge interlaminar stress distributions through the thickness in baseline laminates with piezoelectric layer. (case 4)

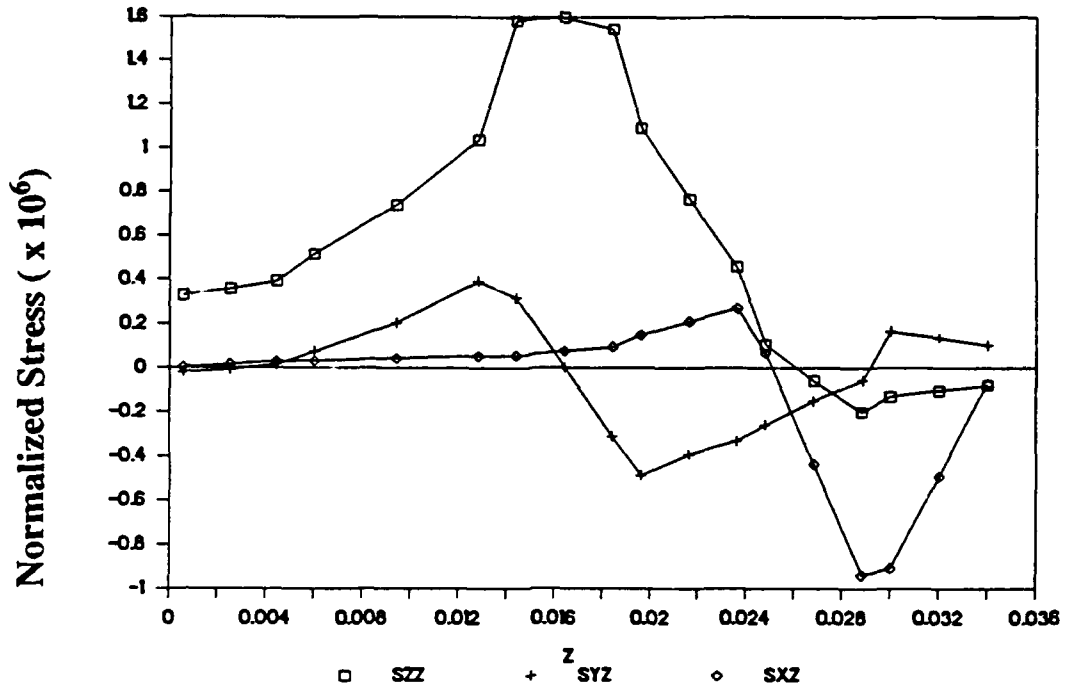


FIGURE 3.48 Free edge interlaminar stress distributions through the thickness in laminates with piezoelectric layer and adjacent glass plies. (case 1)

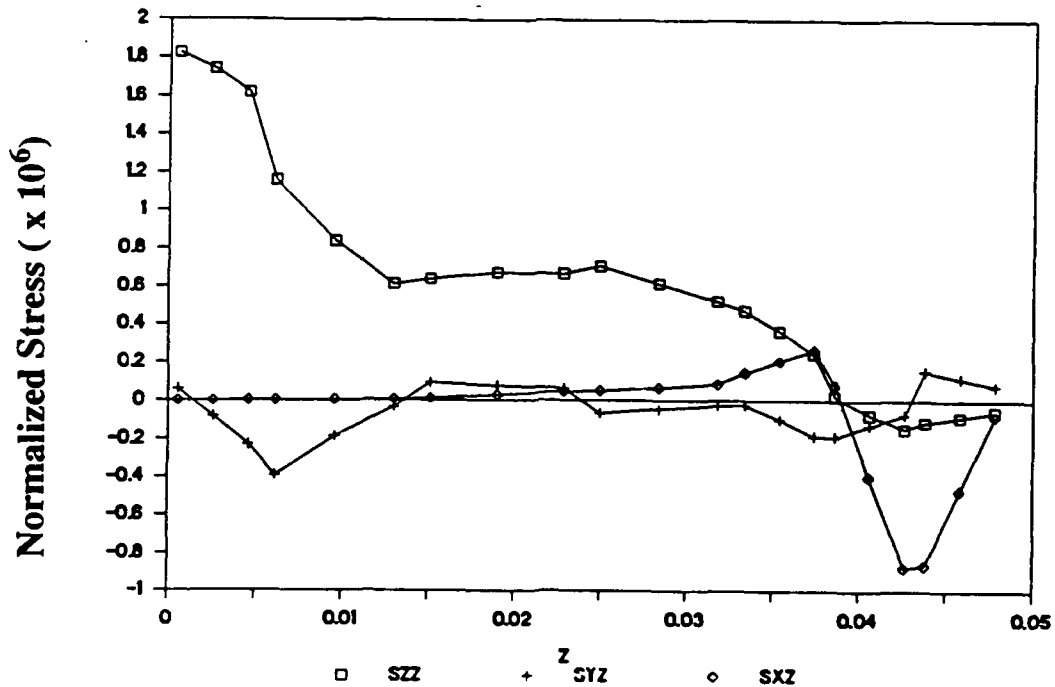


FIGURE 3.49 Free edge interlaminar stress distributions through the thickness in laminates with piezoelectric layer and adjacent glass plies. (case 2)

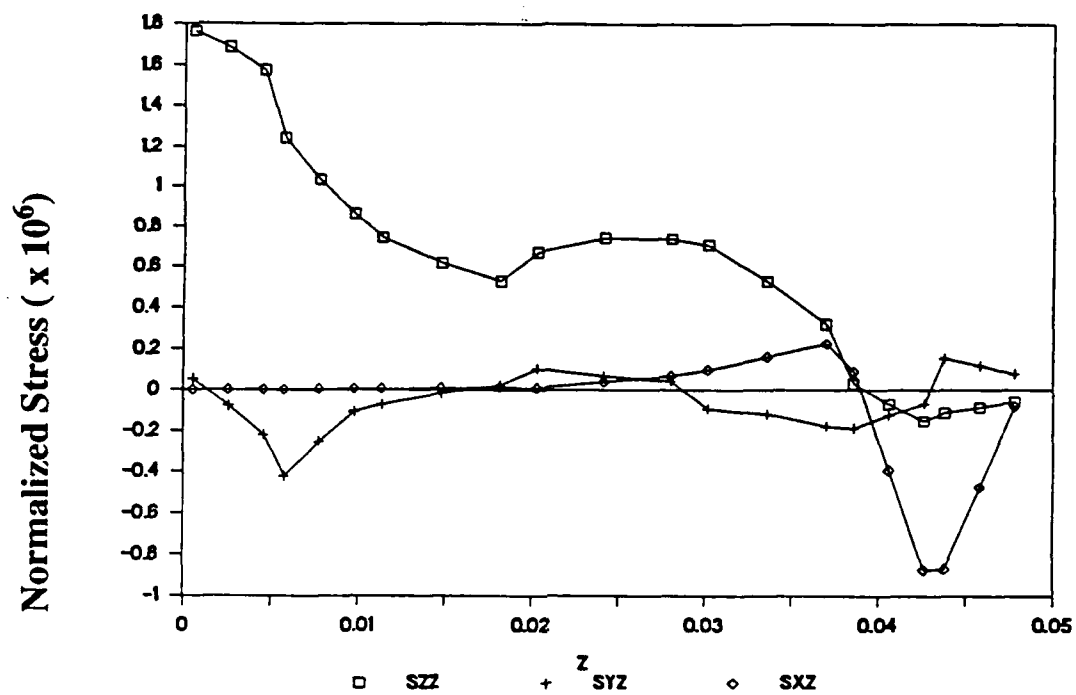


FIGURE 3.50 Free edge interlaminar stress distributions through the thickness in laminates with piezoelectric layer and adjacent glass plies. (case 3)

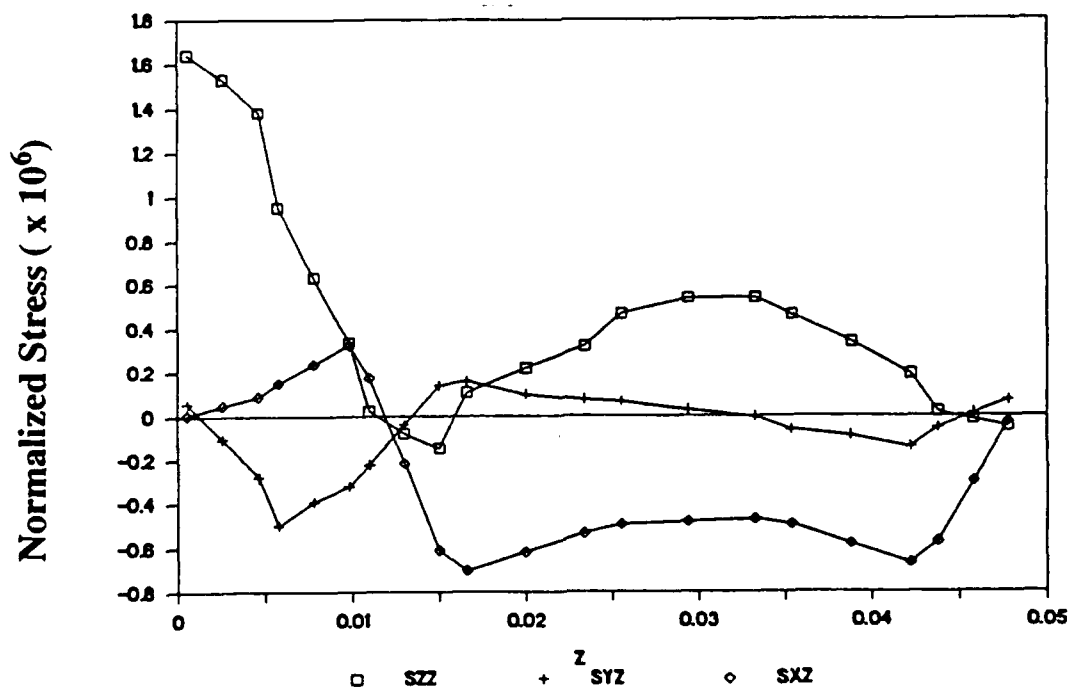


FIGURE 3.51 Free edge interlaminar stress distributions through the thickness in laminates with piezoelectric layer and adjacent glass plies. (case 4)

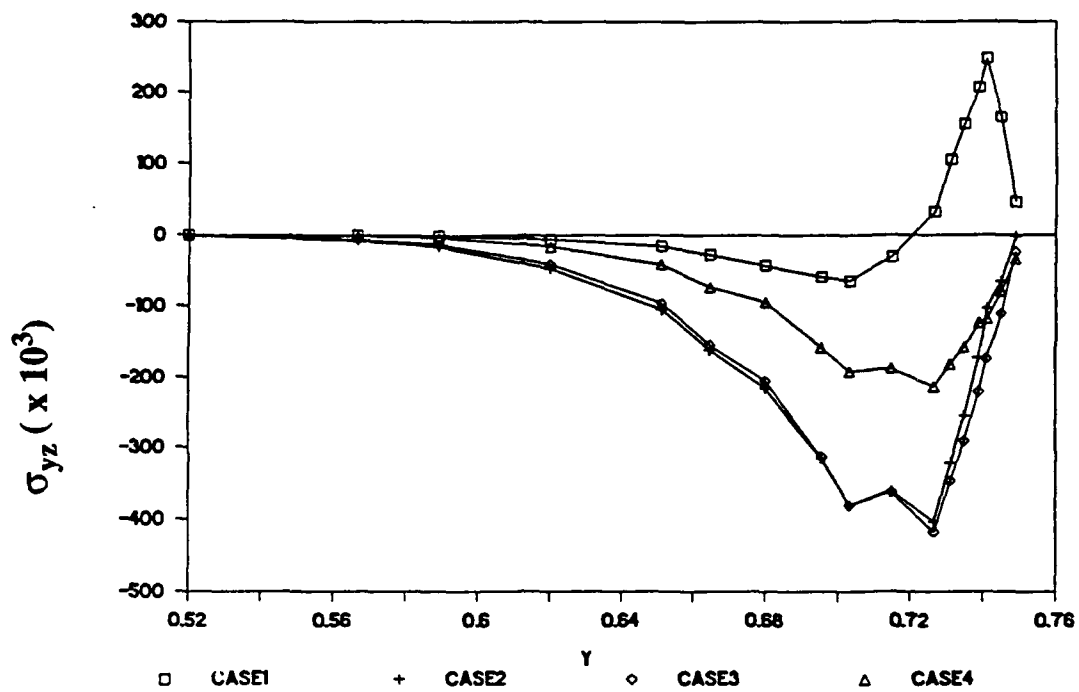


FIGURE 3.52 Comparison of interlaminar stress at the glass/piezoelectric interface for all four cases.

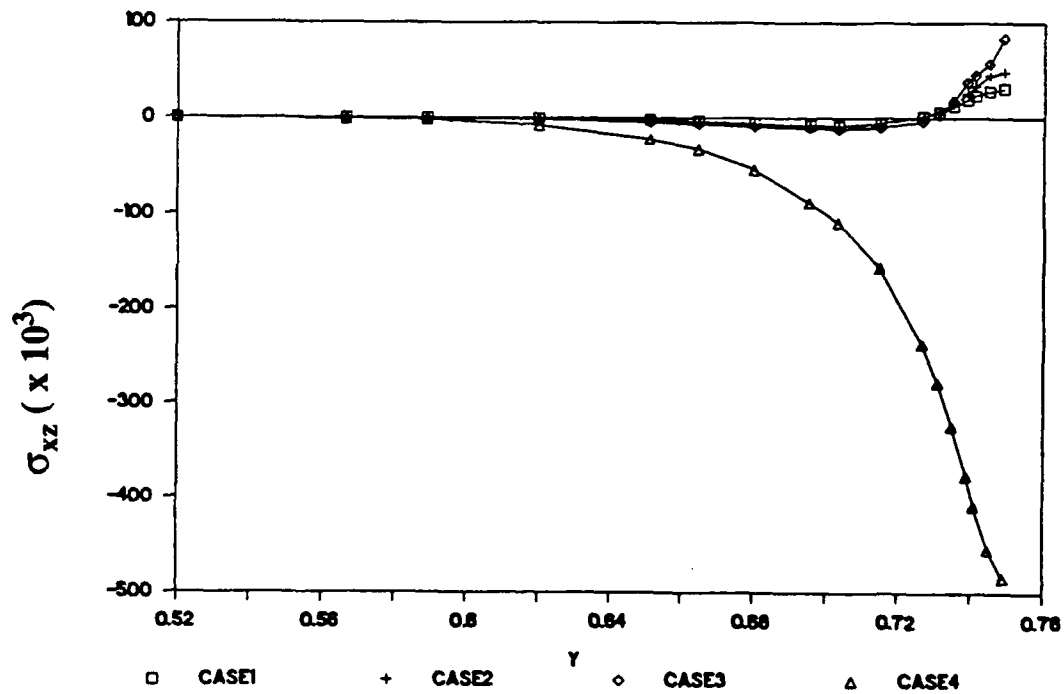


FIGURE 3.53 Comparison of interlaminar stress at the glass/piezoelectric interface for all four cases.

The compressive stress in the region of the piezoelectric layer alleviates the possibility of delamination between the layer and the composite ply. Comparing the stresses in both laminates, it is found that the laminates with a glass ply slightly reduces the peak of the interlaminar normal tensile stress through the thickness and the compressive stress in the piezoelectric layer region. It is well conceived that delamination initiation is governed by the interlaminar normal tensile stress. Reducing this stress would result in the increase of delamination strength. Therefore, the addition of glass layer not only helps in electrically insulating the piezoelectric layer but also increases the delamination strength.

Figure 3.52 shows the comparison of the normalized interlaminar shear stress at the [-/glass/piezoelectric/-] interface for all the four cases. As shown in the Figure, Case 4 exhibits the smallest peak of among the laminates. A comparison of interlaminar shear stress, at the same interface is shown in Figure 3.53. The highest peak is obtained in the Case 4 laminate. However, the peak of is about one third of the peak of the interlaminar normal stress. Therefore the shear stress will not be a significant factor that causes delamination failure.

From all the figures, it is observed that the interlaminar stresses, and tend to vanish at the outer surface of the laminate. This is consistent with the stress free boundary conditions. Furthermore, all the shear stresses and are nil at the midplane. The result confirms the structural response of symmetric laminates.

Free edge stress analysis of laminates with embedded piezoelectric layers was performed. It is observed that the addition of glass layer, in general, not only helps in electrically insulating the piezoelectric layer but also reduces the interlaminar stresses. The placement of the piezoelectric layer does not alter the peak of the interlaminar normal stress regardless of its location. The placement of the piezo electric layer at the [-/45/-45/-] interface results in a compressive normal stress in its region. It is suggested that the layer should be embedded at the [45/-45] interface without lower the delamination strength. In this study only one laminate stacking sequence was considered. More work needs to be done with various commonly used laminate stacking sequences.

3.4.4 Response of Piezoelectric Layer Due to Surface Electrodes

An element of piezoelectric medium of symmetry of 6mm (a piezo-ceramic polarized in the z-direction) and infinite dimension in the x and y directions as shown in Figure 3.54 is used to study the stress distributions. The material used in this study was Piezoceramic G1195 with the material properties listed below in Table 3.6

The electroelastic field in the piezoelectric layer $z < h$ is excited by a periodic array of infinitely thin strip electrodes deposited on the surfaces $z = h$ and $z = -h$. Each electrode on the lower surface is placed exactly below the upper surface counterpart, the potential of the two being exactly equal in magnitude and opposite in sign. The infinite dimensions of the layer result in a plane-strain state of stress in the piezoelectric layer.

The problem can be treated by electroelastic theory combined with methods for solving boundary value problems with discontinuous boundary conditions. However an efficient finite element technique to solve the above problem can be devised to reduce the complexity of the problem. Due to complexities in satisfying equations of equilibrium and boundary conditions, exact solution is not available for these types of problems. Hence finite element technique is used in the analysis.

TABLE 3.6 Material properties for the piezoceramic G1195.

Property	Cons. Electric Field	Cons. Electric Displacement
E_1, E_2	63 GPa	71 GPa
E_3	49 GPa	85 GPa
G_{12}	24 GPa	24 GPa
G_{13}, G_{23}	22 GPa	38 GPa
$\nu_{12}, \nu_{13}, \nu_{23}$	0.31	0.31
d_{31}, d_{32}	$-166 \times 10^{-12} \text{ m/V}$	
d_{33}	$360 \times 10^{-12} \text{ m/V}$	
d_{15}, d_{24}	$540 \times 10^{-12} \text{ m/V}$	
Thickness	$254 \times 10^{-6} \text{ m}$	

Since the electrodes are placed in a periodic array on the piezoelectric later, a repeating unit as shown in Figure 3.55 is considered for the analysis. It is conceived that high stress gradient occurs at the region near the edge of the electrode. A fine mesh is used in that area. The material is constrained at $z=0$ in the z -direction and at $y=0$ and $y=L$ in the y -direction because of its symmetric boundary conditions. The finite element load is induced only in the region due to electric charge. The voltage applied in the model was 100 volt per unit thickness resulting in a 1713 Pa of both σ_x and σ_y for this model

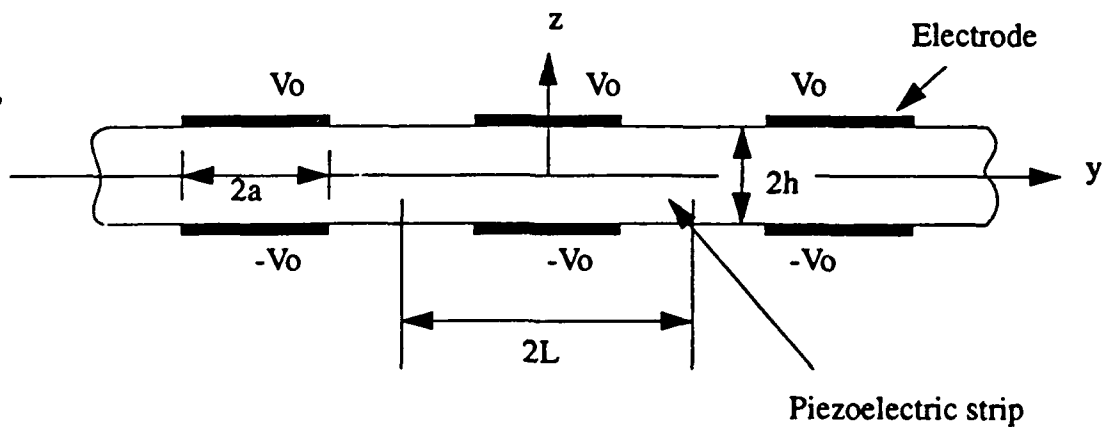


FIGURE 3.54 Piezoelectric strip with an array of electrodes

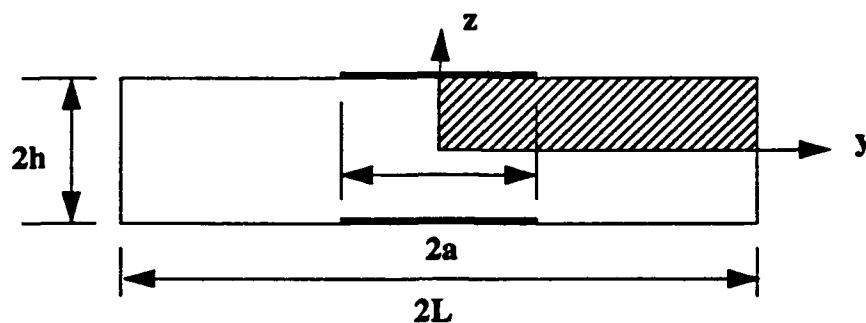


FIGURE 3.55 A repeating unit of the strip for finite element analysis

RESULTS

All the stresses presented here were normalized by the corresponding stress, σ_{x0} [13]. The stress σ_{x0} is computed as

$$\sigma_{x0} = E_3 \beta_{31} \left[1 - \frac{C_{13}^E \beta_{33}}{C_{33}^E \beta_{31}} \right] \quad (83)$$

In order to verify the finite element result, a finite element model with electric charge over the entire region is conducted. For this case, the boundary condition at $y=L$ in the finite element model is set to be free. The stress result was confirmed with the value computed by the above equation.

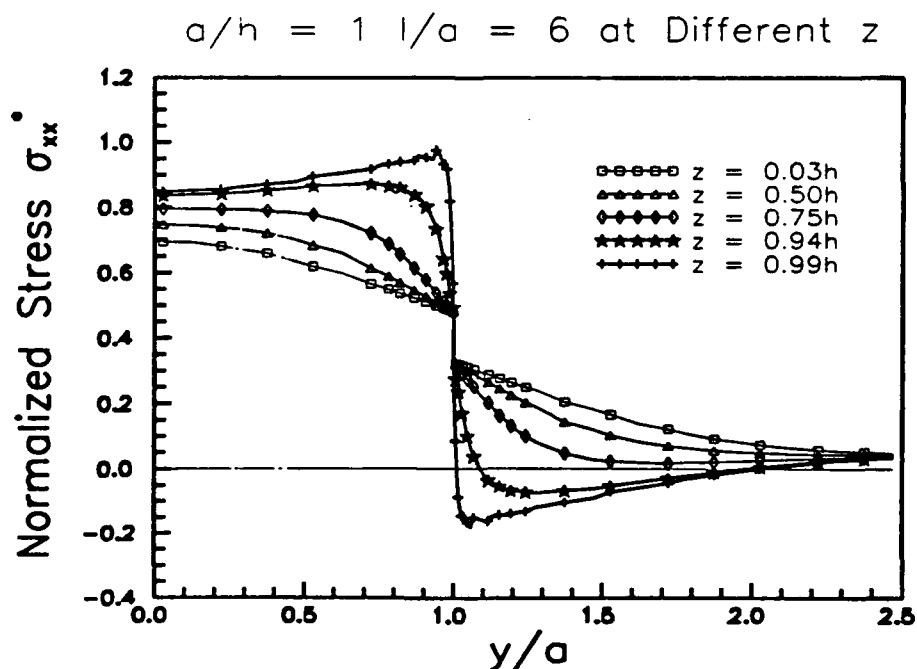


FIGURE 3.56 Distribution of normalized stress σ_{xx} versus y/a

Figures 3.56 through 3.59 show the stress distribution at various locations for σ_x , σ_y , σ_z , and σ_{yz} respectively. It is shown that the normal stresses are discontinuous at $y/a = 1$ which is the edge of the electric charge region. For the region $y/a > 1$, the piezo layer was in open circuit. The stress in this region converges to a constant non-zero value. In this stress gradient zone, σ_x has a higher gradient at the outer surface (see Figure 3.56), however, σ_z has at the midplane surfaces (Figure 3.58)

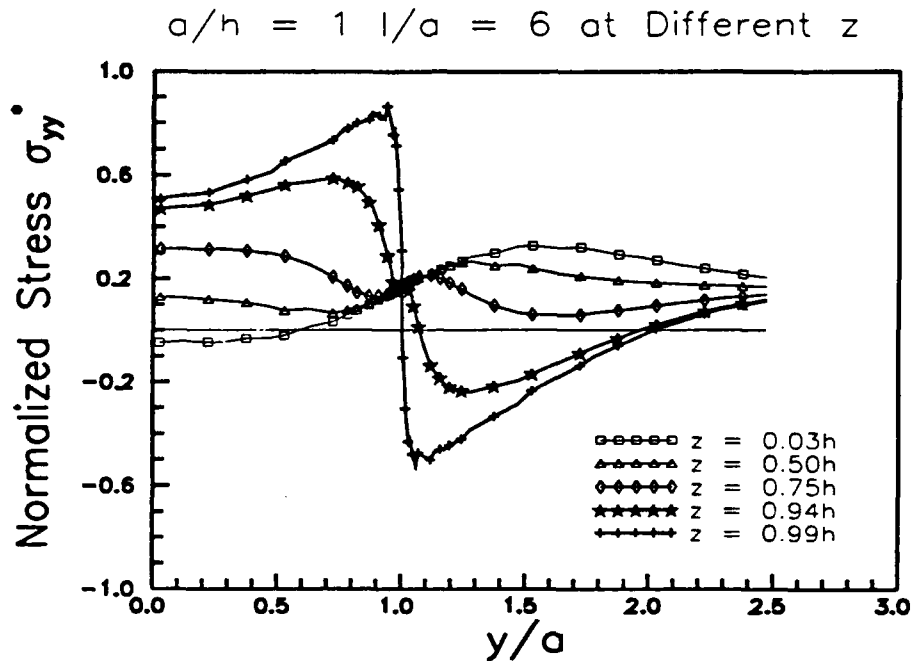


FIGURE 3.57 Distribution of normalized stress σ_{yy} versus y/a

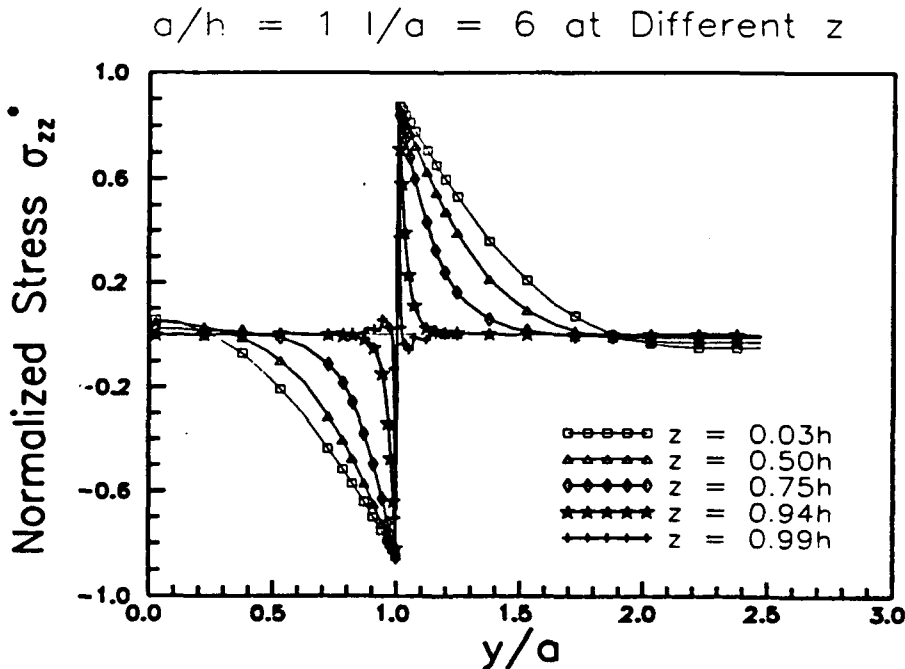


FIGURE 3.58 Distribution of normalized stress σ_{zz} versus y/a

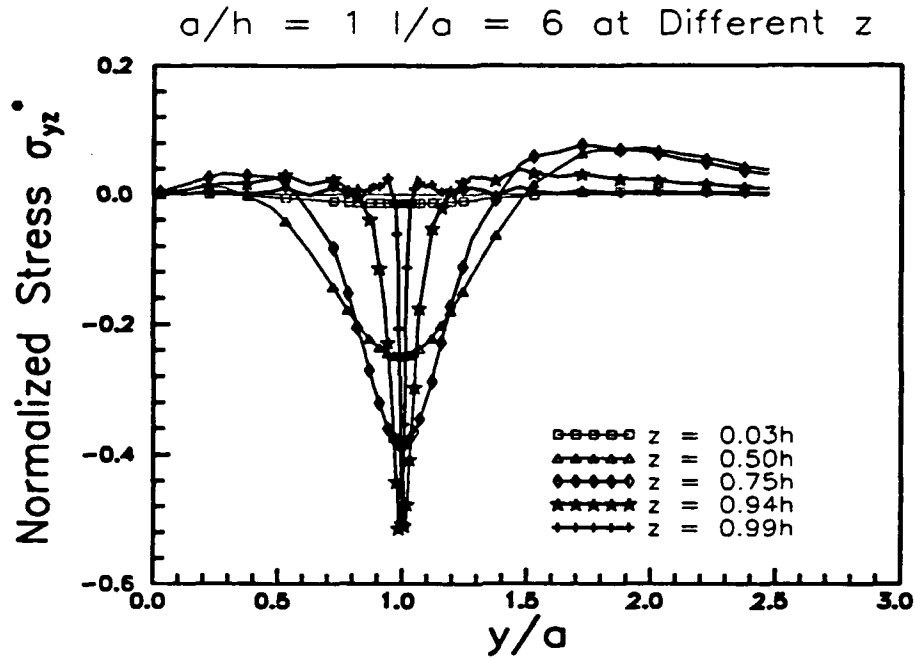


FIGURE 3.59 Distribution of normalized stress σ_{yz} versus y/a

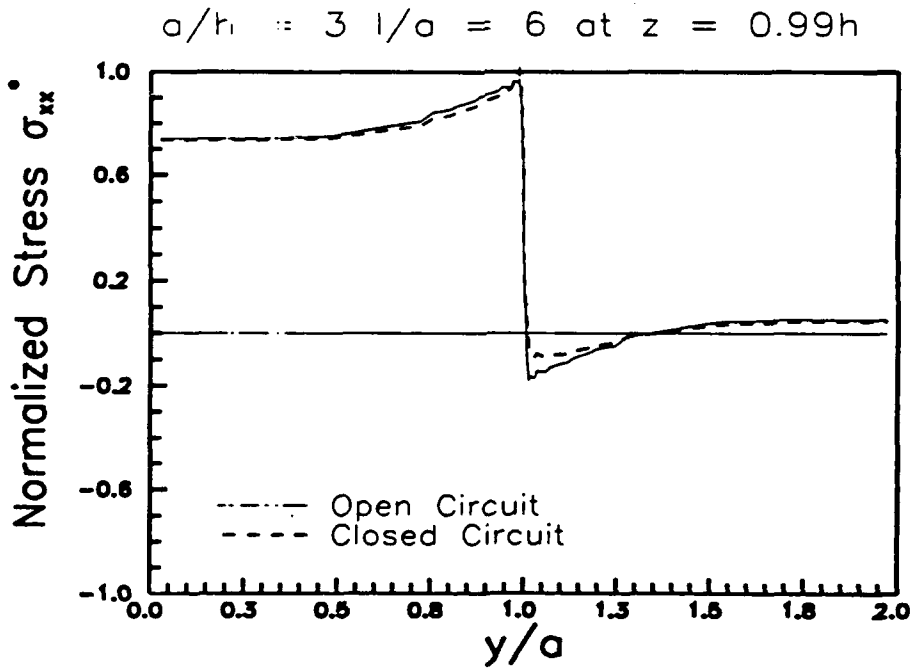


FIGURE 3.60 σ_{xx} comparison in open and closed circuit region without surface electrode charge.

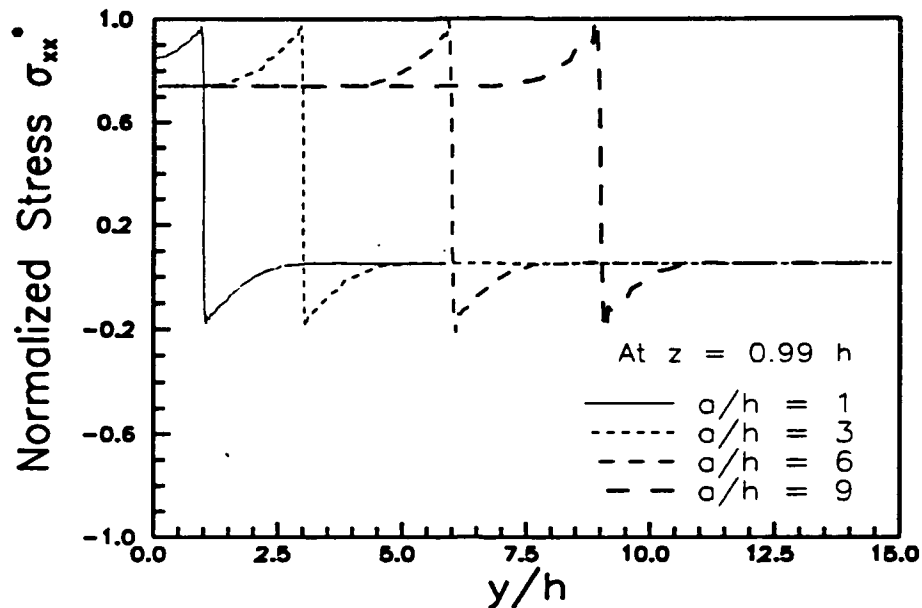


FIGURE 3.61 Normalized stress σ_{xx} for various sizes of surface electrodes.

Figure 3.60 shows the normalized σ_{xx} distribution versus y/a for the case of open and closed circuit in the region without surface electrode charge. The result indicates that except the peak value having a slight difference the stress is the same. The difference in the peak value of σ_{xx} is mainly due to the difference in Young's modulus in the z -direction. For the various sizes of surface electrode under a constant voltage per unit thickness, the stress σ_{xx} remains unchanged as shown in Figure 3.61. It is interesting that the stress only concentrates in the region of about 2 times the thickness of the piezoelectric layer. This suggests that a minimum distance of periodical array of electrode is required without aggravating the stress magnitude.

An analytical method was developed to investigate the response of piezoelectric layer due to electromechanical loads. Finite element equations were formulated to incorporate constitutive equations for piezoelectric material into a quasi-three-dimensional finite element model. Response of a piezoelectric layer with a periodic array of electrodes was used to demonstrate the capability of the analytical method. The numerical results indicate that a singular stress gradient occurs at the edge of the electrode region.

REFERENCES

- 1 Wada, B.K., Fanson, J.L., and Crawley, E.F., "Adaptive Structures", Proceedings of the Winter Annual Meeting of the ASME, 1990, AD-Vol 15, pp 1-8.
- 2 Forward, R.L. and Swigert, C.J., "Electronic Damping of Orthogonal Bending Modes in a Cylindrical Mast Theory," Journal of spacecraft and rockets, Jan-Feb 1981.

- 3 Crawley, E.F., and Anderson, E.H., "Detailed Modeling of Piezoelectric Actuation of Beams," Proceedings of the 30th AIAA/SDM conference, 1989, Mobile, AL.
- 4 Bailey, T. and Hubbard, J.E., "Distributed Piezoelectric-Polymer Active Vibration Control of a Cantilever Beam," Journal of Guidance, Control and Dynamics, Vol.7, No. 4, 1984, pp.437-442.
- 5 Hanagud, S., Obal, M.W. and Calise, A.J., "Optical Vibration Control by the use of Piezoceramic Sensors and Actuators", Proceedings of the 27th AIAA/SDM Conference, San Antonio, TX, 1986.
- 6 Lee, C., Chiang, W., O'Sullivan, T., "Piezoelectric Modal Sensors and Actuators Achieving Critical Damping on a Cantilever plate," Proceedings of the 30th AIAA/SDM Conference, Mobile AL, 1989.
- 7 Fanson, J.L., and Chaughy, T.K., "Positive Position Feedback Control for large Space Structures," Proceedings of the 28th AIAA / SDM conference, Monterrey, CA., 1987, pp 588-598.
- 8 Crawley, E.F. and Lazarus K.B., "Induced Strain Actuation of Isotropic and Anisotropic plates," Proceedings of the 30th AIAA/SDM Conference, Mobile AL., 1989.
- 9 Crawley, E.F. and Deluis, J., "Use of Piezoelectric Actuators as Element of Intelligent Structures," AIAA Journal, Vol.25, No.10
- 10 Hinton, E. and Campbell, J.S., "Local and Global Smoothing of Discontinuous Finite Element Functions Using Least Squares Method", International Journal of Numerical Methods in Engineering, Vol.8, pp 461-480, 1974.
- 11 Chan, W.S. and Ochoa, O.O., "An Integrated Finite Element Model for Edge Delamination Analysis of Laminates Due to Tension, Bending and Torsion Loads," AIAA Paper, Proceedings of AIAA SDM Conference, April 1987, pp. 27-35. To appear in the Journal of Computational Mechanics.
- 12 Shah, D.K. and Chan, W.S., "Delamination Characteristics Around A Hole in Laminates with a Softening Strip" AIAA Paper, Proceedings of AIAA SDM Conference, April 1990, pp. 1191-1200. To appear in the journal of Aerospace Engineering, April 1993.
- 13 Parton, V.Z. and Kudryavtsev, B.A., Electromagneto-elasticity, Gordon and Breach Science Publishers, 1988, p.202.

Appendix 3A : Nodal Loads Due to Piezoelectric Stress Traction.

Consider a plate as shown in Figure 3.62

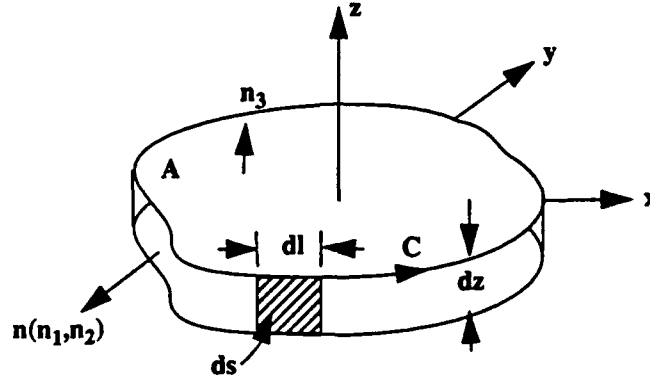


FIGURE 3. 62 Plate element showing tractions on the plate.

Tractions on the surface ds are expressed as

$$T_i = \sigma_{ij}n_j \quad (84)$$

The stresses produced due to piezoelectric effect can be seen as traction on the element. Thus work done due to traction can be written as

$$W = \int_S u_i T_i dS + \int_A u_i T_i dA = \int_S u_i \sigma_{ij} n_j dS + \int_A u_i \sigma_{i3} n_3 dA \quad i = 1, 2, 3 \quad j = 1, 2 \quad (85)$$

Expressing the displacements as

$$u_i = u_i^o + z\theta_i \quad i = 1, 2, 3 \quad \theta_3 = 0 \quad (86)$$

we get

$$W = \int_S u_i^o \sigma_{ij} n_j dS + \int_S z \theta_p \sigma_{pj} n_j dS + \int_A u_i \sigma_{i3} n_3 dA \quad i = 1, 2, 3 \quad j = 1, 2 \quad p = 1, 2 \quad (87)$$

Let us take the first term in the above equation. This term is due to the extensional displacements in the 1,2,3 directions. The work done is given by

$$W = \int_S u_i^o \sigma_{ij} n_j dS \quad i = 1, 2, 3 \quad j = 1, 2 \quad (88)$$

Expressing the displacements as a function of nodal displacements and the nodal shape functions, and since the normal vector to the surface S is independent of z , the above expression becomes

$$W = \int_C \tilde{u}_{ik}^o \tilde{N}_k \left(\int_z \sigma_{ij} dz \right) n_j dl \quad i = 1 \text{ to } 3 \quad j = 1, 2 \quad k = 1 \text{ to } 9 \quad (89)$$

where \tilde{u}_{ik}^o are nodal displacements and \tilde{N}_k are the corresponding shape functions. The integration of the stresses through the thickness gives us stress resultants R_{ij} in the plate.

$$W = \int_C \tilde{u}_{ik}^o \tilde{N}_k R_{ij} n_j dl \quad i = 1 \text{ to } 3 \quad j = 1, 2 \quad k = 1 \text{ to } 9 \quad (90)$$

Differentiating w.r.t the nodal displacements \bar{u}_{ik}^o , the nodal forces due to extensional displacements are

$$F_{ik} = \int_C \bar{N}_k R_{ij} n_j dl \quad i = 1 \text{ to } 3 \quad j = 1, 2 \quad k = 1 \text{ to } 9 \quad (91)$$

Using Green's theorem the above line integral can be converted to area integral over the area of the element in the x-y plane.

$$F_{ik} = \int_A \frac{\partial \bar{N}_k}{\partial x_j} R_{ij} dA + \int_A \bar{N}_k \frac{\partial R_{ij}}{\partial x_j} dA \quad i = 1 \text{ to } 3 \quad j = 1, 2 \quad k = 1 \text{ to } 9 \quad (92)$$

From the equilibrium equations for the plate the second term in the above equation is zero. Thus

$$F_{ik} = \int_A \frac{\partial \bar{N}_k}{\partial x_j} R_{ij} dA \quad i = 1 \text{ to } 3 \quad j = 1, 2 \quad k = 1 \text{ to } 9 \quad (93)$$

or expanding the above terms for any index i we get

$$F_{ik} = \int_A \left(\frac{\partial \bar{N}_k}{\partial x} R_{ix} + \frac{\partial \bar{N}_k}{\partial y} R_{iy} \right) dA \quad i = 1 \text{ to } 3 \quad k = 1 \text{ to } 9 \quad (94)$$

Resultants R_{ij} can be represented in the conventional resultant notations of plate theory as N_x , N_y , N_{xy} , and Q_x and Q_y as given in eqn. 6 in section 1.2. Thus the nodal loads in the x-, y-, and z- directions are given by

$$\begin{aligned} F_{xk} &= \int_A \left(\frac{\partial \bar{N}_k}{\partial x} N_x + \frac{\partial \bar{N}_k}{\partial y} N_{xy} \right) dA \quad k = 1 \text{ to } 9 \\ F_{yk} &= \int_A \left(\frac{\partial \bar{N}_k}{\partial x} N_{xy} + \frac{\partial \bar{N}_k}{\partial y} N_y \right) dA \quad k = 1 \text{ to } 9 \\ F_{zk} &= \int_A \left(\frac{\partial \bar{N}_k}{\partial x} Q_x + \frac{\partial \bar{N}_k}{\partial y} Q_y \right) dA \quad k = 1 \text{ to } 9 \end{aligned} \quad (95)$$

The second term in the expression for work as given in eq.4 represents the work due to bending loads.

$$W = \int_S z \theta_p \sigma_{pj} n_j dS \quad j = 1, 2 \quad p = 1, 2 \quad (96)$$

Again expressing the rotations in terms of nodal rotation and nodal shape functions, and since n_j are independent of z, we get

$$W = \int_C \bar{\theta}_{pk} \bar{N}_k \left(\int_z \sigma_{pj} dz \right) n_j dl \quad j = 1, 2 \quad p = 1, 2 \quad k = 1 \text{ to } 9 \quad (97)$$

The integral over z represents the moment results expressed by M_{pj}

$$W = \int_C \bar{\theta}_{pk} \bar{N}_k M_{pj} n_j dl \quad j = 1, 2 \quad p = 1, 2 \quad k = 1 \text{ to } 9 \quad (98)$$

Differentiating w.r.t the nodal rotations the bending loads on the element are given by

$$FB_{pk} = \int_C \bar{N}_k M_{pj} n_j dl \quad j = 1, 2 \quad p = 1, 2 \quad k = 1 \text{ to } 9 \quad (99)$$

Again the above line integrals can be converted to surface integral using Green's theorem

$$FB_{pk} = \int_A \left(\frac{\partial \bar{N}_k}{\partial x_j} M_{pj} + \bar{N}_k \frac{\partial M_{pj}}{\partial x_j} \right) dA \quad j = 1, 2 \quad p = 1, 2 \quad k = 1 \text{ to } 9 \quad (100)$$

Using the equilibrium equations the above equation becomes

$$FB_{pk} = \int_A \left(\frac{\partial \bar{N}_k}{\partial x_j} M_{pj} + \bar{N}_k Q_p \right) dA \quad j = 1, 2 \quad p = 1, 2 \quad k = 1 \text{ to } 9 \quad (101)$$

Expanding the above equations for a given p we get

$$FB_{pk} = \int_A \left(\frac{\partial \bar{N}_k}{\partial x} M_{px} + \frac{\partial \bar{N}_k}{\partial y} M_{py} + \bar{N}_k Q_p \right) dA \quad p = 1, 2 \quad k = 1 \text{ to } 9 \quad (102)$$

Thus the bending loads on the element are

$$FB_{xk} = \int_A \left(\frac{\partial \bar{N}_k}{\partial x} M_x + \frac{\partial \bar{N}_k}{\partial y} M_{xy} + \bar{N}_k Q_x \right) dA \quad k = 1 \text{ to } 9 \quad (103)$$

$$FB_{yk} = \int_A \left(\frac{\partial \bar{N}_k}{\partial x} M_{xy} + \frac{\partial \bar{N}_k}{\partial y} M_y + \bar{N}_k Q_y \right) dA \quad k = 1 \text{ to } 9$$

Similarly the third term in eq.4 represents the loads due to tractions on the element top and bottom surfaces.

$$W = \int_A u_i \sigma_{iz} dA \quad i = 1 \text{ to } 3 \quad (104)$$

Since the only loads that appear on the top and bottom surfaces are the transverse pressures, expressing the displacement w in terms of nodal displacements and nodal shape functions, we have

$$W = \int_A \bar{w}_k \bar{N}_k \sigma_{zz} dA \quad k = 1 \text{ to } 3 \quad (105)$$

Thus the nodal loads can be obtained by differentiating the work w.r.t the nodal displacements

$$F_{zk} = \int_A \bar{N}_k \sigma_{zz} dA \quad k = 1 \text{ to } 9 \quad (106)$$

The stresses σ_{ij} used in the above equations to produce traction on the element are computed using the strain - electric field relations for a piezoelectric material. Thus

$$\sigma_{ij} = c_{ijkl} d_{mkl} E_m \quad (107)$$

The integration in all the expressions for loads derived above, is carried out over all the gaussian points in a manner similar to the evaluation of the loads given by eqn. 23. The unnecessary line integrals are thus avoided.

Chapter 4.

IMPACT SENSING BY PIEZOCERAMIC PATCHES

Piezoelectric material can be used as sensors and actuators in a smart structure because of its unique electric properties. Piezoelectric material creates an electric charge when it is contracted or expanded, and conversely expands or contracts when under an electric field. Control systems can be designed to use piezoelectric elements to detect the onset of loads by measuring the charge they create under strains and to then apply a charge to react to the loading.

Previous work in this field has investigated the numerical modeling of structures with piezoelectric elements and the deflections induced by actuator loadings [1]. Successful damping of both isotropic and laminated cantilevered beams has also been completed [2,3].

The current work involves numerical simulation of a laminated plate under impact containing piezoelectric patches using a finite element program. The program uses nine-noded, two-dimensional elements based on Mindlin plate theory. Linear constitutive relations are used to calculate the electric field generated by strains on the piezoelectric patches at nine Gaussian points for each element. The plate is fixed at opposite ends and impacted at the center with a steel ball. Two different plates are modeled, both containing AS4/3501-6 laminas and G-1195 piezoelectric patches.

Several changes were made to expand the capabilities of the finite element program. These changes included enabling the program to model more than one layup sequence in the same structure, simplifying the element layup input format, and calculation of the electric field created by the piezoelectric elements.

The electric field generated by the piezoelectric elements is dependent on the strains in the structure. Several cases are analyzed to determine the effect the piezoelectric patches had on the impact load curve and the global stress levels [4]. Cases are also analyzed with piezoelectric patches in different regions of the plate to investigate the effect of patch location on electric field. The electric field across individual piezoelectric patches with different sizes and shapes is also investigated.

4.1 Linear Constitutive Relations

The interaction between electrical, mechanical and thermal systems can be derived using thermodynamic relations. Piezoelectric constitutive relationship between mechanical and electrical variables (ignoring any thermal effect) produces coupling between Maxwell's equations of electromagnetism and the elastic stress equations of motion. The following derivation will describe how the strain on a piezoelectric element is related to the electric field it produces [5].

The electric field $[E]$ is related to the strain $\{\epsilon\}$ by:

$$[E] = -[h]^T \{\epsilon\} \quad (1)$$

where:

$$[h] = [g] [\beta^E], \quad [g] = [C^E] [d], \quad [\beta^E]^{-1} = [\epsilon^0] - [g]^T [d] \quad (2)$$

In these equations $[C^E]$ is the ply stiffness matrix for the transversely isotropic piezoelectric material, $[d]$ is the matrix of piezoelectric strain constants and $[\epsilon^0]$ is the dielectric permittivity matrix. The format of the matrices are as follows:

$$[E] = \begin{bmatrix} E_1 \\ E_2 \\ E_3 \end{bmatrix}, \quad \{\epsilon\} = \begin{bmatrix} \epsilon_x \\ \epsilon_y \\ \epsilon_z \end{bmatrix} \quad (3)$$

$$[d] = \begin{bmatrix} 0 & 0 & d_{31} \\ 0 & 0 & d_{31} \\ 0 & 0 & d_{33} \\ 0 & d_{15} & 0 \\ d_{15} & 0 & 0 \\ 0 & 0 & 0 \end{bmatrix}, \quad [\epsilon^\sigma] = \begin{bmatrix} \epsilon_{11} & 0 & 0 \\ 0 & \epsilon_{11} & 0 \\ 0 & 0 & \epsilon_{33} \end{bmatrix} \quad (4)$$

Combining the above equations and solving for only the transverse electric field, the relation becomes:

$$E_3 = \frac{(C_{11}d_{31} + C_{12}d_{31} + C_{13}d_{33})(\epsilon_x + \epsilon_y) + (2C_{13}d_{31} + C_{33}d_{33})\epsilon_z}{2C_{11}d_{31}^2 + C_{12}d_{31}^2 + 4C_{13}d_{31}d_{33} + C_{33}d_{33}^2 - \epsilon_{33}} \quad (5)$$

In the plane stress formulation ϵ_z does not exist, therefore transverse strain can be represented by:

$$\epsilon_z = S_{13}(\sigma_{xx} + \sigma_{yy}) \quad (6)$$

where S_{13} is a compliance coefficient and

$$\sigma_{xx} = C_{11}\epsilon_x + C_{12}\epsilon_y + C_{13}\epsilon_z \quad (7)$$

$$\sigma_{yy} = C_{12}\epsilon_x + C_{11}\epsilon_y + C_{13}\epsilon_z \quad (8)$$

The resulting equation representing the transverse strain is:

$$\epsilon_{zz} = \frac{S_{13}}{(1 - 2S_{13}C_{13})} [(C_{11} + C_{12})(\epsilon_{xx} + \epsilon_{yy})] \quad (9)$$

This results in an equation for transverse electric field in terms of only the in-plane strains:

$$E_3 = C_p(\epsilon_x + \epsilon_y) \quad (10)$$

where:

$$C_p = \frac{\left(C_{11}d_{31} + C_{12}d_{31} + C_{13}d_{33} + \frac{S_{13}(C_{11} + C_{12})(2C_{13}d_{31} + C_{33}d_{33})}{1 - S_{13}C_{13}} \right)}{2C_{11}d_{31}^2 + C_{12}d_{31}^2 + 4C_{13}d_{31}d_{33} + C_{33}d_{33}^2 - \epsilon_{33}} \quad (11)$$

This constant C_p can be calculated using the stiffness and electric properties of the piezoelectric material and then later multiplied times the sum of the in-plane strains to calculate the transverse electric field.

4.2 Finite Element Code Modification

The finite element program SDACLIP (Static and Dynamic Analysis for Composite Laminated Plates) was used to model the smart plate. The program was developed at Purdue University and written in Fortran [6].

Some of the capabilities of the program include anisotropic laminate stiffness calculations, Mindlin plate elements and impact force calculations. The Mindlin plate elements are important in that they can account for extension, bending and transverse shear deformation [7]. Although the plates being tested are thin, including the transverse shear deformation can be important due to the

large shear loading induced by the impact which is perpendicular to the plane of the plate. Calculation of the impact force of the ball on the plate is made in a subroutine of the program. The applied load is a function of the radius of the ball, the displacement and velocity of the ball relative to the impact node on the plate and the compression of the ball [8].

In order to model a plate with piezoelectric elements in small regions of the structure, several changes were made to the finite element program. Because the existing program could not model more than one layup in a single structure, the program's code was changed so that any number of layups could be included in a single model. This change included expanding the material property arrays to include the layup number so that any time the mass, stiffness, or thickness properties were needed in the program, the values for the appropriate layup were used.

To accommodate more than one layup, the format in the input file was modified. The input data for SDACLIP is arranged in macros which specify the type of data which is being input and the data values. The MATE macro, which inputs the material properties, was changed to specify the lamina properties in more than one layup. Table 4. 1 shows an example of the MATE macro format. The line after the macro name specifies the layup number and total number of laminas in that layup. The properties of each ply are represented by two lines of data. The two data lines for each ply input the ply mass density, poisson ratio, Young's moduli, shear moduli, ply number, ply angle and thickness.

TABLE 4. 1 Macro MATE

mate							
1	2						
1.52e-6	0.25	1.41e6	1.02e5	5.10e4	5.10e4	5.10e4	5.10e4
1	90.0	0.071667					
1.52e-6	0.25	1.41e6	1.02e5	5.10e4	5.10e4	5.10e4	5.10e4
2	0.0	0.071667					
2	3						
1.52e-6	0.25	1.41e6	1.02e5	5.10e4	5.10e4	5.10e4	5.10e4
1	90.0	0.071667					
1.52e-6	0.25	1.41e6	1.02e5	5.10e4	5.10e4	5.10e4	5.10e4
2	0.0	0.071667					
1.52e-6	0.25	1.41e6	1.02e5	5.10e4	5.10e4	5.10e4	5.10e4
3	90.0	0.071667					

The macro ELEM, which specifies the node connections for each element, was also changed to allow for more than one layup. The ELEM macro, as shown in Table 4. 2, inputs the element layup and node numbering in groups (i.e. 1-4,5-8 etc.). The first column of numbers gives the first element number for that group. The column of numbers labeled A shows the element layup for that group of elements followed by the nine nodes for each element. The last column of numbers specify the numbering increment used for node numbering between consecutive elements. The element layups can also be specified individually. Label B shows the number of elements which will have a layup specified separately from the element connectivity data. Label C shows the elements and layup number assigned to them. The ability to specify the element layup number either in the element connectivities or separately makes the user's job easier when the layup arrangement will be changed frequently, as in this work.

TABLE 4.2 ELEM Macro

elem	2	←	B
1	1 1 19 21 3 10 20 12 2 11 18		
5	1 3 21 23 5 12 22 14 4 13 18		
9	1 5 23 25 7 14 24 16 6 15 18		
13	1 7 25 27 9 16 26 18 8 17 18		
7	2	←	A
11	2	←	C

The calculation of the electric field in the finite element program involves multiplying the sum of the in-plane strains by the constant represented by equation (12). The in-plane strains is a function of the midplane curvature of the plate element, and the piezoelectric ply's distance from the midplane. The information needed for calculating the electric field is included in a newly created macro PIEZ. An example of the macro PIEZ is shown in Table 4.3. The input data includes the layup number the piezoelectric ply is located in, the ply number, the Young's moduli, Poisson ratio, piezoelectric strain constants, and dielectric permittivity of the piezoelectric material.

TABLE 4.3 PIEZ Macro

piez	1 5 6.43e5 5.00e5 0.31 0.31 -166e-10 360e-10 1.505e-6
------	-------------------------------------------------------

TABLE 4.4 Lamina and Piezoceramic Properties

	Lamina Properties (S4/3501-6)	Piezoceramic Properties (G-1195)
E1	138 GPa	63.02 GPa
E2	10 GPa	63.02 GPa
E3		49 GPa
G12	5 GPa	24.06 GPa
nu12	0.25	0.31
nu13		0.31
rho	1490 kg/m ³	7650 kg/m ³
d31		-166x10 ⁻¹² m/V
d33		360x10 ⁻¹² m/V
e33		1.505x10 ⁻⁸ N/V ²
thickness	0.143 mm	0.254 mm

The changes stated above were made to the finite element code written in Fortran and run on the University of Texas System's Convex C220 computer. Two other versions of the program

were modified to run on a Sun SPARCstation and a Cray Y-MP. The version of the program on the Convex was created because of the large storage space available, the Sun version was created because of unlimited free computer time, and the Cray version was created because of its high speed. This speed was necessary because of the large number of time steps taken.

4.3 Model Properties

Two rectangular plate models were simulated, each containing the same laminate, impact conditions, and boundary conditions. The plates contained AS4/3501-6 laminates in a $[90_5/0_5/90_5]_T$ layup. Piezoelectric material G-1195 was modeled attached to the top of the laminates. The stiffness and electric properties of the lamina and piezoceramic plies are given in Table 4. 4. The rectangular plates were rigidly fixed at the two short ends and impacted from below at the center of the plate with a 12.7 mm diameter steel ball at 1.8 m/s.

Because of the model symmetry with respect to boundary conditions, cross-plyed layup and applied load, only one quarter of the plate was actually modeled.

Model 1 is one quarter of a 152.4x25.4 mm rectangular plate containing 610 rectangular elements of dimensions 1.249x1.27 mm. Figure 4. 1 shows the element layout for model 1 which represents the top left-hand corner of the plate. The left end is rigidly fixed, the right and lower sides have symmetric boundary conditions, and the lower right-hand corner is the impact location. For this model, the longer horizontal direction is considered the principle direction and the shorter vertical direction is the transverse direction.

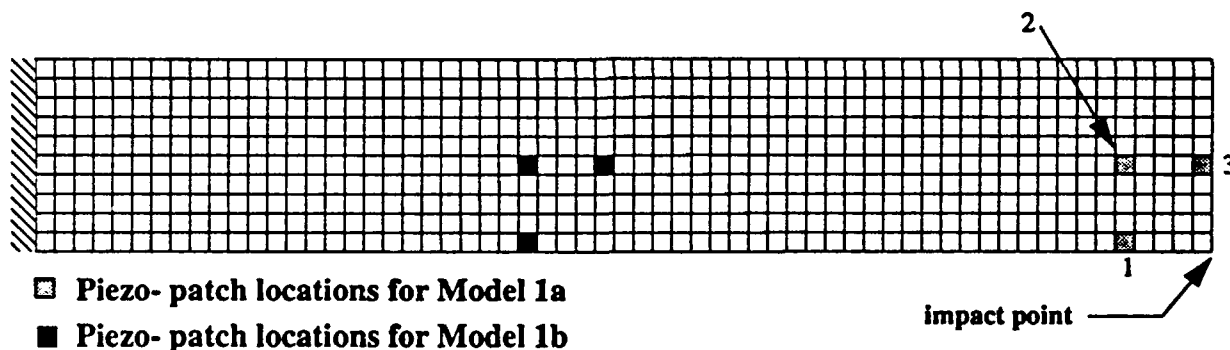


FIGURE 4. 1 Model 1 Layout, Piezo-patch Locations and Numbering

The shaded regions show the locations of the elements containing piezoelectric plies. The model was run with these piezoelectric patches near the impact as in Model 1a and also with the piezoelectric patches away from the impact as in model 1b. Note that because of symmetry, the three piezoelectric patches for each quarter model translates into twelve patches for the full model. Model 1 will be used to show how placement of piezoelectric patches near the impact point can affect the stress levels in the surrounding elements.

Model 2 is a 406x188 mm rectangular plate with one quarter of the plate modeled with 520 rectangular elements. Each element has the dimensions of 7.8x4.7 mm. The boundary conditions are the same as for Model 1 and the impact point is at the lower right hand corner of the quarter model.

Figure 4. 2 shows the element layout for Model 2. As in model 1, the longer horizontal direction is considered the principle direction. This model will be used to show how the electric field created by a piezoelectric patch changes when the dimensions and position of the patch change. In this model more than one element will be used to model a piezoelectric patch. The patches will

be modeled with 2x2, 4x4, 6x6, 8x8, 7x5, 5x7 and a triangular group of elements.

Patches which have an equal number of elements on two adjacent sides will be referred to as square such as the 2x2 patch in Figure 4. 2. Larger square patches such as 4x4, 6x6 or 8x8 are centered about the same point. Figure 4. 3 shows the patch layout for the 7x5 and 5x7 patch. Figure 4. 4 shows the piezoelectric element layout for the triangular patch.

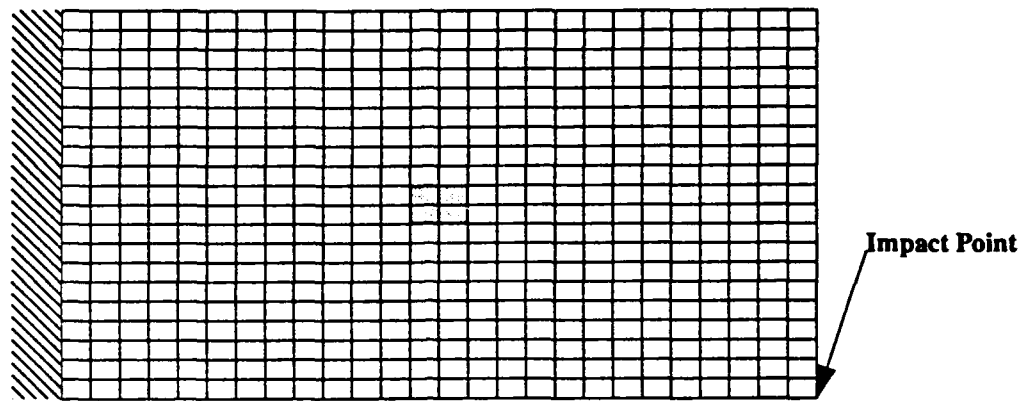


FIGURE 4. 2 Model 2 Element Layout with 2x2 Piezoelectric Patch

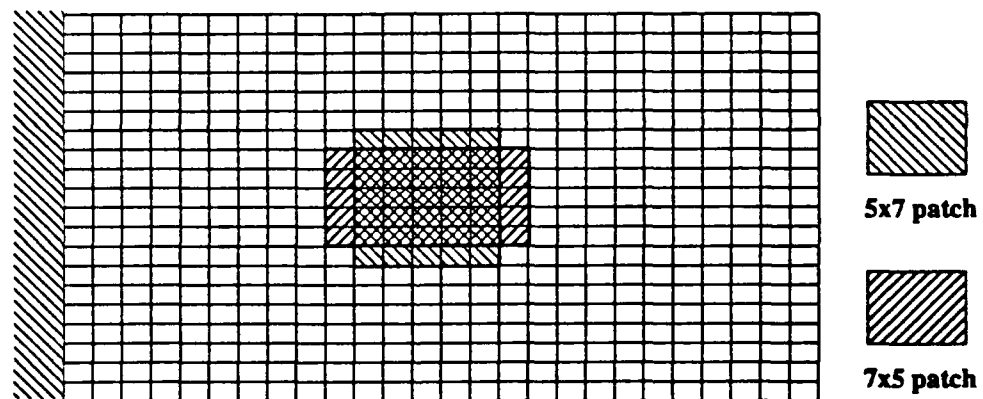


FIGURE 4. 3 Model 2 Element Layout with 7x5 and 5x7 Piezoelectric Patches

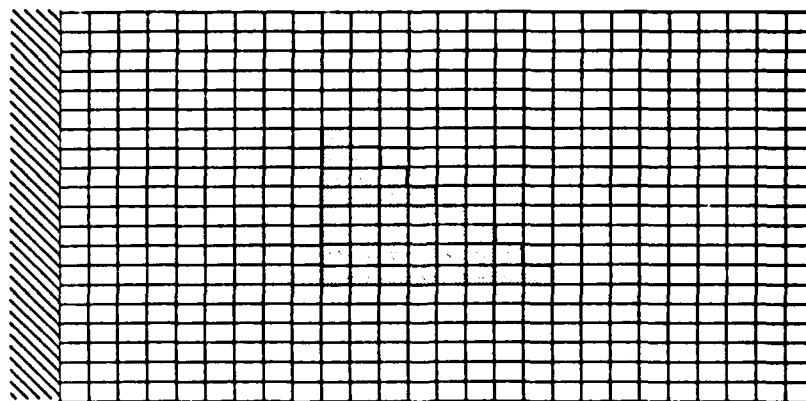


FIGURE 4. 4 Model 2 Element Layout with Triangular Piezoelectric Patches

Model 2 will also be used to compare the electric field generated by patches of the same size which are located in different regions of the plate. For these cases, a 4x4 element patch is moved in the plane of the plate as shown in Figure 4. 5. The seven patch locations are labeled a, b, c, d, e from left to right across the plate and f, g, h, i from the lowest to the uppermost patch.

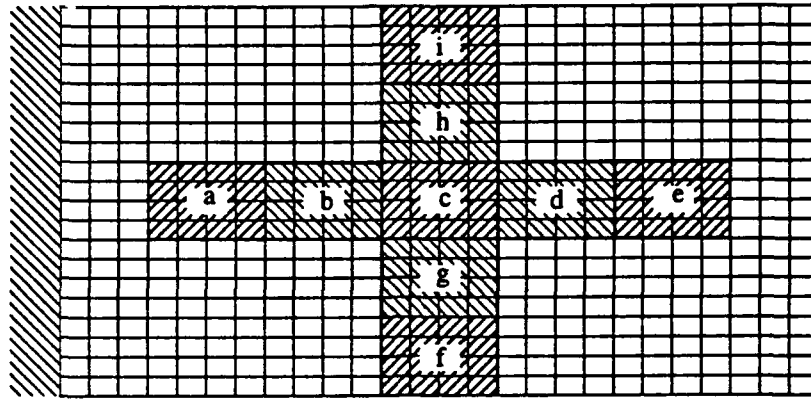


FIGURE 4. 5 Model 2 Element Layout with Nine 4x4 Piezoelectric Patches

4.4 Model Verification

Several test cases were run to ensure the accuracy of the model results. After the changes to the program code were made, it had to be checked to ensure that some programming error was not created in the program. The models which were used to produce results were also checked for solution convergence.

In order to verify the changes to the stiffness property calculations, several static loading cases were run. Identical models without piezoelectric patches were run on the original program and the modified program. The results showed all the stress, strain and displacement results matched up.

Two more static test cases were run to show how a local increase in stiffness due to a piezoelectric patch affects the global stresses. According to St. Venant's principle, a localized change in stiffness should only affect the localized stresses [12]. One case involved a cantilever plate containing piezoelectric elements under a unidirectional tensile force. A comparison with a similar model without piezoelectric elements showed that the stress level between the two models converges within three element widths. A similar case using a uniform moment showed that the stresses between the two cases with and without piezoelectric elements converges within four element widths.

The final element mesh configurations for Models 1 and 2 were found by experimentation with several different element distributions and element sizes. In order to save on computing time, some of the earlier mesh patterns were nonuniform with smaller elements near areas of particular interest such as piezoelectric patches. The results of the nonuniform meshes were inconsistent with each other and did not match the results of uniform mesh cases. These differences can be attributed to the variation in wave transmission and reflection as they pass between elements with different sizes.

In order to reduce on the degrees of freedom of the models and reduce computing time, the in-plane translational degrees of freedom of the models were constrained. This assumption was made because the transverse impact loading should not create any significant in-plane translation. To verify this, a two test cases were run with and without the translational degrees of freedom ac-

tivated. The results of these cases matched very closely.

The modeling of an unbalanced layup with a piezoelectric ply on one side of the laminate creates a discontinuity in ply stresses due to the laminate midplane being offset. The laminate midplane is shifted by half the thickness of the piezoelectric element, as shown in Figure 4. 6 (a). To prevent this, a fake or dummy ply with the same thickness as the piezoelectric ply is added to maintain the laminate midplane location as shown in Figure 4. 6 (b). This dummy ply is specified to have a mass density of zero and near-zero stiffness properties (for calculation purposes). In order to verify that the addition of a fake layer does not affect the results of the model, a layup with a fake layer on top and bottom of the laminate was compared to a layup without fake layups. The results showed no differences.

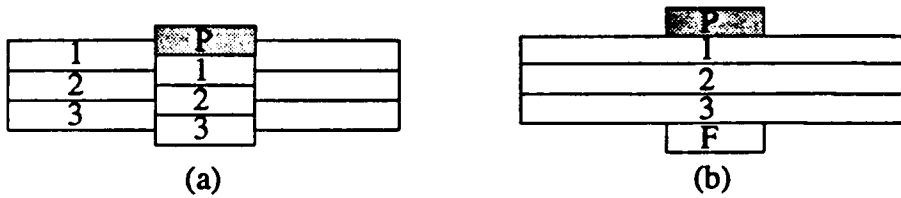


FIGURE 4. 6 Lamina Offset Using a Fake Layer

4.5 Results And Discussion

The following section reports on the findings of numerous computer runs involving Models 1 and 2. The results show that a piezoelectric patch near the impact point changes the impact loading and affects the stresses of the entire model. The results also show that the electric field generated by a piezoelectric element is affected by its shape and location on the structure.

4.5.1 Effect of Piezoelectric Patch Location on Load and Global Strain

Results were obtained for model 1a and 1b with different piezoelectric ply thicknesses on the top side of the laminate. Figure 4. 7 shows how the impact load history changes when different thickness piezoelectric elements are used in model 1a. The solid line is for the plate without any piezoelectric elements and the dashed lines are for elements with piezoelectric plies of thickness of one and two times the standard piezoelectric ply thickness of 0.254 mm. The impact load slightly increased when the thickness of piezoelectric patch was increased. This trend was also consistent in the cases of piezoelectric patches one-half and three-half times the standard piezoelectric patch thickness. The peak impact load increased about two percent due to the presence of the single standard thickness piezoelectric ply.

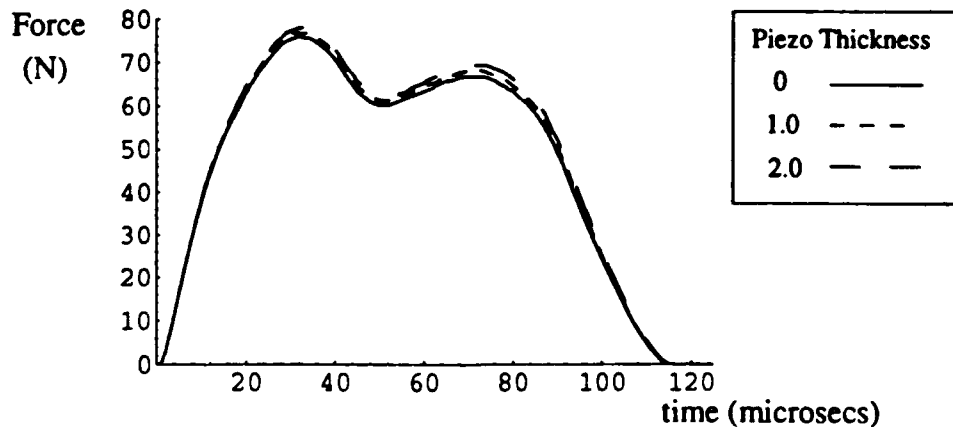


FIGURE 4. 7 Load History for Model 1a

Figure 4.8 shows the load history for model 1b. The thickness of the piezoelectric patches had no effect on the impact loading on model 1b and all the load histories converged to one curve. Locating the piezoelectric elements near the impact point in model 1a has a larger effect on the applied load than for model 1b where the piezoelectric elements are farther away from the impact.

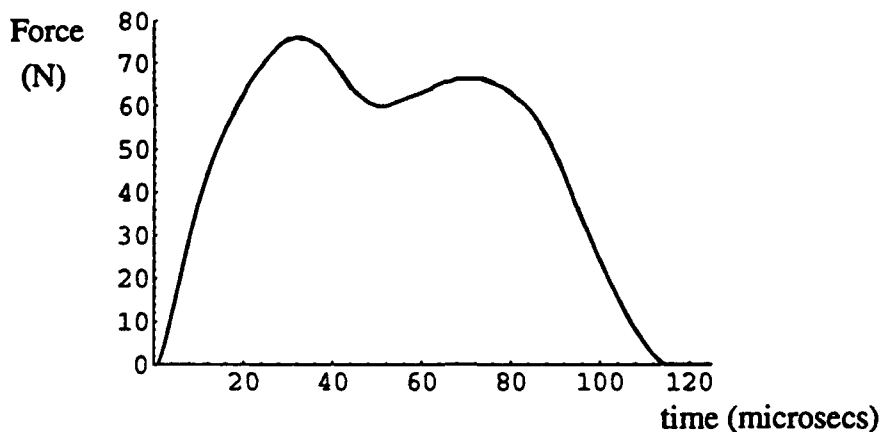


FIGURE 4.8 Load History for Model 1b

For the static force and moment cases, the piezoelectric patches have only a localized effect on the stresses and strains. However, in the case of impact, the location of piezoelectric patches can effect the load which in turn effects the global behavior of the structure. Figure 4.9 shows a three-dimensional plot of the curvatures k_x in the 10×10 element region near the piezoelectric elements in model 1a. The curvature k_x is the negative of the change in slope along the plate's principle direction. The impact point can be seen to increase the curvature on lower right-hand corner of the plot. The effect of the added stiffness of the three piezoelectric elements decreases the local curvature at the piezoelectric patch locations. The larger curvature of the surrounding areas shows these elements are more flexible.

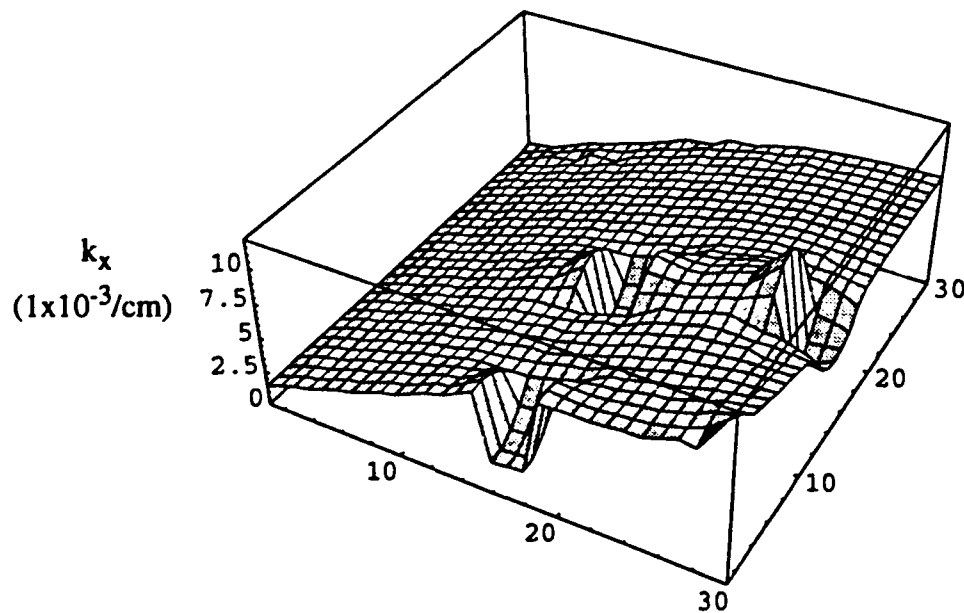


FIGURE 4.9 Curvatures Near Piezoelectric Elements in Model 1a

Figures 4. 10 and 4. 11 show k_x , along the model symmetry line four elements away from piezoelectric patch number 1 (as labeled in Figure 4. 1) for models 1a and 1b. As with the load histories, the curvatures values vary only when the piezoelectric elements are near the impact point as in model 1a. This shows that piezoelectric elements near the impact point can affect the global strains in the plate by changing the applied impact loading.

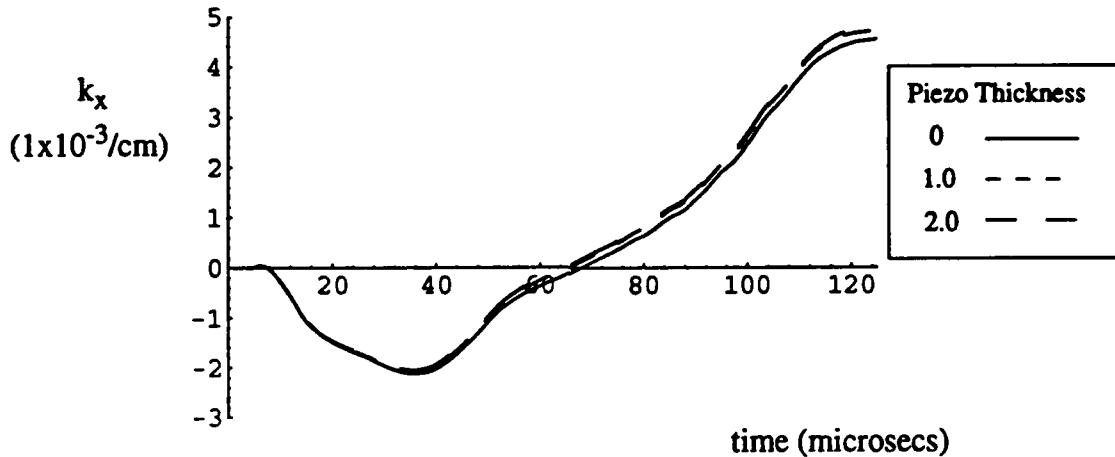


FIGURE 4. 10 Curvatures Four Elements Away From Piezoelectric Elements in Model 1a

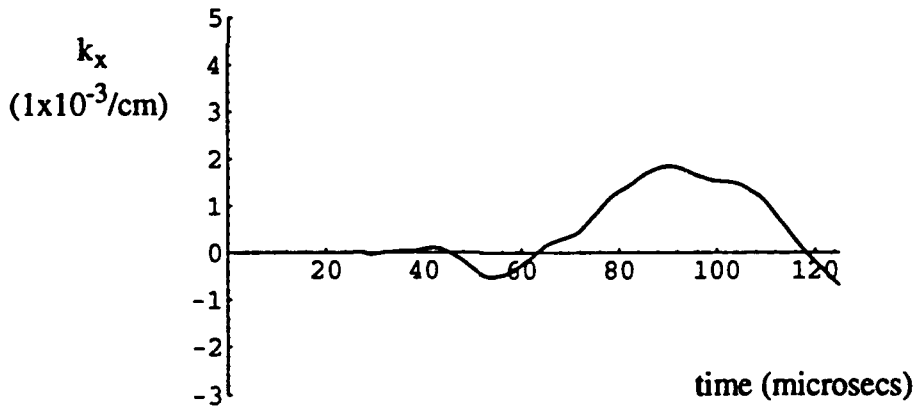


FIGURE 4. 11 Curvatures Four Elements Away From Piezoelectric Elements in Model 1b

There are two noticeable differences between the curvatures four elements away from piezoelectric element number 1 in models 1a and 1b. The first difference is the larger magnitude of curvatures in model 1a versus 1b. This is due to the model 1a curvature readings being taken closer to the impact point. The curvatures in model 1b are farther from the impact point, but more importantly closer to the constrained ends of the plate. The second difference between the models is the time lag between the curvature peaks. These peaks occur much sooner in model 1a due to its closer proximity to the impact point.

Two test cases run show that the change in load history in model 1a caused by piezoelectric elements near the impact is due to both the added stiffness and inertial properties of the piezoceramic material.

4.5.2 Electric Field Variation Due to Piezoelectric Patch Location

Both small and large piezoelectric patches were moved in the plane of the plate to observe how the location of the piezoelectric patch affected the electric field it generated.

Figure 4. 12 shows the electric field calculated at the center node of the three piezoelectric patches of model 1a as numbered in Figure 4. 1. The electric field is produced by a single piezoelectric ply on top of the $[90_5/0_5/90_5]_T$ layup. The moment at the middle of the plate is at its maximum negative value and therefore the electric field is at a maximum at the middle of the plate near patch number 3 and decreases toward the fixed ends. Since patches 1 and 2 are farther from the middle of the plate, the moment, curvature, and therefore electric field are less than for patch 3. The electric field for the piezoelectric patches number 1 and 2 are similar due to their similar locations along the principle direction of the plate.

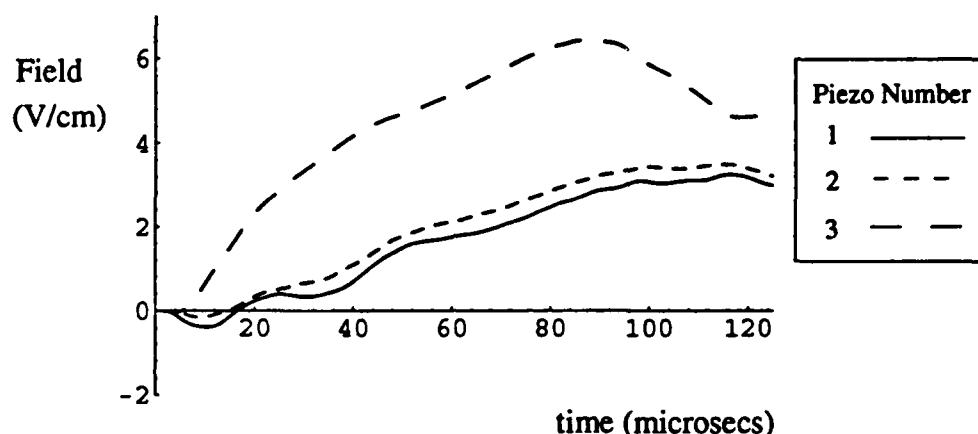


FIGURE 4. 12 Electric Field in Model 1a due to One Piezoelectric Ply

Figure 4. 13 shows the electric field from the three piezoelectric elements near the middle of the length of the plate in model 1b. The electric field generated from the patches in the middle of the plate is much smaller than the electric field generated near the impact point due to the large distance from the impact point. Again, the electric field generated by patches 1 and 2 are similar because of their similar location along the principle direction of the plate. The time lag is clearly visible in Figure 4. 13 because of the different distances from the impact point to patches 3 or 1 and 2.

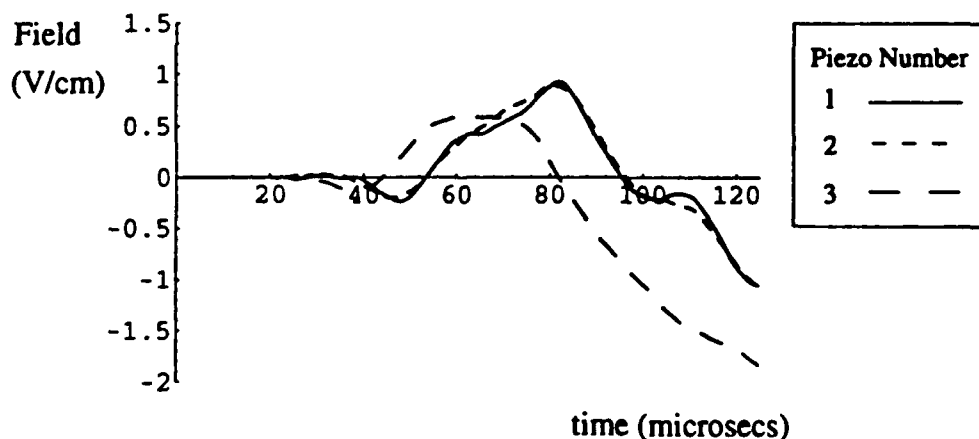


FIGURE 4. 13 Electric Field in Model 1b due to One Piezoelectric Ply

Figure 4. 14 shows the electric field generated by the top piezoelectric ply in a layup with piezoelectric elements on both the top and bottom of the laminate. In comparison, with Figure 4. 13, the electric field for a laminate with two piezoelectric plies is simply a scaled down version of the electric field for one piezoelectric ply. This difference is a result of the added stiffness of the extra piezoelectric ply which reduces the deformation and curvature of the piezoelectric elements. The waviness in the electric field curves for model 1b in figures 13 and 14 comes from the transverse curvature k_y while the overall shape of the electric field curve comes from k_x . The waviness is not clearly visible in model 1a because of the large magnitude k_x which dominates over the effect of k_y .

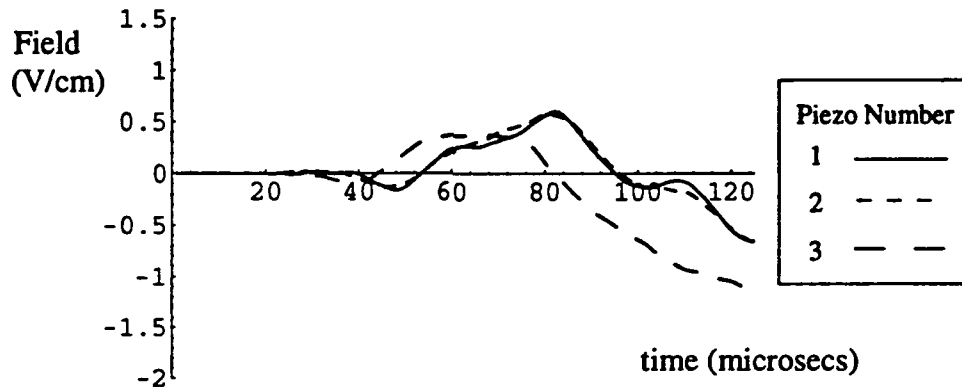


FIGURE 4. 14 Electric Field in Model 2 due to Two Piezoelectric Plies

Model 2 was used to analyze the effect of location of a 4x4 element patch on the electric field it generates. Figure 4. 5 shows the locations of the 4x4 element patches labeled a through i. The location of the piezoelectric patch along the principle direction of the plate can change the average electric field output and when the electric field is generated. The location of the piezoelectric patch along the transverse direction has a less dramatic effect due to the similar distance from the patches to the impact point.

Figure 4. 15 shows the average electric field in the first 125 microseconds after impact for the horizontally placed piezoelectric patches 'a' and 'b'. The electric field for patch 'a' is smaller because it is farther from the impact. Because patch b is closer to the impact point, it generates a visible electric field sooner.

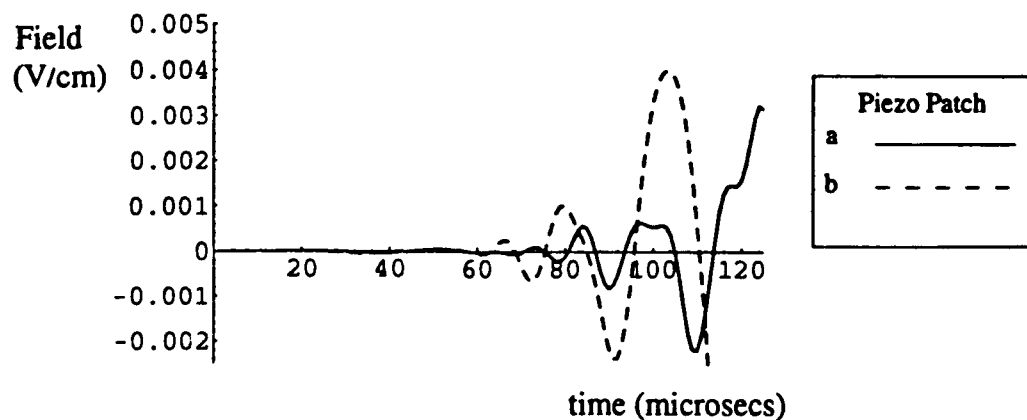


FIGURE 4. 15 Average Electric Field Generated by Piezoelectric Patches 'a' and 'b'

Figure 4. 16 shows the electric field generated by patches 'c' through 'e'. Once again, the piezoelectric patch furthest from the impact point (patch 'c') generates less electric field and at a later time than the patches closer to the impact point. Patch 'e', which is closest to the impact point, begins generating electric field well before the other patches and at a much larger magnitude.

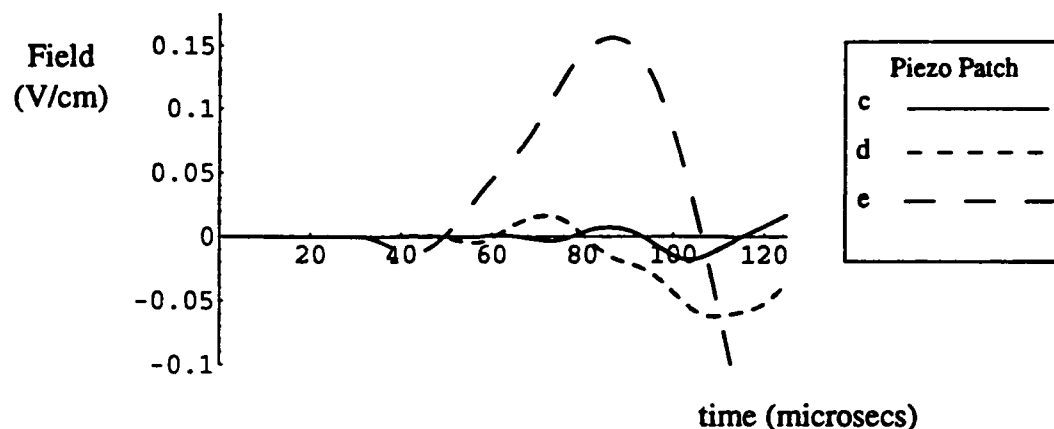


FIGURE 4. 16 Average Electric Field Generated by Piezoelectric Patches 'c' Through 'e'

The elastic wave created by the impact takes a finite amount of time to travel between the impact point and the piezoelectric patch. Because of this, the time from impact until some nominal value of electric field is generated is directly related to the distance between impact and sensor. Figure 4. 17 shows the time necessary for the piezoelectric patches to generate a minimum average electric field of 0.002 V/cm. This demonstrates that the time is directly related to the distance from the impact point. The five data points are fitted to a least squares linear line through the origin. Since the cross plied layup does not have an equal number of 0 and 90 degree plies, the waves travel at different speeds in different directions. This accounts for some of the variations about the least squares line.

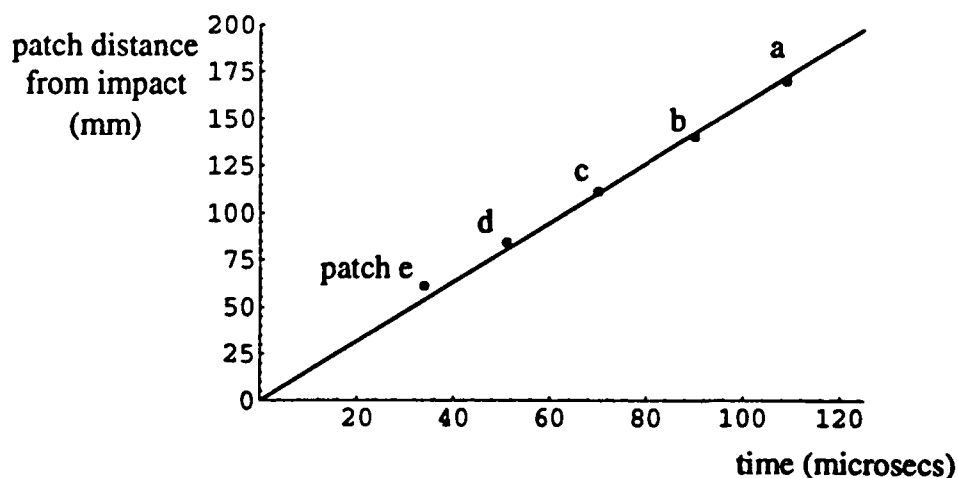


FIGURE 4. 17 Time Between Impact and Generation of 0.002 V/cm Average Electric Field

Figure 4. 18 shows the average electric field for the piezoelectric patches f, g, c, h, and i which run transverse to the length of the plate. As shown in Figure 4. 5, patch 'f' is the lowest patch and 'i' is the uppermost patch. Figure 4. 18 shows that the piezoelectric patches closest to the im-

point generate more electric field. The lag time from the impact wave traveling along the plate until it induces an electric field is also clearly visible.

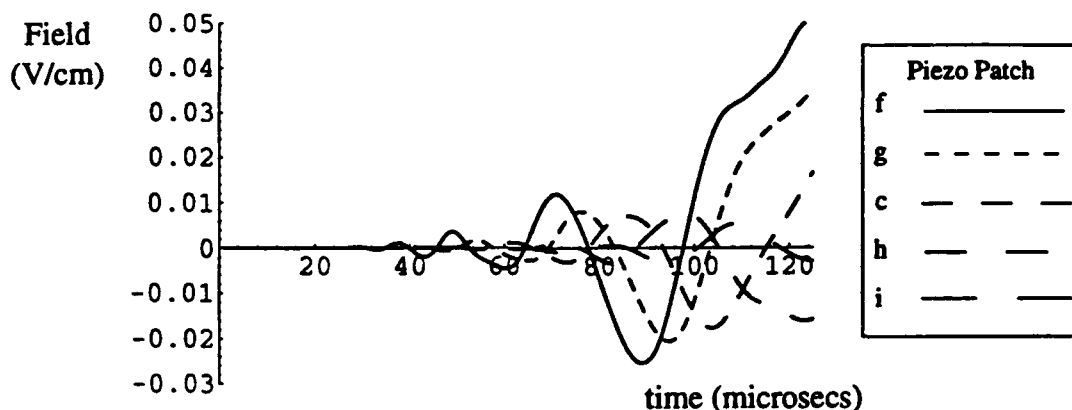


FIGURE 4.18 Average Electric Field for Piezoelectric Patches f, g, c, h, and i

4.5.3 Electric Field Variation Due to Piezoelectric Patch Size and Shape

Several cases with square piezoelectric patches were run to find the relationship between patch size and the average electric field generated. The patches for these cases were far enough from the impact location so that they did not affect the impact load history.

Figure 4.19 shows the average electric field generated by 2x2, 4x4, 6x6, and 8x8 element patches. These square piezoelectric patches were centered about the same point as shown in Figure 4.2. The trend in the plots demonstrate that as the size of the piezoelectric patch grows, the average electric field it generates decreases. This decrease is due to averaging out oscillating waves of electric field. Larger piezoelectric elements are able to average more waves at the same time and thereby reduce the average electric field generated. This wave averaging will be discussed in more detail later.

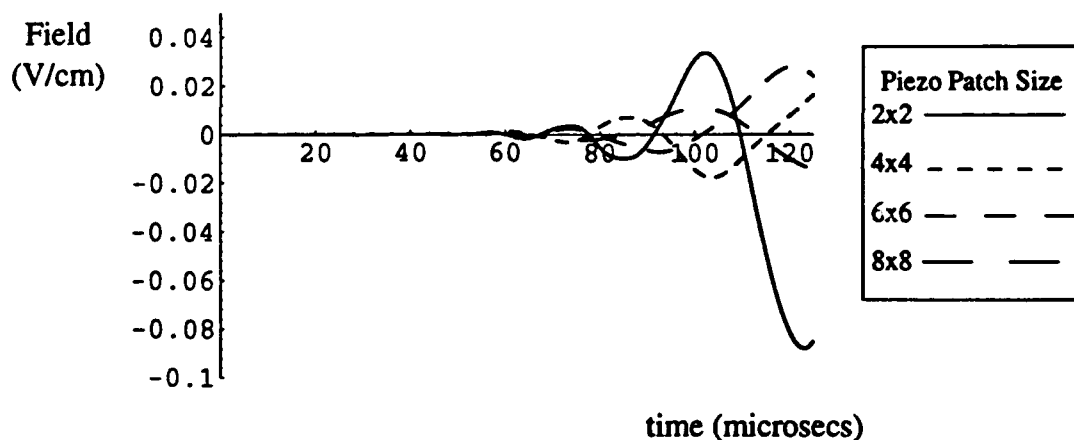


FIGURE 4.19 Average Electric Field for Square Piezoelectric Patches

Several cases were run with different patch shapes covering approximately the same amount of area. The element shapes were 5x7, 6x6, 7x5 and triangular as shown in figures 2, 3 and 4. The loading curves for these four cases were identical, ensuring that the piezoelectric patch

shape was not affecting the impact force. The four patches were centered about approximately the same point on the plate.

Figure 4. 20 shows the average electric field generated by the four patch shapes. The general trend seems to be that the patches which are longer along the principle direction of the plate, such as the triangular patch which is 8 elements long, generate a lower magnitude electric field. The short patches, such as the 5x7 patch which is 5 elements long, generate more electric field. This again, is due to the larger patches being able to average the oscillating electric field over more waves.

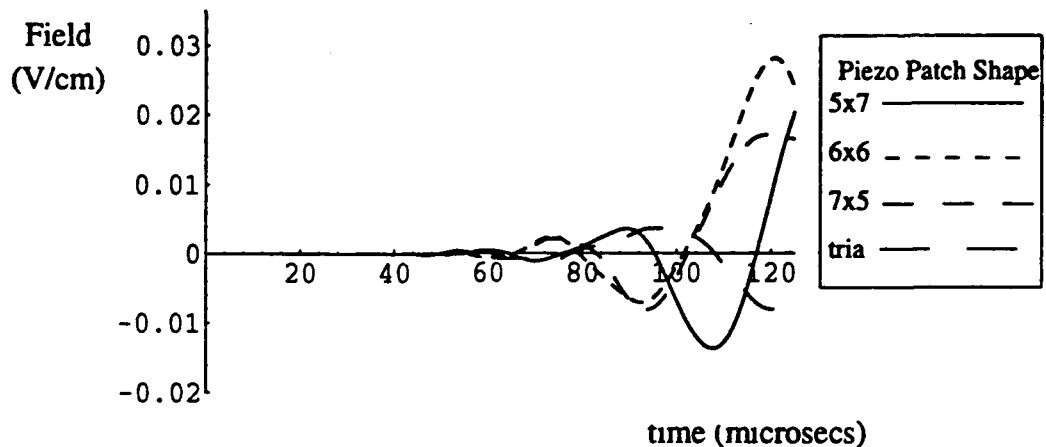


FIGURE 4. 20 Average Electric Field for Different Shaped Piezoelectric Patches

4.5.4 Electric Field Across Piezoelectric Patches

As explained before, the distance between the piezoelectric patch and impact point affects the magnitude of the electric field generated and the time at which it is generated. This section will use three-dimensional plots to show how the electric field moves across the piezoelectric patches.

Figure 4. 21 shows ten plots of the electric field generated across the 4x4 element piezoelectric patch in model 2. The ten plots are taken at 10 microsecond intervals from 30 to 120 microseconds after the time of impact and show the electric field in V/cm. Figure 4. 21a is 30 microseconds after impact and shows that no electric field has been generated at this time. Figure 4. 21c shows a slightly negative electric field being generated at the lower right-hand corner of the piezoelectric patch. This corner of the patch is closest to the impact point and experiences the strains created by the impact first. As more time elapses, visible waves of positive and negative electric field begin to grow and move along the length of the patch. Note that the electric field waves are not aligned along the length of the patch but are moving radially away from the impact point.

Figure 4. 22 shows the electric field plots for the 7x5 element piezoelectric patch. The rolling motion of the electric field is more clearly visible in these plots. Since the 7x5 element patch is longer in the principle direction of the plate, it can hold more waves of electric field than the 4x4 patch. Because the waves oscillate about the 0 V/cm axis the more waves that are included in the patch result in a lower average electric field across the patch.

The electric field plots for the 4x4 element match up well with the middle of the 7x5 electric field plots because of their similar location on the plate. This demonstrates that the electric field does not tend to vary near the edges due to the different material properties of the surrounding layup.

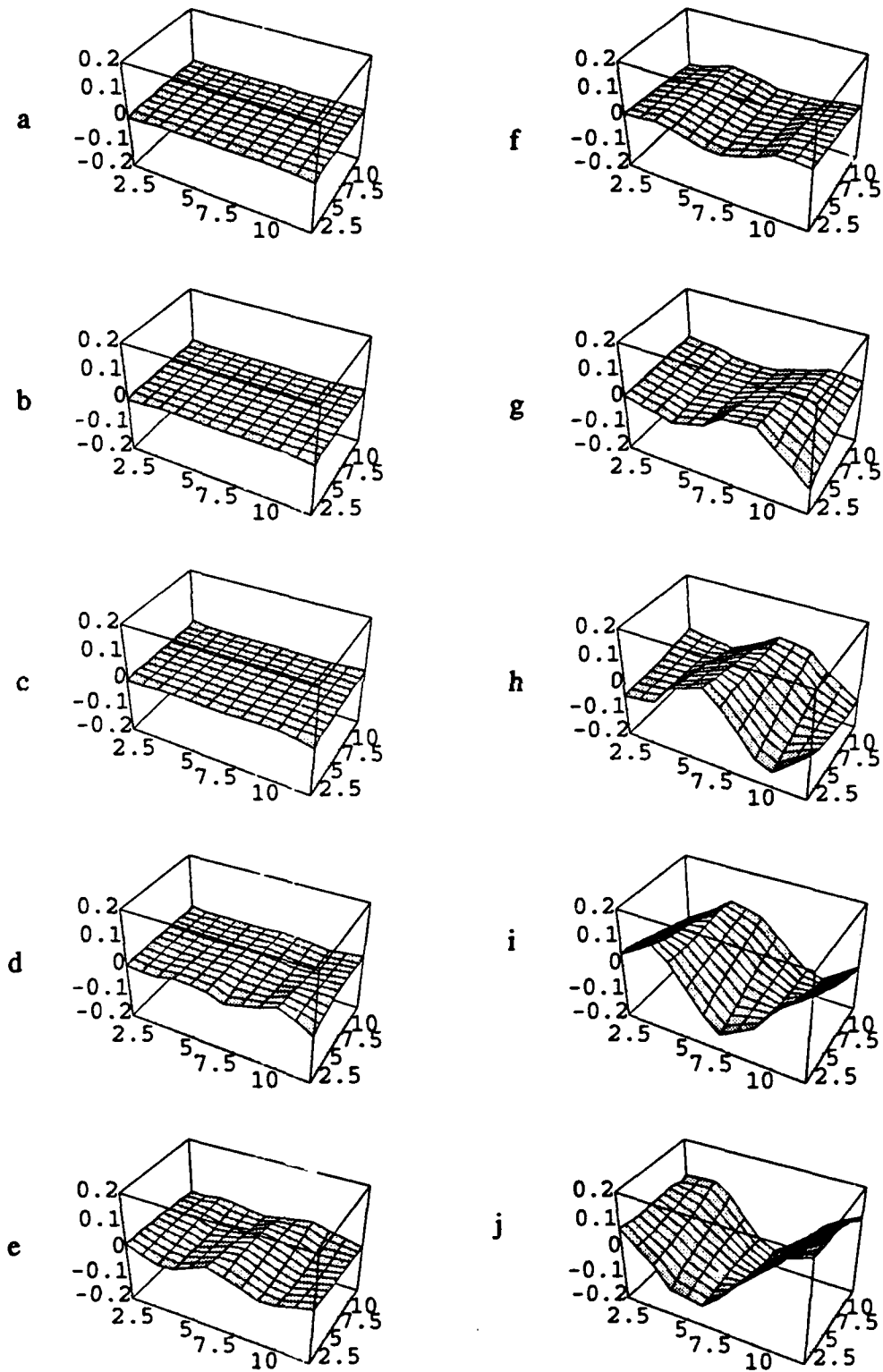


FIGURE 4.21 Electric Field Plots for 4x4 Element Piezoelectric Patch

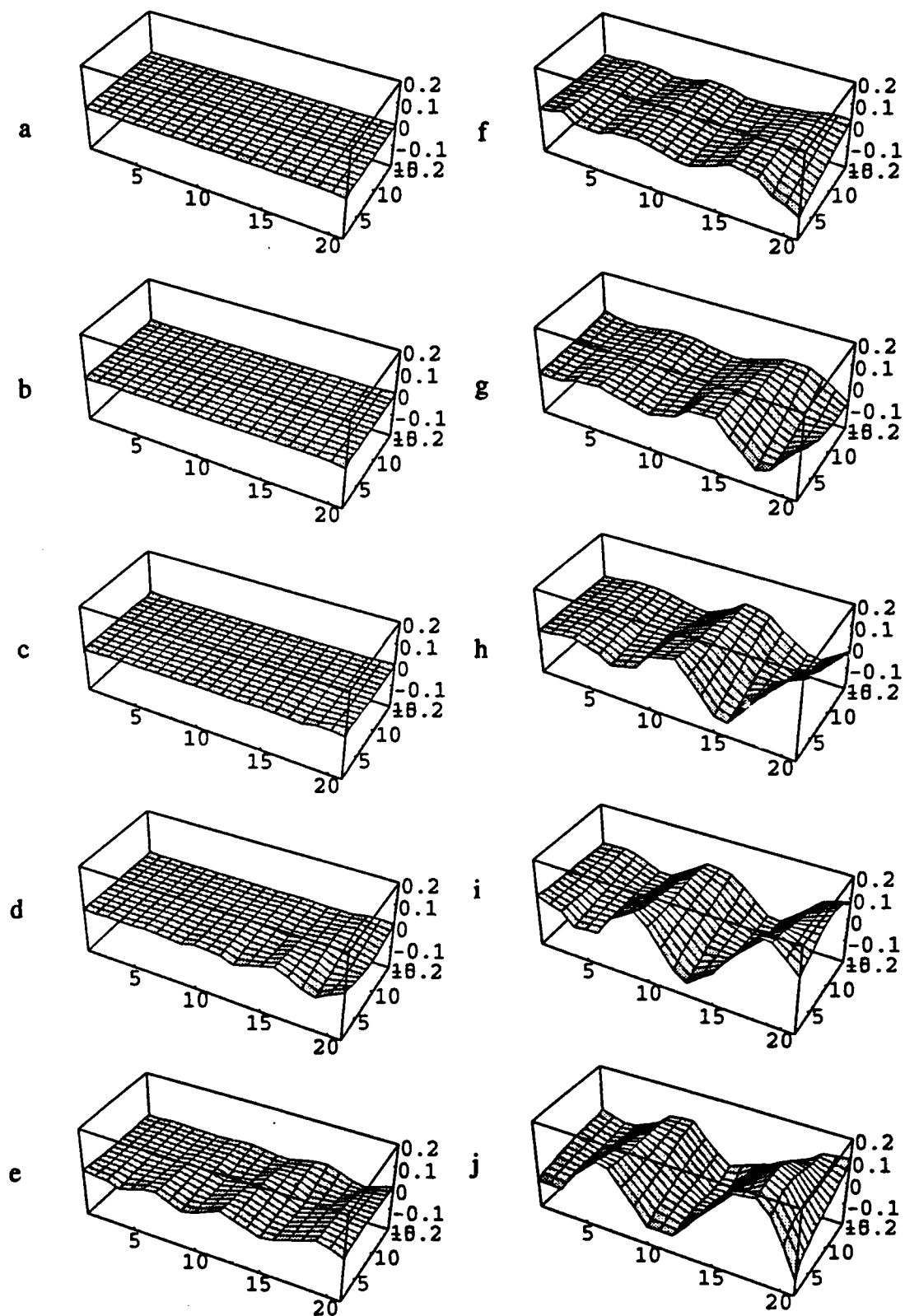


FIGURE 4.22 Electric Field Plots for 7x5 Element Piezoelectric Patch

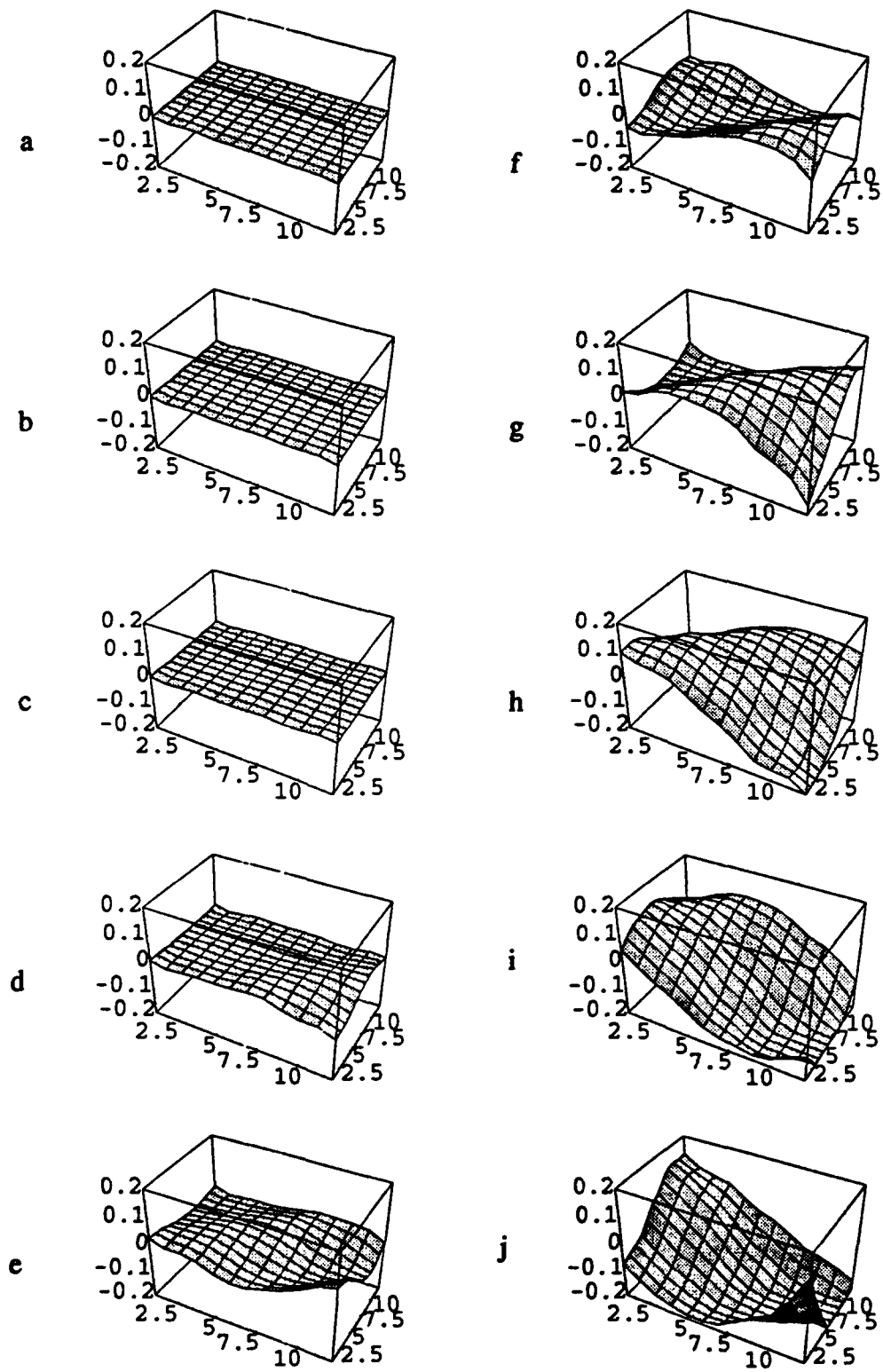


FIGURE 4.23 Electric Field Plots for 4x4 Element Piezoelectric Patch on $[0_p/90_p/0_s]_T$ Layup

Figure 4. 23 shows a 4x4 element patch in a $[0_5/90_5/0_5]_T$ layup. This layup was modeled in order to observe the effect of layup sequence on electric field. The magnitude of the electric field is the same of for the $[90_5/0_5/90_5]_T$ layup but the waves have a longer wavelength and are oriented at a larger angle from the principle direction of the plate. The waves change direction due to the transverse direction of the plate being more flexible this layup.

4.6 Conclusions And Recommendations

Piezoelectric patches close to the impact point were found to slightly increase the impact load and subsequently increase the entire plate stresses. The time from impact until the electric field begins to become nonzero was found to be proportional to the distance between the piezoelectric patches and the impact point. Use of this data could help in being able to pinpoint the location of an impact with several piezoelectric patches.

The size and shape of piezoelectric patches was found to affect the output voltage readings. The elements which were short in the principle direction of the plate tended to read higher values than longer patches which averaged out oscillations in the electric field.

There is still a considerable amount of work left on this project which involves more changes to the finite element program and verification of the current results. The next step in the program's evolution should be the addition of piezoelectric actuation and development of a control loop to be able to lower lamina stresses. Plate impact tests should also be run to verify the program results. Both plate models were sized for existing test specimens at the University of Texas at Arlington.

REFERENCES

1. Crawley, E.F., and Lazarus, K.B., "Induced Strain Actuation of Isotropic and Anisotropic Plates," *AIAA Journal*, Vol. 29, No.6, June 1991, pp.944-951.
2. Baily, T., and Hubbard, J.E., "Distributed Piezoelectric-Polymer Active Vibration Control of a Cantilever Beam," *J. of Guidance, Control and Dynamics*, Vol. 8, No. 5, 1985, pp 605-611.
3. Ha, S.K., Keilers, C., and Chang, F.K., "Finite Element Analysis of Composite Structures Containing Distributed Piezoceramic Sensors and Actuators," *AIAA Journal*, Vol. 30, No.3, March 1992, pp.772-781.
4. Mannas, John R., and Joshi, Shiv P., "Numerical Simulation of a Smart Laminated Plate Under Impact," *Proceedings of the American Society for Composites, Seventh Technical Conference*, 1992.
5. Joshi, S.P., 1992, "Nonlinear Constitutive Relations for Piezoceramic Materials", *Journal of Smart Materials and Structures*, No. 1, Vol. 2 .
6. Joshi, S.P., and Sun, C.T., "Impact-Induced Fracture Initiation and Detailed Dynamic Stress Field in the Vicinity of the Impact," *Proceedings of the American Society for Composites, Second Technical Conference*, 1987, pp 177-185.
7. Cook, R.D., Malkus, D.S., and Plesha, M.E., *Concepts and Applications of Finite Element Analysis*, John Wiley and Sons, New York, 1989, pp 323-328.
8. Timoshenko, S. P., and Goodier, J. N., *Theory of Elasticity*, McGraw-Hill Publishing Company, New York, 1987, pp 39-40.

Chapter 5.

IMPACT LOCATION ESTIMATION

Monitoring a structure for an impact event is important in many engineering applications. For example, the maintenance of a space platform requires knowledge of the severity and the location of the impact event in real time. Impact detection techniques are also required in smart structures. There is a vast amount of research literature which has concentrated on nondispersive waves. These waves do not change their shapes as they propagate. Consequently, it is easy to keep track of the waves in space and time. A more complicated range of problems arise when the waves are dispersive. The ability to identify the waves as they propagate is difficult because the phase speed is frequency dependent.

Holms (1974) showed that the measurement of time delays and attenuation factors by correlation techniques offers a useful complement to the measurement of the frequency response in system characterization. The technique is not useful in obtaining the origin of a dispersive signal. Recompression of the dispersive signal by a time varying pulse-compression filter to give a sharp arrival time is discussed by Booer (1977) and Brazier-Smith (1981). The scheme is based on the conversion of the frequency transform of the signal to a wavelength transform as originally introduced for imaging faults in coal seams by Booer (1977). This method can not tell the absolute position but if there exist multiple reflections then the distance between the boundary can be told. Whiston and Jordan (1984) and Whiston (1984) presented a different approach. First an estimate of a position is obtained by the transient duration. This estimate is refined successively until the reconstructed force has no significant negative portions. The phase difference in signals recorded at two points to locate the impact source is used by Doyle (1987).

The goals of this research are to find the distance of the origin of the signal from the recording site and the magnitude of the pulse at the origin. The dispersive signals from the measurement sites and the dispersive relations for the medium are the only two known conditions. Three approaches for achieving the above-mentioned objectives are presented. These three methods are all based on the Fast Fourier Transform (FFT) and its inverse. Two methods are based on the formulation presented by Whiston (1984) and Doyle (1987).

5.1 Dispersive Signal Analysis

Consider the 1-D wave equation.

$$\frac{\partial^2 u}{\partial x^2} = a^2 \frac{\partial^2 u}{\partial t^2} \quad (1)$$

a is real and positive. Assume $Ce^{i(kx+\omega t)}$ is a solution of the wave equation. Substituting in eq. 1, we obtain,

$$(-k^2 + a^2\omega^2)C = 0 \quad \text{or} \quad k = \pm\omega a \quad (2)$$

and, therefore, the general solution is,

$$u(x, t) = \sum [C_1 e^{i\omega ax} + C_2 e^{-i\omega ax}] e^{i\omega t} = \sum C_1 e^{i\omega(ax+t)} + \sum C_2 e^{-i\omega(ax-t)} \quad (3)$$

which corresponds to the initial disturbance moving to the left and right, respectively. The phase speed is constant.

$$c = \frac{x}{t} = \frac{1}{a} = \frac{\omega}{k} \quad (4)$$

A signal whose frequency components travel with constant phase speed is called a nondispersive signal. The nondispersive signal maintains its shape as it moves.

Consider the differential equation of motion of an Euler beam,

$$\frac{\partial^4 u}{\partial x^4} + \frac{\rho A}{EI} \frac{\partial^2 u}{\partial t^2} = 0 \quad (5)$$

where u is transverse displacement, ρ is mass density, A is cross section area, E is Young's modulus, and I is moment of inertia. Assume $Ce^{i(kx + \omega t)}$ is a solution of the wave equation. Substituting in eq. 5, we obtain,

$$[k^4 - \omega^2 a^4] C = 0 \quad (6)$$

$$k = \pm a\sqrt{\omega} \quad \text{or} \quad \pm ia\sqrt{\omega}$$

where,

$$a = \sqrt[4]{\frac{\rho A}{EI}} \quad (7)$$

and the phase speed is given by

$$c = \frac{\omega}{k} = \frac{1}{a} \sqrt{\omega} \quad (8)$$

The phase speed depends on the frequency. The original signal distorts as it travels because the frequency component of the signal travels with different phase speeds. The signal is considered dispersive when its phase speed is not constant with respect to frequency.

5.2 Moving Window Approach

If the arrival time difference between frequency components is known, the dispersive distance can be obtained by utilizing the phase speeds of frequency components and the arrival time differences. The information about the relation between frequencies and arrival times can not be obtained by using the power spectrum analysis of the dispersive signal. However, if the signal is divided into small windows, the power spectrum of each small window differs from other small windows. Small time windows can be overlapping or adjacent. The time difference between windows in conjunction with the information about the variation of the power spectrum can be utilized to estimate the arrival time difference between distinct frequency components of the signal.

Let us consider a flexural signal in a Euler beam. The frequency components ω_n and ω_{n+1} arrives at the sensor location at t_n and t_{n+1} , respectively. The location of the origin of the signal can be obtained by using eq. 8.

$$x = \frac{1}{a} \sqrt{\omega_n} t_n \quad x = \frac{1}{a} \sqrt{\omega_{n+1}} t_{n+1}$$

$$x = \frac{\Delta t}{a \left(\frac{1}{\sqrt{\omega_n}} - \frac{1}{\sqrt{\omega_{n+1}}} \right)} \quad (9)$$

Where, $\Delta t = t_{n+1} - t_n$. Only the time difference between the arrival of two frequency components is sufficient for estimating the origin of the signal, as it is evident from eq. 9. The relative arrival time of a frequency component with respect to the other frequency components is estimated by comparing the amplitude of the power spectrum of the component in all the windows. The frequency component is assumed to arrive in the window in which its amplitude attains the pre-set level for the first time. Therefore, the time difference between windows plays an important role in estimating the origin of the signal. The minimum time difference between the non-overlap-

ping windows is the window size. The arrival time difference between frequency components could be small compared to the window size. The only way to reduce the time difference between the non-overlapping windows is to reduce the window size. If the window size is reduced, the bias of the power spectrum increases and this reduces the accuracy. On the other hand, the time difference between the overlapping windows can be reduced by increasing the overlap-time. The window size remains the same, so the bias of the power spectrum does not increase.

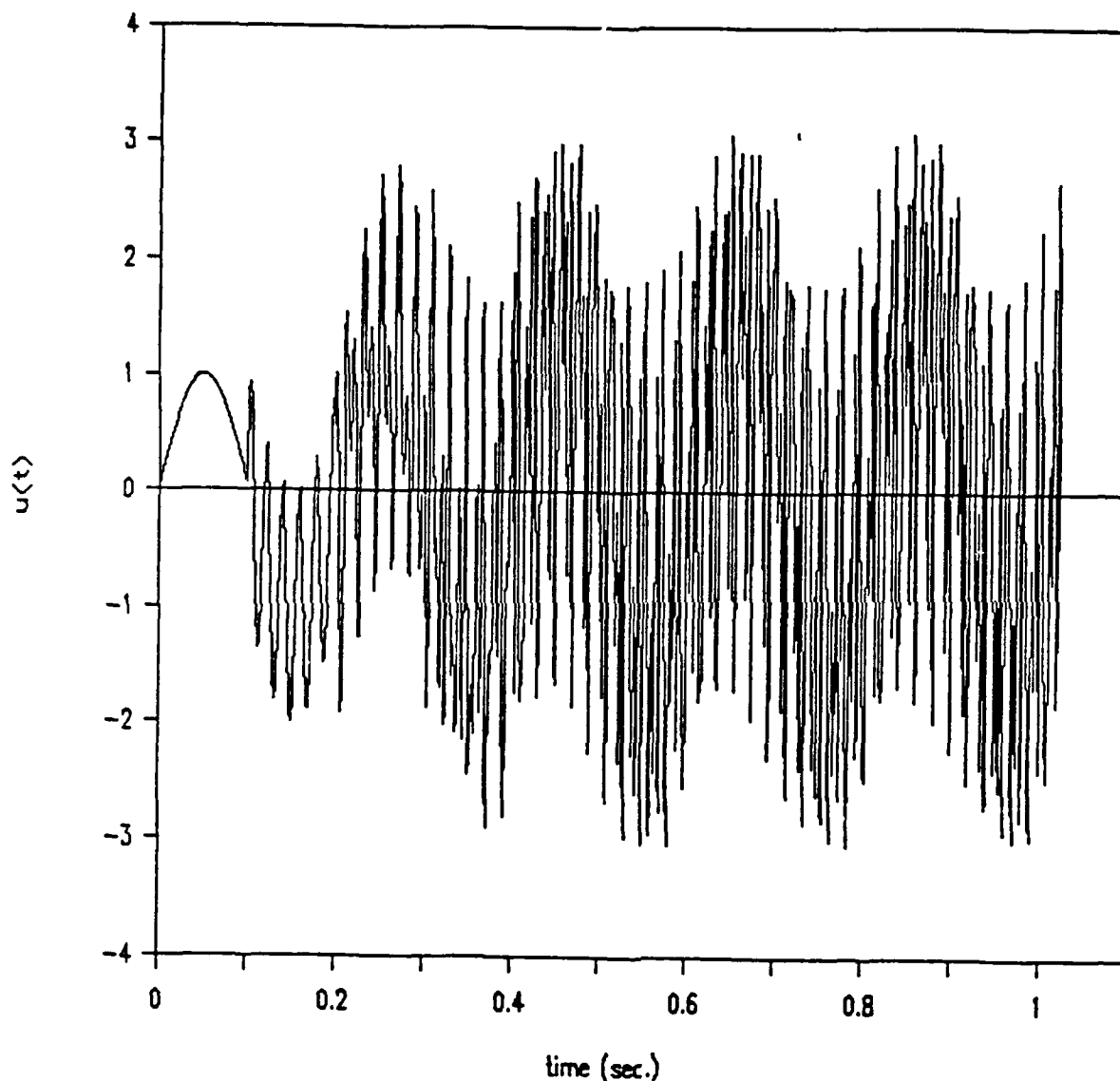


FIGURE 5.1 Artificial Dispersive signal

Figure 5.1 shows a hypothetical dispersive signal. A higher frequency sine wave is superimposed on lower frequency sine waves after every 0.1 sec. time interval. This simulates the arrival time difference of 0.1 sec. between frequency components. 200 points (0.2 sec.) of the signal shown in Figure 5.1 are taken for each small window. In order to increase the resolution of the power spectrum of the windows, 200 data points are appended by zeros up to 1024 points in each small window. These data are multiplied by Dolph-Chebyshev data windows and then the power spectra are estimated for each window. The overlap-time is 0.175 sec. Therefore, the time difference between the overlapping windows is 0.025 second.

The power spectra of the small overlapping windows are shown in Figures 5.2 to 5.7. The amplitude of the second frequency component attains -5 db (preset level) in the second window

shown in Figure 5. 2. The amplitude of the third frequency component attains the pre-set level in the sixth window shown in Figure 5. 7. The arrival time difference between two consecutive frequency components is the time difference between four consecutive windows that is 0.1 sec. This is an accurate estimate of the arrival time difference used in constructing the signal. The distance from the origin of the pulse to the recording point can be calculated by using the dispersion relation for the medium.

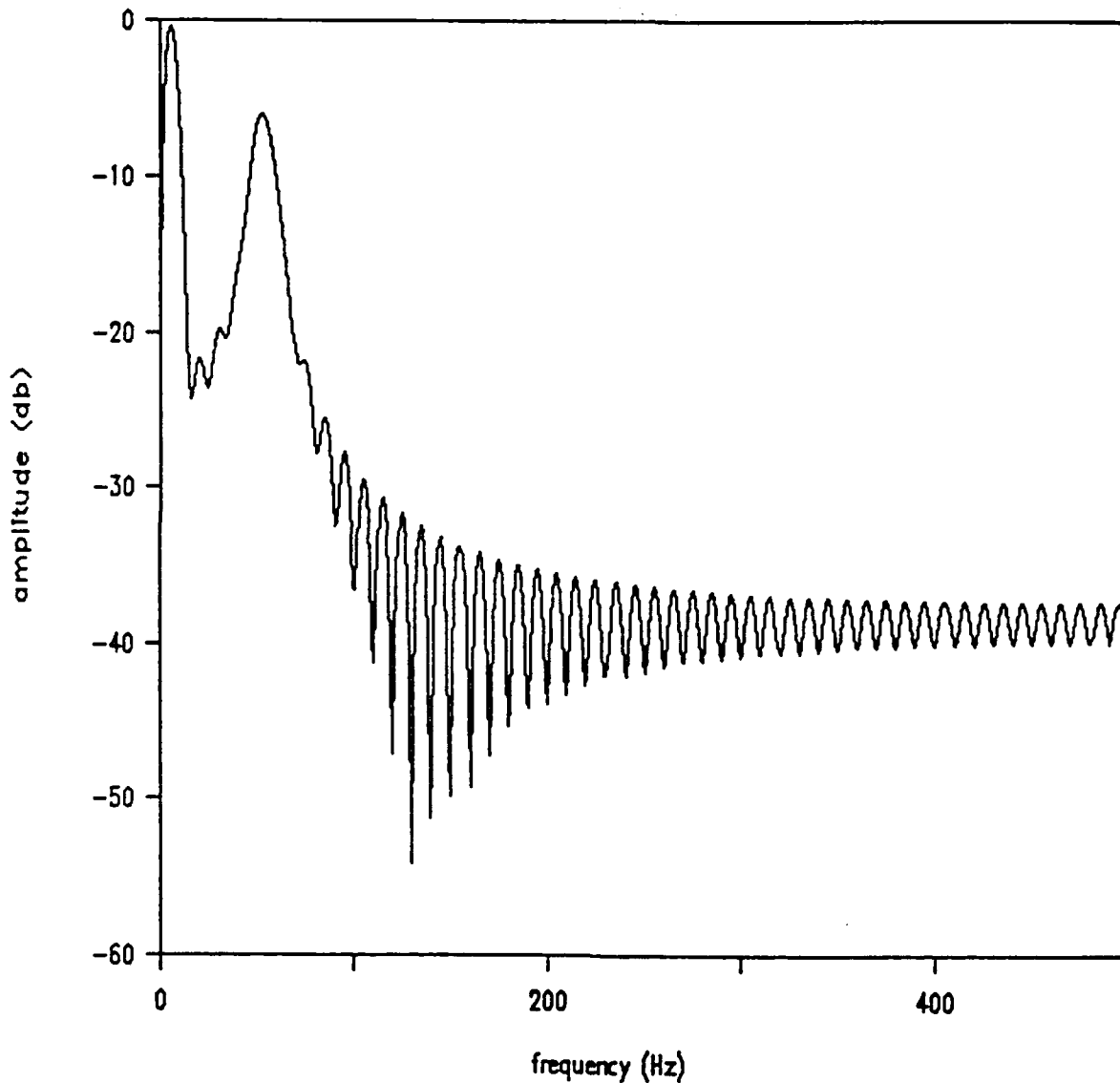


FIGURE 5. 2 The first overlapping window (0-200 point of the artificial dispersive signal)

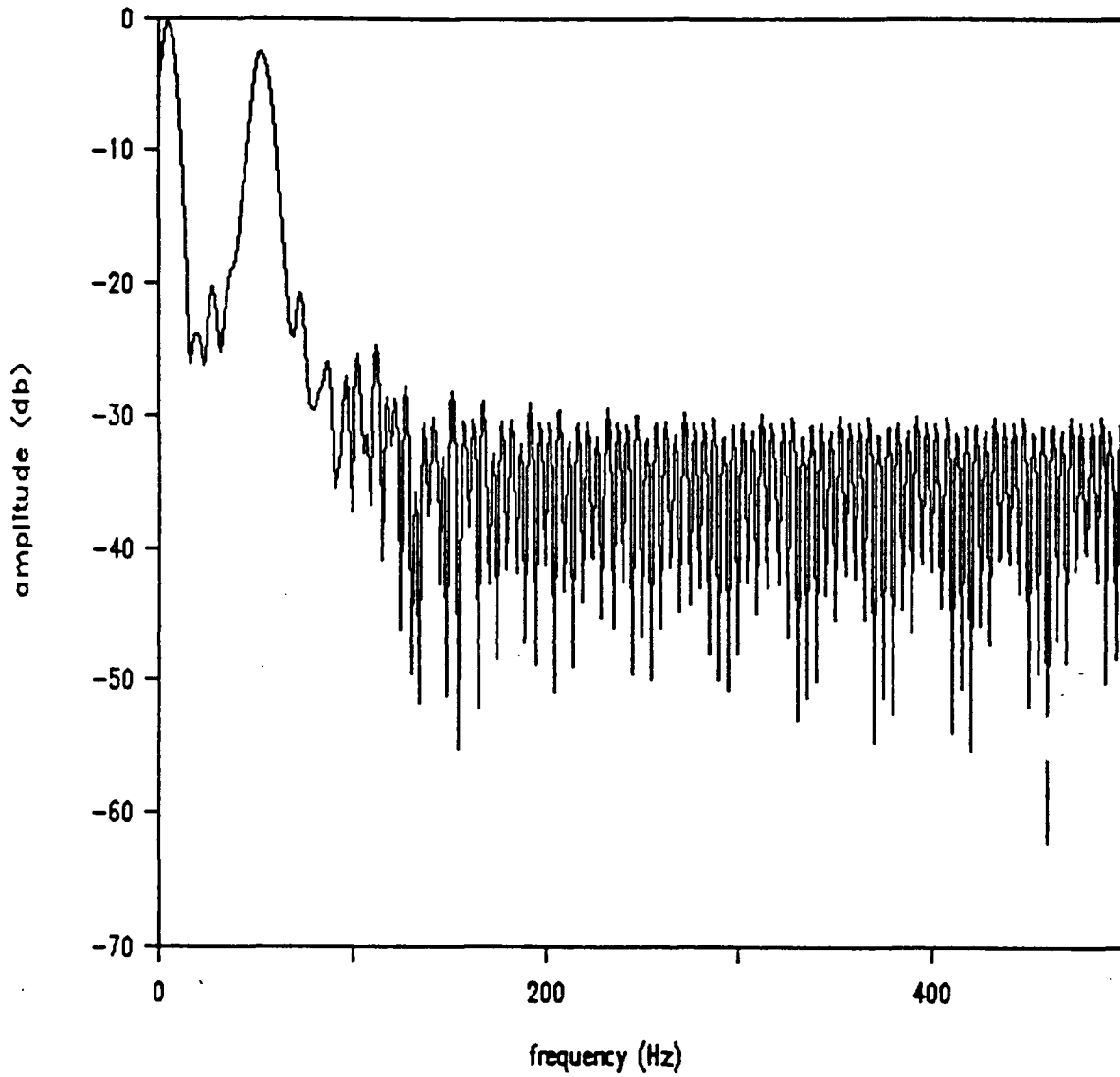


FIGURE 5.3 The second overlapping window (25-225 point of the artificial dispersive signal)

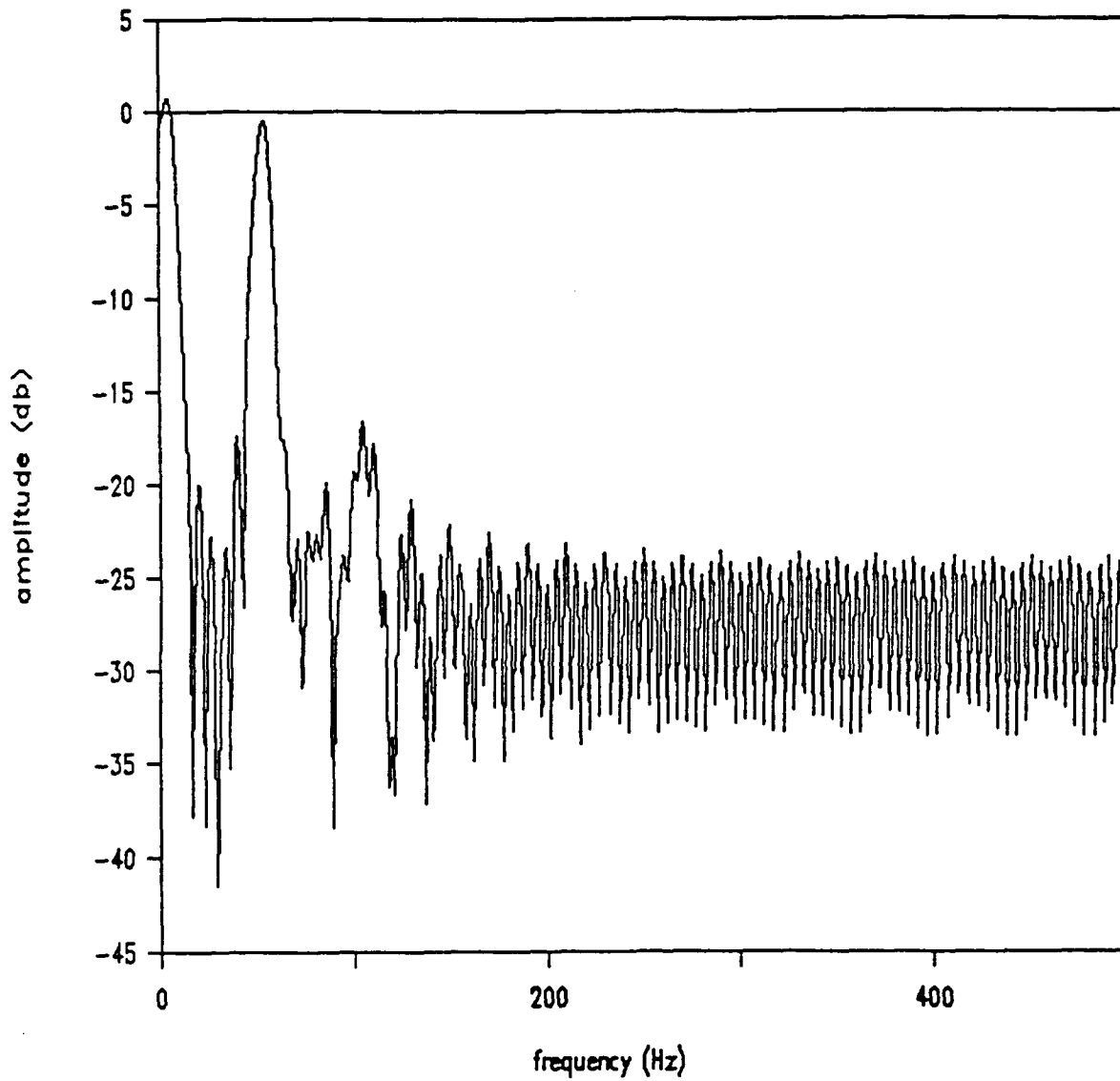


FIGURE 5.4 The third overlapping window (50-250 point of the artificial dispersive signal)

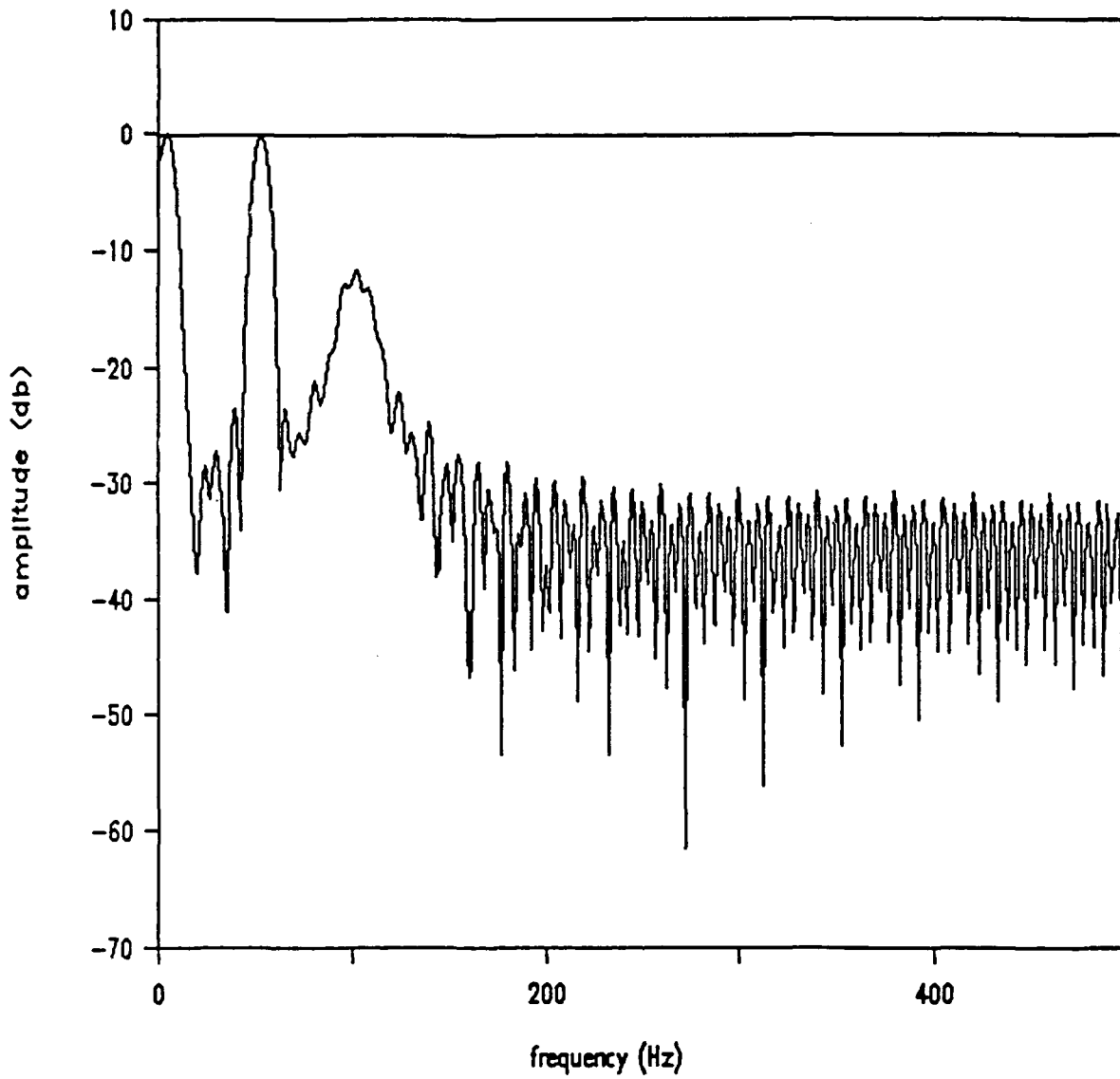


FIGURE 5.5 The fourth overlapping window (75-275 point of the artificial dispersive signal)

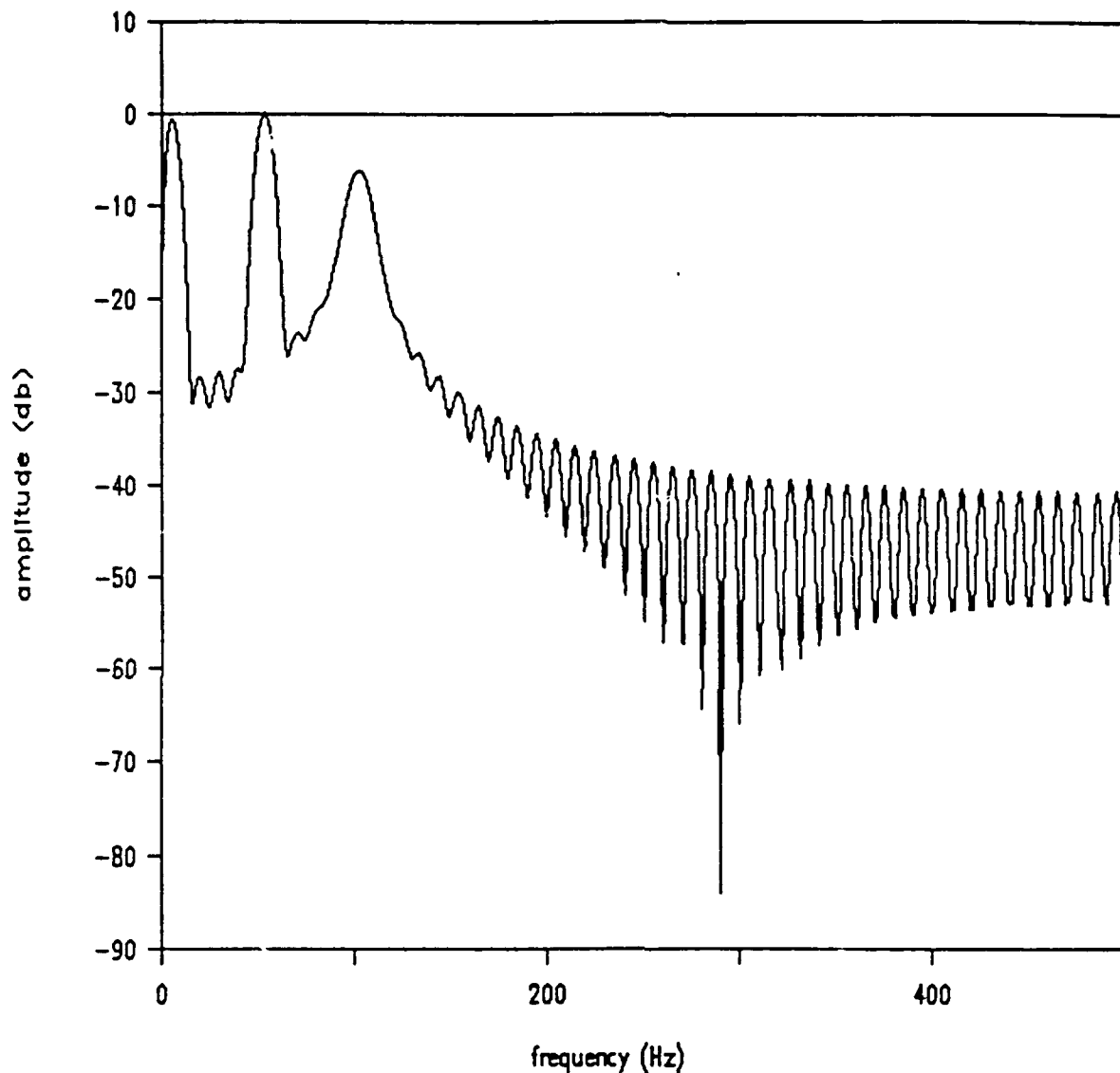


FIGURE 5.6 The fifth overlapping window (100-300 point of the artificial dispersive signal)

5.3 Phase Difference Approach

This method is based on the technique presented by Doyle (1987). The relationship between the phase and the distance from the origin is utilized in this method. Fourier transform of signals can be obtained easily by using a FFT algorithm. The phase of the signal is deduced from the transform signal. In the case of a Bernoulli-Euler beam, the relation between the phase and the position is expressed as:

$$\begin{aligned}\phi_n &= \phi_{0n} + \theta_n - k_n x \\ C_n e^{i\phi_n} &= C_{0n} e^{i\phi_{0n}} [D_n e^{i\theta_n}] e^{-ik_n x} = k_n^2 A_n [1 + i e^{ik_n x} e^{-k_n x}] e^{-ik_n x}\end{aligned}\quad (10)$$

where ϕ_n is the phase of the n th frequency component of the strain signal, ϕ_{0n} is the initial phase and θ_n is phase of the spatially damped vibration mode. Signals from two locations are used to eliminate the initial phase. The distance between the recording points and the origin of the signal can be deduced from eq. 1.

$$\begin{aligned}x_1 + x_2 &= L \\ x_1 &= \frac{L}{2} - \frac{1}{2} \frac{d}{dk_n} [(\phi_{1n} - \phi_{2n}) - (\theta_{1n} - \theta_{2n})] \\ x_2 &= \frac{L}{2} + \frac{1}{2} \frac{d}{dk_n} [(\phi_{1n} - \phi_{2n}) - (\theta_{1n} - \theta_{2n})]\end{aligned}\quad (11)$$

Where L is the absolute spacing between the recording points. A good estimate is obtained for θ by assuming a x . An iterative scheme is used to improve the guess for the signal origin by improving the estimate of θ at every iteration step.

5.4 Reconstruction Approach

This method is based on the technique presented by Whiston (1984). First an estimate of the impact point is obtained by the arrival time difference between the maximum frequency and the minimum frequency. This estimate is refined successively until the reconstructed signal has no significant negative portions. Timoshenko beam theory is utilized in this method. The high frequency components of the signal arrive first followed by the lower frequency components. Because phase speed $c(\omega)$ asymptotes to c_s , the highest phase speed is assumed as c_s and the lowest is assumed as $c(\omega_0)$.

$$t_s = \frac{x}{c_s} \quad t_{\omega_0} = \frac{x}{\omega_0} \quad (12)$$

Where t_s is the arrival time for the maximum frequency component and t_{ω_0} is the arrival time for the chosen minimum frequency component.

$$\tau_1 = t_{\omega_0} - t_s \quad (13)$$

Where τ_1 is the arrival time difference between the maximum frequency and the minimum frequency. The distance of the origin of the impact point x is expressed as

$$x = \frac{\tau_1 c_s c(\omega_0)}{c_s - c(\omega_0)} \quad (14)$$

This initial estimate is successively refined to get a single impact pulse at the origin.

An impact force is assumed as a concentrated force at the point x_0 : i.e.,

$$f(x, t) = N(t) \delta(x - x_0) \quad (15)$$

where δ denotes the Dirac Delta function and $N(t)$ denotes an arbitrary impact force-time history. It follows that

$$\hat{f}^*(k, \omega) = \frac{\bar{N}(\omega) e^{-ikx_0}}{(2\pi)^{1/2}} \quad (16)$$

The expression of \bar{N} can be written in terms of \bar{A} [5],

$$\bar{N}(\omega) = T(x, \omega) \bar{A}(x, \omega) \quad (17)$$

where $T(x, \omega)$ is the spectral transfer function at distance x away from the origin of the impact force, $\bar{A}(x, \omega)$ is the transfer function of the acceleration field $A(x, t) = \frac{\partial^2 v(x, t)}{\partial t^2}$ at distance x away from the origin of the impact force.

If the distance of the origin is known, equations (15-17) can be used to reconstruct the impact force. The formulation for obtaining the transfer function and estimating the distance of the impact point from the recording point is presented for the case of a transverse impact of a beam. Timoshenko beam theory is utilized for this purpose.

The equation of motion for the Timoshenko beam is:

$$c_0^2 \frac{\partial^4 v}{\partial x^4} - \left(\frac{c_0^2}{c_s^2} + 1 \right) \frac{\partial^4 v}{\partial x^2 \partial t^2} + \frac{A}{I} \frac{\partial^2 v}{\partial t^2} + \frac{1}{c_s^2} \frac{\partial^4 v}{\partial t^4} = \frac{f}{\rho I} - \frac{c_0^2}{\gamma A G} \frac{\partial^2 f}{\partial x^2} + \frac{1}{\gamma A G} \frac{\partial^2 f}{\partial t^2} \quad (18)$$

where γ is a constant describing the distribution of shear force across a cross-section, I is moment of inertia, ρ is mass density, E is Young's modulus, G is shear modulus, A is cross section area. c_0 and c_s are defined as $\left(\frac{E}{\rho}\right)^{1/2}$ and $\left(\frac{\gamma G}{\rho}\right)^{1/2}$, respectively. Taking successive Fourier transform of eq. 18 to the frequency domain and then to wavenumber domain, we obtain,

$$\left\{ c_0^2 k^4 - \left(\frac{c_0^2}{c_s^2} + 1 \right) \omega^2 k^2 - \frac{A \omega^2}{I} + \frac{\omega^4}{c_s^2} \right\} \bar{v}^* = \left\{ \frac{1}{\rho I} + \frac{c_0^2 k^2 - \omega^2}{\gamma A G} \right\} \bar{f}^* \quad (19)$$

where

$$\begin{aligned} \bar{v}^*(k, \omega) &= (2\pi)^{1/2} \int_{-\infty}^{\infty} \left[(2\pi)^{1/2} \int_{-\infty}^{\infty} v(x, t) e^{-i\omega t} dt \right] e^{-ikx} dx \\ \bar{f}^*(k, \omega) &= (2\pi)^{1/2} \int_{-\infty}^{\infty} \left[(2\pi)^{1/2} \int_{-\infty}^{\infty} f(x, t) e^{-i\omega t} dt \right] e^{-ikx} dx \end{aligned} \quad (20)$$

Eq. 21 yields a particular solution for $\bar{v}(x, \omega)$ by taking inverse Fourier transform of eq. 19.

$$\bar{v}(x, \omega) = (2\pi)^{-1/2} \int_{-\infty}^{\infty} \frac{\left\{ \frac{1}{\rho I} + \frac{c_0^2 k^2 - \omega^2}{\gamma A G} \right\} \bar{f}^*(k, \omega) e^{ikx} dk}{\left\{ c_0^2 k^4 - \left(\frac{c_0^2}{c_s^2} + 1 \right) \omega^2 k^2 - \frac{A \omega^2}{I} + \frac{\omega^4}{c_s^2} \right\}} \quad (21)$$

Substituting eq. 16 into eq. 21 yields,

$$\bar{v}(x, \omega) = \frac{\bar{N}(\omega)}{2\pi} \int_{-\infty}^{\infty} \frac{\left\{ \frac{1}{\rho I} + \frac{c_0^2 k^2 - \omega^2}{\gamma A G} \right\} e^{ik(x-x_0)} dk}{\left\{ c_0^2 k^4 - \left(\frac{c_0^2}{c_s^2} + 1 \right) \omega^2 k^2 - \frac{A \omega^2}{I} + \frac{\omega^4}{c_s^2} \right\}} \quad (22)$$

performing integration by the method of residues, yields,

$$\bar{v}(x, \omega) = \frac{\bar{N}(\omega)}{c_0^2} \left[\frac{1}{2k_*} \frac{c_0^2 k_*^2 - \omega^2}{\gamma A G} e^{-ik_* |x-x_0|} + \frac{1}{2k_+} \frac{c_0^2 k_+^2 - \omega^2}{\gamma A G} e^{-ik_+ |x-x_0|} \right] \quad (23)$$

where

$$k_{\pm}^2(\omega) = \frac{\omega^2 \left\{ (c_0^2 + c_s^2) \pm \left[(c_0^2 + c_s^2)^2 + \frac{4Ac_0^2c_s^2}{I\omega^2} \right]^{1/2} \right\}}{2c_0^2c_s^2} \quad (24)$$

Eq. 23 is inverted to obtain an expression for \bar{N} in terms of $\bar{v}(x, \omega)$. In some cases, it may be useful to replace the displacement field $\bar{v}(x, \omega)$ by the acceleration field. Substituting the Fourier transform of $A(x, t)$ in eq. 17 and comparing with eq. 23, the expression for $T(x, \omega)$ is written as,

$$T(x, \omega) = \frac{-\left(\frac{c_0^2}{i\omega^2}\right)}{\left[\frac{\frac{1}{\rho I} + \frac{c_0^2k_+^2 - \omega^2}{\gamma AG}}{2k_+(k_-^2 - k_+^2)} e^{-ik_+|x-x_0|} + \frac{\frac{1}{\rho I} + \frac{c_0^2k_-^2 - \omega^2}{\gamma AG}}{2k_+(k_-^2 - k_+^2)} e^{-ik_-|x-x_0|} \right]} \quad (25)$$

In practice the k_- can be neglected if $|x-x_0| \geq 0.1$ m, so the expression for $T(x, \omega)$ is simplified as,

$$T'(x, \omega) = \left\{ \frac{2ic_0k_+(k_-^2 - k_+^2)}{\left[\frac{1}{\rho I} + \frac{c_0^2k_+^2 - \omega^2}{\gamma AG} \right] \omega^2} \right\} e^{ik_+|x-x_0|} \quad (26)$$

5.5 Computer Simulations

The impact force $f(t)$ for the purpose of simulation is given by the eq. 27,

$$f(t) = \begin{cases} \frac{16P(t-t_1)^2(t-\tau)^2}{\tau^4} & t_1 \leq t \leq \tau + t_1 \\ 0 & \text{otherwise} \end{cases} \quad (27)$$

where P defines the peak value and τ is the duration of the applied force. t_1 is defined as the time by which the signal is shifted to the right in the window. The impact force history is calculated for the following values of the parameters.

$$P = 1 \text{ KN}$$

$$\tau = 625 \mu\text{s}$$

$$t_1 = 800 \Delta t$$

The dispersive signal at 20cm and 40cm from the impact point is obtained by using the Euler beam dispersive relationship. Each dispersive signal is transformed by using a 4096 point FFT. The total sampling time used is 40 ms. The Δt is total sampling time divided by 4096. This gives a Nyquist frequency of 51.2 KHz.

5.5.1 Moving Window Simulation

The moving window approach is described in section 5.2 with the help of an artificially constructed dispersive signal with a few discrete frequency components. The real dispersive signal has a continuous frequency spectrum. The area under a function is equal to the value of its Fourier transform at the origin. The zero frequency has significant magnitude in the power spectra if the area under the function is non-zero. The area under the function in the small windows are not zero. In order to avoid the maximum amplitude in the power spectra occurring at zero frequency, the function is modified according to the following equation:

$$u(t_n) = u(t_n) - \frac{\sum u(t_n)}{t_n} \quad (28)$$

Small windows cut the signal abruptly. This introduces spurious high frequency components in the power spectrum of the small windowed signal due to the Gibbs' phenomenon (Chen, 1979). This causes the difficulty in estimating the arrival time difference between windows. The power spectrums of small overlapping windows is shown in Figures 5.7 to 5.9. It is difficult to obtain unambiguous information from these Figures. It appears that the moving window approach may be applicable to signals which are highly dispersive. In the present case, if the signal has travelled long enough distance, the moving window approach may distinguish between the arrival time between frequency components.

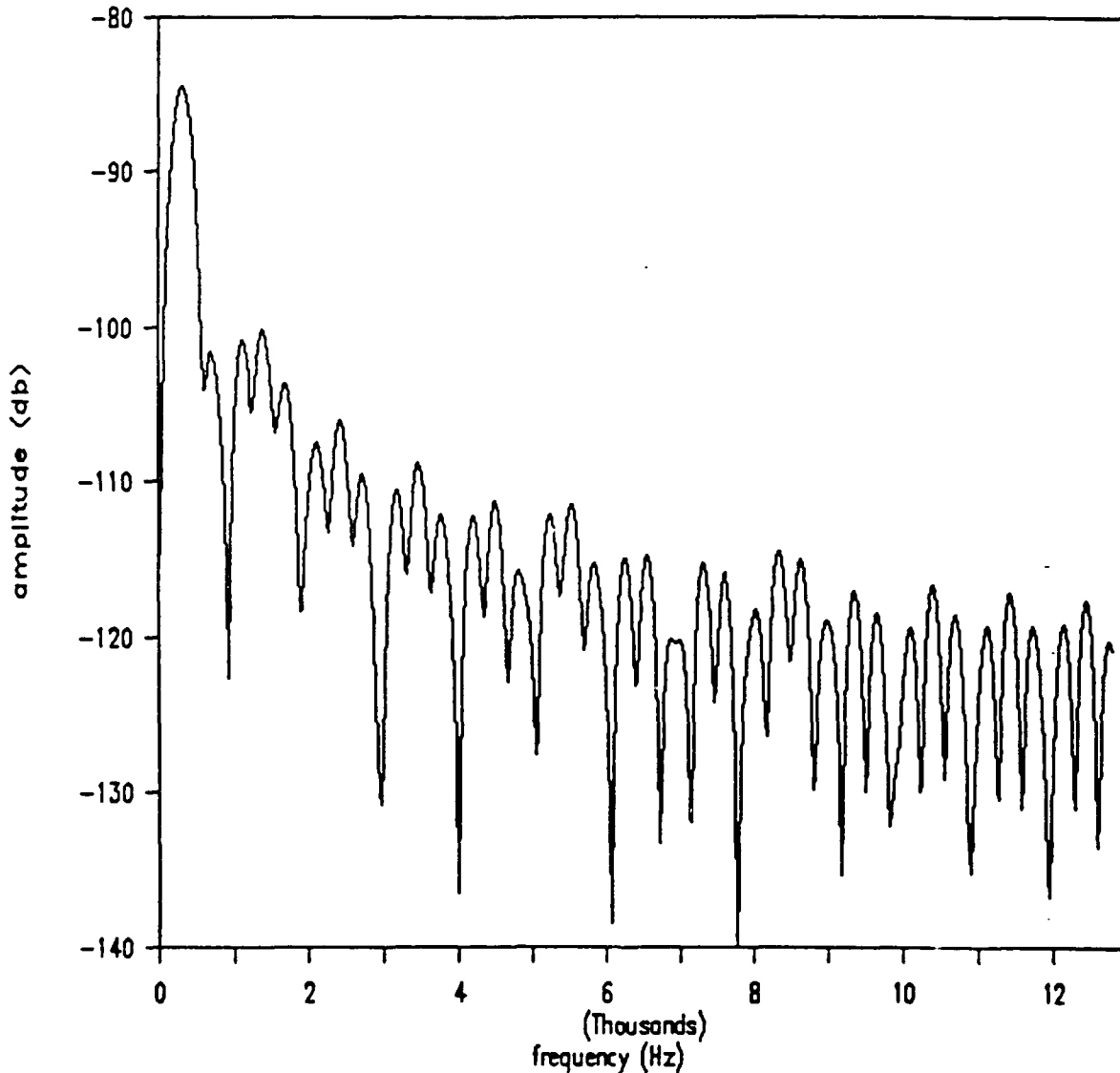


FIGURE 5.7 The first window of the moving window approach (0-400 points)

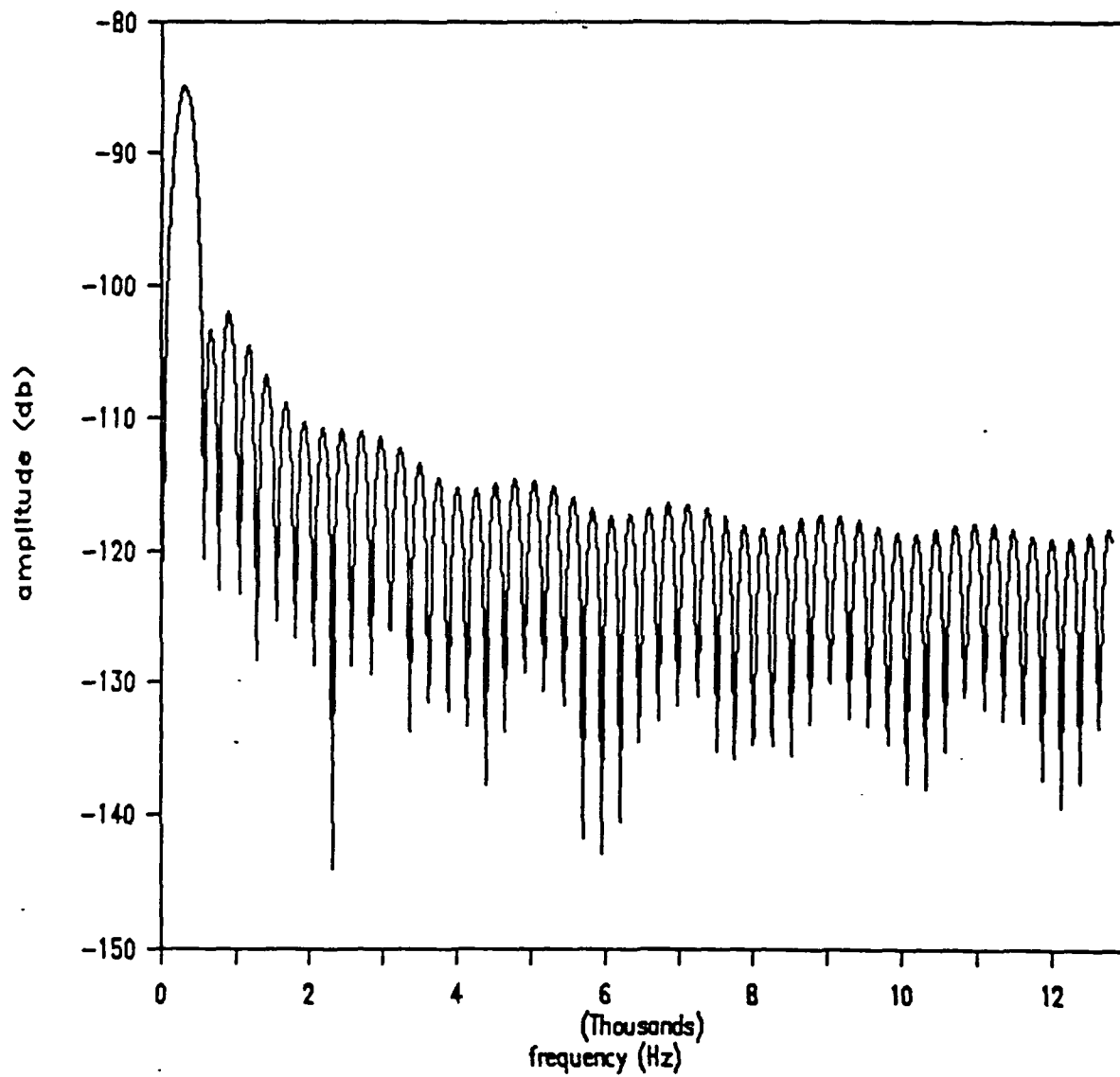


FIGURE 5.8 The second window of the moving window approach (50-450 points)

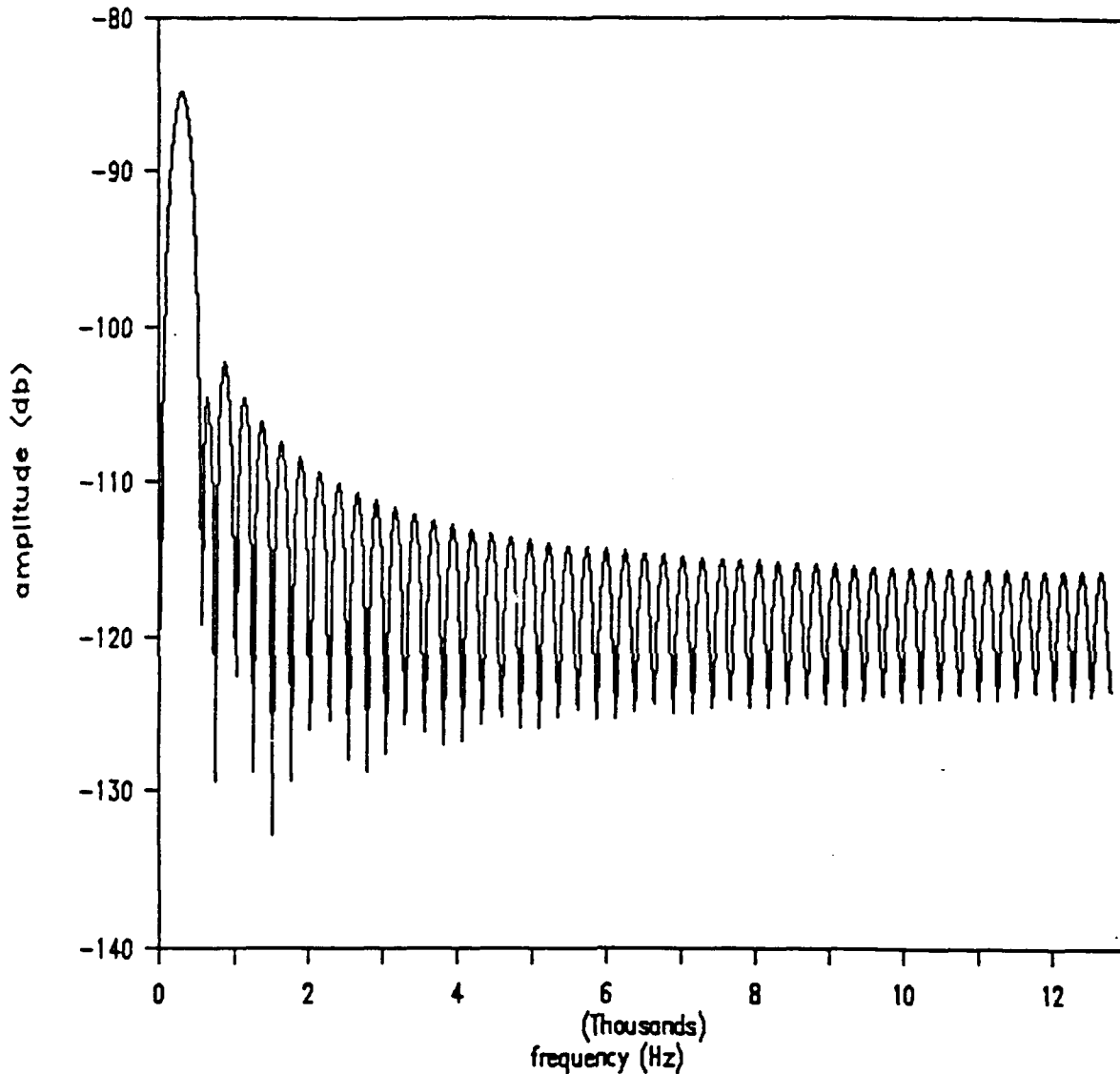


FIGURE 5.9 The third window of the moving window approach (100-500 points)

5.5.2 Phase Difference Simulation

The dispersive signal at two locations, as required in this method, is numerically obtained by taking FFT of impact force (eq. 27) and substituting in the following equation.

$$e(x, t) = \sum \frac{F_n h}{8EI k_n} [ie^{-ik_n x} - e^{-k_n x}] e^{i\omega_n t} \quad (29)$$

This simulates recorded strain history due to the impact force given by eq. 27. The phase ϕ_n at two locations are obtained by taking FFT of the recorded signals. The first guess of the origin of the impact point is chosen to be in the middle of the two recording locations. θ_n s are obtained by eq. 10. θ_n and ϕ_n are substituted into eq. 11 for every frequency component. The moving average

method is used to take the derivatives in eq. 2. The distance x_1 and x_2 is never greater than the total distance L because the impact is assumed to be in between the two recording points. Therefore, all frequencies where the estimate of the distance exceeds L are not considered in calculating the average values of x_1 and x_2 . Figure 5. 10 shows the estimates of location of the impact point after two iterations. The exact locations of the recording points from the impact location are 0.2 m and 0.46 m, respectively. The accurate position of the impact point can be obtained accurately after two or three iterations. Once the position is known, the pulse can be determined by the force-strain relationships given by eq. 29.

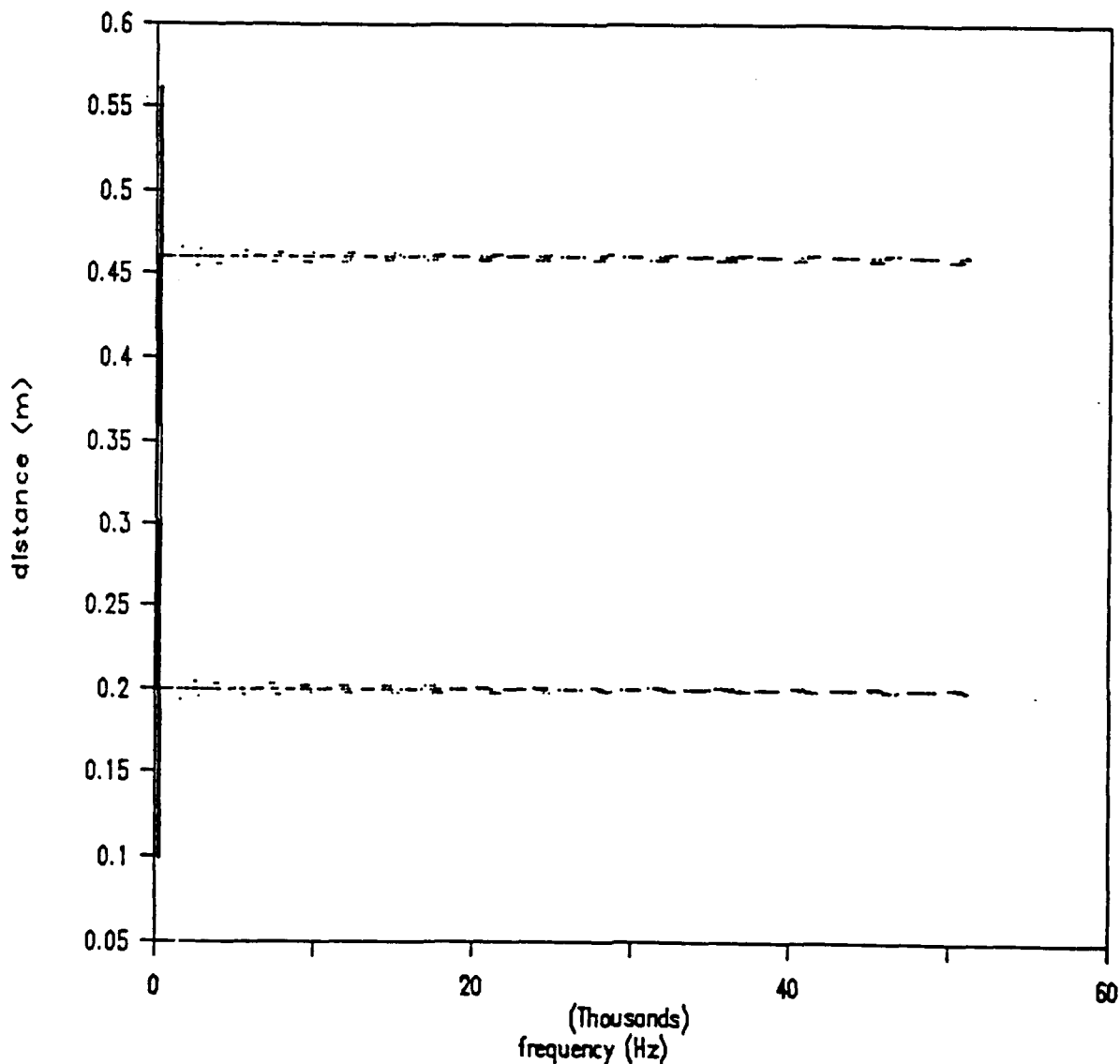


FIGURE 5. 10 Estimates of the impact point after the second iteration of the phase difference method

5.5.3 Reconstruction Simulation

As described in section 5.4, the minimum frequency and the percentage of the maximum amplitude of the signal must be chosen to determine τ_1 (eq. 13). Two hundred fifty hertz and five percent of the maximum signal are chosen to calculate τ_1 . The arrival time difference between the maximum and minimum frequency components is estimated as the time between the transient rising to 5% of the maximum amplitude of the signal and then permanently falling down below 5%.

The first guess of the distance x is made by using eq. 14. The minimum frequency is assumed to be 250 Hz. The distance x is used to reconstruct the signal at the first estimate of the origin. The reconstructed signal should be all positive. If the distance is not accurate, the reconstructed signal will not be all positive. The iterative scheme is adopted to refine the estimate of the origin.

The distance x will be under or over estimated during the iterative procedure. There are three rules provided to determine the under and over estimation of the distance. In the first rule, the numbers of local extrema before and after the absolute extremum are evaluated first. If the number of local extrema before the absolute extremum is greater than the number of local extrema after the absolute extremum then the distance is under estimated. If the number of local extrema before the absolute extremum is smaller than the number of local extrema after the absolute extremum then the distance is over estimated. If the number of local extrema before the absolute extremum is equal to the number of local extrema after the absolute extremum then the other two rules are activated.

The second rule is used when the numbers of local extremum on both sides of the absolute extremum are equal. If the value of the before the absolute extremum is greater than the value of the local extremum after the absolute extremum then the distance is under estimated, otherwise it is over estimated.

The third rule applies when a constructed signal contains only one extremum which means the accurate estimate of the origin of the impact is made. The iterative procedure is terminated in this case.

The percentage of the maximum amplitude of the dispersive signal used for estimating τ_1 is varied from the chosen 5% to bracket the distance estimate. Two consecutive percentages which give an over estimate and an under estimate are obtained and then successively the difference between the two estimated distances is reduced during the iteration procedure. The difference between the over estimate and the underestimate is reduced in half during each iteration. The number of the local extrema left of the absolute extremum is greater than the number of the local extrema on the right in Figure 5. 11 which shows a signal at an under estimated distance. Figure 5. 12 shows the signal at the overestimated distance. These signals are obtained by using 4% and 3% of the maximum amplitude of the dispersive signal, respectively. Therefore, the distance is between 0.143 m and 0.29 m. After some iterations, the under estimate and the overestimate are very close to the exact value. Figure 5. 13 shows the results of the under estimate after the sixth iteration where the distance is 0.1989 m. Figure 5. 14 shows the results of the over estimate after the seventh iteration where the distance is 0.208 m. After the seventh iteration, the exact distance is bracketed between 0.1989 m and 0.208 m. Figure 5. 15 shows the results after the final iteration. The iterative procedure is terminated by the use of the third rule.

5.6 Conclusions

Three different methods are described to accurately locate the origin of a dispersive signal in space and time. The moving window approach is suitable for a highly dispersive signal. The basic problem arises because of the slow dispersion of the signal. This approach can not be used in case of a transverse impact of a finite structure member. The phase difference approach can accurately locate the position of the origin of the dispersive signal. The moving window approach and the reconstruction approach use the arrival time difference between frequency components. The limited exploratory examples suggest that the phase difference method is suitable for the intended application of obtaining the impact location in a small structure.

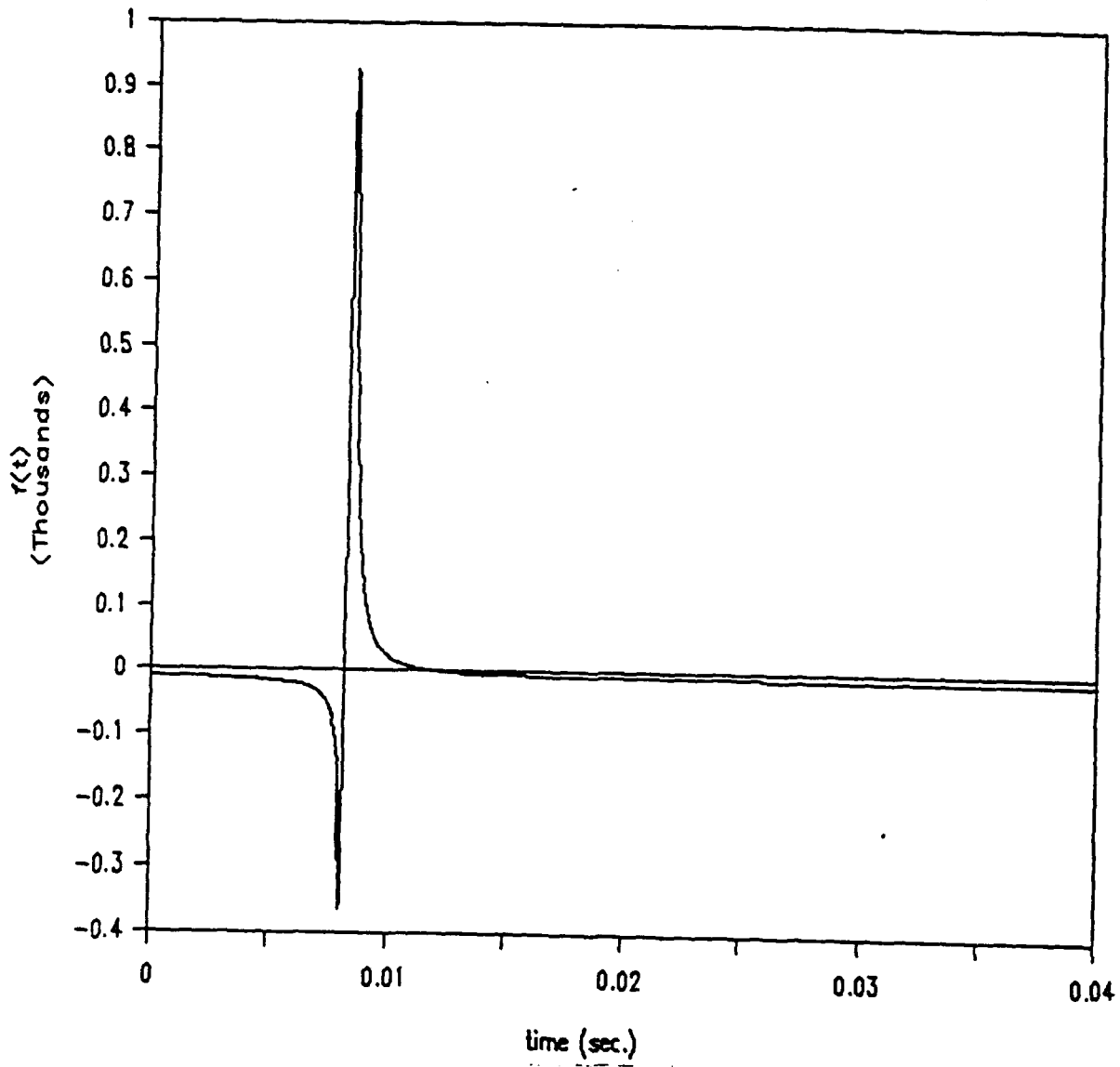


FIGURE 5. 11 Underestimate at $\epsilon = 143$ m (exact $x = 0.2$ m)

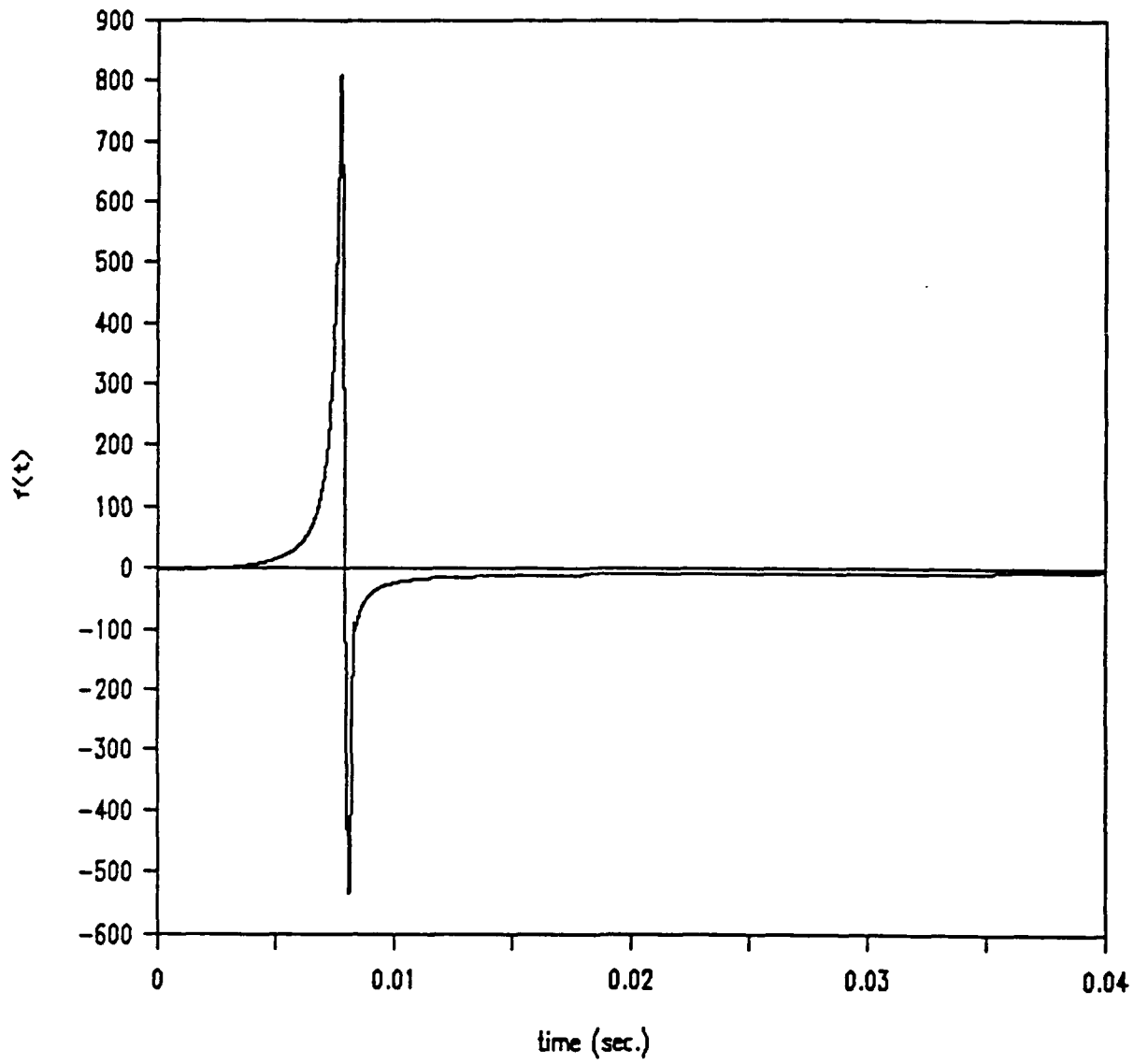


Figure 27 Overestimate $x=0.29$ m (exact $x= 0.2$ m)

FIGURE 5. 12 Overestimate at $x=0.29$ m (exact $x=0.2$ m)

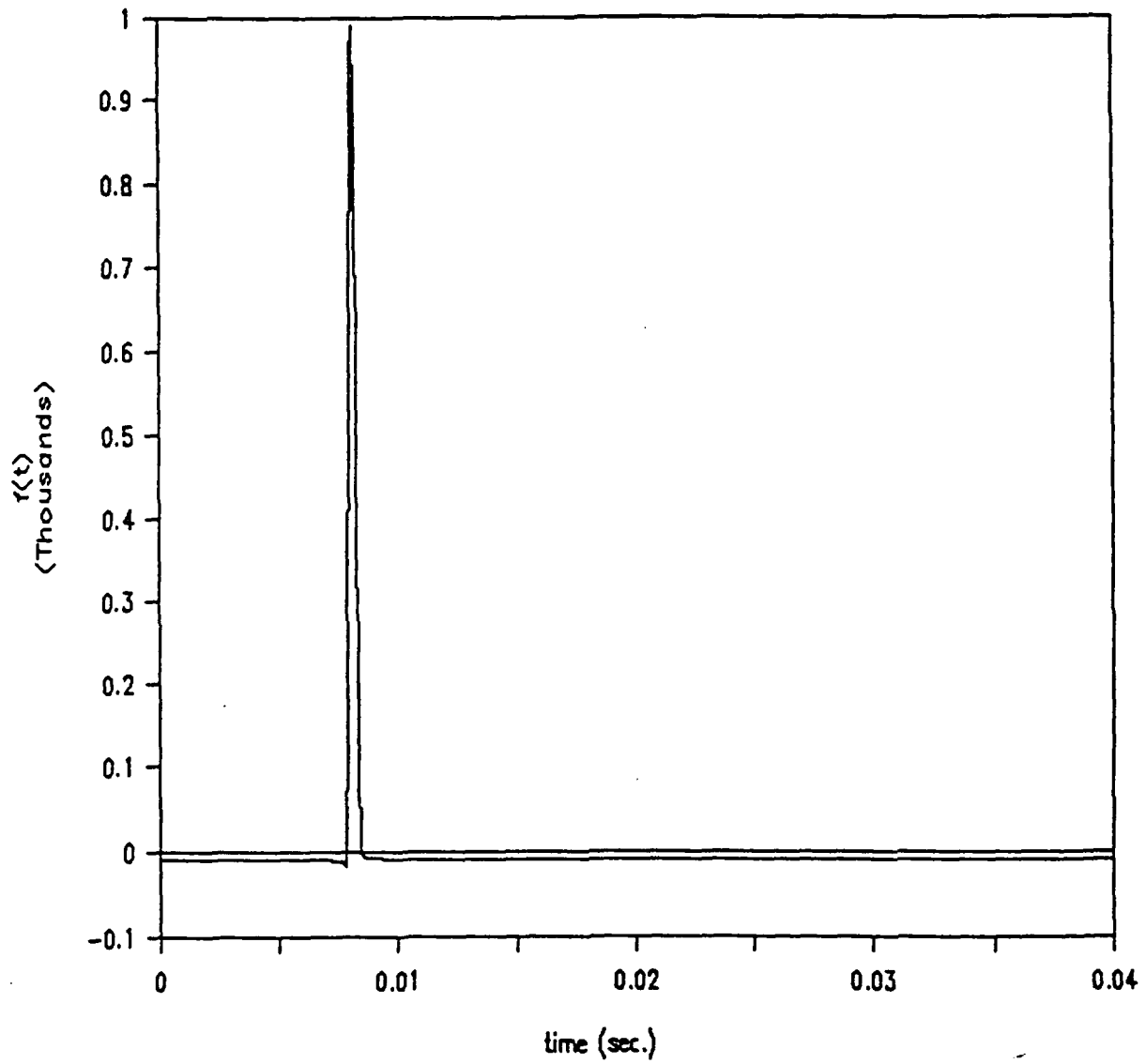


FIGURE 5.13 Underestimate at $x=0.1989$ (exact $x=0.2$ m)

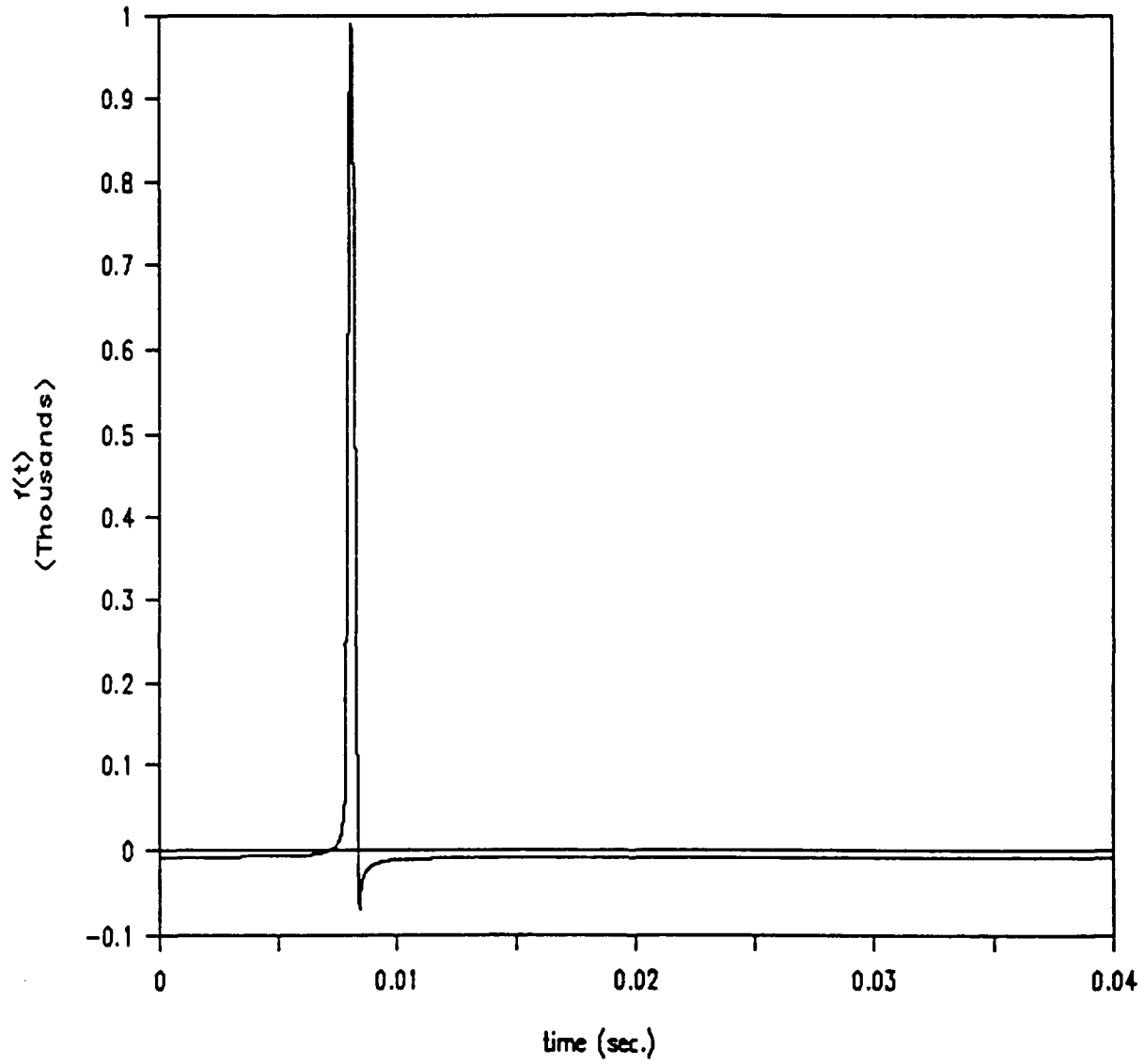


FIGURE 5.14 Overestimate at $x=0.208$ m (exact $x=0.2$ m)

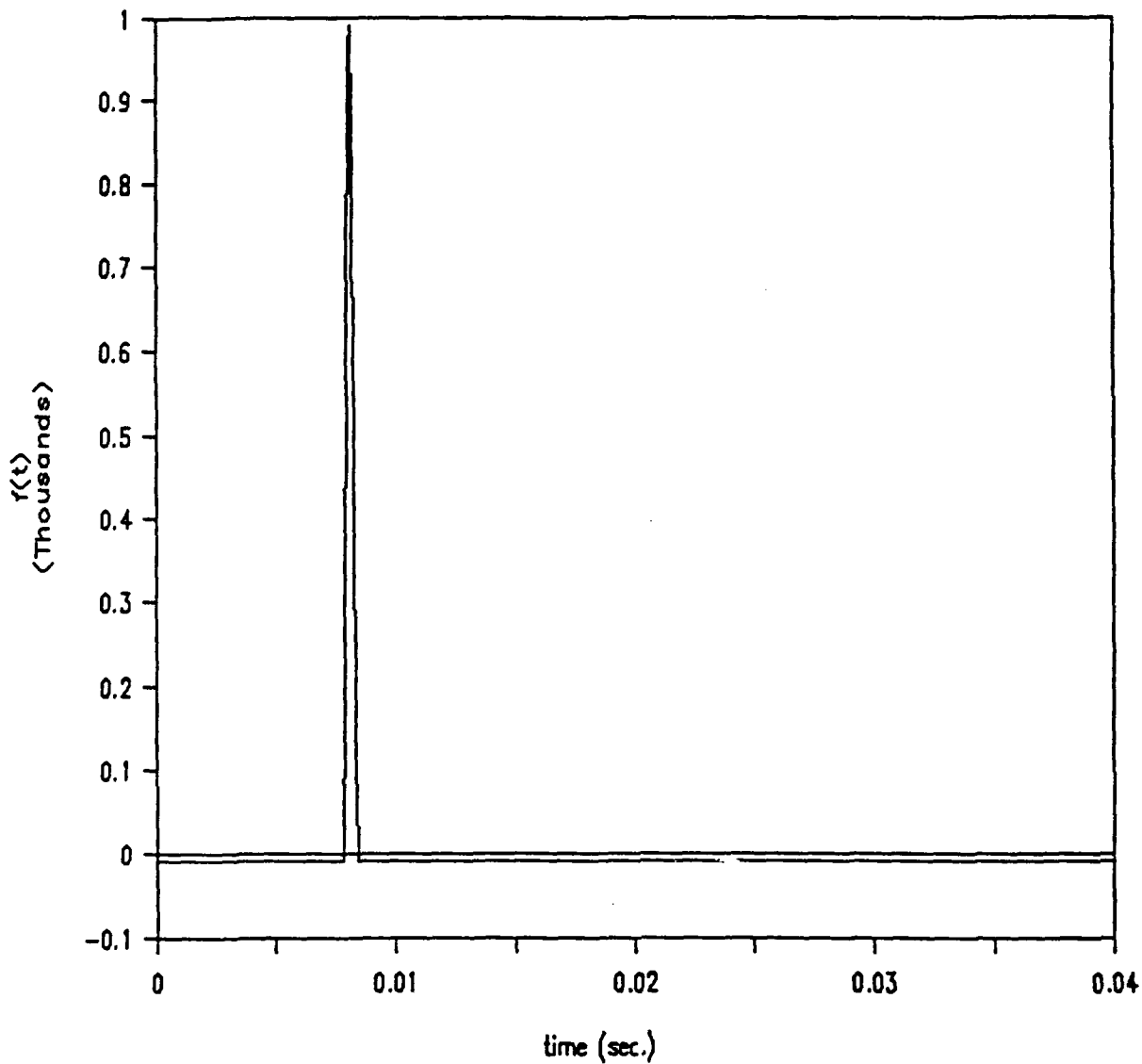


FIGURE 5.15 Final iteration of the reconstruction approach estimating exact impact location $x=0.2$ m

REFERENCES

1. Booer, A.K., Chambers, J. and Mason, I.M., 1977, *Electronics Letters*, 13, pp. 453-455.
2. Brazier-Smith, P.R., Butler, D. and Halstead, J.R., 1981, *Journal of Sound and Vibration*, 75 (3), pp. 453-457.
3. Chen, C.T., 1979, *One-Dimensional Digital Signal Processing*, New York: Marcel Dekker, Inc., pp. 194-195.
4. Doyle, J.F., 1987, *Experimental Mechanics*, 27, pp. 229-233.
5. Holmes, P.J., 1974, *Journal of Sound and Vibration*, 35(2), pp. 277-297.
6. Jordan, R.W. and Whiston, G.S., 1984, *Journal of Sound and Vibration*, 97 (1), pp. 53-63.
7. Whiston, G.S., 1984, *Journal of Sound and Vibration*, 97 (1), pp. 35-51.

Chapter 6.

RESIDUAL THERMAL STRESSES IN SMART LAMINATES

In the future, aerospace structures will be "smart structures". Such structures will have a network of embedded sensors and actuators. For example, laminated composite plates with embedded piezoceramic patches have been proposed as smart skins for aircraft wings. Typically, piezoceramics have an allowable strain to failure that is one tenth that of most graphite/epoxy composites. Residual thermal stresses and strains gain importance in designing such composite laminates. The residual stress field in the vicinity of the edges of a finite size patch in a composite laminate is three dimensional. This chapter examines the residual thermal stress/strain field in finite dimensional laminated plates without piezoceramic layers. The results obtained using classical lamination theory are compared to the results obtained using three dimensional analysis to investigate the applicability of the classical lamination theory to residual thermal stress problems. The results of this study are the basis for discussing the placement of piezoceramic patches in laminated plates.

Raghava et al. (1984) demonstrated a variation of strain through the thickness of a thick laminated composite. Fulong et al. (1989) experimentally investigated the Coefficient of Thermal Expansion (CTE) of a composite cube, including edge effects. These studies show a variation in the planar strain with location through the thickness. Barth et al. (1989), Tsai (1984) and Tauchert (1989) have utilized closed-form solutions for various cases of thermally induced strain in laminates. The thermal stress in a short fiber composite was investigated by Hatta and Toya (1987). Bowles (1984) used a two-dimensional finite element method to investigate CTE in laminates. The effect of element density in finite element modelling of thermally stressed laminates was evaluated by Crose et al. (1987).

TABLE 6.1 Mechanical properties of the graphite/epoxy used in the analysis

E_{11} (GPa)	132.7
E_{22} (GPa)	12.4
E_{33} (GPa)	12.4
$G_{12} = G_{13} = G_{23}$ (GPa)	5.8
$\nu_{12} = \nu_{13} = \nu_{23}$	0.3
α_{11} (mm/mm °K)	$-0.45 \cdot 10^{-6}$
α_{22} (mm/mm °K)	$27.5 \cdot 10^{-6}$
α_{33} (mm/mm °K)	$27.5 \cdot 10^{-6}$
t (mm)	0.254

6.1 Analysis

A group of simple laminates is selected for the purpose of comparison. These laminates are $[0_4/90_4]_s$, $[0_2/90_2]_{2s}$, $[0/90]_{4s}$. The residual stress field in the laminates is obtained by assuming that the laminate's stress-free temperature is 154°C. The stress field is obtained at 24°C. This tem-

perature history is compatible with the cure cycle that the materials in this study require. Table 6.1 lists the mechanical and thermal properties of the graphite/epoxy composite considered in this study.

The classical lamination theory assumes a continuous planar shell with small bending displacements. For a balanced and symmetric laminate, with no applied bending stresses, the assumptions produce a constant planar strain throughout the thickness of the laminate. This constant strain is then used to calculate the stress in each lamina (Halpin, 1984). The classical lamination theory produced no differences in the strain distribution for the three laminates studied. These results are due to each of the laminates having the same percentage of 0° and 90° plies. These analyses showed a midplane strain of $-3.2449 \cdot 10^{-4}$ mm per mm in both the X and Y directions for all of the laminates.

The three dimensional analysis in this study is conducted using the ABAQUS version 4.8 finite element analysis code by Hibbitt, Karlsson and Sorensen, Inc. The laminates are typically modelled as shown in Figure 6. 1. The ABAQUS C3D8 element was used for this analysis. This is an eight-node linear displacement three-dimensional brick element. In order to obtain an accurate representation of stress and strain variation through the thickness of each ply, each material orientation is modelled with at least two elements in the thickness direction. This is done so that stress and strain variations through the thickness of the laminate could be accurately represented.

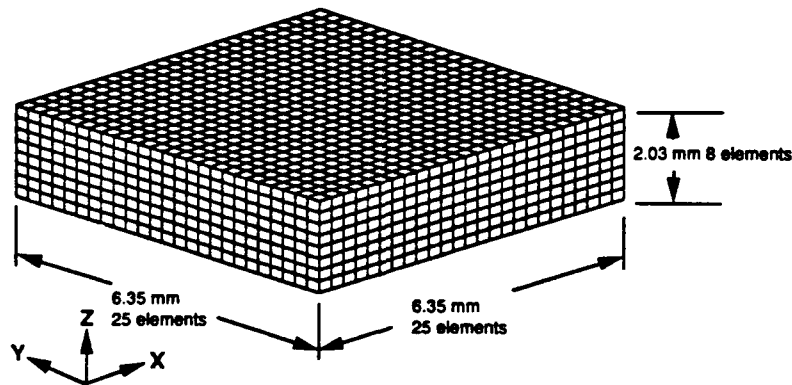


FIGURE 6.1 Typical three-dimensional model used for finite element analysis

In order to ascertain that the finite element analysis provides convergent results and also to ensure that the thermal stress/strain field is stabilized with respect to the planer coordinates in the middle part of the laminates, the effect of several model variables is evaluated.

The first variable is the model's physical size. The comparison is accomplished by changing the X and Y dimensions of the model without changing the number of elements or the dimension in the thickness direction. As the physical size of the model increased beyond 12.7 mm the X direction strain becomes almost constant through the thickness. The next model variable investigated is the aspect ratio of the elements. For aspect ratios up to four, the results showed no change. An aspect ratio of six showed a small variation in the X direction strain. As the final verification of the effect of the physical size on the measured X direction strain, models of the same physical size are represented in three different ways. A laminate modelled using four elements in the thickness di-

rection is referred to as a four element model. Another model with eight elements in the thickness direction is referred to as an eight-element model. The third model, referred to as a quarter model, has the X-y, X-Z and Y-Z planes all defined as planes of symmetry, with the corner nodes falling on the X or Y axis restrained to only move along the axis. For the four-element and eight-element models, the physical size is the actual model dimensions in the X or Y directions. For the quarter model dimension is half that of the physical model size.

As the result of the model variable study, it is concluded that the most accurate model size was a 50.8 mm model. At this physical size there is no apparent variation in the X direction strain through the thickness of the model. To achieve this model dimension and minimize the effect of the element aspect ratio, a quarter model is selected. It should be noted that the X-Z and Y-Z planes of symmetry can only be used if the laminate being modelled contains only 0° and 90° plies.

6.2 Discussion Of Results

The stacking sequence comparison for $[0_4/90_4]_s$, $[0_2/90_2]_{2s}$ and $[0/90]_{4s}$ laminates was run using the 50.8 mm quarter model which was found optimum from the model variable study. Figure 6. 2 shows the results of the comparison. There is no variation in the X direction strain through the thickness of the laminates at the mid point. However, there is a slight difference in the value of the strain obtained using three dimensional analysis and the classical lamination theory. The lack of variation of strain through the thickness of the laminate can be verified by the following analysis:

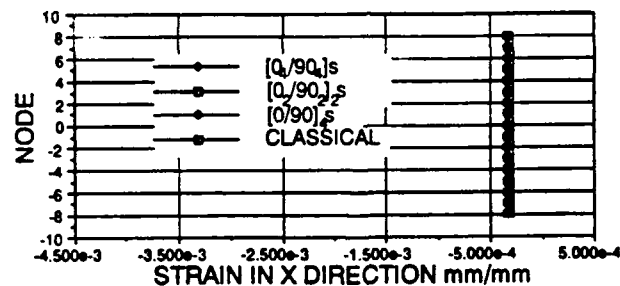


FIGURE 6. 2 In-plane normal strain distribution through the thickness of laminates shown sufficiently far away from the free edges.

Consider a laminated orthotropic plate whose thickness is very small compared to its planar dimensions. Let us assume that the strain components are not a function of the planar coordinates sufficiently far away from the edges of the plate, that is ϵ_{xx} , ϵ_{yy} , ϵ_{zz} , ϵ_{xz} , ϵ_{yz} , ϵ_{xy} strains are a function of the Z coordinate only. Using linear elastic constitutive relations, we find that σ_{xx} , σ_{yy} , σ_{zz} , σ_{xz} , σ_{yz} , σ_{xy} stress components are a function of Z only.

Substitute the stress components into the equilibrium equations yield:

$$\frac{\partial \sigma_{xz}}{\partial z} = 0; \quad \frac{\partial \sigma_{yz}}{\partial z} = 0; \quad \frac{\partial \sigma_{zz}}{\partial z} = 0; \quad (1)$$

which implies that $\sigma_{xz} = \text{constant}$, $\sigma_{yz} = \text{constant}$ and $\sigma_{zz} = \text{constant}$.

Assuming that lateral plate surfaces are traction free (no mechanical loading) implies that:

$$\sigma_{xz} = 0; \quad \sigma_{yz} = 0; \quad \sigma_{zz} = 0. \quad (2)$$

Substituting in the constitutive relations, yields $\epsilon_{xz} = 0$, $\epsilon_{yz} = 0$ and $C_{13}\epsilon_{xx} + C_{23}\epsilon_{yy} + C_{33}\epsilon_{zz} = 0$ which implies $\epsilon_{xx} = \text{constant}$, $\epsilon_{yy} = \text{constant}$ and $\epsilon_{zz} = \text{constant}$.

This shows that the initial assumption is not true. Normal strains are constant and shear strains are identically zero throughout the thickness of the plate sufficiently away from the edges (where strains are no longer functions of the planar coordinates). These analytical arguments can be applied to each layer of the laminate one by one, starting from the surface layer.

6.2.1 Edge Effects

Edge effects will be discussed for $[0_4/90_4]_s$, $[0_2/90_2]_{2s}$ and $[0/90]_{4s}$ laminates in this section. These laminates are modelled using the quarter model geometry. For the $[0_4/90_4]_s$ and $[0_2/90_2]_{2s}$ laminates, 25 elements are used in the X and Y directions and eight elements are used in the Z direction. All models have physical dimensions of 4.06 X 50.8 X 50.8 mm.

The variation of the X direction strain as the distance from the edge increases is shown in Figure 6. 3. The strain shown in this Figure is for the nodes that lie on the X axis of a quarter model. This represents the midplane strain in the center of the model. The midplane strain is shown for three different laminates, $[0_4/90_4]_s$, $[0_2/90_2]_{2s}$ and $[0/90]_{4s}$, with results of classical lamination theory shown for comparison.

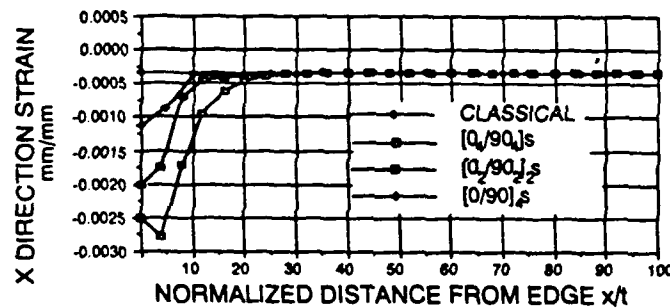


FIGURE 6.3 X-direction strain at the midplane of the laminates with 0° outer-plyes.

All three, three-dimensional models converge to the results of the classical lamination theory at a distance of 8.89 mm from the edge of the model. The magnitude of the strain at the free edge appears to vary in a linear manner with respect to the number of plies of the same orientation that are located adjacent to one another. The rate of convergence to the classical lamination theory results varies in the same manner.

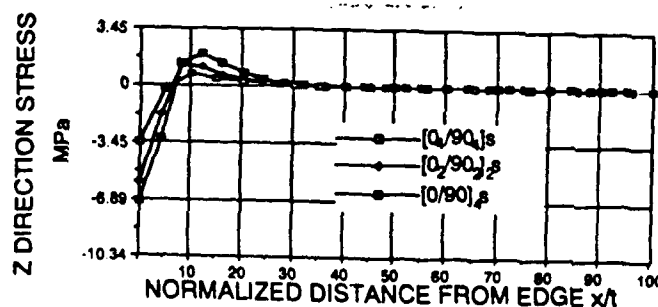


FIGURE 6.4 Z-direction stress at the first $0^\circ/90^\circ$ interface away from the laminate midplane

The variation of the interlaminar normal stress is also investigated. The interlaminar normal stress is plotted for the nodes that lie on the first $90^\circ/0^\circ$ material interface away from the mid plane of the lamina. For the $[0_4/90_4]_s$ case, this is the fifth node from the midplane. For the $[0_2/90_2]_{2s}$ and $[0/90]_{4s}$ laminates, this is the third node from the center. Figure 6. 4 shows the interlaminar normal stress for the cases studied. Once again the edge effects diminishes with 8.89 mm from the edge of the model. A high compressive stress can be seen at the edge of the laminate. This stress is compensated for by a tensile stress 2.03-8.89 mm from the edge of the model. The magnitude of the stress varies in proportion to the number of adjacent similar plies.

In Figure 6. 5 the X-Z shear stress is reported at the same interface as the interlaminar normal stress. the shear stress shows the same response as reported by Fulong et al. (1989). The shear stress approaches zero with in four to six lamina thicknesses from the edge of the laminate.

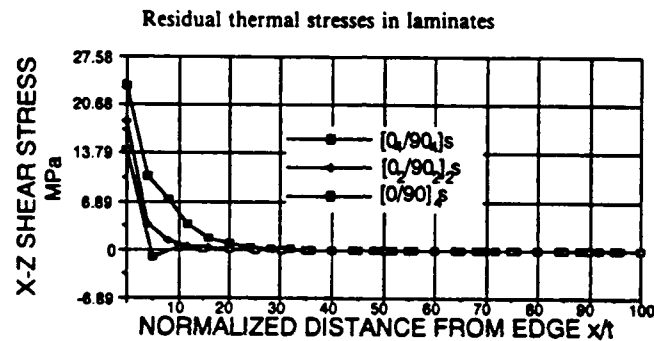


FIGURE 6. 5 X-Z shear stress at the first $0^\circ/90^\circ$ interface away from the laminate midplane

The variation of the X direction strain through the thickness of the laminate at the free edge is shown in Figure 6. 6. The strain at the midplane is equivalent to the strain of a lamina twice the thickness of the rest of the lamina, due to the midplane symmetry condition used. It can be seen that the midplane strain of the $[0_4/90_4]_s$ laminate is the same as the strain of the $[0_2/90_2]_{2s}$ laminate at the fifth node from the center line. Both of these lamina have two plies of 90° materials at these locations.

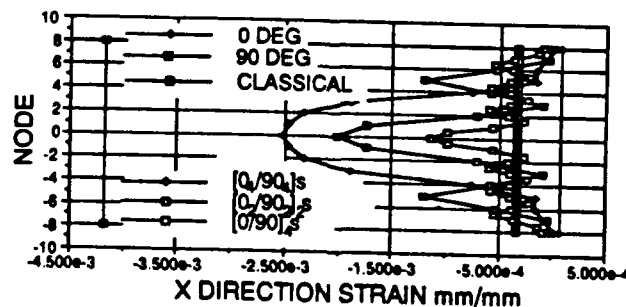


FIGURE 6. 6 X-direction strain at the free edge shown through the thickness of the laminates with 0° outer plies

It can also be seen that at the surface of the models the strains tend toward the strain of an unrestrained 0 degree lamina. However, the fewer the number of plies in a lamina, the closer its free surface strains are to the classical approximation. The edge effects seen in the $[90/0]_s$ class of laminates are similar to the edge effects seen in the $[0/90]_s$ class. The X direction results for the $[90/0]_s$ class are identical to the Y direction results for the $[0/90]_s$ class of laminate. The influence of the distance from the edge is almost identical. The stresses and strain change sign, as would be expected when the stacking sequence is reversed. The magnitude of the stresses changes due to the stiffness of the 0° and 90° material.

The free edge X direction strain for $[90/0]_s$ class laminates is shown in Figure 6. 7. At the surface the strains tend to the strain of an unrestrained 90° lamina. The magnitude of the strain shows a linear response at the free surface for the one-ply and two-ply layers. The magnitude of the strain of the four-ply layer is not twice that of the two-ply layer due to its proximity to the magnitude of an unrestrained lamina.

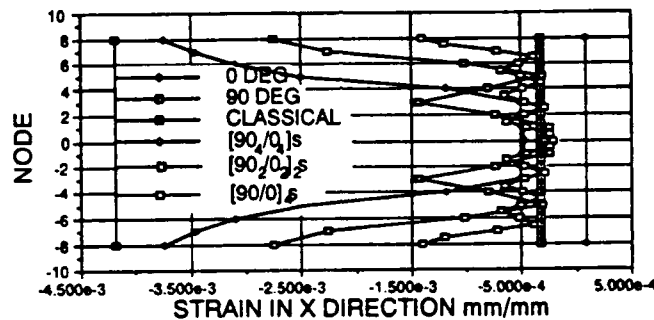


FIGURE 6. 7 X-direction strain at the free edge shown through the thickness of the laminates with 90° outer-ply

The X direction strain at the midplane is shown in Figure 6. 8 for the $[90/0]_s$ class of laminates which shows similar behavior to the $[0/90]_s$ class. In both cases the strains converge to the value predicted by the classical lamination theory within 8.89 mm from the free edge. However, the magnitude of the free edge strain is smaller when compared to the $[0/90]_s$ laminates. This is caused by the smaller CTE and greater modulus of the 0° material.

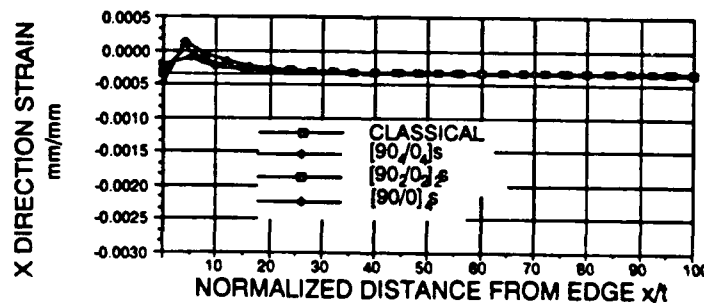


FIGURE 6. 8 X-direction strain at the midplane of the laminates with 90° outer-ply

The interlaminar normal stresses at the $90^\circ/0^\circ$ interface are shown in Figure 6.9. A tensile stress can be seen at the free edge of the laminate. This is consistent with the contraction of the 90° plies on the surface of the laminate and the expansion of the 0° plies at the midplane of the laminate.

The X-Z shear stress edge effect, as shown in Figure 6.10, for the $[90/0]_s$ laminates demonstrates the same trends as the shear stress of the $[0/90]_s$ laminates. In both cases the stress diminishes within six lamina thicknesses from the edge of the laminate.

It has been shown that for large laminates the in-plane strains do not vary with respect to the thickness location when observed sufficiently far away from the edges of the laminate. For these cases, the classical lamination theory predicts an accurate residual thermal stress/strain field inside the laminates.

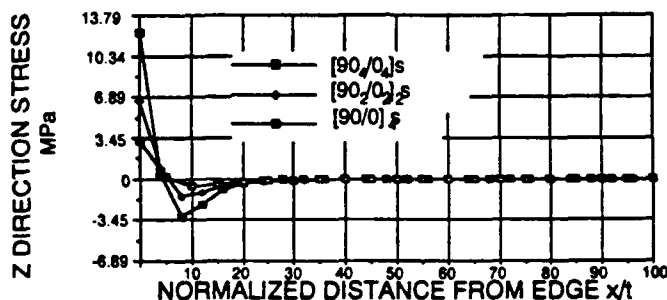


FIGURE 6.9 Z-direction stress at the first $90^\circ/0^\circ$ interface away from the laminate midplane

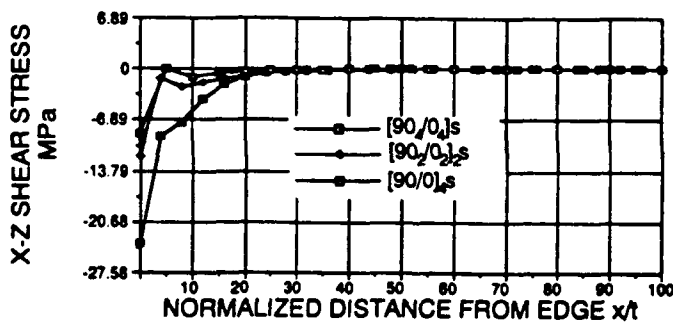


FIGURE 6.10 X-Z shear stress at the first $90^\circ/0^\circ$ interface away from the laminate midplane

The three dimensional analysis has shown that for the laminates studied, the magnitude of the in-plane strains measured at a free edge is proportional to the total thickness of the adjacent material with like orientation. Also, the in-plane strains converge to the value predicted by the classical lamination theory in less than six times the maximum thickness of a single orientation of the material. The magnitude of the normal interlaminar stress was also proportional to the maximum total thickness of the adjacent material with like orientation. The analysis also showed that an opening stress at a free edge was compensated for by a compressive stress further away from the edge.

6.3 Smart Laminate Design Implications

The results of the residual thermal stress analysis presented above implies that the CLT can be employed to obtain residual stresses in embedded piezoceramic patches of planer dimensions a few orders of magnitude larger than the thickness dimension. It means that the average residual thermal stress in a piezoceramic patch is independent of the interface location through the thickness of a laminate. However, it should be pointed out that the edge stresses, residual thermal or otherwise, have to be considered for delamination initiation analysis.

One method to help the piezoceramic withstand the thermally induced residual stresses from laminate curing is to modify the CTE of the laminate. This modification will produce a laminate with a CTE that more closely matches the ceramic's CTE. The analysis in this chapter has shown that, for sensor placement away from the edges of a laminate, the classical lamination theory may be used to obtain the residual strains.

REFERENCES

1. Barth, T.S., Joshi, S.P. and Pearlstein, A. J. (1989). Three-dimensional thermoelasticity formulation for laminated transversely isotropic solids. In Proc. Seventh Int. Conf. on Composite Materials, Vol. 2, pp. 192-197.
2. Bowles, D.E. (1984). Effect of microcracks on the thermal expansion of composite laminates. *J. Compos. mater.* 17, 173-187.
3. Crose, J.G., Holman, R.L. and Pagano, N.J. (1987). Validation of advanced composite thermal stress analysis methods. *Trans. ASME J. Engng Mater. technol.* 109 (1), 40-46.
4. Fulong, D., Yinyan, W. and Post, D. (1989). Residual thermal strains in a laminated composite. In Proc. Seventh Int. Conf. on Composite Materials, Vol. 2, pp. 177-180.
5. Halpin, J.C. (1984). *Primer on Composite Materials: Analysis.* Technomic Publishing, Lancaster.
6. Hatta, H. and Taya, M. (1987). Thermal Stress in a coated short fiber composite. *Trans. ASME J. Engng Mater. Technol.* 109(1), 59-63.
7. Raghava, R.S., Valentich, J. and Nathenson, R.D. (1984). Thermoelastic behavior of thick glass/epoxy composite laminates. *J. Compos. Mater.* 18, 81-93.
8. Tauchert, T.R. (1989). Thermal shock of symmetric cross-ply laminates. In Proc. Seventh Int. Conf. on Composite Materials, Vol. 2, pp. 165-170.
9. Tsai, Y.M. (1984). Orthotropic thermoelastic problem of uniform heat flow disturbed by a central crack. *J. Compos. Mater* 18, 122-131.

Chapter 7.

FABRICATION AND CURING PROCESSES

The fabrication and curing processes for advanced laminated composites have been optimized for the last two decades. Curing processes involve control of pressure and temperature over the curing time. Recent research in this area has increased our understanding of the curing processes and has resulted in real time control of curing parameters (Kranbuehl et.al.,1988). Real time control of the curing processes has reduced the costs and time associated with a trial and improvement procedure for thick laminated composites (Tam and Gutowski, 1988).

The fabrication and curing processes for smart composite laminates involve additional parameters arising from the placement of sensors and actuators. This chapter describes various aspects of the fabrication and curing processes for laminates with multiple embedded piezoceramic sensors and actuators. Graphite epoxy laminates with embedded piezoceramic wafers are discussed in detail.

Chapin and Joshi (1991) considered residual thermal stresses due to the curing process in deciding the optimum placement of piezoceramics in a laminate. Shaw et.al. (1990) discussed edge stress distribution due to the presence of piezoceramic layers in a laminate. Crawley and Luis (1989) briefly discussed the manufacturing aspects of intelligent structures with embedded piezoceramics. The following is a detailed discussion of fabrication and curing methodology.

7.1 Piezoceramics

The discussion of the fabrication and curing process in the following sections is limited to the placement of a piezoelectric material known as Lead Titanate Zirconate (PZT). The piezoceramic, commercially known as G-1195, is selected on the basis of some desirable properties such as curie temperature, relatively high elastic moduli etc. The fabrication and curing processes are modified to reduce the risk of mechanical or electrical failure to the network of embedded piezoceramics. In addition, it is necessary to minimize the deterioration, if any, of piezoelectric and mechanical properties of the sensors and actuators.

7.2 Fabrication

The lay-up and geometry of the structural elements are known at the time of the fabrication. In addition, the planer positions and through-the-thickness placement of actuators and sensors in the laminate are provided to the fabricator. Figure 7.1 shows a schematic of a laminated plate lay-up with multiple piezoceramic wafers. Piezoceramic wafers are placed in cut-outs in a glass-epoxy prepreg ply. The brass electrodes run on opposite sides of the glass-epoxy ply. This ply with piezoceramics placed in cut-outs is placed between two glass plies to insulate the piezoceramics and electrodes from the conductive graphite-epoxy plies.

The brass ribbon electrodes (thickness 0.001 inch) cut in a required pattern are bonded to piezoceramic wafers. Electrodes are bonded to a piezoceramic patch prior to the placement in the glass-epoxy ply with cut-outs. Echo bond 57C conductive epoxy is used for bonding electrodes because it does not require the application of heat which can adversely affect the piezoelectric properties. The bonding epoxy should be applied uniformly. The brass electrodes should cover the piezoceramic area completely but should not extend over the edges. Electrodes extending over the edges may short-circuit the piezoceramic wafer. One should also be careful in applying the conductive epoxy to avoid short-circuiting. An uneven application of the conductive epoxy will result

in cracked piezoceramic wafers after curing.

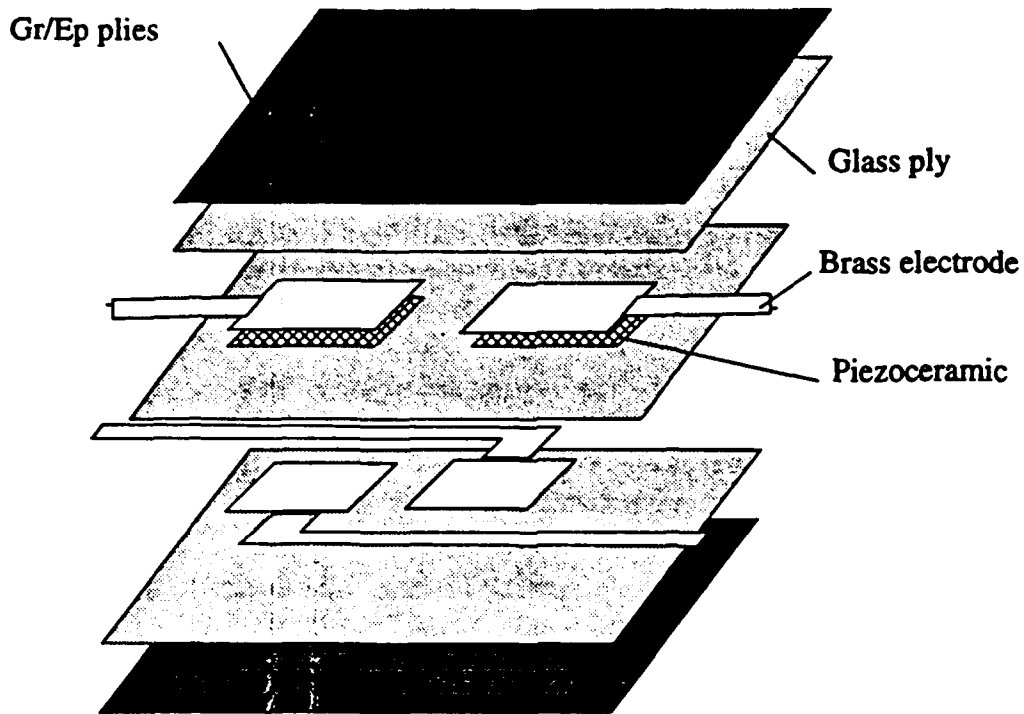


FIGURE 7.1 Schematic of a laminated plate lay-up with multiple piezoceramic wafers

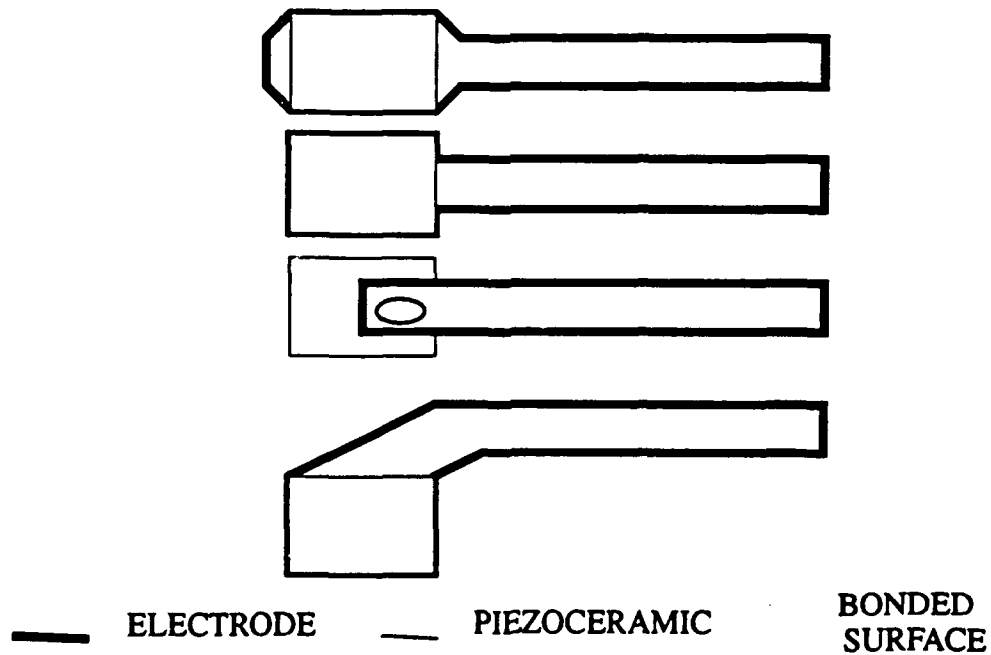


FIGURE 7.2 Brass ribbon electrode patterns, piezoceramic patches and bonding surfaces

Various electrode patterns tried before an optimum configuration was chosen, are shown in Figure 7.2. Figure 7.3 shows X-ray radiographs of the laminated panels containing electrode patterns shown in Figure 7.2. The brass electrode configurations are chosen to avoid overlap of reverse polarity electrodes. Although an insulating glass/epoxy ply is between the electrodes, even in the case of a cracked glass/epoxy ply, such a pattern will reduce a possibility of sparking. Cut-outs of the same size as the wafers are cut in the glass/epoxy ply and wafers are placed in the cut-outs with electrodes running on the opposite sides of the ply. A glass/epoxy ply is placed on each side to encapsulate piezoceramic wafers and electrodes to avoid a connection between conductive graphite/epoxy plies and sensors and actuators. These multiple sensors and actuators encapsulated in glass/epoxy plies are placed at required locations in a stacking sequence for a graphite/epoxy laminate. Figure 7.4 shows nine piezoceramic wafers with brass strip terminals in insulating glass/epoxy plies. The bonding spots are visible in this Figure. An x-ray radiograph of cured laminates showing cracked piezoceramic wafers as a result of the uneven application of the conductive epoxy is shown in Figure 7.5. Note that brass electrodes do not cover the whole surface of the wafers which resulted in cracked wafers after curing. There is no specific requirement on the width of the brass strips extending out from the wafers to the edges of the laminate. The brass electrodes are chosen on an ad-hoc basis. They can be replaced by any other type of electrodes.

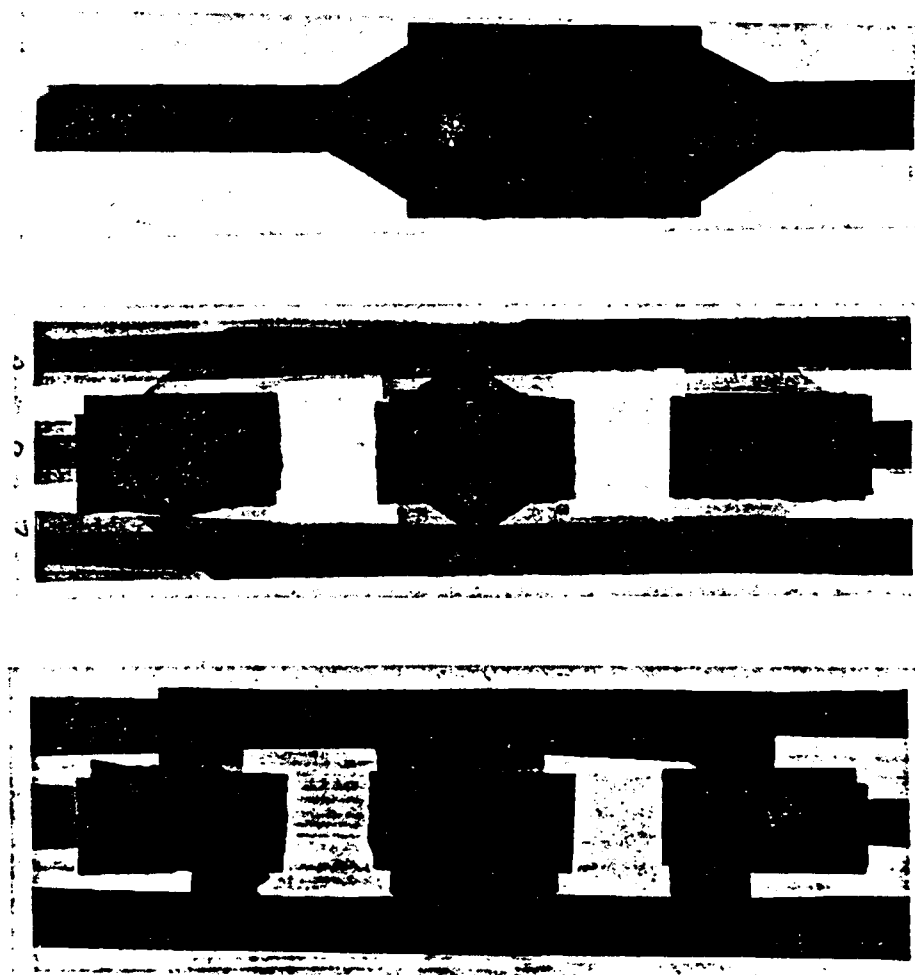


FIGURE 7.3 X-Ray radiographs showing the electrode configurations in laminated panels with embedded piezoceramic patches.

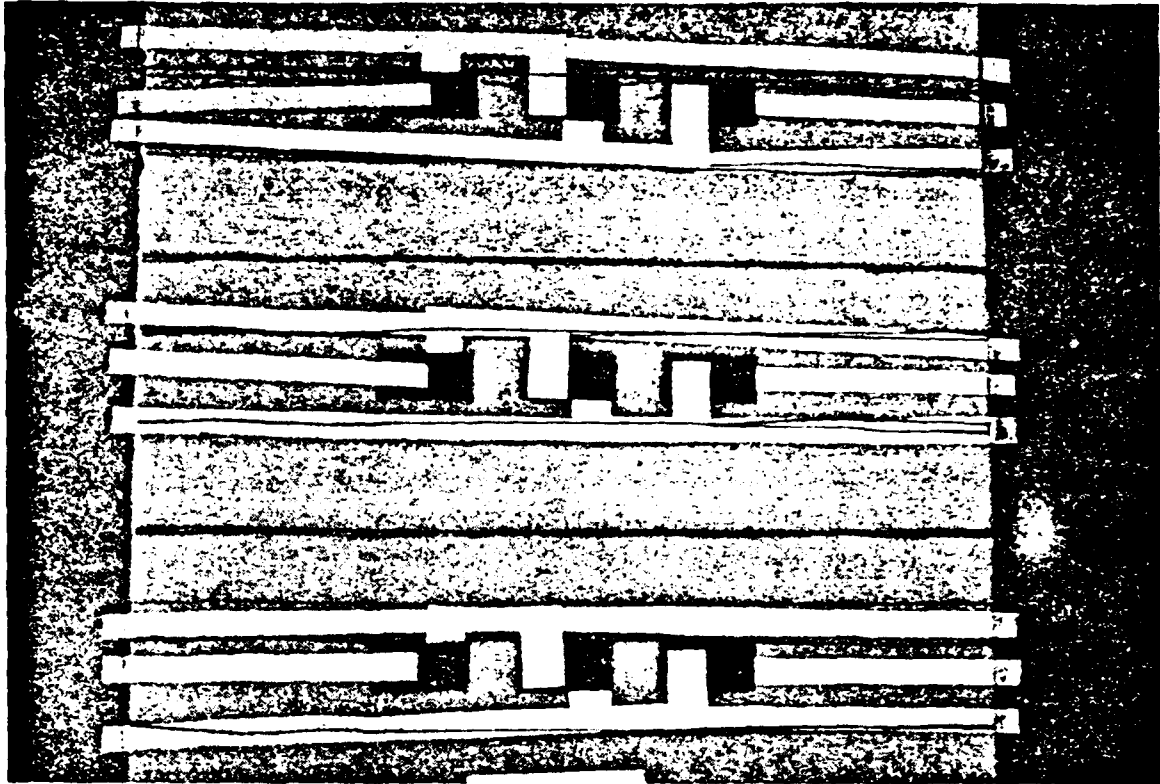
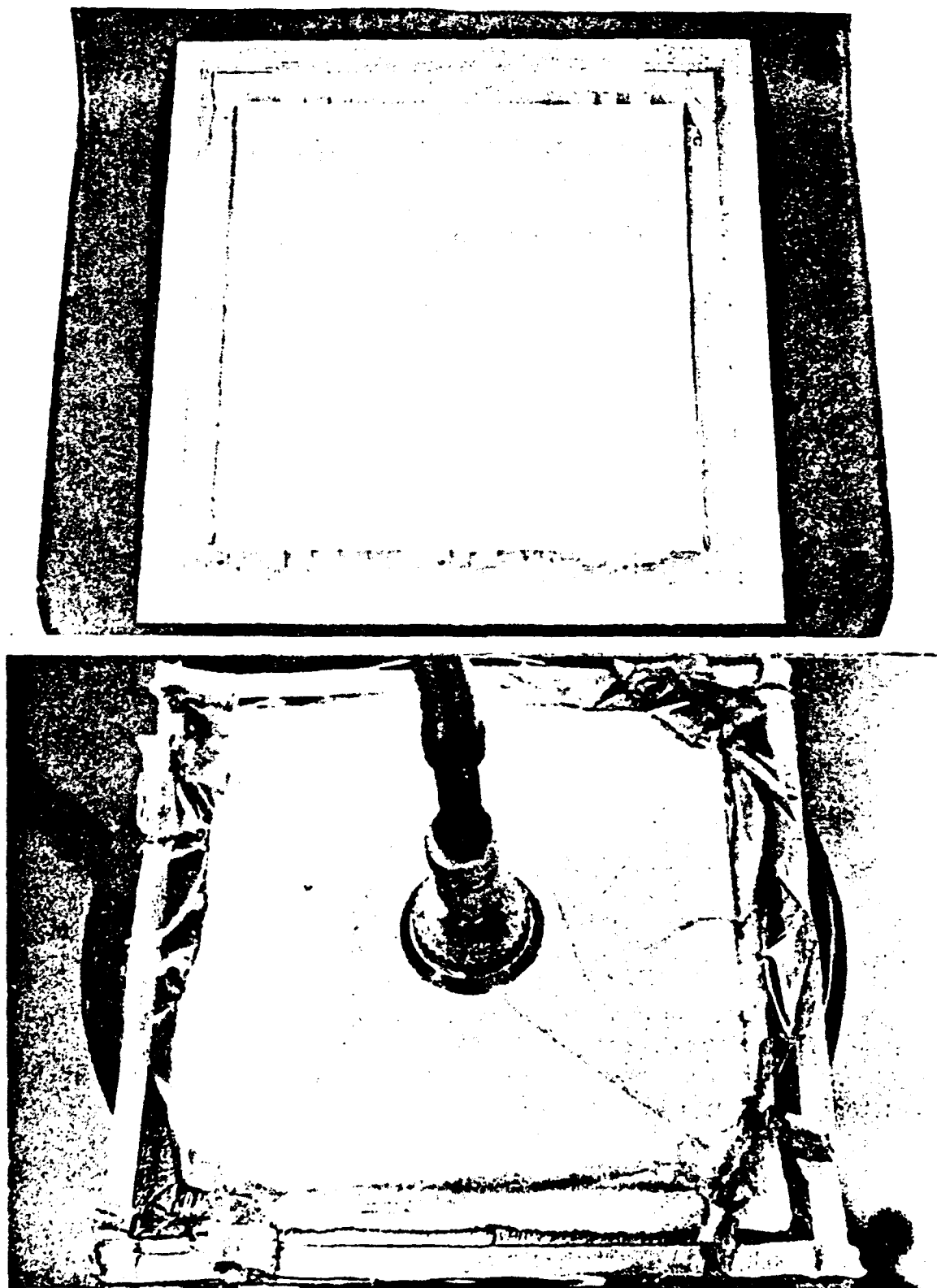


FIGURE 7.4 Nine piezoceramic wafers with brass terminal strips encapsulated in glass/epoxy insulating plies.



FIGURE 7.5 X-ray radiograph showing undamaged and damaged embedded piezoceramic wafers in the insulating glass/epoxy plies. The cracks initiated at the edges of thick patches of cold-solder epoxy

The vacuum bagging procedure is the same as the commonly used bagging procedure. The procedure may vary depending on the complexity of the structural part. However, extra precautions should be taken to avoid breaking electrode terminals extending out of the laminate for external electric connections. Figure 7.6 shows a laminated panel with multiple embedded piezoceramic patches at various stages of fabrication and vacuum bagging.



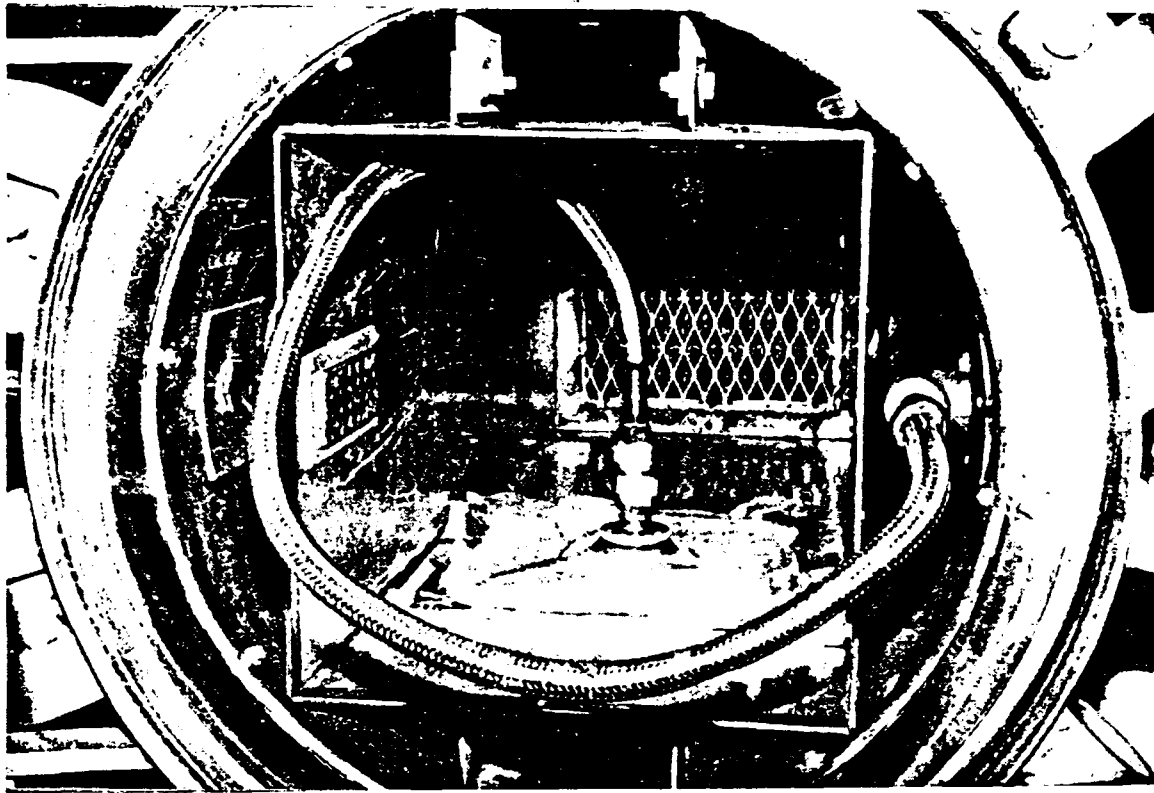


FIGURE 7.6 A laminated plate with embedded piezoceramic patches being prepared for autoclave curing.

7.3 Curing Procedure

Two curing procedures are tried. The first one is a recommended curing procedure for graphite/epoxy (AS4/3501-6) laminates of moderate thickness (see Figure 7.7). In our case the laminate also contains glass/epoxy and piezoceramic wafers (G-1195). The maximum temperature and pressure applied in this cycle is 350 degree F and 80 psi, respectively. The 350 degree F temperature is slightly higher than one half of the curie temperature. Curie temperature is the temperature at which ceramic lose piezoelectric properties. Piezoelectric properties may deteriorate if the piezoceramic is subjected to temperatures higher than one half of the curie temperature. Effects of curing on piezoelectric behavior of the G-1195 wafer is discussed later in this chapter.

The second curing procedure uses the recommended curing cycle for glass/epoxy laminates to separately cure glass plies containing piezoceramics (see Figure 7.7). These cured plies are then placed in graphite/epoxy pre-preg lay-up and cured according to the first cycle. The second curing procedure almost doubles the curing time, however, it has certain advantages over the first curing procedure. The second curing procedure minimizes the piezoceramic wafer cracking and shorting between brass terminals and graphite fibers. The shorting between graphite fibers and brass terminals occurs frequently in the single cure cycle procedure because graphite fiber penetrated the epoxy rich areas of the glass/epoxy pre-preg during co-curing. Cured glass/epoxy plies with embedded piezoceramics can be screened for cracks in piezoceramics and electric connections before curing them with the graphite/epoxy lay-up. This results in a higher percentage of undefective specimens.

The two cycle curing procedure is now routinely used in preparing test specimens at the University of Texas at Arlington laboratory facilities.

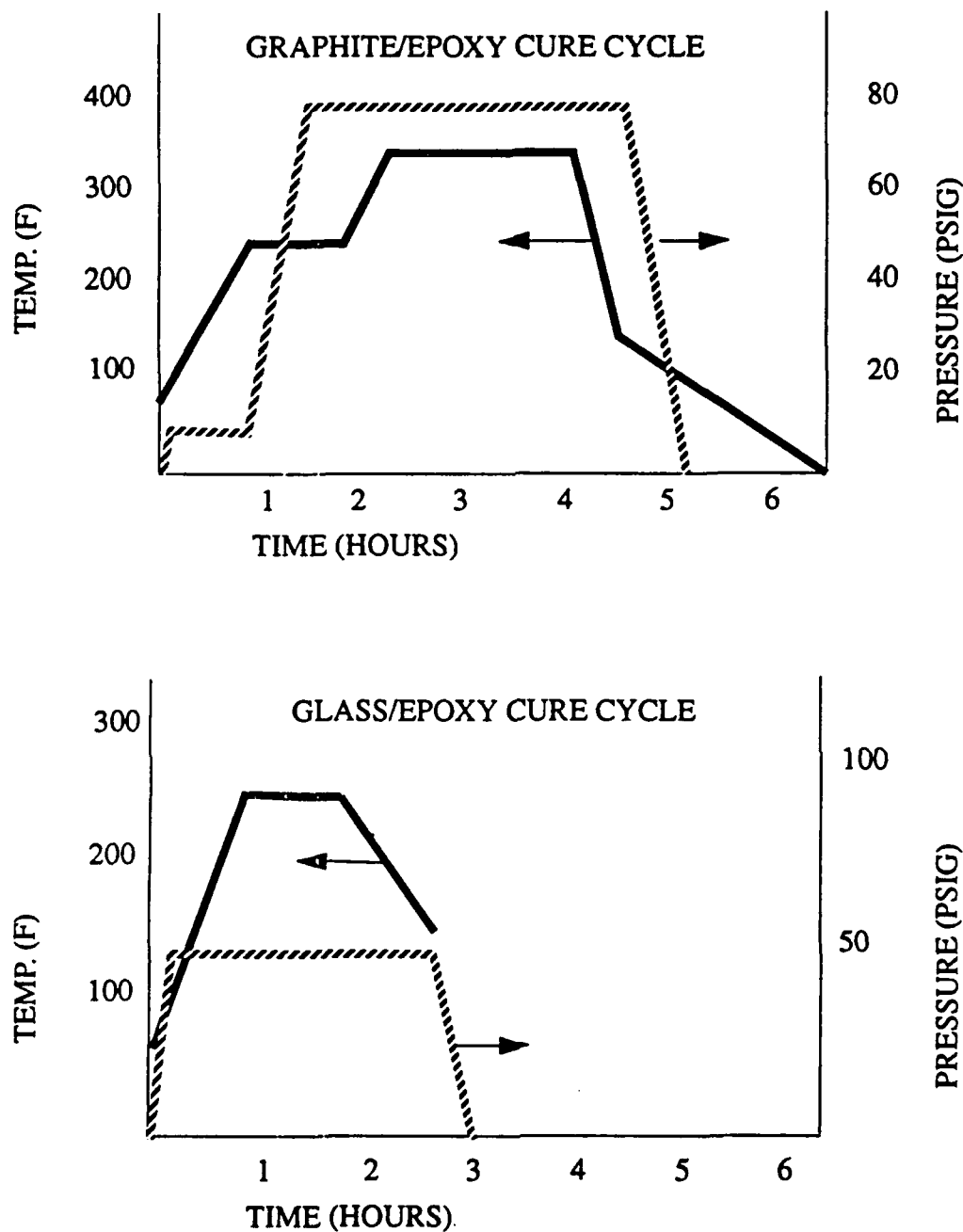


FIGURE 7.7 Curing cycles for graphite/epoxy and glass/epoxy prepregs.

7.4 Effect of Curing on a Piezoceramic

Piezoceramic wafers are subjected to the curing cycle's pressure and temperature without embedding them in a laminate. These wafers are tested to evaluate the effect of the curing cycle on piezoelectric properties. Electric potential is applied in 10 volt increments. Strain and electric potential is recorded every second. The increment of electric potential is done every ten to fifteen seconds. Figure 7.8 shows the electric potential as a function of time and corresponding variation of the in-plane normal strain.

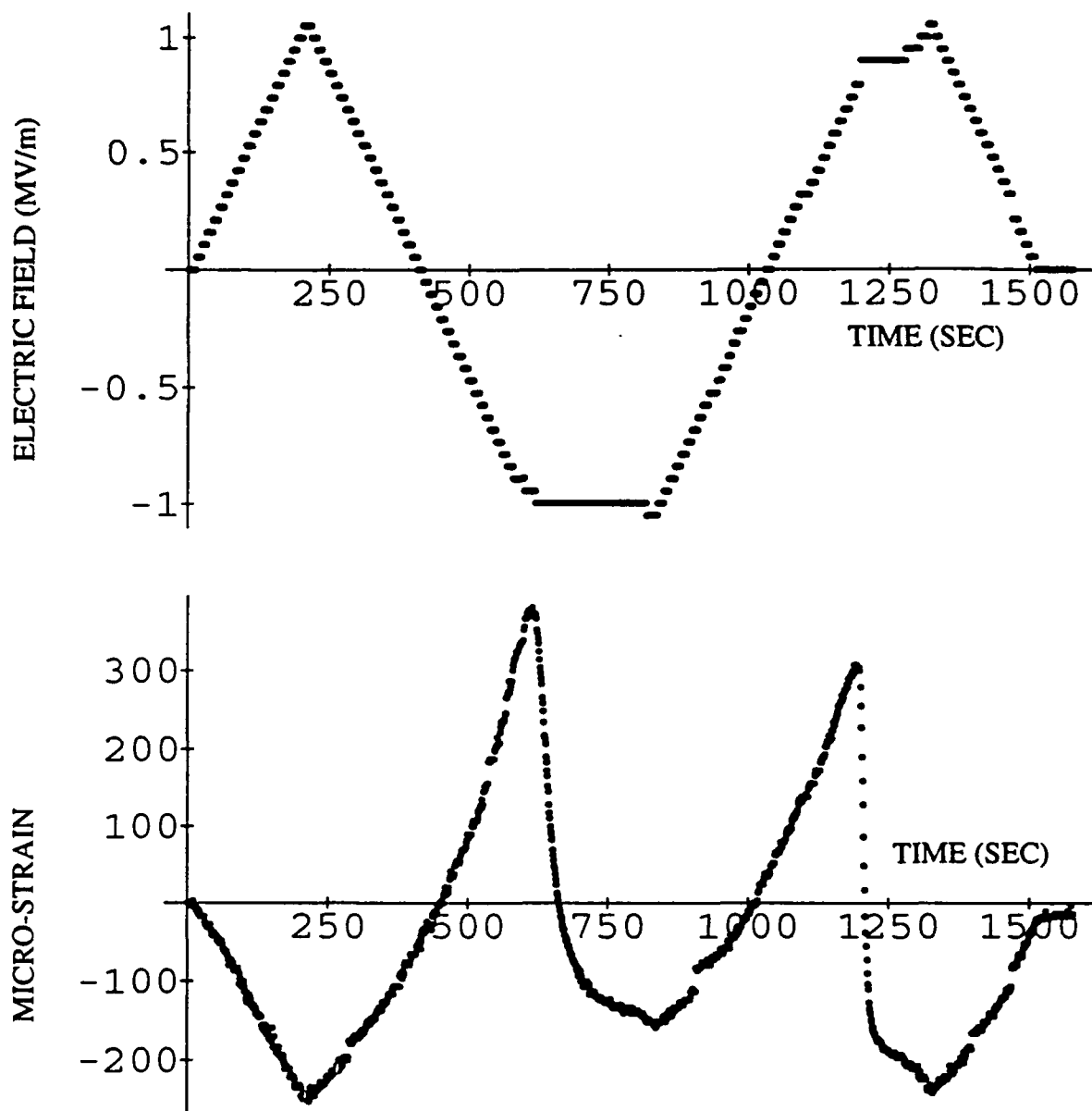


FIGURE 7.8 Variation of the in-plane normal strain due to application of electric field in the thickness direction

The piezoelectric behavior of virgin (not subjected to curing cycle) piezoceramics is shown in Figures 7.9-7.15. Electric potential is raised to a hundred volts, reversed to a negative hundred volts and back to zero volts in increments of ten volts. The first three specimens are tested three times to ensure repeatability of the behavior. One of the specimens showed two distinct behaviors in three tests. The first test showed initially less nonlinear behavior when electric potential is raised to one hundred volts, resulting in substantial residual strain when potential is brought back to zero after reversing it to a negative one hundred volts. The other two subsequent tests showed initial nonlinear behavior which compensated the nonlinear behavior in the reverse potential application.

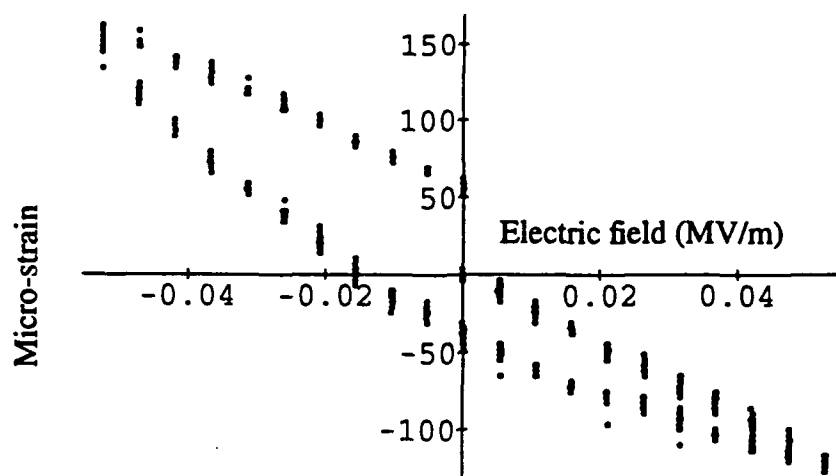


FIGURE 7.9 In-plane normal strain induced by the transverse electric field in the uncured piezoceramic NC1

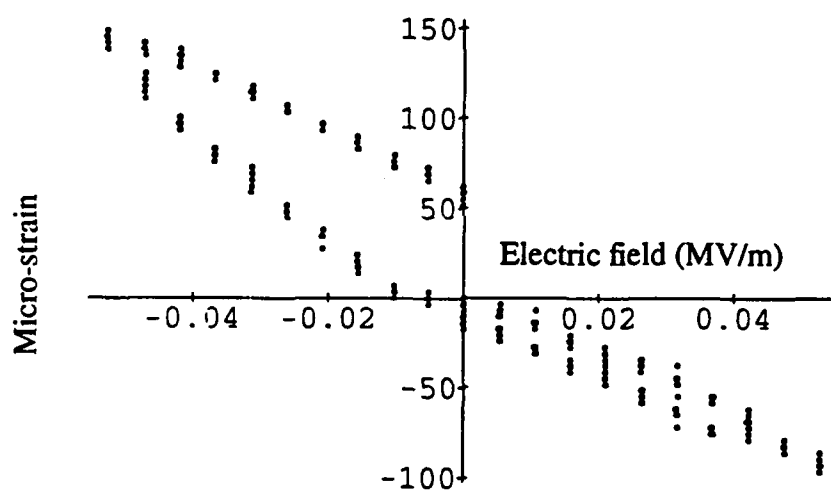


FIGURE 7.10 In-plane normal strain induced by the transverse electric field in the uncured piezoceramic NC3

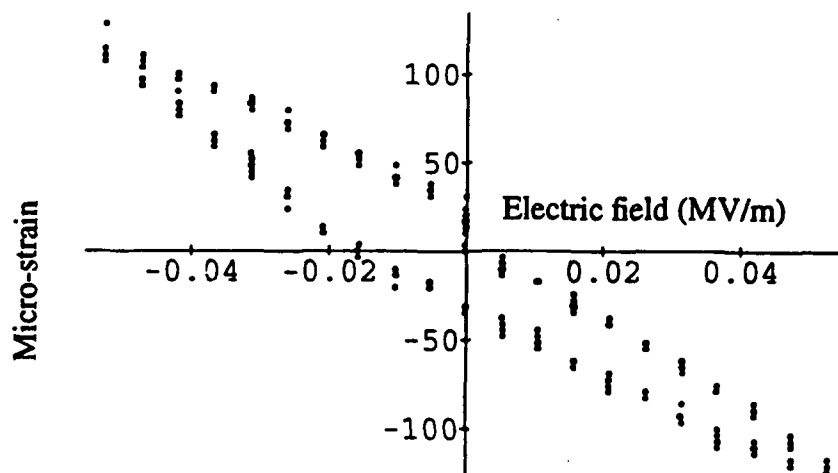


FIGURE 7.11 In-plane normal strain induced by the transverse electric field in the uncured piezoceramic NC4, data-set 1.

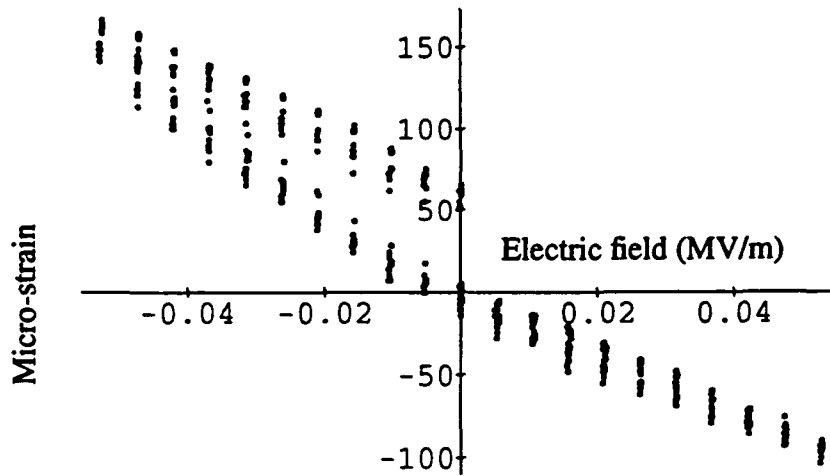


FIGURE 7.12 In-plane normal strain induced by the transverse electric field in the uncured piezoceramic NC4, data-set 3 and 4

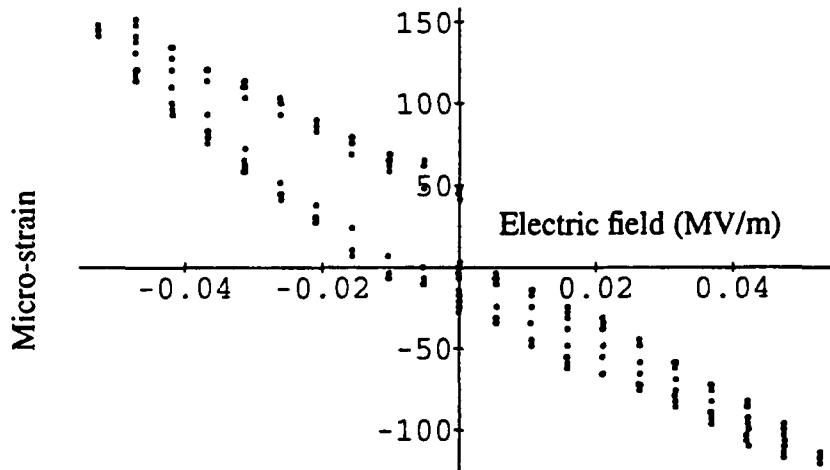


FIGURE 7.13 In-plane normal strain induced by the transverse electric field in the uncured piezoceramic NC5

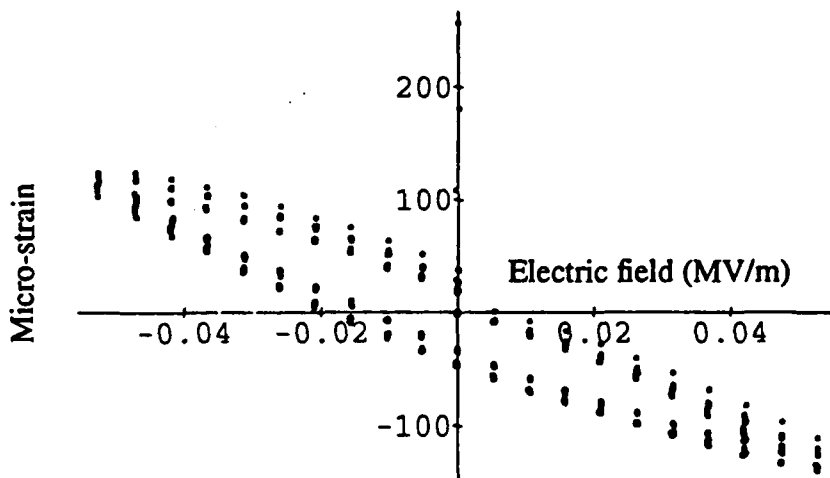


FIGURE 7.14 In-plane normal strain induced by the transverse electric field in the uncured piezoceramic NC6, data-set 1,2 and 3

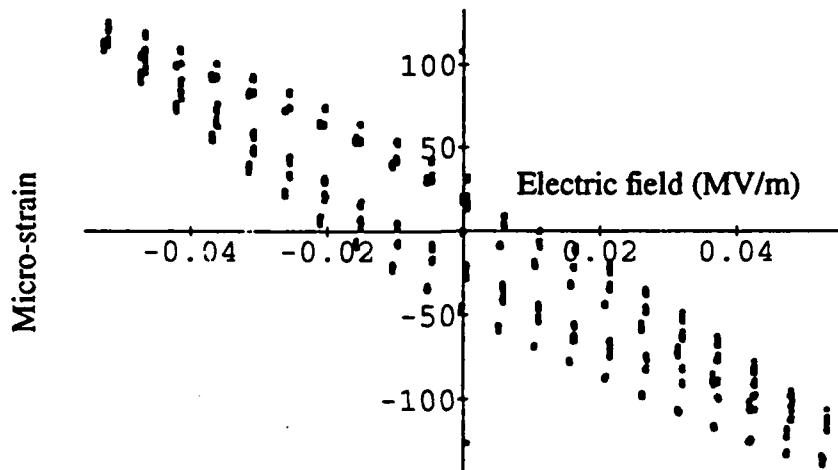


FIGURE 7.15 In-plane normal strain induced by the transverse electric field in the uncured piezoceramic NC9, data-set 1,2 and 3

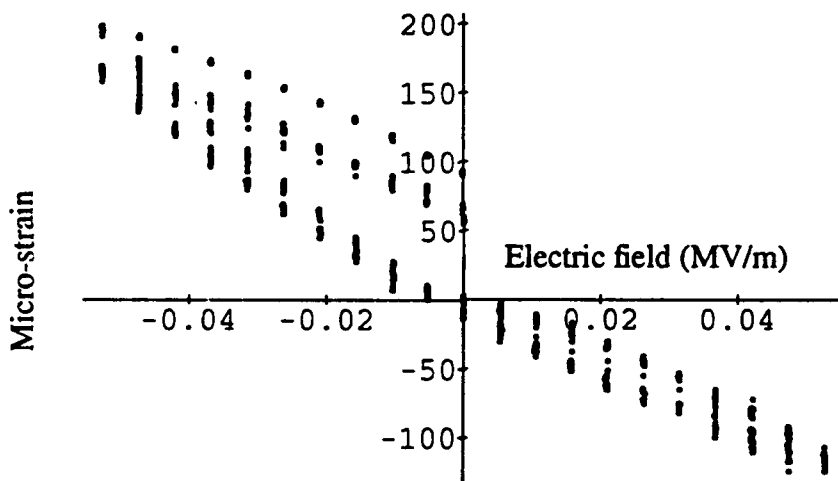


FIGURE 7.16 In-plane normal strain induced by the transverse electric field in the cured piezoceramic C1, data-set 1, 3 and 6

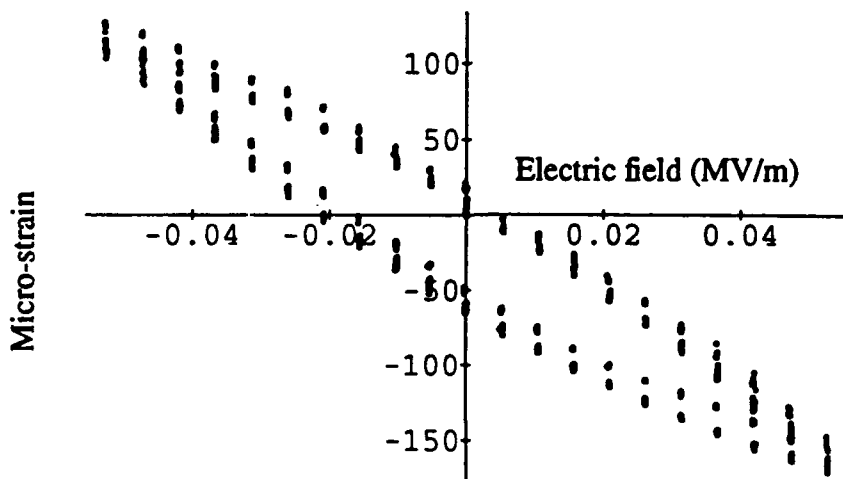


FIGURE 7.17 In-plane normal strain induced by the transverse electric field in the cured piezoceramic C1, data-set 2, 4 and 5

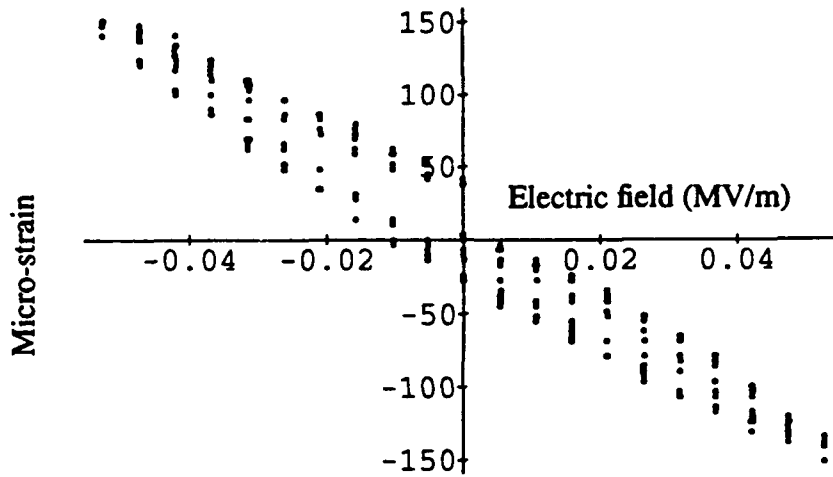


FIGURE 7.18 In-plane normal strain induced by the transverse electric field in the cured piezoceramic C2

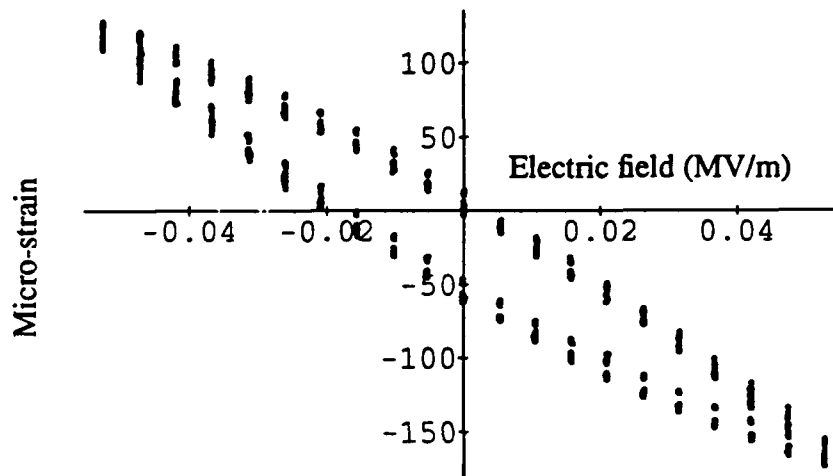


FIGURE 7.19 In-plane normal strain induced by the transverse electric field in the cured piezoceramic C4, data-set 1, 2, 3 and 4

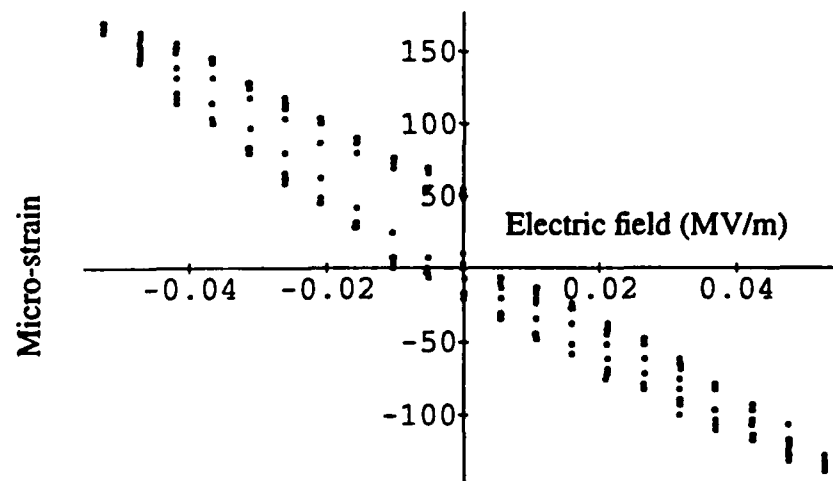


FIGURE 7.20 In-plane normal strain induced by the transverse electric field in the cured piezoceramic C4, data-set 5

Figures 7. 16-7. 20 show response of cured (subjected to curing cycle) piezoceramics to the electric potential. A quadratic least square fits to the first set of recorded data for uncured and cured piezoceramic specimens are presented below. Electric field is measured in MVolts/meter and strain is measured in micro-strain.

NC1	$\begin{cases} \epsilon = -219.8E - 15.3E^2 & 0 < E < 0.525 \\ \epsilon = -37.6 - 245.0E + 181.1E^2 & -0.525 < E < 0.525 \\ \epsilon = 54.7 - 229.4E - 73.3E^2 & -0.525 < E < 0 \end{cases}$	
NC3	$\begin{cases} \epsilon = -122.0E - 96.5E^2 & 0 < E < 0.525 \\ \epsilon = -12.4 - 212.2E + 134.1E^2 & -0.525 < E < 0.525 \\ \epsilon = 56.8 - 199.3E - 54.6E^2 & -0.525 < E < 0 \end{cases}$	
NC4	$\begin{cases} \epsilon = -139.9E - 82.0E^2 & 0 < E < 0.525 \\ \epsilon = -8.9 - 224.8E + 119.8E^2 & -0.525 < E < 0.525 \\ \epsilon = 52.9 - 211.8E - 48.0E^2 & -0.525 < E < 0 \end{cases}$	
NC5	$\begin{cases} \epsilon = -146.6E - 142.1E^2 & 0 < E < 0.525 \\ \epsilon = -23.0 - 237.4E + 130.2E^2 & -0.525 < E < 0.525 \\ \epsilon = 45.7 - 222.4E - 53.7E^2 & -0.525 < E < 0 \end{cases}$	(1)
C1	$\begin{cases} \epsilon = -115.7E - 214.2E^2 & 0 < E < 0.525 \\ \epsilon = -12.0 - 274.0E + 129.5E^2 & -0.525 < E < 0.525 \\ \epsilon = 64.0 - 240.5E - 71.7E^2 & -0.525 < E < 0 \end{cases}$	
C2	$\begin{cases} \epsilon = -170.6E - 200.9E^2 & 0 < E < 0.525 \\ \epsilon = -28.0 - 272.7E + 99.3E^2 & -0.525 < E < 0.525 \\ \epsilon = 33.5 - 226.4E - 17.1E^2 & -0.525 < E < 0 \end{cases}$	
C4	$\begin{cases} \epsilon = -146.6E - 207.9E^2 & 0 < E < 0.525 \\ \epsilon = -17.4 - 282.8E + 121.6E^2 & -0.525 < E < 0.525 \\ \epsilon = 50.7 - 260.5E - 67.5E^2 & -0.525 < E < 0 \end{cases}$	

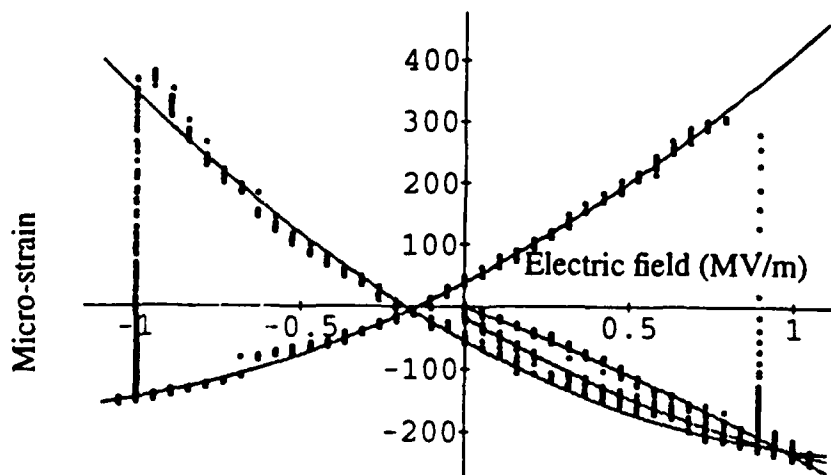


FIGURE 7. 21 Domain reorientation in piezoceramic (NC2_200) when subjected to corrosive electric field

Figure 7.21 shows domain reorientation in piezoceramics when subjected to a corrosive electric field. It appears that curing does not affect the piezoelectric properties permanently. Application of the electric field in the poling direction appears to align the domain orientation and therefore increase the piezoelectric strain coefficient. The application of a reverse electric field of the same strength does not seem to deteriorate the piezoelectric strain coefficient to the same extent. The nonlinear behavior is dominated by domain reorientation rather than electrostrictive properties.

REFERENCES

1. Chapin, C.M. and Joshi, S.P., 1991, *Composites Design, Manufacture, and Application, ICCM VIII, Hawaii*, ed. S W. Tsai and George S. Springer (Covina: SAMPE) pp. 30-D-1,10.
2. Crawley, E.F. and Anderson, E.H., 1989, *American Institute of Aeronautics and Astronautics, Inc.*, pp. 2000-2010.
3. Kranbuehl, D.E., Hoff, M., Eichinger, D.A., Loos, A.C., Freedman, W.T., Jr., 1988, *Proceedings of the American Society for Composites, Third Technical Conference*, (Lancaster: Technomic) pp. 313-323.
4. Shah, D.K., Chan, W.S., Joshi, S.P., and Subramanian, S., 1990, *Recent Developments in Composite Materials Structures*, Ed. D. Hui and C.T. Sun, AD-Vol. 19, AMD-Vol. 113, The American Society of Mechanical Engineers, pp. 19-24.
5. Tam, A.S. and Gutowski, T.G., 1988, *Proceedings of the American Society for Composites, Third Technical Conference*, (Lancaster: Technomic) pp. 255-262.

Chapter 8.

EXPERIMENTAL CHARACTERIZATION OF SMART LAMINATES

A key aspect of the research described in this report is an experimental verification of smart laminates. It is essential to demonstrate that the insertion of the piezoelectric patches within the laminate creates no microstructural defects that may be detrimental to the structural performance. In order to validate these performance characteristics of the smart laminates a full compliment of experimental evaluations are performed. Some of the results presented in this chapter should be considered as typical rather than definite because of the insufficient number of tests performed. Limited number of tests were performed because of budgetary constraints.

Panels with embedded piezoceramic patches are fabricated and cured according to the procedure described in chapter 7. A panel with a piezoceramics patch (2.5 in X 1.5 in X 0.0075 in) in a cut-out in the middle glass ply of the lay-up $[0_2^{Gr}/90_2^{Gr}/0_3^{Gl}/90_2^{Gr}/0_2^{Gr}]_T$ is cured to evaluate the bonding and fracture due to residual thermal stresses and edge stresses. Figure 8.1 shows a microscopic picture of a cross section containing piezoceramic edges. The brass electrodes are also visible in the lay-up seen in Figure 8. 1. A high magnification cross section microscopic picture (Figure 8.2) clearly shows the conductive epoxy between piezoceramic and brass electrodes. The quality of bonding is critical to the success of both embedded and surface adhered piezoelectric patches. The microscopic pictures show that a good quality bonding is achieved between the embedded piezoceramic patches and surrounding glass/epoxy plies. Extensive microscopic inspection showed no microcracks in the piezoceramic patch, conductive epoxy, electrodes and surrounding glass/epoxy plies.



FIGURE 8.1 Microscopic cross section view of an embedded piezoceramic patch.



FIGURE 8.2 High magnification microscopic view showing conductive epoxy and brass electrodes

In order to ascertain that the piezoceramic subjected to the curing cycle temperature and pressure does not have microscopic damage, scanning electron microscope pictures are taken of the cured and uncured piezoceramic. The surface of the piezoceramic patches are etched by 10% hydrofluoric acid, 10% Nitric acid and 80% distilled water by volume. The electron microscope pictures of uncured and cured piezoceramic patches is shown in Figures 8.3 and 8.4, respectively. These Figures suggest that piezoceramics subjected to curing temperature and pressure do not sustain microstructural damage.

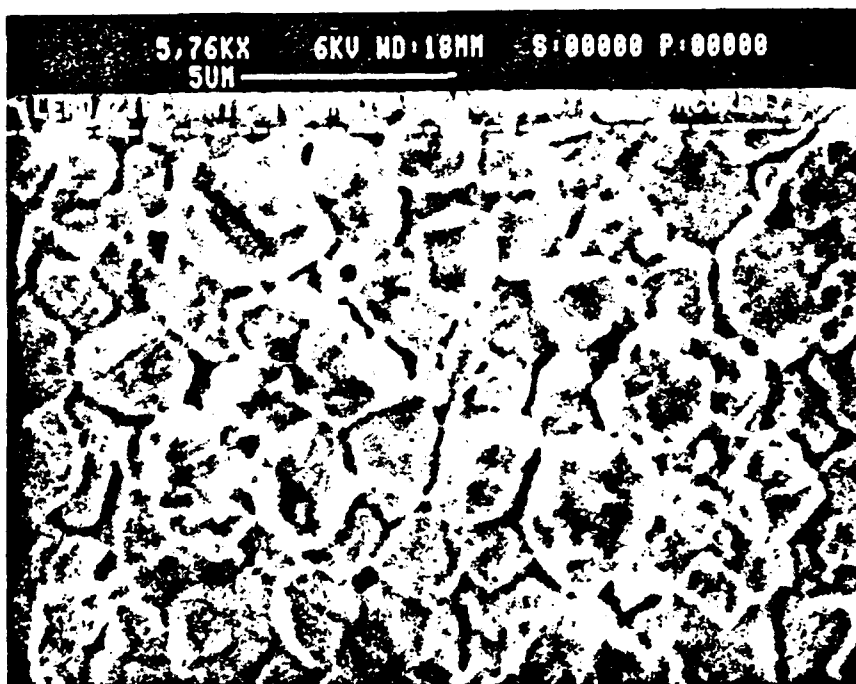


FIGURE 8.3 Scanning electron microscope photograph of uncured piezoceramic

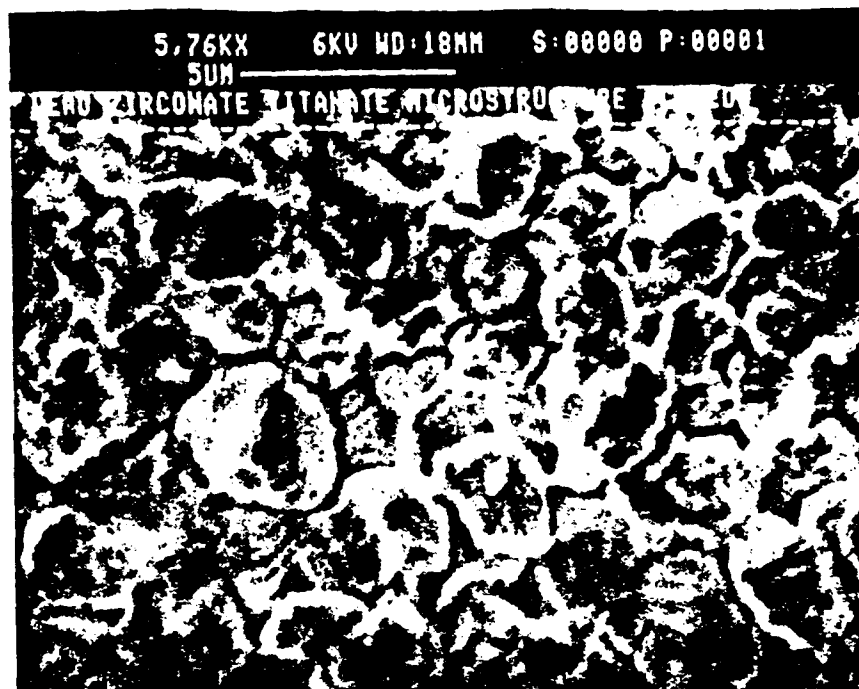


FIGURE 8.4 Scanning electron microscope photograph of cured piezoceramic

8.1 Mechanical Properties Characterization

Hercules AS4/3501-6 graphite/epoxy and 3M S250 glass/epoxy plies are laid up and cured at the Composite Materials Center autoclave facility at the University of Texas at Arlington. The fabrication and curing procedure is described in the previous chapter. Square panels (9 inch X 9 inch) are fabricated and cured. The placement of piezoceramic patches in a panel is schematically shown in Figure 8.5.

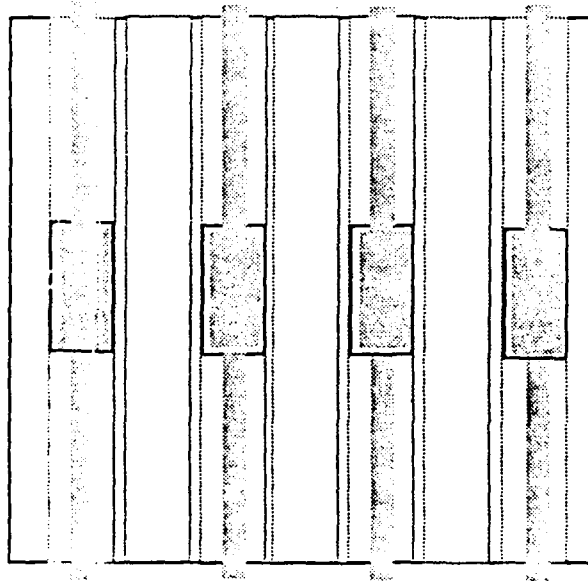


FIGURE 8.5 Schematic of the 9 inch X 9 inch panel showing placement of piezoceramic patches, brass terminals and test coupon outlines

The piezoceramic patches are two and a half inch long and one inch wide. They are placed in cut-outs in a middle glass/epoxy ply of the $[0_2^{Gr}/0_3^{Gl}/0_2^{Gr}]$ lay-up. The panels are X-ray radiographed to mark the coupon cutting lines accurately so that the cuts do not pass through the piezoceramic patches. Each panel produced four test coupons with embedded piezoceramic patches and three test coupons without piezoceramic patches. The test coupons are of nominal 1 inch width and 9 inch long with one and a half inch tabs bonded on each end. X-ray radiographs are again used to reject the test coupons with cracked piezoceramics. Strain gages in longitudinal and transverse direction are mounted on each coupon. A Servo-hydraulic MTS machine is used for tensile testing. Load and strain data are recorded using an automated data acquisition system. The stress-strain plots for coupons with embedded piezoceramic patches and without piezoceramic patches are shown in Figure 8.6. All graphite/epoxy plies and all glass/epoxy ply bounds are also shown in the Figure. The difference in apparent modulus of laminates with and without piezoceramic patches is insignificant.

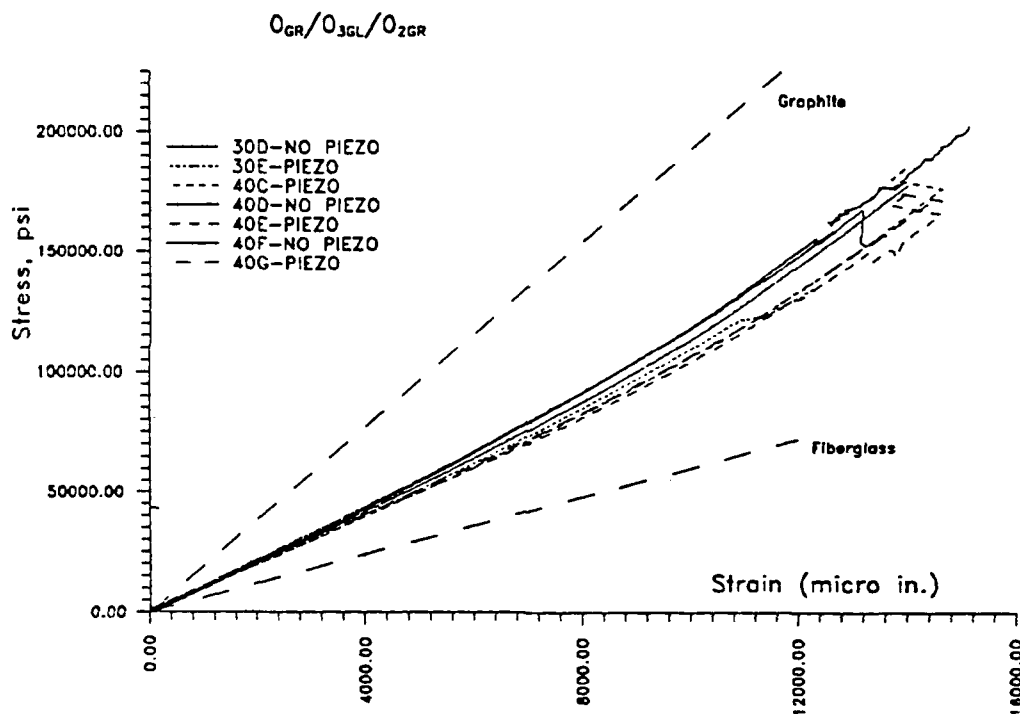


FIGURE 8.6 Stress-strain plots of coupons with and without symmetrically placed piezoceramic patches subjected to longitudinal tensile load

The final failure occurs at about 14,000 microstrain which is fiber failure strain in graphite epoxy plies. The glass/epoxy plies remain intact but the piezoceramic encapsulated in glass/epoxy plies cracks into small pieces. The failure of graphite epoxy plies is a typical brittle failure with debonding and matrix failure in the transverse direction. The photographs of the failed specimens showing a broom-type failure mode are shown in Figure 8.7.

Another set of coupons with and without piezoceramic patches are subjected to incremental tensile load. The load increments are in 20% of the ultimate failure load. The test coupons are C-scanned and X-ray radiographed after each load increment. The specimens are subjected up to 60% of the ultimate tensile load at which extensive transverse matrix cracking near the edges occurred due to improper placement of the tabs. The X-ray radiographs revealed no cracks in the piezocer-

amic patches up to 60% of the ultimate load. There is no definite evidence of delamination from C-scans and microscopic inspection of the edges of the test coupons. Destructive microscopic inspection of the sequence of longitudinal and transverse cross sections providing definite evidence of cracks and delaminations has not been done.

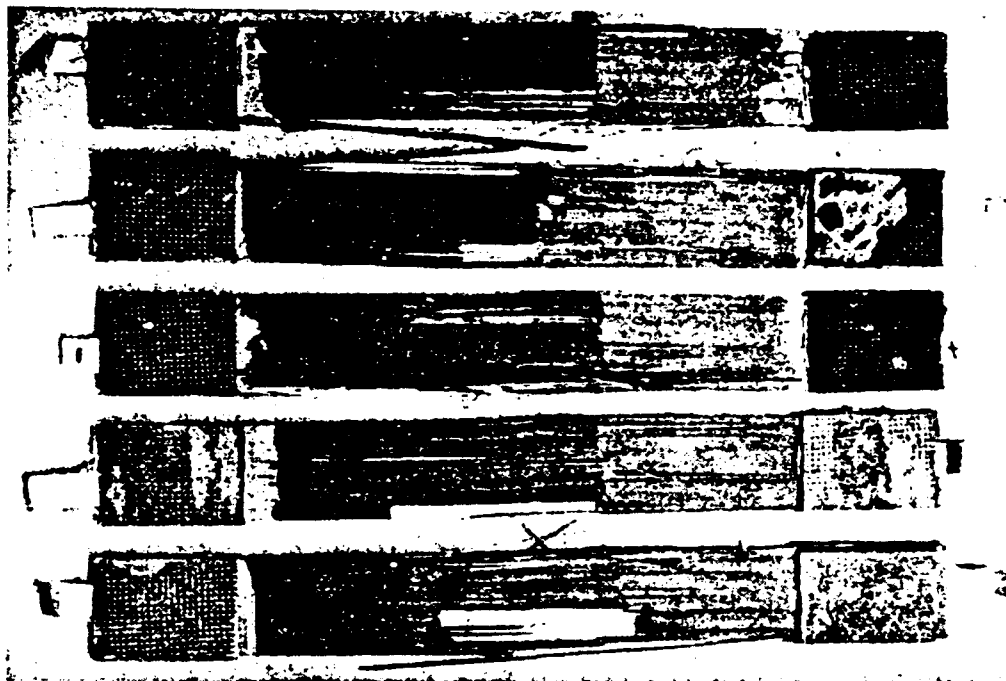


FIGURE 8.7 Photographs showing mode of failure of unidirectional laminated composite with embedded piezoceramic patches

8.2 Impact Induced Fracture

It is well known that a transverse impact by a foreign object creates extensive damage in the form of matrix cracking and delamination [1-5]. A set of impact tests are performed to evaluate the effect of the presence of piezoceramic patches on impact induced damage. Initial results indicate that a presence of a piezoceramic patch does not adversely affect the incipient damage due to a transverse impact. The damage to piezoceramics in the vicinity of an impact is also minimal. Optical microscopic pictures of selected cross sections, X-ray radiographs and ultrasonic C-scans are employed to characterize the impact damage.

The coupons for impact testing are cut from the panels used to demonstrate the placement of multiple piezoceramic patches in laminated composites. The base laminate is chosen to be $[0_5/90_5/0_5]$ graphite epoxy cross-ply. Three glass plies with zero degree orientation with piezoceramics in cut-outs in the middle ply are placed at each $0/90$ interface. The test coupons are 1.5 inch wide and 9 inch long. Three piezoceramic patches are placed at each $0/90$ interface. Piezoceramic patches are 0.5 inch wide and 1 inch long. The piezoceramic patches are placed at the same planer locations at two interfaces. The piezoceramic and terminal strips placement is shown in Figure 8.8. Some Coupons have a different pattern of terminal strip placement but all of them have the same placement of piezoceramic patches.

An equal number of specimens are impacted at the center of the center piezoceramic patch, at the edge of the center piezoceramic patch and between the center and left or right side piezoc-

ramic patch, respectively. A half inch diameter steel ball is used as an impactor. A pressurized air gun is employed to propel the steel ball to a nominal speed of 30 m/sec. The specimens are clamped six inches apart.

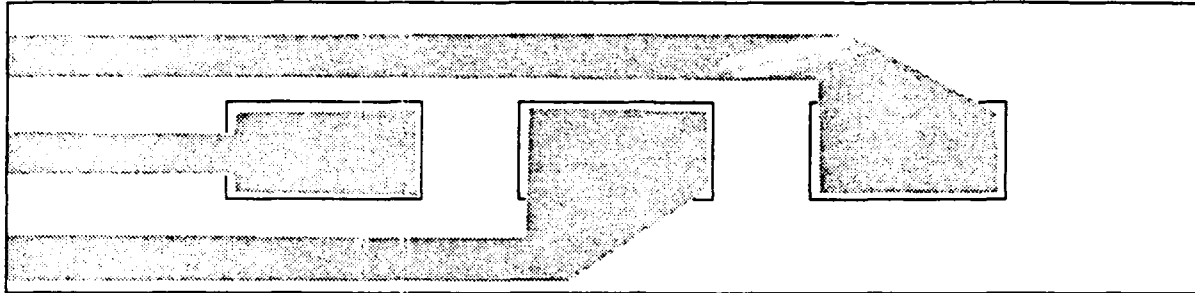


FIGURE 8.8 Schematic showing placement of piezoceramic patches and terminals at each 0/90 interface of the base laminate

Each specimen is X-ray radiographed after impact to identify cracks in the piezoceramic patches. Major cracks in piezoceramics can be identified this way. However, microcracks are hard to identify because of the placement of piezoceramics at the same planer locations at two interfaces. C-scans are produced with the transducer focused at three planes through the thickness. The scanned planes are the top interface, mid-plane and bottom interface. The C-scans are taken from both sides producing six scans for each specimen. The C-scans of the base lay-up specimens (without piezoceramic patches) showed the typical delamination pattern. However, the presence of piezoceramic patches made the interpretation of C-scans for delamination a difficult task. The observation of C-scans in the vicinity of piezoceramic patches showed less delamination compared to the base laminates.

All the specimens are cut at selective cross sections and photographed through an optical microscope. The base laminates showed typical incipient damage due to transverse impact. Figure 8.9 shows a transverse cross section at the impact center. Shear cracks in the proximal plies that turn in to delamination between 0° glass/epoxy plies and middle 90° graphite/epoxy plies are clearly seen in the cross section micrograph. The flexural crack in distal plies that results into delamination of 90° graphite/epoxy plies and 0° glass/epoxy plies is also clearly visible. Figures 8.10 and 8.11 show a transverse cross section at the impact point of a laminate with embedded piezoceramic patches. The laminate is impacted at the center of the middle piezoceramic patches. The shear crack in proximal layers cracks the piezoceramic patch and debonds the brass electrodes. It should be noted that electrodes do not cover whole surfaces of the piezoceramic patches as shown in Figure 8.8. The flexural crack in the distal layer results in extensive damage to the piezoceramic patch in the distal side glass/epoxy plies. Figure 8.12 shows a longitudinal cross section passing through the impact center. The shear cracks in the middle 90° graphite/epoxy plies and piezoceramics are visible. The piezoceramic patch on the distal side shows flexural cracks in the vicinity of the impact center. Delamination is restricted to a 90° graphite/epoxy middle layer and 0° glass/epoxy distal layers.

C-scans and X-ray pictures are also utilized in characterizing the impact induced damage. These observations support the conclusions drawn from the microscopic cross sectional views of incipient damage due to transverse impact.



FIGURE 8.9 Transverse cross section through the impact center of a base laminate showing matrix cracks and delamination.

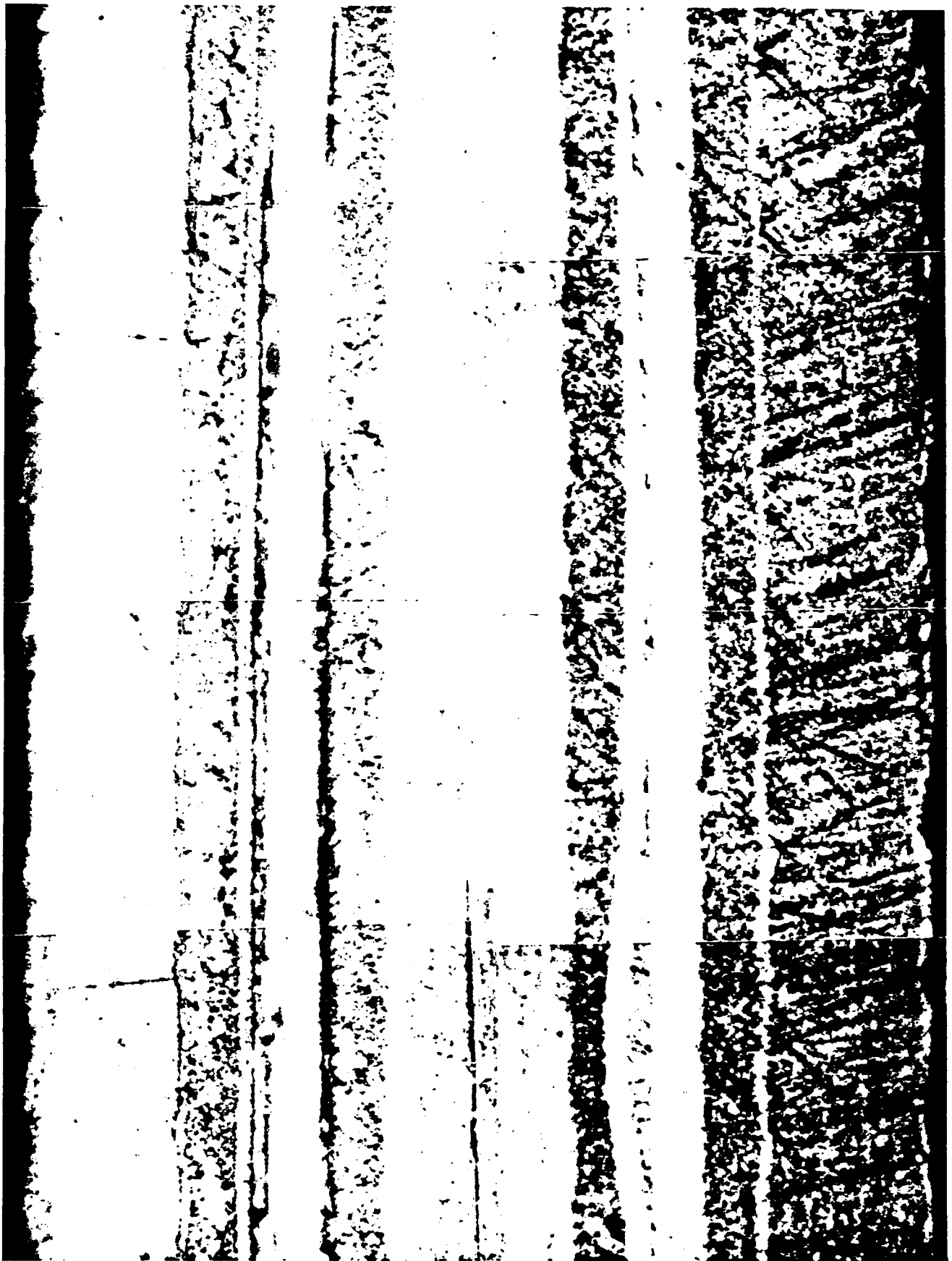


FIGURE 8.10 Part of the transverse cross sectional view of an impacted specimen containing embedded piezoceramic patches.

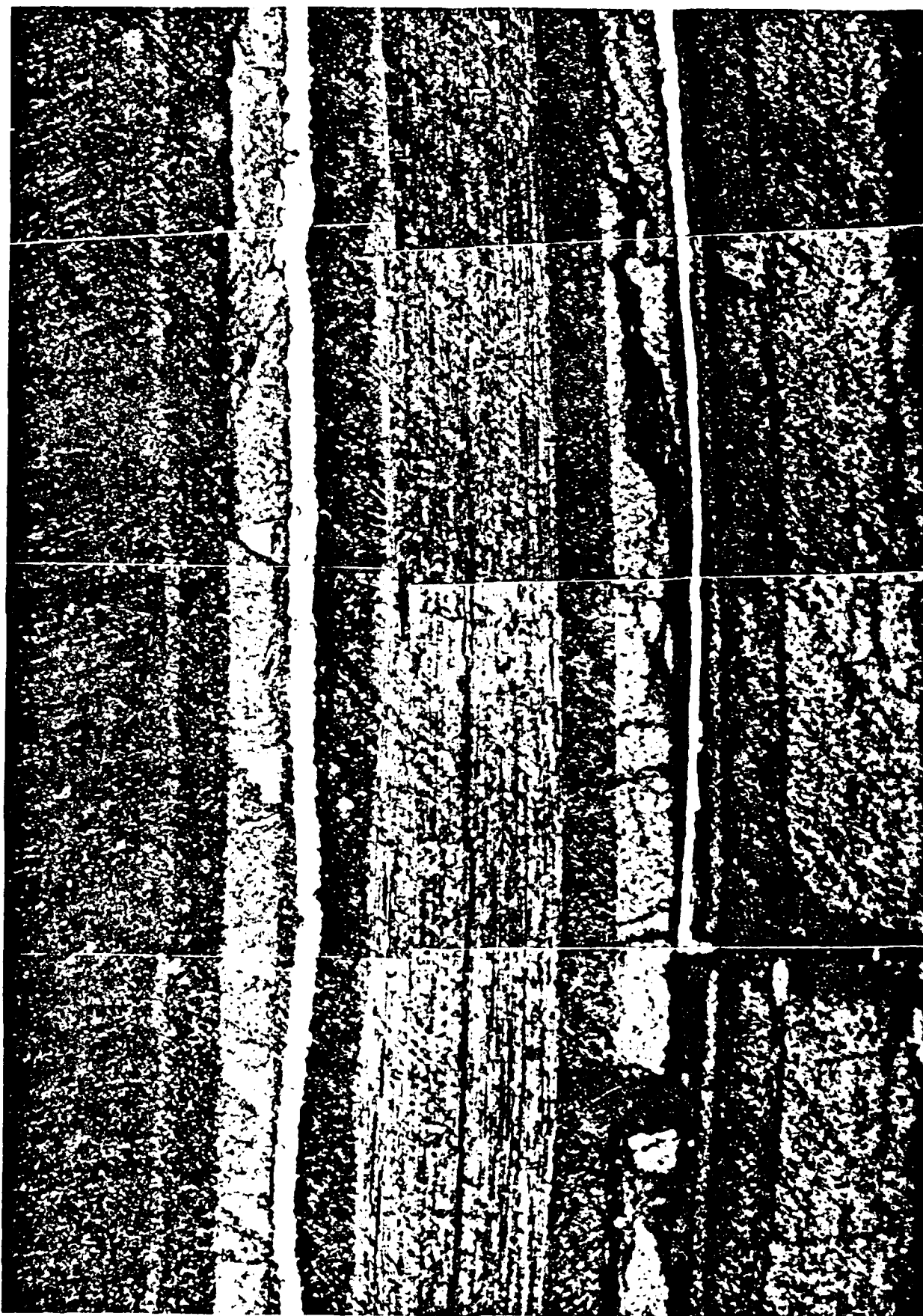


FIGURE 8. 11 The continuing part of the cross sectional view of an impacted specimen shown in Figure 8.10.

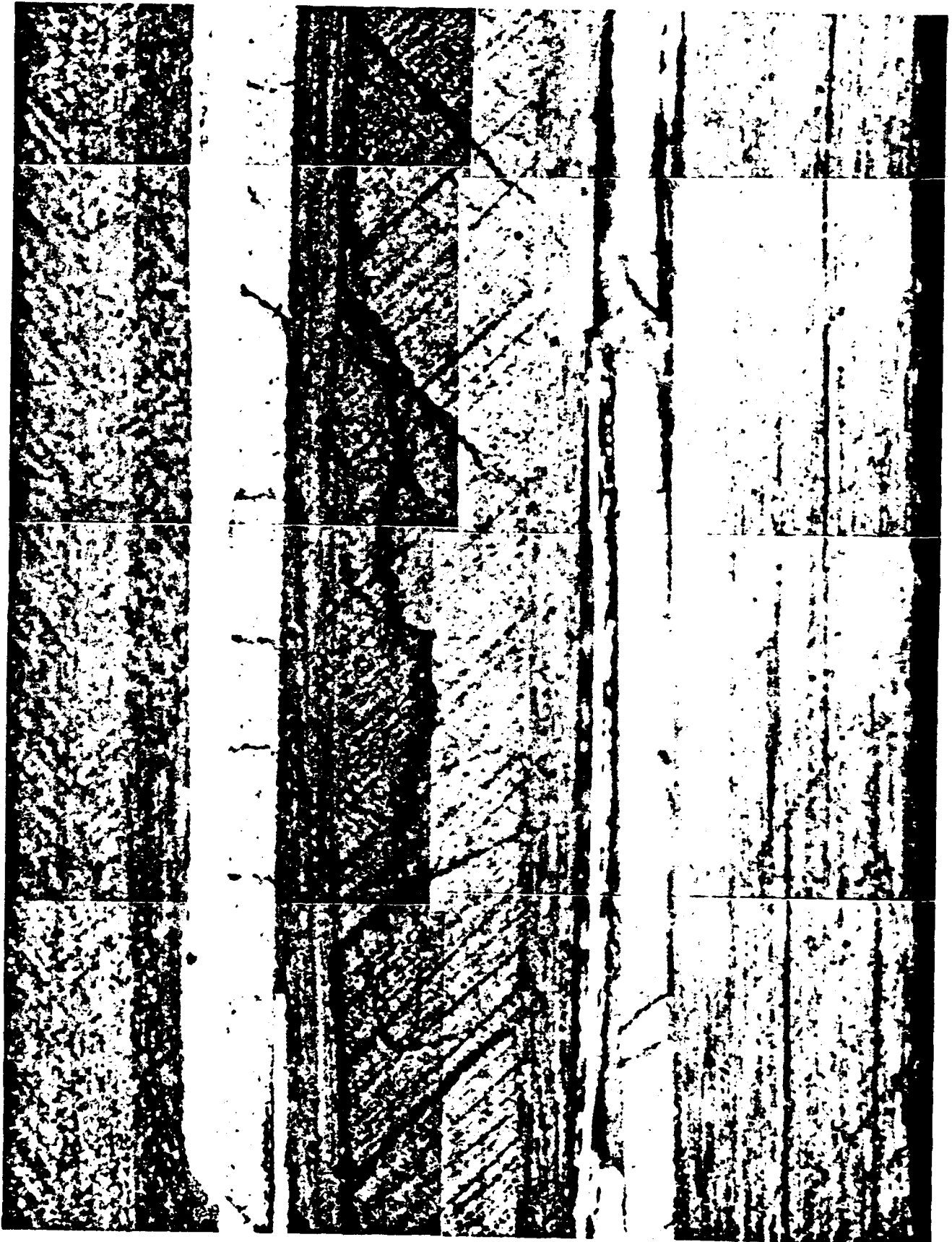


FIGURE 8. 12 The longitudinal cross section of an impacted specimen showing matrix cracks and delamination

REFERENCES

1. Joshi, S.P., Sun, C.T., "Impact Induced Fracture in Laminated Composites", *Journal of Composite Materials*, Vol. 19, No. 1, 1985, pp 51-66.
2. Joshi, S.P., Sun, C.T., "Impact Induced Fracture in a Quasi-Isotropic Laminate", *ASTM Journal of Composite Technology and Research*, Vol. 9, No. 2, 1987, pp 40-46.
3. Joshi, S.P. and Sun, C.T., "Impact Induced Fracture Initiation and Detailed Dynamic Stress Field in the Vicinity of the Impact", *Joint Symposium on Composite Materials Science and Engineering*, Delaware, September 23-25, 1987.
4. Joshi, S.P., "Impact-Induced Damage Initiation Analysis: An Experimental Study", *ASC Third Technical Conference on Composite Materials*, Seattle, Washington, September 25-29, 1988.
5. Bogdanovich, A.E., Iarve, E.V. and Joshi, S.P., "Impact Deformation and Failure Analysis of Laminated Composite Plates", *Impact and Buckling of Structures* (Ed: David Hui and Isaac Elishakoff), Ad-Vol. 20, AMD-Vol. 114, presented at the Winter Annual Meeting of the American Society of Mechanical Engineers, Dallas, Texas, November 25-30, 1990, pp 1-5.

